Experimental Study of Micro-/Nano-Scale Cutting of Aluminum 7075 and P20 Mold Steel

A Thesis
Presented to
The Academic Faculty

by

Chee Keong Ng

In Partial Fulfillment
of the Requirements for the Degree
Master of Science in Mechanical Engineering

Woodruff School of Mechanical Engineering
Georgia Institute of Technology
Feburary, 2005

Experimental Study of Micro-/Nano-Scale Cutting of Aluminum 7075 and P20 Mold Steel

Approved by:

Dr. Shreyes N. Melkote
School of Mechanical Engineering
Georgia Institute of Technology

Dr. Thomas R. Kurfess
School of Mechanical Engineering
Georgia Institute of Technology

Dr. Jack Lackey
School of Mechanical Engineering
Georgia Institute of Technology

Date Approved: March 3, 2005

ACKNOWLEDGEMENTS

This project would not have been possible without the support of National Science Foundation (NSF) Grant # DMI-0300457 for providing the research funds. In addition, I would also like to show my heartfelt appreciation to Professors M. Rahman and A.S. Kumar of The National University of Singapore (NUS) for providing advice and access to the facilities in the Advanced Manufacturing Laboratory, NUS. The access to the Toshiba ULG-100(H^3) machine as well as the Scanning Electron Microscope (SEM) facilitated the execution of the experiments and was instrumental in the success of this project.

In addition, several organizations provided advice as well as additional resources that contributed to the successful completion of this project. I would like to thank Dr. Ed Oles, Mr. Kenneth Niebauer and Mr. Bill Alexander of Kennemetal Inc. for answering my queries, providing advice and assistance in the measurement of the cutting edge radius of the carbide inserts used in this project. I would also like to take this opportunity to thank Mr. Jim Merzlak of Tennalum for his kind assistance in measuring the grain size of the aluminum workpiece used in the experiments.

I would also like to express my sincere appreciation to the lab officers, Mr. Neo Ken Soon, Mr. Tan Choon Huat and Mr. Nelson Yeo for showing patience and providing invaluable assistance and guidance in coaching me in operating various machines and equipment during my time in the Advanced Manufacturing Laboratory. In addition, special thanks also goes out to Mr. Steven Sheffield, for his invaluable assistance and

guidance in providing me with an opportunity in learning to operate numerous machines and equipment here at Georgia Tech.

I would also like to thank the faculty members of the Precision Machining Research Consortium and my thesis committee at Georgia Tech especially my advisor, Dr. Shreyes Melkote for providing an outstanding research environment. The completion of this project would not have been possible without the patience, invaluable advice and guidance provided by Dr. Melkote during the course of my research.

I would also like to thank my fellow students, Sathyan, Ramesh, Kai, Xavier and Sangil for their willingness to assist me and their insightful discussions throughout the course of my research.

My most sincere and heartfelt gratitude goes out to my parents. All this would not have been possible without their love, numerous sacrifices and support. Their constant words of encouragement and advice have never failed to spur me on to greater heights.

Last but certainly not least, I would like to take this opportunity to show my most heartfelt appreciation to my wife, Chern Phing. You have always been there for me with infinite encouragement, support and unconditional love. You have been my constant source of inspiration and the other half that makes me complete. I would have never been able to complete this task without the sacrifices you made.

TABLE OF CONTENTS

LIST OF TABLES

LIST OF FIGURES

LIST OF SYMBOLS

A	Material constant in Johnson and Cook equation
B	Material constant in Johnson and Cook equation
C	Material constant in Johnson and Cook equation
c	Constant in Manjunathaiah and Endres' model
D	Material constant in Johnson and Cook equation
E	Material constant in Johnson and Cook equation
F_c	Cutting Force
F_T	Thrust Force
h	Undeformed chip thickness in Manjunathaiah and Endres' model
k	Normal stress factor in Manjunathaiah and Endres' model
m	Material constant in Johnson and Cook equation
n	Material constant in Johnson and Cook equation
p	Penetration depth
r	Cutting ratio
r_n	Cutting edge radius in Manjunathaiah and Endres' model
r_e	Cutting edge radius
S	Shear stress factor in Manjunathaiah and Endres' model
S_a	Areal surface roughness parameter
S_q	Areal surface roughness parameter
t	Undeformed chip thickness
t_c	Deformed chip thickness

T	Instantaneous temperature in Johnson and Cook equation
T_m	Melting point temperature in Johnson and Cook equation
T_∞	Ambient temperature in Johnson and Cook equation
u	Total energy per unit volume
u_s	Shear energy per unit volume consumed on the shear plane
u_f	Friction energy per unit volume consumed on the tool face
w	Width of cut
V	Cutting velocity
α	Effective rake angle
γ_{ave}	Predicted average rake angle
γ_0	Nominal orthogonal rake angle of the tool
δ	Deformation depth
ε	Strain,
$\dot{\varepsilon}$	Strain rate
$\dot{\varepsilon}_o$	Reference strain rate
φ	Shear angle
ψ	Inclination angle of deformation zone
σ	Flow stress
θ	Angle which defines the separation point
τ	Shear stress

SUMMARY

The marked increase in demand for miniaturized consumer products in a broad range of potential applications including medical, telecommunication, avionics, biotechnology and electronics is a result of advancements in miniaturization technologies. Consequently, engineering components are being drastically reduced in size. This coupled with the quest for higher quality components, has imposed more stringent requirements on manufacturing processes and materials used to produce micro components. Hence, the development of ultra precision manufacturing processes to fabricate micro-scale features in engineering products has become a focal point of recent academic and industrial research.

However, much attention in the area of micro-manufacturing, especially micro-mechanical machining, has been devoted to building miniature machine tools with nanometer positioning resolution and sub-micron accuracy. There is lack of fundamental understanding of mechanical machining at the micro and nano scale. Specifically, basic understanding of chip formation mechanisms, cutting forces, size-effect in specific cutting energy, and machined surface integrity in micro and nano scale machining and knowledge of how these process responses differ from those in macro-scale cutting are lacking. In addition, there is a lack of investigations of micro and nano scale cutting of common engineering materials such as aluminum alloys and ferrous materials.

This thesis proposes to advance the understanding of machining at the micro and nano scale for common engineering alloys. This will be achieved through a series of systematic micro and nano cutting experiments. The effects of cutting conditions on the

machining forces, chip formation and machined surface morphology in simple orthogonal micro-cutting of a ferrous, P20 mold steel (30 HRC), and a non-ferrous structural alloy, aluminum AL7075 (87 HRB), used in the mold making and rapid prototyping industry will be studied. The data will also be compared with data obtained from conventional macro-scale cutting. In addition, the applicability of conventional metal cutting theory to micro and nano cutting test data will be examined. The analysis will provide a better understanding of machining forces, chip formation, and surface generation in micro and nano scale cutting processes and how they differ from macro-scale cutting.

CHAPTER 1

INTRODUCTION

The insightful lecture, “There’s Plenty of Room at the Bottom”, by acclaimed Nobel laureate Dr. Richard Feynman, sparked a revolution in miniaturization technology in the late 1950s. Since then, much of the world’s miniaturization technology has advanced at an astonishing pace. In particular, there has been a marked increase in demand for miniaturized consumer products in a broad range of applications including medical, telecommunication, avionics, biotechnology and electronics as a result of emerging miniaturization technologies.

Current microfabrication techniques can be broadly categorized into three main process groups, namely Bulk Micromanufacturing, Surface Micromachining and the LIGA Process. These techniques are also commonly referred to as “micro-engineering”, “micro-manufacturing” and more recently, “nano-manufacturing”.

Bulk micromachining has been widely used since the 1960s in the production of microelectronics. It involves the physical or chemical removal (dry or wet etching) of material from bulk substrates in forming three dimensional micro-components. This technique involves high material losses and is also limited to primarily silicon-based components with low aspect ratios. Surface Micromachining is an additive technique where the micro-components are manufactured through building up materials in a layered format onto the substrate. Although this technique is suitable for micro-components with more complex geometries and is not as restrictive in terms of the materials used, it involves the design and production of complex masks used in the fabrication process. The

technique is tedious, expensive and the fabricated products also face serious engineering-related issues regarding interfacial stresses and stiction. The LIGA Process draws on x-ray lithography, electroforming and plastic molding processes in the production of parts. The LIGA Process allows production of metallic components and is also capable of fabricating parts with high aspect ratios. However, it is a very expensive process and involves high material losses during the fabrication process. In general, current techniques in microfabrication can be described as costly, time-consuming, geometrically and material restrictive and not environmentally friendly due to the chemical processes involved (Hsu, 2002).

The quest and demand for even smaller, more reliable and durable engineering components, while greatly increasing the number of functions these micro-components offer, has imposed more stringent requirements on both the microfabrication processes and the materials used. Consequently, there has been an increased demand for micro-scale engineering components to be fabricated using harder common engineering alloys such as titanium alloys, steels, stainless steels, aluminum alloys, ceramics and other ferrous alloys and composites (Aronson, 2003).

Mechanical machining (cutting) is a well established material removal process for fabricating three dimensional macro-scale components. With recent advancement in micro and nano actuation devices, mechanical machining can, in principle, be used in the fabrication of micro-scale components. Mechanical machining at the micro-scale, more commonly referred to as micro-/ nano-cutting, is able to produce intricate three-dimensional features while at the same time satisfy stringent dimensional tolerance and surface finish requirements required of micro and nano scale components. However,

there are still numerous challenges in micro-cutting to be overcome before it can emerge as a technically sound, economically viable and reliable process to fabricate micro-components. Hence, the development of ultra precision micro-cutting manufacturing processes to fabricate micro-components in engineering products has become a focal point of recent academic and industrial research.

In the last few decades, much attention in the area of micro-manufacturing, especially micro-mechanical machining, has been devoted to building miniature machine tools with nanometer positioning resolution and sub-micron accuracy. In recent times, there have been extensive studies of tool life, edge radius effect, surface generation, "size-effect", minimum chip thickness, microstructural effects as well as finite element modeling and molecular dynamics simulation of micro and nano scale cutting. However, fundamental understanding and general consensus on the mechanism that dominates mechanical machining at the micro and nano scale is still lacking. Specifically, basic understanding of chip formation mechanisms, cutting forces, size-effect in specific cutting energy, and machined surface integrity in micro and nano scale machining and knowledge of how these process responses differ from those in macro-scale cutting are lacking. In addition, the range of thickness of cut in published data of current scientific investigation in micro and nano scale machining is limited. Furthermore, there is a lack of investigations of micro and nano scale cutting of common engineering materials such as aluminum alloys and ferrous materials. Hence, a methodical study conducted over a wider range of cutting conditions with common engineering materials would complement existing data, thereby allowing for further enhancement of knowledge in micro and nano scale machining processes.

1.1 Objectives

The objective of this thesis is to advance the understanding of machining at the micro and nano scale for common engineering alloys. This will be achieved through a series of systematic micro and nano cutting experiments. The effects of cutting conditions on the machining forces, chip formation and machined surface morphology in simple orthogonal micro-cutting of a ferrous, P20 mold steel (30 HRC), and a non-ferrous structural alloy, aluminum AL7075 (87 HRB), used in the mold making and rapid prototyping industry will be studied. The data will also be compared with data obtained from conventional macro-scale cutting. In addition, the applicability of conventional metal cutting theories, such as those of Merchant and Oxley (Merchant, 1945; Oxley, 1989), to micro and nano cutting test data will also be examined in this investigation.

1.2 Outline of Thesis

Chapter 2 provides a critical review of prior and on-going research in micro and nano scale machining with emphasis being placed on cutting force, chip geometry, surface morphology, size-effect and process modeling. A detailed description of the machines, selection of workpiece materials and cutting tools, experimental procedures used to acquire the experimental data in this study is provided in Chapter 3. Chapter 4 will present the experimental data and general discussion and possible explanations of the significant trends observed for both AL7075 and P20. The discussion will focus on the cutting force, chip geometry, surface morphology of the machined workpieces as well as derived parameters using Merchant's theory. The applicability of two existing macro-scale metal cutting process models will be examined in Chapter 5. Chapter 6 will

summarize the significant findings of this experimental study, outline the current limitations raised by this study as well as provide some recommendations for future work that would further enhance the fundamental understanding of the mechanism that dominate mechanical machining at the micro and nano scale.

CHAPTER 2

LITERATURE REVIEW

This chapter aims to provide an overview of past and on-going scientific investigations relating to micro and nano scale machining. A general synopsis of micro and nano scale cutting experiments, precision machines, cutting tools and workpiece materials employed in past studies will also be presented. The emphasis of this literature review is placed on experimental studies of cutting forces, size-effect, chip geometry and surface morphology.

2.1 Introduction

Precision machining has emerged as a vital aspect in meeting the requirements of technological advancement. The continuing quest for smaller, more reliable consumer and industrial products is also pushing current limits in miniaturization technology. In view of this, the fabrication of micro and meso scale devices has presented researchers with new and exciting challenges. Several scientific investigations in the field of micro and nano scale machining have also been rigorously conducted in order to better comprehend the influence of the underlying and dominant mechanisms of the machining process.

Current scientific investigations into micro and nano scale machining can be broadly classified into two main groups, namely experimental and modeling studies. Experimental investigations in micro and nano scale machining can be further sub-categorized into the following groups: (i) The construction and evaluation of meso and

micro scale machine tools in creating micro and nano scale structures (Nomura and Suzuki, 1992; Weck and Fischer, 1999; Gao et al., 2000; Shinno and Hashizume, 2001; Tanaka, 2001; Vogler et al., 2002; Cox et al., 2004) and (ii) the use of conventional ultra-precision machines and cutting tools in micro and nano scale cutting tests (Ohmori and Takada, 1982; Eda et al., 1985; Sato et al., 1991; Moriwaki et al., 1993; Lucca et al., 1991, 1993, 1994). Modeling studies, of which there are many, includes the use of molecular dynamics simulation and finite element method to predict and characterize both the material behavior as well as process parameters when cutting at the micro and nano scale is being performed (Komanduri et al., 1998; Kim et al., 1999; Raczy et al., 2004; Lin et al., 2004; Liu and Melkote, 2004).

2.2 Overview of Meso-/ Micro-Scale Machine Tools

Recent advances in actuation and control systems have initiated the development of meso and micro scale ultra-precision machine tools (Tanaka, 2001). The development of meso and micro scale machine tools provides researchers with instruments to perform nanometric cutting experiments as well as to fabricate micro-components.

In addition, because smaller machine tools are less affected by environmental fluctuations such as changes in temperature, pressure and humidity as compared to their macro-scale counterpart, they are perceived to be superior in terms of accuracy (Cox et al., 2004). Furthermore, the reduced mass of the miniature machine tool reduces the inertia force required to drive the machine tool system, thus consuming less energy and yet providing higher positioning accuracy. Hence, the use of miniature machine tools is also seen as having immense potential in reducing production costs (Breguet et al., 2000;

Tanaka, 2001; Cox et al., 2004). Consequently, extensive research involving the construction of meso and micro scale ultra-precision machine tools has since been pursued.

The majority of meso and micro scale machine tools utilize piezoelectric actuators to provide positioning resolution in the nanometer range. Other actuation systems employed for nanometric level positioning include direct drive linear motor with crossed roller bearing (Cox et al., 2004) and voice coil actuated drive technology (Vogler et al., 2002). In addition, materials with high stiffness and low thermal deformation response such as Invar 36 steel alloy are often employed to provide structural support in the construction of meso and micro scale machine tools. Contact devices such as strain gauges, thermocouples and force dynamometers are typically integrated into the meso and micro scale machine tools to monitor process parameters such as cutting forces and cutting temperatures. The meso and micro scale machine tools are subsequently assembled on a vibration isolation platform. Typical meso and micro scale machine tools are illustrated in the following diagram, Figure 2.1.

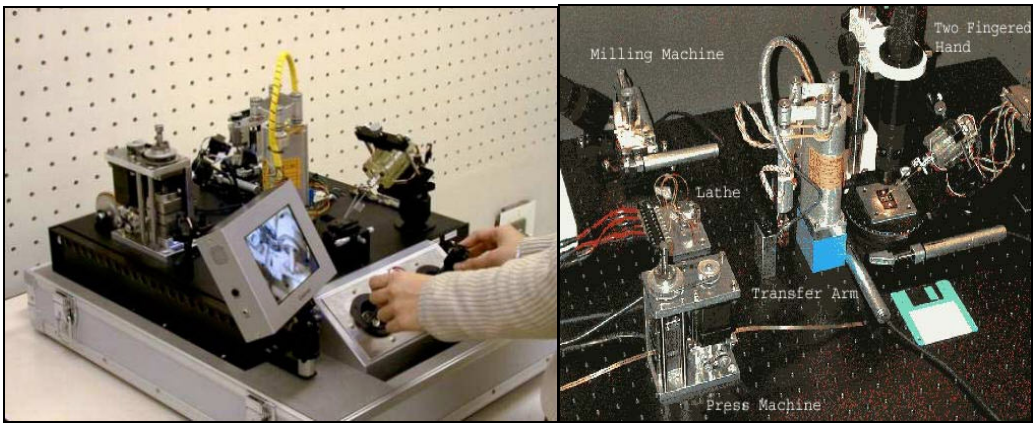

(a) (b)

Figure 2.1: (a) Microfactory (b) Meso-/ Micro-Scale Machine Tools in Microfactory (Tanaka, 2001)

The main focus in the development of meso and micro scale machine tools is the performance evaluation of these ultra-precision miniature machine tools in the assembly and fabrication of micro-components. The performance, response and accuracy of the positioning system, dynamic rigidity of the system as well as the sensitivity of the force sensors are often evaluated to ensure that the miniature machine tool satisfies pre-defined machining requirements (Lu and Yoneyama, 1999; Vogler et al., 2002; Cox et al., 2004).

These meso and micro scale machine tools are subsequently used to fabricate micro and nano scale components as illustrated in Figure 2.2. Diamond tools are most often employed in meso and micro scale machine tools since diamond is the hardest material that can be sharpened to an atomic scale (Nakayama, 1997). Cutting tools used in scratch tests include Atomic Force Microscope probes (Ashida et al., 2001) and Scanning Tunneling Microscope diamond probes (Lu and Yoneyama, 1999).

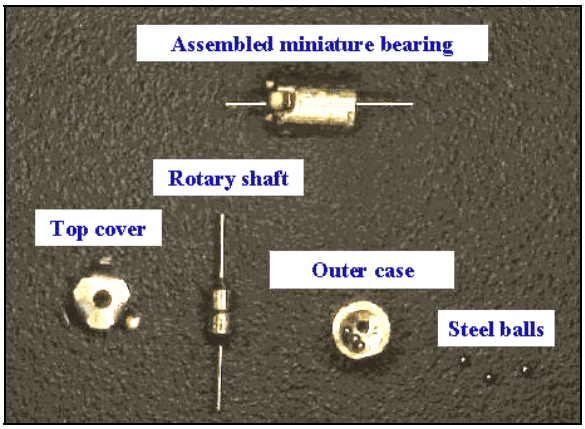

Figure 2.2: Micro-Components Fabricated by Meso-/ Microscale Machine Tools (Tanaka, 2001)

Another objective in developing meso and micro-scale machine tools is to provide researchers with an instrument to conduct micro and nano scale cutting, nano-scratching

and nano-indentation experiments. These experiments will be discussed in the following section.

2.3 Overview of Micro-/ Nano-Scale Cutting Experiments

Micro and nano scale cutting is a relatively new field that has been explored over the last 50 years in the pursuit of the miniaturization of engineering components. Due to the lack of prior comprehensive understanding of micro and nano scale cutting, the approach to micro and nano scale cutting has been predominantly governed by more established macro-scale machining knowledge.

Hence, scientific investigations were subsequently conducted to investigate and better comprehend the mechanisms that govern micro and nano scale cutting. Various elements such as the edge radius of the tool, microstructure of the work material and the behavior of the work material were observed to influence cutting processes at the micro and nano scale. Numerous experiments were subsequently conducted to seek qualitative and quantitative explanations for phenomena observed in micro and nano scale cutting.

These micro and nano scale cutting experiments were generally conducted using ultra-precision diamond turning machines, ultra-precision flying cutting machines, grinding machines and specially-built meso and micro scale machine tools. Cutting experiments in the undeformed chip thickness range of 1 nm to 80 μm have been reported.

As discussed in the preceding section, single crystal diamond tools are the preferred choice for cutting tools in micro and nano scale cutting experiments. The cutting edge radius of single crystal diamond tools used in micro and nano scale cutting

experiments are reported to be in the range of 10 – 100 nm. Other cutting tools used in micro and nano scale cutting experiments include polycrystalline diamond, cubic boron nitride, high speed steel (Nakayama and Tamura, 1968) and tungsten carbide tools (Weule et al., 2001). The edge radii of these alternative cutting tools range between 2 μm and 635 μm.

Aluminum, brass and copper are some of the common work materials employed in micro and nano scale cutting experiments. The choice of work materials in micro and nano scale cutting experiments is normally constrained by the diamond cutting tools used because these tools are known to exhibit rapid tool wear when used to machine ferrous materials. Hence, most of the work materials used in past and on-going research are soft, ductile and non-ferrous in nature. Nevertheless, micro and nano scale cutting of steel (Weule et al., 2001), stainless steels (Evans, 1991), silicon (Gao et al., 2000) and tungsten carbide (Liu et al., 2003) have also been conducted.

2.3.1 Cutting Forces and Size-Effect

Cutting force is a parameter widely studied by researchers in the attempt to grasp a better understanding of the mechanism of the cutting process. The study of cutting forces is also essential in the development of meso-/ micro-scale machine tools (Lu and Yoneyama, 1999), understanding the cutting process in micro and nano scale cutting (Backer et al., 1952; Nakayama and Tamura, 1968; Hasegawa et al., 1975; Furukawa et al., 1988; Sato et al., 1991; Lucca et al., 1991, 1993, 1994; Gao et al., 2000) as well as the verification of process models and molecular dynamics simulations (Shimada et al., 1992; Shimada et al., 1993; Kim and Kim, 1996; Kim et al., 1999; Vogler et al., 2004).

In these studies of cutting forces, it is observed that the specific cutting energy increases as the undeformed chip thickness decreases, and this phenomenon has since been termed size-effect. Numerous studies have been conducted in an attempt to explain the size-effect phenomenon in cutting processes. Although many explanations have also been proposed to elucidate the cause of size-effect (Kopalinsky and Oxley, 1984; Kim and Kim 1996; Dinesh et al., 2001; Shaw, 2003; Atkins, 2003; Joshi and Melkote, 2004), there is still no general consensus and definitive explanation established for the size-effect phenomenon.

Nakayama and Tamura (1968) performed an experimental investigation on the cutting of brass with high speed steel tools with edge radii measuring 3 – 4 μm at different rake angles (0º, -20º, -40º). The cutting and thrust forces were reported to have a positive intercept at a zero depth of cut, indicating the existence of size-effect, except when cutting with a 0º rake angle tool. It was suggested that the disproportional consumption of energy in plastic flow in the subsurface layer, together with the change in undeformed chip thickness and the blunting of the cutting edge, might be possible sources contributing to size-effect.

Lucca et al. (1991) discovered in their experimental investigation that at small undeformed chip thickness values, rubbing on the flank face of the cutting tool due to workpiece material elastic recovery and ploughing become important components in the cutting process as the undeformed chip thickness becomes comparable to the edge radius of the tool. These components are consequently proposed as possible causes of the increase in specific energy. In a separate experimental investigation, Lucca et al. (1993) found that the nominal rake angle and the tool edge profile exerted considerable influence

on the resulting forces and the energy dissipation over an undeformed chip thickness range of 10 nm to 20 μm. However, when the undeformed chip thickness becomes comparable to the edge radius of the cutting tool, the effective rake angle, rather than the nominal rake angle, has a more significant effect on the cutting forces. Lucca et al. (1994) also suggested that the tool edge condition has a significant effect on the resulting forces at undeformed chip thickness values smaller the tool edge radius.

Sato et al. (1991) also reported the presence of size-effect in the cutting force at an undeformed chip thickness of 1 μm in their investigation of micro-cutting of single crystal aluminum. Furukawa et al (1988) observed the initiation of size-effect in the cutting force at an undeformed chip thickness of 3 μm. They proposed that the initiation point of size-effect is influenced by a combination of factors such as work material property, cutting edge sharpness and chip geometry.

Nakayama and Tamura, Lucca et al. and Furukawa et al.'s experimental investigations indicate that the edge radius of the tool has significant influence on the cutting forces at very small undeformed chip thicknesses. Hence, it is not surprising that numerous scientific investigations involving the edge profile of the cutting tool in micro and nano scale cutting have been conducted (Waldorf et al., 1998; Manjunathaiah and Endres, 2000; Fang, 2003). These investigations involving edge-radiused tools will be discussed in section 2.4.1

2.3.2 Chip Geometry

The study of chip geometry provides researchers with fundamental information on the cutting process as the type of chip produced influences both the surface morphology

and integrity. In addition, process parameters such as shear angle can be derived from the chips produced. The thickness of cut, more commonly referred to as undeformed chip thickness, is also the primary factor influencing the best machining accuracy attainable (Ikawa et al., 1992).

Ikawa et al. (1992) studied the minimum thickness of cut in diamond turning. The minimum thickness of cut is defined by Ikawa et al. as the minimum undeformed thickness of the chip that can be removed stably from the work surface under perfect performance conditions of a machine tool. Stable chip formation at an undeformed chip thickness at the nanometric length scale is observed. The images of the chip obtained from single point diamond cutting of electroplated copper at undeformed chip thicknesses of 1 nm and 30 nm are presented in Figure 2.3. Thus, Ikawa et al. inferred from their experimental findings that if the edge radius of the cutting tool is maintained sharp enough, highly accurate and precise workpieces can be machined with nano-scale cutting operations.

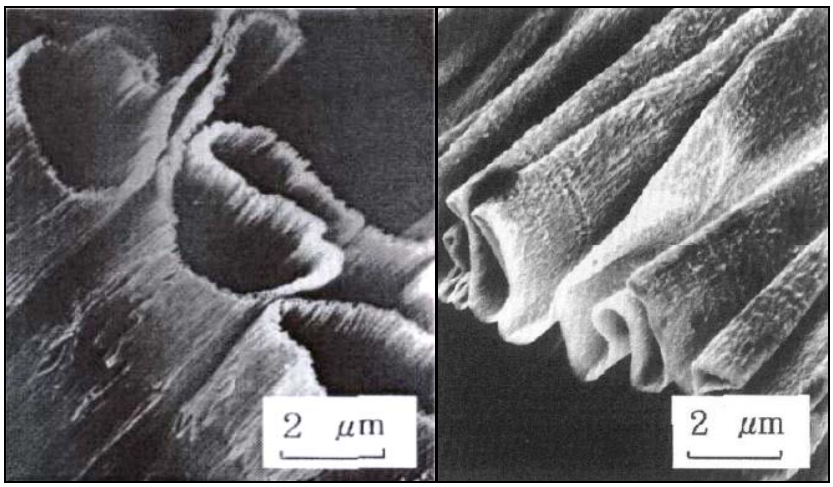

(a) (b)

Figure 2.3: Image of Chip Produced at an Undeformed Chip Thickness of (a) 1 nm and (b) 30 nm (Ikawa et al., 1992)

Moriwaki et al. (1993) conducted a detailed study of chip geometry. Moriwaki et al. observed that the thickness of the chip is influenced by the crystallographic orientation. In addition, spiral chips are formed at undeformed chip thicknesses greater than 1 μm and wavy chips formed at undeformed chip thicknesses smaller than 1 μm. It is also reported by Moriwaki et al. that there are no observable distinctions between the deformed chip thicknesses when the undeformed chip thickness is reduced to less than 0.01 μm.

In another experimental investigation of micro-cutting of brass conducted by Lu and Yoneyama (1999), a flow type chip with deformed chip thickness 30 times greater than the undeformed chip thickness of 30 μm was observed.

Weule et al. (2001) reported that the achievable surface roughness in micro-milling depends on the behavior of the material during the cutting process. They further added that chip separation will only occur at a defined minimum cutting depth (minimum chip thickness). The minimum chip thickness in micro-milling, according to Weule et al. (2001), can be estimated as being approximately 30% of the edge radii of the cutting tool.

Kim et al. (2002) studied chip formation in micro-milling and reported that the minimum chip thickness of a micro-milling system is dependent on the stiffness of the system and the edge radius of the tool. If the feed per tooth is relatively smaller than either the stiffness of the system or the edge radius of the tool, a chip may not form with each pass of the tool. It is also reported that the chip thickness and width of the chips collected in the experimental study tend to be similar. The chips collected are also fragile and weak and break easily. Further analysis of the chips indicated that the measured chip volume is significantly larger than the nominal chip volume at small feed per tooth.

Hence, Kim et al. (2002) concluded that chips were not formed at each pass of the cutting tool. An examination of the feed marks on the surface of the workpiece further provided convincing evidence to support the statement.

2.3.3 Surface Morphology

The desire to create surfaces of exceptional accuracy and quality for micro-components is the driving force behind research into surface generation from micro and nano scale machining. An improved understanding of the effect and dominant mechanisms that govern surface generation in micro and nano scale machining aids in the fabrication of micro-components with ultra-smooth functional surfaces and highly precise dimensions, which is essential in many electronics and optics applications. Specific applications include micro-scale fuel cells, micro-holes for fiber optics and micro-molds for optical lenses.

Nakayama (1997) suggested that the quality of the surface finish generated in micro and nano scale machining can be attributed to the inaccurate motion of the cutting tool relative to the workpiece, as well as the presence of a built-up edge. The inaccuracies of the cutting tool's motion can be eliminated through a combination of the use of higher precision machines and designing a more rigid experimental setup. In addition, built-up edge can similarly be avoided by (i) selecting mutually non-adhesive materials for tool and work material, (ii) machining the work material at cutting temperatures above the recrystallization temperature of the work material, (iii) using a high rake angle (> 30º), (iv) maintaining a sharp cutting edge and (v) machining at very high cutting speeds.

The pursuit of better surface finish has promoted continued investigation in surface morphology in micro and nano scale cutting. The constituents of the work materials and the crystallographic orientation of the work material are other factors found to have an influence on the surface finish of the machined surface.

Experimental investigations by Eda et al. (1985) on single point diamond machining of aluminum and copper alloys, within the undeformed chip thickness range of 2 – 70 μm, suggests that the quality of the surface finish is influenced by the alloys and constituents of the work material and the deformation of the crystal boundary and separations. Alloyed particles that were cracked and fractured by the tool during the cutting process and voids observed on the machined surface supported this deduction. In addition, it was verified that the machined surface roughness values are close to the theoretical roughness values, in conformance with the form of the diamond tool. The smoothest surface finish achievable on pure aluminum workpiece in this investigation was reported to be 50Å.

The surface finish of the work material is also influenced by the crystallographic orientation of the work material (Sato et al., 1991; Moriwaki et al., 1993; To et al., 1997). Sato et al. (1991) and To et al. (1997) described similar findings - that surface roughness and flatness are affected by the cutting direction in machining single crystal aluminum. Sato et al. (1991) reported that when the single crystal aluminum is machined along the $[0\ \bar{1}\ 1]$ direction, corresponding to its sliding direction, the surface finish produced has the lowest roughness values. Alternatively, machining perpendicular to the sliding direction along the $[1\ \bar{2}\ 1]$ direction generates a surface finish with the highest roughness values. To et al. (1997) reported that machining the aluminum single crystal workpiece along (1 0 0)

plane yields the best surface finish when compared to machining along the (1 1 0) and (1 1 1) planes. Sato et al. (1991) together with To et al. (1997) concluded from their respective investigations that controlling the crystallographic orientation of the work material during the machining operations is effective in improving the surface finish. Moriwaki et al. (1993) describes similar findings in machining single crystal copper. However, Moriwaki et al. (1993) further highlighted that the influence of crystallographic orientation on surface roughness is significantly reduced when the undeformed chip thickness is reduced. Moriwaki et al. (1993) suggested that the improvement of the quality of the surface finish at small undeformed chip thicknesses was because the surface was not generated at the grain boundaries.

Lee and Cheung (2001) presented and experimentally verified a dynamic surface topography model used to predict the local variation of surface roughness in diamond turning of crystalline materials. The model incorporates the micro-plasticity theory, theory of system dynamics and machining theory to account for materials induced vibration in ultra-precision machining. The model predicts both the magnitude and the effect of materials-induced vibration to provide quantitative estimates in the local variation of the surface roughness caused by these material induced vibrations.

2.4 Overview of Process Modeling

Process modeling methods such as the finite element method (FEM) and molecular dynamics simulation (MDS) are commonly used to evaluate and predict process parameters in micro and nano scale cutting. Numerous studies have been conducted to employ these modeling techniques to accurately evaluate and predict micro

and nano scale cutting process parameters such as cutting force, chip geometry, strain and stress distribution and cutting temperature (Shimada et al., 1993; Liang et al., 1994; Maekawa et al., 1995; Komanduri et al., 1998; Kim et al., 1999; Rentsch, 2000; Lin and Huang, 2004; Raczy et al., 2004; Liu and Melkote, 2004).

FEM analyzes micro scale machining based on the principle of macro-scale continuum mechanics (Liu et al., 2004). It is a well-established technique used to predict process parameters for macro-scale cutting operations. MDS technique departs from continuum mechanics, analyzing cutting operations at the atomistic level. This is a newly developed technique and is widely perceived to be more ideal in modeling micro and nano scale cutting (Liu et al., 2004).

The majority of work in this area involves the formulation and development of either FEM techniques or MDS techniques to investigate the influence of cutting conditions on the process parameters in two-dimensional orthogonal cutting. Material behavior, friction characteristics and tool geometry are incorporated into these process models with the aim of better describing the complex nature of micro and nano scale cutting operations. Experimental studies are subsequently conducted to verify the applicability of the finite element or molecular dynamics models developed. Some of the notable findings from these modeling studies are summarized as follows:

Ikawa et al. (1991) analyzed chip removal at the nanometric level using an atomistic simulation. It was reported that although the minimum thickness of cut is influenced by interaction between the tool and the work material, it is more significantly influenced by the cutting edge of the tool. Both the simulation and experimental work

suggested that the minimum thickness of cut is at the order of $\frac{1}{10}$ of the edge radius of the tool.

Liang et al. (1994) employed the FEM to analyze the influence of the crystallographic characteristics of the material on the micro-cutting process. The analysis indicated that grain orientation has a significant effect on the yielding cutting force for both aluminum and copper. The cutting force also becomes a minimum when cutting is performed along the (1 1 1) plane when compared with the (0 0 1) and (1 1 0) planes. Furthermore, the yielding cutting force also changes at the grain boundary of polycrystalline materials.

In the study of tribological phenomena in nano-scale machining using MDS, Maekawa et al. (1995) reported that friction and tool wear exert the same influence in nano-cutting as that observed in macro-scale cutting.

Komaduri et al., (1998) investigated the effect of tool geometry in nano-scale cutting using MDS and reported that the tool edge geometry has significant influence on nano-scale cutting. The tool edge geometry is found to have significant influence on the cutting and thrust forces, force ratio, specific energy and the sub-surface deformation.

Kim et al. (1999) proposed a FEM technique to predict the stress and temperature distribution in micro-scale machining of oxygen-free-high-conductivity copper. The results indicated that the temperature effect is a very important factor to be considered in micro-scale cutting process due to its influence on the flow stress distribution. The cutting force and flow stress were over-predicted when the temperature effect was neglected.

Liu and Melkote (2004) presented a strain gradient based FEM technique to predict the size effect in orthogonal cutting. The analysis showed that strain gradient strengthening has minimal effect on the distribution of temperature, effective plastic strain and effective stress within the workpiece. However, strain gradient strengthening led to higher effective stress in the deformation zones and the finished surface and lower plastic strain in the primary deformation and secondary deformation zones. Furthermore, the strain gradient effect also led to higher cutting temperatures.

2.4.1 Edge-Radiused Tool Process Model

Many conventional macro-scale machining models such as Merchant's theory and Oxley's theory do not account for the size of the cutting tool's edge radius. The tool is assumed to be perfectly sharp since the size of the edge radius is often negligible when compared to the thickness of cut performed in macro-scale cutting operations. However, as the undeformed chip thickness is significantly reduced in micro and nano scale machining, the edge radius of the cutting tool becomes comparable to the undeformed chip thickness. The interaction between the edge radius of the cutting tool and the work material is found to significantly influence the cutting process in micro and nano scale cutting as highlighted in the previous section. Hence, numerous studies considering the edge radius of the cutting tool in micro and nano scale machining have since been conducted (Albrecht, 1960; Komanduri, 1971; Manjunathaiah and Endres, 2000; Kountanya and Endres, 2001; Schimmel et al., 2002). Various edge-radiused tool process models have also been proposed (Kim and Kim, 1996; Waldorf et al., 1998; Manjunathaiah and Endres, 2000; Fang, 2003).

There are basically two schools of thought in edge-radiused tool modeling. Albrecht (1960), Endres et al. (2000) and Fang (2003) assume that the chip separation point exists on the edge radius of the cutting tool. On the other hand, Waldorf et al. (1998) considers a stable build-up of work material adhering to the cutting edge and that the separation point exists at the extreme edge of the work material build-up. Although scientific investigations were performed to determine the applicability of both theories (Waldorf et al., 1999; Kountanya and Endres, 2001), the results drawn from these studies remain inconclusive. Hence, there is no general consensus on the applicability of either theory.

Difficulties in measuring and separating the shearing and ploughing components of the cutting forces also compound the problem. Hence, verifications of edge-radiused tool process models are limited by experimental measurement techniques. Most edge-radiused tool process models are not totally predictive in nature; prior knowledge of some variables and some form of experimental work is required to determine several empirical relationships required as inputs to these models. Therefore, Manjunathaiah and Endres (2000) comments that there is no perfect model that can reliably predict cutting forces when cutting with edge-radiused tools across a wide and practical range of cutting conditions.

2.5 Summary

A general synopsis of past and on-going scientific investigations related to micro and nano scale machining was presented in this chapter. The significant findings from these micro and nano scale machining researches were also summarized and highlighted.

It is noticed from this review that the work materials studied in previous investigations were limited in variety. Work materials such as soft aluminum alloys, brass and copper are soft, ductile, easily machinable and are not extensively used to fabricate miniature engineering components with small features. Although the range of the undeformed chip thicknesses reported in experimental studies in micro and nano scale machining is between 1 nm to 80 μm, individual scientific investigations in micro and nano scale cutting are generally limited to a small undeformed chip thickness range. There is a lack of systematic analysis of micro and nano scale cutting data over a wide range of undeformed chip thicknesses. Comparison of trends observed in micro and nano scale cutting with existing macro-scale data is also lacking. In addition, applicability studies of existing process models using micro and nano scale machining data are also lacking. Furthermore, there is no general consensus on the explanations for observed trends in micro and nano scale cutting.

Hence, a more detailed study and analysis of cutting forces, size-effect phenomenon, chip geometry and surface morphology over a wider range of undeformed chip thicknesses using more precise machines and sharper cutting tools can be conducted. New studies involving harder engineering materials commonly used in the production of micro-components would also supplement existing micro and nano scale cutting data. These studies would further enhance our understanding of micro and nano scale machining.

CHAPTER 3

EXPERIMENTAL PROCEDURE

This chapter illustrates the experimental work conducted to further the understanding of the dominating mechanism in micro and nano scale machining. A full factorial experimental design with five replications was executed to analyze the statistical repeatability and accuracy of the data. The selection criteria of the machines, workpiece materials and cutting tools used in this study is presented in this chapter. A detailed description of the machines, cutting tools, workpiece materials, experimental setup and the experimental procedure used will also be presented.

3.1 High Precision Machines

Many researchers have highlighted that one of the major disparities between macro-scale and micro and nano scale machining is the positional accuracy and resolution requirement of the machines used. Further miniaturization of engineering components is often limited by the accuracy and resolution of the machine tool's actuation and sensor systems (Van Brussel et al., 2000). However, recent technical developments in ultra-precision machines have significantly improved both the achievable accuracy and resolution of the machines. Therefore, to ensure the precise position and movement of cutting tools with respect to the workpiece in this experimental investigation, ultra- precision machines with excellent positioning and repetition accuracy and nano-scale resolution were used. Detailed descriptions of the high precision machines used in this experimental investigation are presented in the following section.

3.1.1 Toshiba ULG-100C (H^3)

The Toshiba ULG-100C (H^3), shown in Figure 3.1, is a new generation ultra-precision aspheric grinder for micro and nano scale processing of high precision optical components. The machine has a positioning resolution of 1 nm in the X, Y and Z axes through the use of a 1 nm scale feedback system. It features a high precision aerostatic bearing spindle that provides rigidity with enhanced stability while operating at low and high speeds. The machine utilizes rigid aerostatically preloaded V-V roller guideways, which eliminate inaccuracies caused by hydrostatic thermal displacement. This machine also has a temperature and vibration-proof environment to eliminate potential sources of inaccuracies introduced by thermal fluctuations and vibrations. The Toshiba ULG-100C (H^3) was used in micro and nano scale cutting experiments (undeformed chip thickness < 2 μm). A complete technical specification of the Toshiba ULG-100C (H^3) machine is provided in Figure A.1 in Appendix A.

Figure 3.1: Toshiba ULG-100C (H^3)

3.1.2 Hardinge Conquest T42SP Lathe

The Hardinge Conquest T42SP lathe, shown in Figure 3.2, is a 2-axis super precision Computer Numerical Control (CNC) lathe. The machine has a positioning

resolution of 1 μm in the X and Z axes and an overall axis repeatability of 0.76 μm. The machine utilizes heavy duty linear guideways for improved positioning accuracy. The machine is also mounted on a 2200 kg HARCRETE® polymer composite base for increased vibration isolation. The Hardinge Conquest T42SP lathe was used in this study for P20 steel cutting experiments (undeformed chip thickness > 2 μm). A complete technical specification of the Hardinge Conquest T42SP lathe is provided in Figure A.2 in Appendix A.

Figure 3.2: Hardinge Conquest T42SP Lathe

3.1.3 JEOL JSM-5500 Scanning Electron Microscope

The JEOL JSM-5500 Scanning Electron Microscope (SEM), shown in Figure 3.3, is an easily operable SEM equipped with electron optics, specimen chamber and stage for high magnification observation and imaging of specimens. It has a resolution of 3.5 nm, operating at an accelerating voltage range of 0.5 kV to 30 kV. The SEM's magnification capability ranges from 18 to 300,000 times the size of the specimen, with a working depth of 5 to 48 mm. In addition, auto functions provided by the machine's software such as focusing, astigmatism and exposure correction allows for high clarity images to be

taken. This SEM was used to capture images of the cutting tool, deformed micro-scale chip geometry as well as estimation of the deformed chip thickness. A complete technical specification of the JEOL JSM-5500 SEM is provided in Figure A.3 in Appendix A.

Figure 3.3: JEOL JSM-5500 Scanning Electron Microscope

3.1.4 ZYGO NewView 200 White Light Interferometer

The ZYGO NewView 200, shown in Figure 3.4, is a scanning white-light interferometer used for characterization of the surface texture. It is a high-resolution, non-contact, non-destructive, three-dimensional surface measurement device. It is typically used for surface characterization of silicon wafers, automotive parts and machined components. This device utilizes the pairing of a highly precise vertical scanning transducer and a camera to generate a three-dimensional surface image of the sample. This is achieved by using the fringes produced by the optical path difference between the reference and reflected beam. The image of the surface is subsequently processed to provide a precise measurement of the surface topography of the sample. The ZYGO NewView 200 was used to measure the surface roughness of the machined samples. A complete technical specification of the ZYGO NewView 200 is provided in Figure A.4 in Appendix A.

Figure 3.4: ZYGO NewView 200 White Light Interferometer

3.1.5 Cutting Force Dynamometers

A three-component piezoelectric cutting force dynamometer was used to measure the cutting forces in this study. Since the magnitude of the cutting forces in micro and nano scale cutting is expected to be small, an important requirement of the dynamometer used is that it should have a low threshold and high sensitivity so that it can accurately measure small fluctuations in the cutting forces. Two types of force dynamometers were used in the experimental investigation.

A Kistler Type 9256 three-component force mini-dynamometer, shown in Figure 3.5, was used to measure the cutting forces in the micro and nano scale cutting experiments. The type 9256 mini-dynamometer allows measurement of three extremely small orthogonal components of force due to its high sensitivity and low threshold (< 0.002 N). It can accurately measure force components as small as 0.001 N and has a working range of ±250 N.

A Kistler Type 9257 three-component force dynamometer, shown in Figure 3.6, was used to measure the cutting forces in experiments where the undeformed chip thickness exceeded 2 μm. The Type 9257 dynamometer can measure force components

as small as 0.01 N with a working range of ±5 kN. The complete technical specifications of both Kistler force dynamometers used in this study are provided in Figures A.5 and A.6 in Appendix A.

Figure 3.5: Kistler Type 9256, Three-Component Force Mini-Dynamometer

Figure 3.6: Kistler Type 9257, Three-Component Force Dynamometer

3.2 Workpiece Materials

An array of materials has been previously studied in micro-scale machining investigations. OHFC copper, copper alloys, brass, soft aluminum alloys, mild steels and polymers such as polymethyl methacrylate (PMMA) are just some of the materials that researchers have studied previously (Rother, 2004). However, with the exception of some

copper, aluminum alloys and copper alloys components, most engineering components manufactured with these materials do not have precise micro and nano scale features. In addition, the majority of these materials are non-ferrous, soft, ductile and easily machinable.

New developments in various fields ranging from medical devices to telecommunications have created a demand for micro-components fabricated using more exotic materials (Rother, 2004). This demand has been generated as a result of the continued quest for higher quality and more durable engineering components with very precise small features for new products. Some of the exotic materials used to fabricate miniaturized engineering components, shown in Figure 3.7, include titanium alloys, structural aluminum alloys, stainless steels, hardened steels and special alloys.

Figure 3.7: Miniaturized Engineering Components

Although many of these materials have been extensively studied and used to fabricate macro-scale engineering components, not many scientific investigations at the micro and nano scale have been conducted with these materials. Therefore, one of the main aims of this study is to conduct an investigation of ferrous and non-ferrous exotic

materials used in the fabrication of engineering components with micro and nano scale features. This research also hopes to reveal more insight into how micro and nano scale cutting of these materials is different from its macro-scale counterpart.

The mold making and rapid prototyping industry is an example of where engineering components are fabricated with extremely precise and small features as illustrated in Figure 3.8. These miniaturized plastic components are often fabricated using injection molding techniques.

Figure 3.8: Molded Miniature Plastic Components

The small features in the mold are presently machined using material removal processes such as electro-discharge machining (EDM), electro-chemical machining (ECM) and laser machining. Although the mechanical cutting process is widely used to fabricate molds for macro-scale engineering parts, a combination of the lack of extensive knowledge in micro and nano scale cutting processes, ultra-precision machines and tools has restricted this process from being used for the fabrication of molds for micro-scale components. Recent developments in the field of ultra-precision machines and tools have made mechanical cutting process an attractive alternative to EDM, ECM and laser machining for mold fabrication. However, more technical studies have to be conducted

before mechanical cutting process can be established as a reliable method in the fabrication of molds for micro-scale components.

Hence, aluminum 7075-T6 (non-ferrous) and P20 mold steel (ferrous), two materials commonly used as molds in the mold making and rapid prototyping industry, have been selected to be the subject materials used in this study.

3.2.1 Aluminum AL7075

AL7075 is a high strength material commonly used for highly stressed structural components. It has been widely used in the aerospace industry as a structural material and in the fabrication of aircraft fittings, gears, shafts, fuse parts and regulating valve parts. Other applications include missile parts, bicycle frames and all terrain vehicle (ATV) sprockets.

More recently, AL7075 has been gaining popularity in the mold making and rapid prototyping industry due to its favorable material properties (Anon, 2000). AL7075 was selected for this study as it can be used in a wide range of applications as well as its increased usage in the mold making and rapid prototyping industry. The chemical composition and material properties of AL7075 are provided in Tables 1.1 and A.1 in Appendix A, respectively.

Table 3.1: Chemical Composition of AL7075

Component	Weight (%)
Al	87.1 – 91.4
Cr	0.18 – 0.28
Cu	1.2 – 2
Fe	Max 0.5
Mg	2.1 – 2.9
Mn	Max 0.3
Other, each	Max 0.05
Other, total	Max 0.15
Si	Max 0.4
Ti	Max 0.2
Zn	5.1 – 6.1

3.2.2 P20 Mold Steel

P20 mold steel has been traditionally used in molds for plastic injection molding. It is also the most commonly used ferrous material for molds in this industry. Hence, it has been selected as the ferrous material in this study. The chemical composition and material properties of P20 are provided in Table 1.2 and A.4 in Appendix A, respectively.

Table 3.2: Chemical Composition of P20

Component	Weight (%)
C	0.28 – 0.4
Cr	1.4 – 2
Fe	97
Mn	0.6 – 1
Mo	0.3 – 0.55
P	Max 0.03
S	Max .0.03
Si	0.2 – 0.8

3.3 Cutting Tools

The primary objective of this experimental study is to perform mechanical cutting of AL7075 and P20 at very small undeformed chip thicknesses. As highlighted in an earlier section, it is well known that the cutting edge radius of the cutting tool, shown in Figure 3.9, greatly influences various aspects of the cutting process (e.g. cutting forces, chip formation process, surface finish and power consumption) at the micro and nano scale. Furthermore, the minimum thickness of cut attainable is also known to be influenced by the sharpness of the cutting edge (Ikawa et al., 1992).

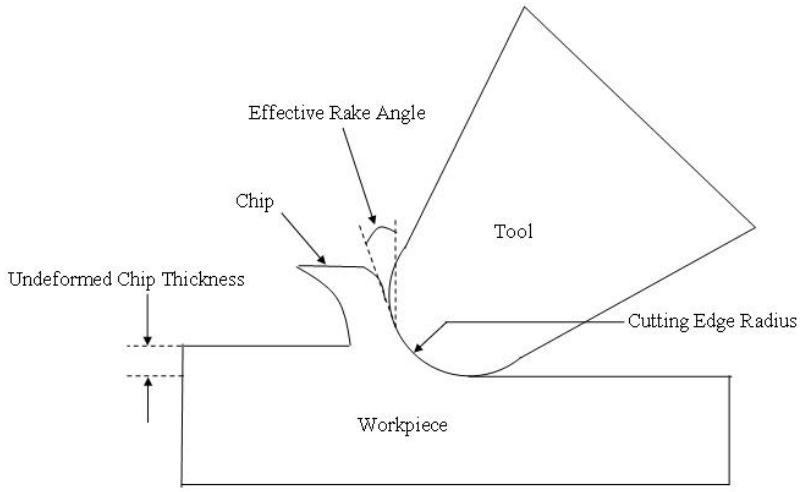

Figure 3.9: Schematic of Cutting Edge Radius of Cutting Tool

Hence, using a cutting tool with the sharpest available cutting edge radius would effectively eliminate the edge radius effect until the cutting edge radius of the tool is of the same order of magnitude as the undeformed chip thickness. In addition, the sharp tool would allow micro and nano scale cutting to be conducted at very small undeformed chip

thicknesses while producing continuous chips. Therefore, the main selection criterion of the cutting tool is to minimize the cutting edge radius.

3.3.1 Single Crystal Diamond Tool

Single crystal diamonds (SCD) are the hardest known material. In addition, SCD tools have the sharpest cutting edge radius currently available. Therefore, SCD tools are commonly used in micro and nano scale cutting of non-ferrous materials.

However, SCD inserts cannot be used for the cutting of ferrous materials due to the high affinity of carbon to ferrous materials at high temperatures (≈ > 500 ˚C) (Evans, 1991). The carbon diffusion process at high temperatures leads to high tool wear when SCD tools are used for machining of ferrous materials. Consequently, in order to prevent rapid tool wear, which would adversely affect the observations of this study, SCD tools are used only for the AL7075 cutting experiments.

SCD tools used in this study are made from natural diamond. It has a cutting edge width of 2 mm, a rake angle of 0˚ and a clearance angle of 5˚. An included angle of 85˚ provides strength to the cutting edge. The cutting edge radius of the SCD tools was measured and estimated to be approximately in the range of 65 nm to 100 nm. This is accomplished via fitting a circle on a highly magnified SEM image of the tool's cutting edge. An example of an SEM image used to estimate the cutting edge radius of the tool is shown in Figure 3.10.

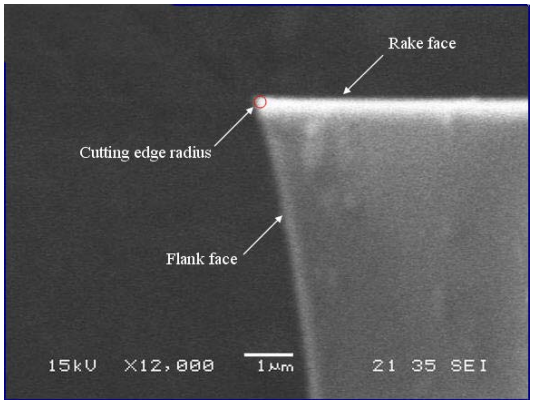

Figure 3.10: SEM Image of the Cutting Edge of SCD Tool

Although there is a degree of uncertainty in this technique, this non-contact and non-destructive measurement technique was used to retain the sharpness of the tool. It is widely anticipated that contact measurement techniques such as that used by Li et al. (2003) and the stylus profiler might inevitably chip and damage the cutting edge during the measurement process. A detailed technical drawing of the SCD tools used in the current study is given in Figure A.7 in Appendix A.

3.3.2 Carbide Tool

A different tool is used for the P20 cutting experiments since SCD tools are unsuitable for the machining of ferrous materials for reasons discussed earlier. A lack of thermo-mechanical models able to predict the cutting temperature variations at the micro and nano scale also contributed to the choice of cutting tool for the ferrous material in this study.

Carbide and cubic boron nitride (cBN) tools are commonly used for macro-scale cutting of ferrous materials as they exhibit low tool wear at high cutting speeds. Additionally, carbide and cBN tools are also two of the sharpest commercially available

cutting tools for the machining of ferrous materials. Furthermore, through special edge preparation techniques, "up-sharp" carbide and cBN tools can have nominal cutting edge radius values ranging from around 5 μm to 15 μm. However, carbide tools are more commonly used in the industry for machining of ferrous materials and are also significantly less expensive than cBN tools. Since the tool selection criterion is based on the sharpness of the tool, carbide tools are used for the P20 cutting experiments as they are more economical.

Tungsten carbide inserts (Kennametal, NGP-3125R) are employed for micro and nano cutting of P20 steel. These inserts have a cutting edge width of 3.175 mm, a rake angle of 5˚ and a clearance angle of 35˚. The inserts are coated with a layer of titanium nitride (TiN) using a physical vapor deposition (PVD) coating technique to improve the life and productivity of the tool.

The cutting edge radius of the carbide inserts were first estimated using a technique similar to SCD tool. An example of the SEM image used to estimate the cutting edge radius of the carbide insert is shown in Figure 3.11. The carbide inserts were subsequently also characterized at the Kennametal Latrobe facility using a stylus technique. The carbide inserts were measured at three separate locations on the cutting edge as shown in Figure 3.12. The three measurements were averaged to characterize the cutting edge radius of the insert. The values obtained using the two techniques were then compared and found to be in good agreement. A sample of the measurement result using the stylus technique is shown in Figure 3.13. A detailed technical drawing and the table containing cutting edge radii of the carbide inserts used in this experimental investigation are given in Figure A.8, Tables A.3 and A.4 in Appendix A.

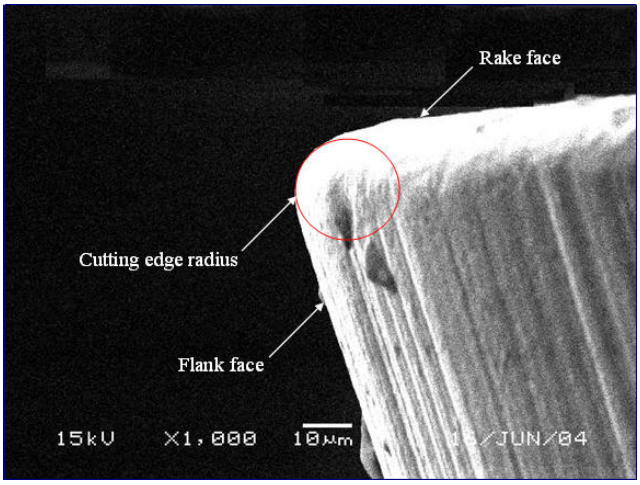

Figure 3.11: SEM Image of the Cutting Edge of the Carbide Insert

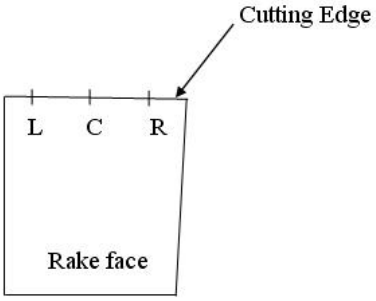

Figure 3.12: Location of Cutting Edge Measurement

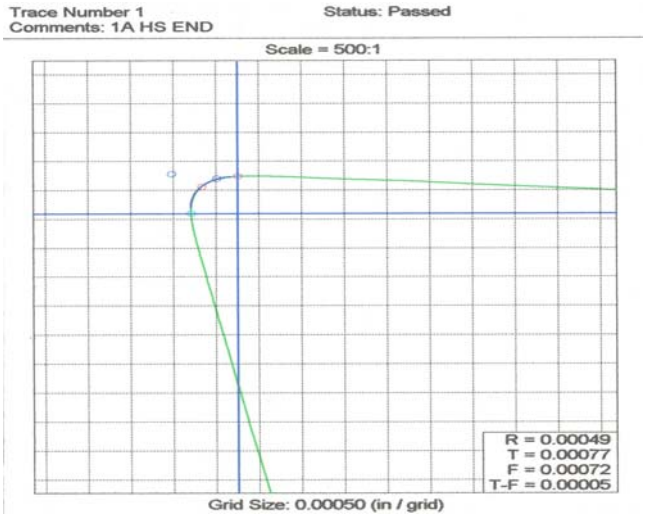

Figure 3.13: Sample Edge Radius Measurement Result Using Stylus Technique

3.4 Experimental Setup

A face grooving (end turning of a tube) dry cutting operation simulating the orthogonal cutting process was conducted on both the Toshiba ULG-100C (H^3) and the Hardinge Conquest T42SP lathe. Since the two machines had different fixturing requirements, two slightly different experimental setups were used. Both setups were designed to reduce the overhang of both the tool and the workpiece in order to maintain the rigidity of the tool and workpiece. The design thus eliminated potential sources of errors caused by the deflection and vibration of the workpiece during the cutting experiments.

3.4.1 Setup on the Toshiba ULG-100C (H^3)

The Toshiba ULG-100C (H^3) is built with a 100 mm diameter vacuum chuck on its work spindle. The vacuum chuck has suction rings at 45 mm and 90 mm from the axis of rotation of the work spindle. This is illustrated in Figure 3.14.

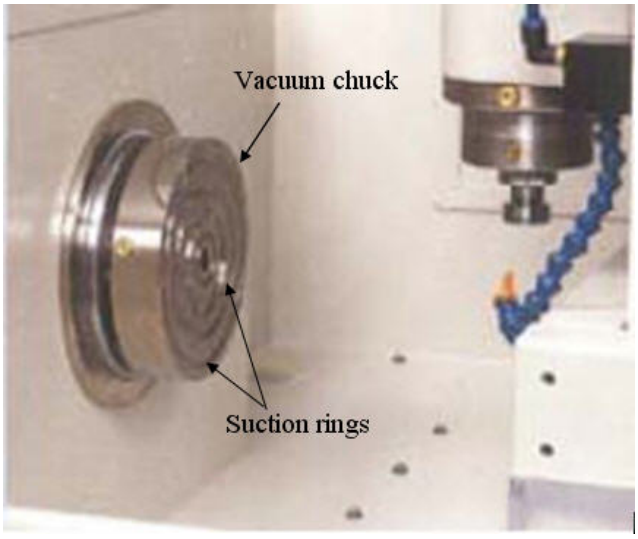

Figure 3.14: Vacuum Chuck on the Toshiba ULG-100C (H^3)

A holder of 100 mm in diameter was designed to mount the workpiece onto the vacuum chuck. The holder was machined with two flat surfaces with an M6 tapped hole in the center of the holder. The tapped hole enables the workpiece to be tightened rigidly onto the holder with an M6 screw and mounted onto the work spindle. The design of the holder and the workpiece is illustrated in Figure 3.15. After the holder and the workpiece are mounted onto the vacuum chuck, a dial gauge is used to align the holder such that the center axis of the workpiece coincides with the axis of rotation of the work spindle to minimize runout. The cutting tool is then mounted directly onto the Kistler Type 9256 dynamometer with its cutting edge orthogonal to the workpiece. The configuration of the experimental setup in the Toshiba ULG-100C (H^3) is presented in Figure 3.16. The dimensions of the holder and the workpiece are provided in Figure A.9 and A.10 in Appendix A.

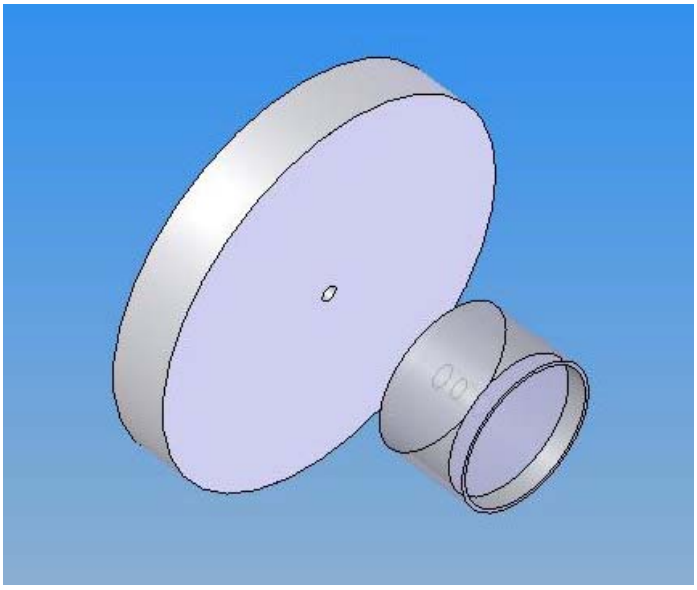

Figure 3.15: Design of Holder and Workpiece

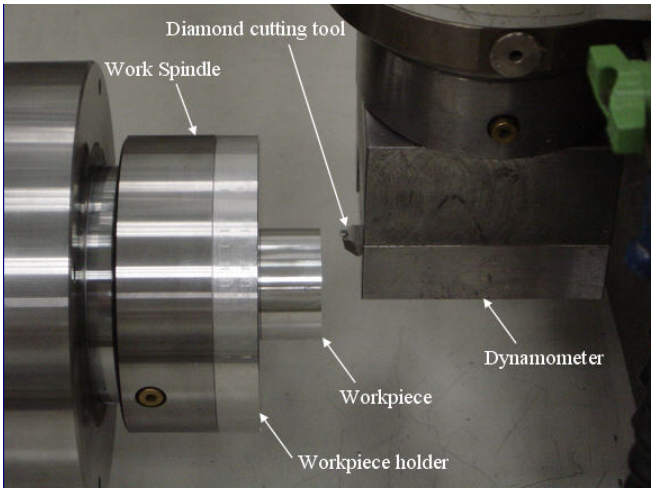

Figure 3.16: Experimental Setup in Toshiba ULG-100C (H^3)

3.4.2 Setup on the Hardinge Conquest T42SP Lathe

The Hardinge Conquest T42SP lathe is built with a collet chuck, hence the workpiece can be directly mounted onto the lathe. The experimental setup in the Hardinge Conquest T42SP lathe is similar to that in the Toshiba ULG-100C (H^3). The workpiece is held rigidly by the collet and its overhang is minimized. Light cuts are made with up-sharp turning tools to reduce the outer diameter of the workpiece to 38.1 mm. This ensures that the center axis of the workpiece is along the axis of rotation of the work spindle to minimize runout. The workpiece is subsequently bored internally to a diameter of 36.1 mm to form a tube of 1 mm wall thickness. The Kistler Type 9257 dynamometer is mounted onto the turret of the machine with the tool being subsequently mounted on the dynamometer. The configuration of the experimental setup in the Hardinge Conquest T42SP lathe is shown in Figure 3.17.

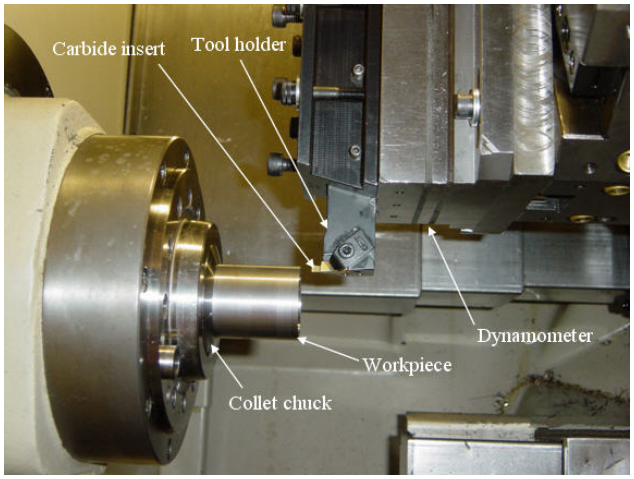

Figure 3.17: Experimental Setup in Hardinge Conquest T42SP Lathe

3.5 Experimental Design

The primary goal of this investigation is to study the variation of forces, chip formation process and surface morphology with the changes in experimental factors, namely cutting speed and undeformed chip thickness. Different sets of factor levels were selected for AL7075 and P20 as a result of the difference in the cutting edge radius of the cutting tool used. Both experiments conducted were full factorial experimental investigations consisting of 2 factors with 5 replications. Tables 3.1 and 3.2 summarize the factors and the factor levels used for AL7075 and P20 steel, respectively.

Table 3.3: Factors and Factor Levels for AL7075

Factor	Factor Levels
Cutting Speed (m/min)	10, 150
Undeformed Chip Thickness (nm)	10, 40, 70, 100, 400, 700, 1000, 1400, 1700, 2000

Table 3.4: Factors and Factor Levels for P20

Factor	Factor Levels
Cutting Speed (m/min)	10, 115
Undeformed Chip Thickness (μm)	0.3, 0.5, 0.7, 0.9, 1.1, 1.3, 1.5, 1.7, 2, 5, 10, 20, 30, 40, 50, 60

The cutting speeds were selected based on two criteria, the work spindle capability of the Toshiba ULG-100C (H^3) machine using a 38.1 mm workpiece and the stability of the setup at that speed. The low and high speeds were determined to be 10 m/min and 150 m/min for AL7075 and 10m/min and 115 m/min for P20. A total of 100 cutting tests were conducted for AL7075 and 160 cutting tests were conducted for P20 steel based on this experimental design.

3.6 Experimental Procedure

Similar procedures were observed for the AL7075 and P20 cutting experiments. The workpiece and tool were prepared and set up as described in the earlier section for the respective machines. Prior to the mounting of the cutting tool onto the dynamometer, the rake face and the cutting edge of the cutting tool were observed and imaged on the SEM. The tool was then mounted and brought into contact with the workpiece to define the datum position and then moved to a start position 3 seconds from the zero datum.

At the commencement of the experiment, the tool travels at a steady feed for 3 seconds before engaging the workpiece and proceeds to cut the workpiece for 12 seconds. This enables the data acquisition device to capture both the transient engagement force as well as the steady state cutting force. The data acquisition device captures the signal from the dynamometer at a rate of 24 kHz. As the tool approach the end of the cut after 12

seconds, the end position of the cut would be set as the new zero datum. The tool was subsequently re-positioned to a location 3 seconds away from the new zero datum. Figure 3.18 shows the force components in a typical orthogonal cutting of AL7075 with a zero rake angle. The forces recorded by the dynamometer during the cutting operation are the cutting force, F_C and the thrust force, F_T.

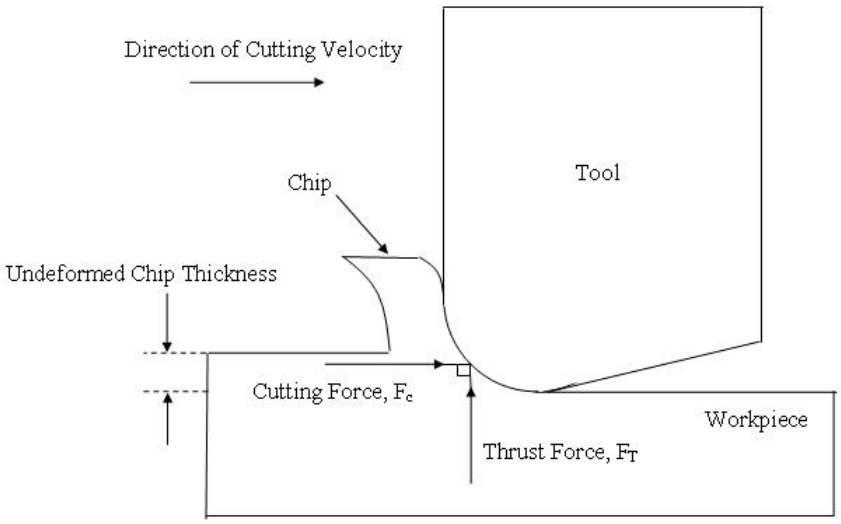

Figure 3.18: Schematic of Force Components

The tool was removed at the end of the cutting operation and the rake face and the cutting edge observed and imaged on the SEM. The chips produced were also collected and imaged using the SEM. The machined surface of the workpiece was also observed and imaged with the SEM. The surface generated was subsequently characterized with a white light interferometer (ZYGO). The cutting tool was then cleaned using a static-free cloth with cleaning solvent before being mounted onto the dynamometer for subsequent experiments.

3.7 Summary

This chapter presented the selection criteria of the machines, cutting tools and workpiece materials used in the experiments. It also provided justification for the selection process used. The technical specifications of all equipment used in this investigation were also highlighted. In concluding this chapter, the experimental setups, design and procedures were also presented.

CHAPTER 4

EXPERIMENTAL RESULTS AND DISCUSSION

Cutting experiments were conducted on the AL7075 and P20 workpieces as described in the experimental design and procedure sections of the previous chapter. The experimental data acquired during the cutting experiments are presented in detail in this chapter. In addition, plausible explanations of significant trends and observations from the cutting experiments are also offered for both materials. The discussion presented in the following sections include the cutting force, chip geometry, surface morphology of the machined workpieces as well as derived parameters using Merchant's theory.

4.1 Introduction

The following section offers a short introduction of the various areas that are widely studied in macro-scale mechanical cutting operations. The study of cutting forces, chip geometry, surface morphology and derived parameters using Merchant's Theory have enabled researchers to better grasp the fundamental mechanisms in macro-scale cutting operations. Hence, this study will similarly focus on these key areas in the hope of revealing more insight into the basic operating mechanisms of micro and nano scale cutting operations. By focusing on these same areas, it would then allow for comparison of the experimental data acquired in this investigation with existing trends in macro-scale cutting operations. The comparison would then serve to offer insight into how micro and nano scale cutting operations differ from macro-scale cutting operations.

4.1.1 Cutting Forces

The study of cutting forces is essential as they provide information on process-level phenomena observed in cutting operations. Cutting forces can be used to determine power consumption as well as to estimate tool wear, tool deflection and workpiece distortion. These derived parameters will provide researchers with more in-depth understanding of the dominating mechanism of micro and nano scale machining. These parameters also offer the necessary data and information for the proper design of machine tools for micro and nano scale machining.

4.1.2 Chip Geometry

Chip geometry is another area where fundamental information on the cutting process can be obtained as the type of chip produced influences both the surface morphology and integrity. In addition, the cutting ratio, which is the ratio of the undeformed chip thickness to the deformed chip thickness, can also be obtained by observing the deformed chip under a high magnification optical device. The cutting ratio is then used to estimate the shear angle, φ, in the cutting process.

4.1.3 Surface Morphology

Surface morphology has emerged as an important feature in many engineering applications, especially so in miniaturization technology. Many applications require miniaturized components to have extremely smooth functional surfaces. This serves to ensure that the dimensional accuracy of the fabricated component satisfies the required tolerance for subsequent assembly operations. A smooth functional surface also reduces

undesired vibrations in certain applications. The study of surface morphology in this investigation involves the characterization of the surface finish of the machined workpiece under pre-determined cutting conditions. This would offer a better understanding of the relationship between cutting conditions and surface generation when machining operations are performed at the micro and nano scale.

4.1.4 Experimental Observations

The rake face and cutting edge radius of the tool were monitored during the cutting experiments. These observations served to provide plausible explanations for fluctuations in cutting forces as well as to detect possible tool wear, which might reduce the sharpness of the cutting tool during cutting experiments.

4.1.5 Derived Parameters using Merchant's Theory

The estimate of the shear angle, φ, and the measured cutting force can be employed to derive other cutting process parameters using Merchant's Theory. Cutting process parameters such as shear stress, shear energy per unit volume and friction energy per unit volume can be evaluated. These derived cutting process parameters will offer an enhanced understanding of possible trends observed in micro and nano scale machining.

4.2 Micro-/ Nano-Scale Machining of Aluminum 7075

Micro and nano scale orthogonal dry cutting experiments were conducted within an undeformed chip thickness range of 10 - 2000 nm. The cutting experiments were conducted at two cutting speeds of 10 m/min and 150 m/min.

4.2.1 Cutting Forces and Size-Effect

4.2.1.1 Time Series Profile

A typical cutting force time series profile for cutting AL7075 at an undeformed chip thickness of 40 nm and a cutting speed of 10 m/min is shown in Figure 4.1. This time series profile is used to identify setup rigidity issues and also to determine the steady state force.

The small oscillations in the observed signal can be attributed to environmental noise. The lack of large oscillations in the profile demonstrates that the setup is rigid and stable. It also reaffirms that possible sources of error such as runout have been minimized. The small oscillations can also be attributed to the rotation of the work spindle as well as the chip formation process during the cutting experiments.

It is also observed from the profile that a transient engagement force is experienced by the tool, which is significantly greater than the steady state cutting force. The steady state force signal is averaged to determine the magnitude of the force for each cutting condition.

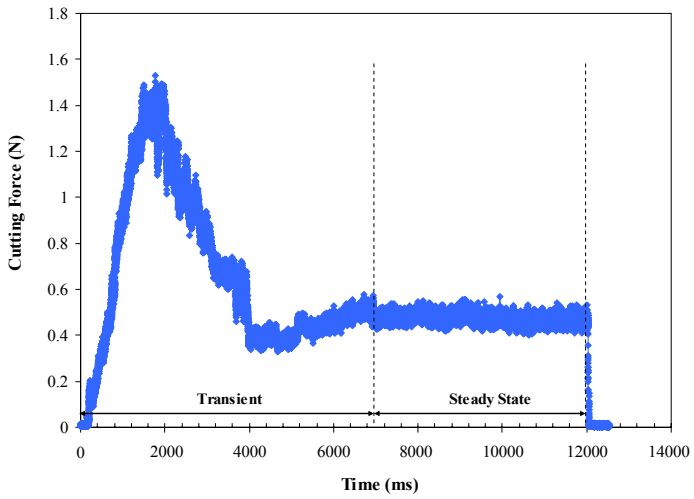

Figure 4.1: Force-Time Series Profile (AL7075)

4.2.1.2 Average Force Values and Trends

The steady state cutting and thrust force for AL7075 at each factor level was averaged over the five cutting experimental replications. The average force values represented in Tables B.1 and B.2 in Appendix B are for cutting speeds of 10 m/min and 150 m/min, respectively. The measured force values for each cutting experiment are also provided in Tables B.3- B.12 of Appendix B. The data presented in Tables B.1 and B.2 show the range and mean force values acquired during the cutting experiments. The data in Tables B.1 and B.2 are subsequently used to generate graphs of force as a function of undeformed chip thickness and these graphs are presented in Figures 4.2 and 4.3. The error bars shown in these graphs indicate the maximum and minimum cutting and thrust forces measured at each factor level.

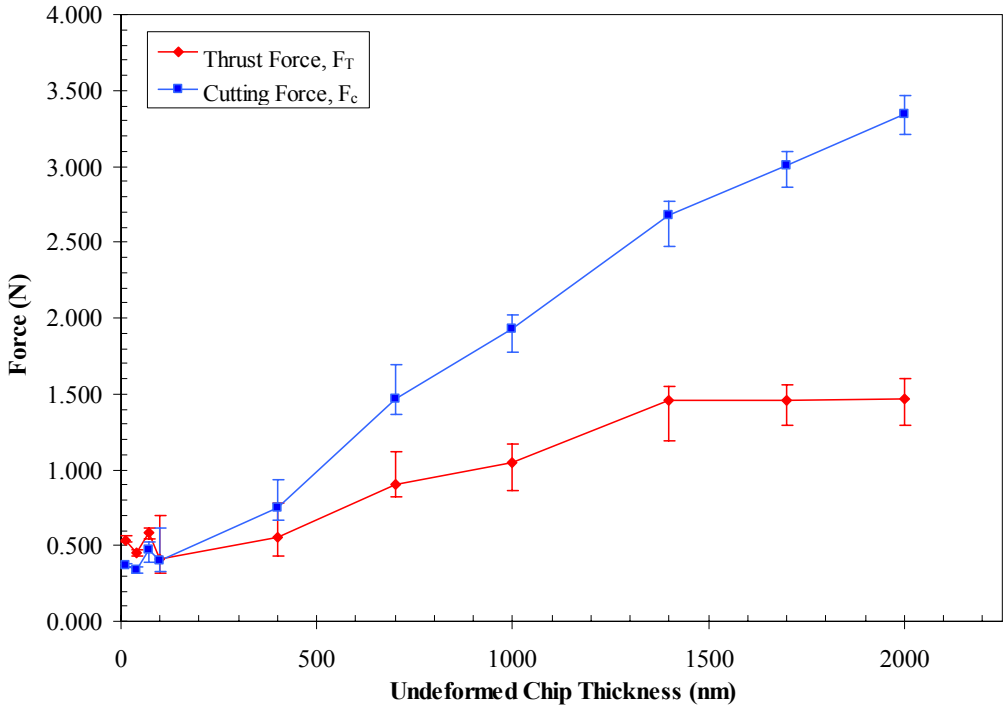

Figure 4.2: Effect of Undeformed Chip Thickness on Cutting and Thrust Forces at a Cutting Speed of 10 m/min (AL7075)

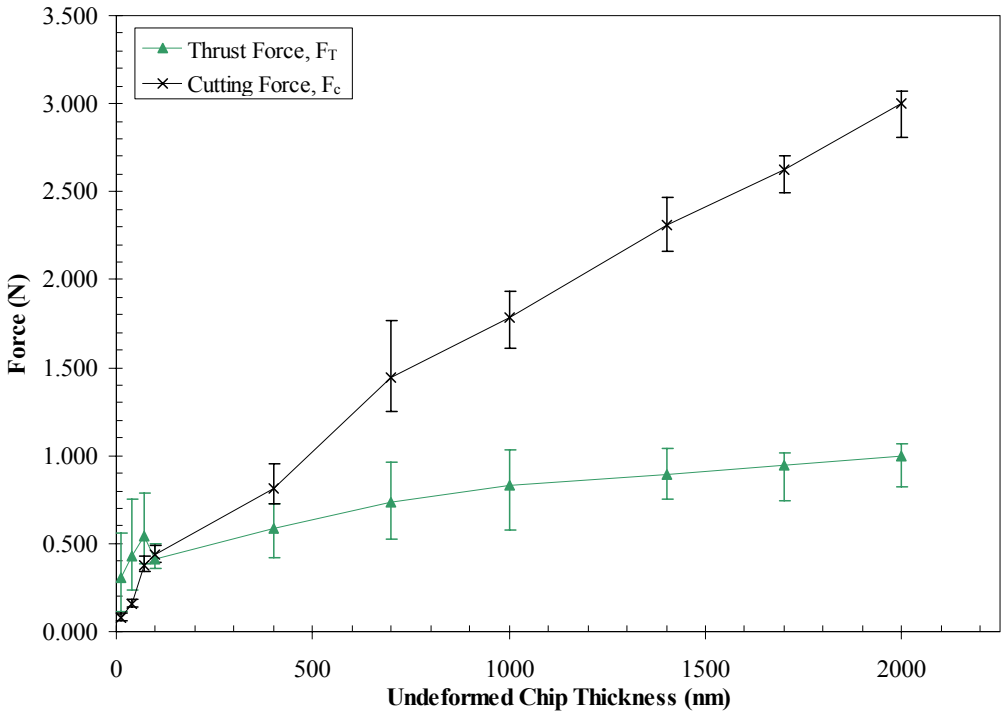

Figure 4.3: Effect of Undeformed Chip Thickness on Cutting and Thrust Forces at a Cutting Speed of 150 m/min (AL7075)

Figures 4.2 and 4.3 illustrate that both cutting and thrust forces increase with an increase in the undeformed chip thickness. The magnitude of the cutting force is also greater than the magnitude of the thrust force at undeformed chip thicknesses greater than 100 nm. However, when undeformed chip thickness is less than 100 nm, there is a reversal in magnitude between the cutting and thrust forces at both cutting speeds.

The cutting force appears to be an increasing linear function for undeformed chip thicknesses greater than 100 nm at both cutting speeds. This linear trend in the cutting force is similar to existing cutting force trends observed in macro-scale cutting data (Zorev, 1966; Sato et al., 1991; Atkins, 2003). However, the thrust force increases at a slower rate than the cutting force and is seen to level off after an undeformed chip thickness value of 1000 nm at both cutting speeds. This trend is similarly reported by

Lucca et al. (1993) and Nakayama and Tamura (1968). A possible explanation for this leveling-off effect in the thrust force will be offered in the section on experimental observations as it can be explained by the smear marks left on the rake face of the diamond cutting tool.

At undeformed chip thicknesses of less than 100 nm, the thrust force is observed to be greater than the cutting force at both cutting speeds. The graphs for undeformed chip thickness values ranging from 10 - 700 nm are presented in Figures 4.4 and 4.5 to provide a magnified view of the force trends in this range.

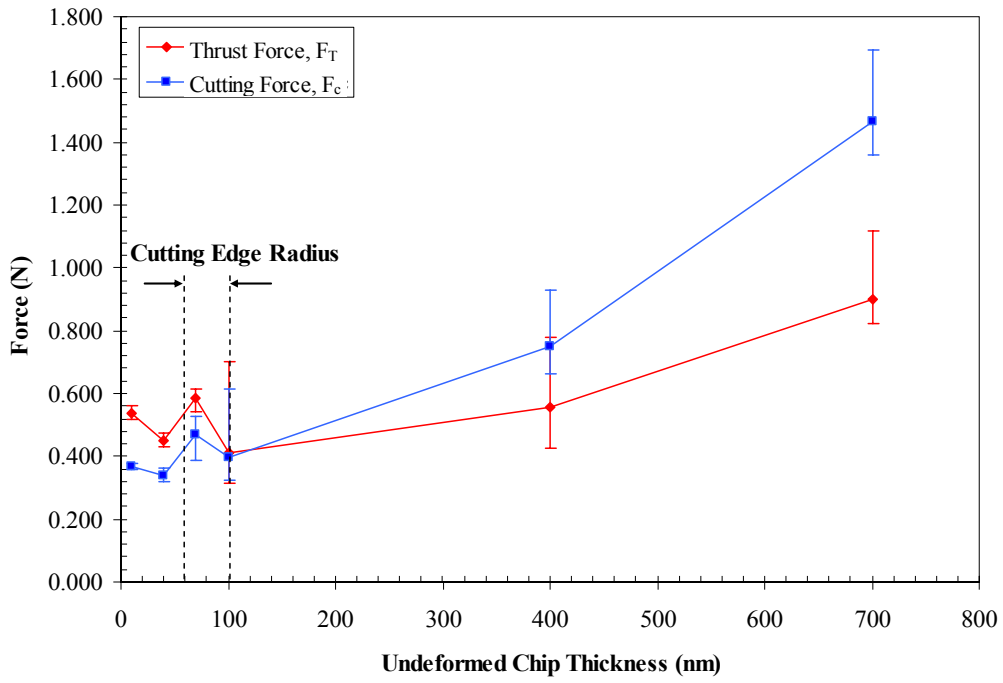

Figure 4.4: Effect of Undeformed Chip Thickness on Cutting and Thrust Forces at a Cutting Speed of 10 m/min (Magnified View of Undeformed Chip Thickness range from 10 - 700 nm; AL7075)

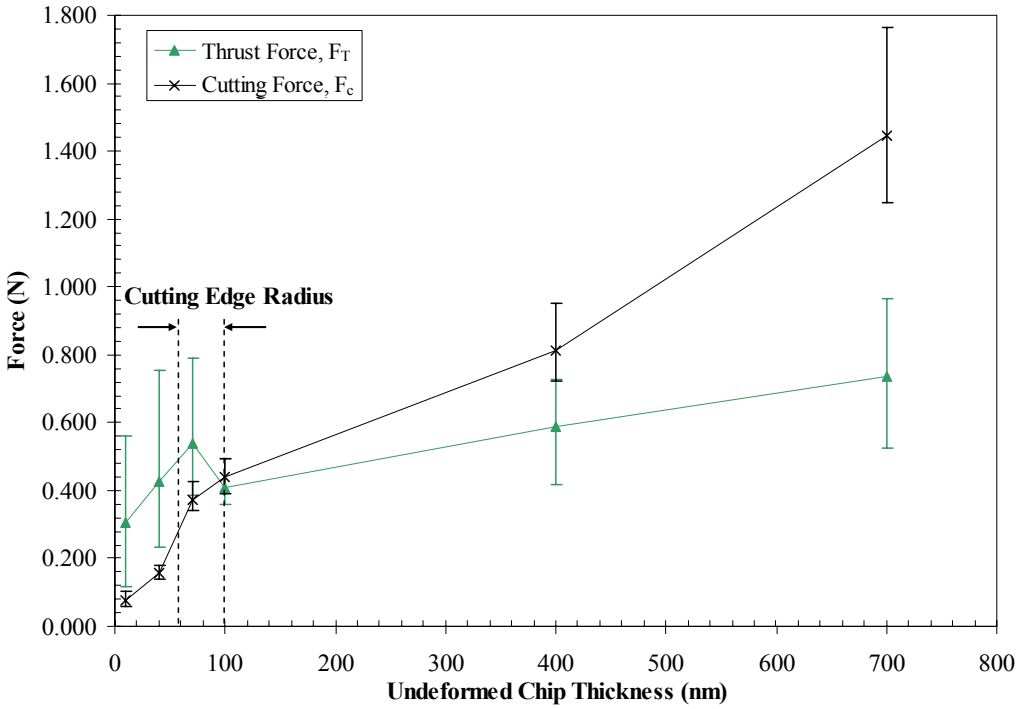

Figure 4.5: Effect of Undeformed Chip Thickness on Cutting and Thrust Forces at a Cutting Speed of 150 m/min (Magnified View of Undeformed Chip Thickness range from 10 - 700 nm; AL7075)

Figures 4.4 and 4.5 illustrate a reversal of the cutting and thrust forces occurring at around 100 nm for both cutting speeds. This value of 100 nm falls in the range of 60 – 100 nm, which is the estimated radius of the SCD tool. When cutting experiments are conducted at or below the cutting edge radius, the effective rake angle of the tool becomes negative (Manjunathaiah and Endres, 2000). At large effective negative rake angles, the cutting process becomes a ploughing dominant process (Albrecht, 1965; Wu, 1988; Endres et al., 1995). In processes such as grinding and hard turning, where the effective rake angle is negative, the thrust force is typically higher than the cutting force. This trend is observed in existing macro-scale cutting data when cutting operations are performed using negative rake angle tools (Komanduri, 1971). Since the cutting edge radius of the SCD tool is estimated to be between 60 and 100 nm, the reversal in the

magnitude of the thrust force and cutting force at around this range is anticipated. Consequently, this observed trend in micro and nano scale cutting experiments is comparable to trends observed in macro-scale cutting operations.

At undeformed chip thicknesses that are equal to or less than the cutting edge radius, the cutting force does not follow a linear trend with a decrease in undeformed chip thickness at both cutting speeds. At cutting speeds of 10 m/min and 150 m/min, the cutting force data can be fitted to a curve of a second order polynomial function. This seems to suggest that cutting force decreases quadratically with a decrease in undeformed chip thickness for this material. This is consistent with existing literature where cutting force is assumed to vary non-linearly with a decrease in undeformed chip thickness (Atkins, 2005).

There is no noticeable trend observed in the thrust force at the cutting speed of 10 m/min at undeformed chip thicknesses smaller than 100 nm. However, at the cutting speed of 150 m/min, the thrust force appears to decrease linearly with a decrease in undeformed chip thickness. Another observed trend is an increase in the thrust force at both cutting speeds when the undeformed chip thickness decreases from 100 nm to 70 nm.

The effect of cutting speeds and undeformed chip thicknesses on cutting and thrust forces are illustrated in Figure 4.6. It is observed that the cutting speed does not have a significant effect on the cutting and thrust forces until an undeformed chip thickness of around 700 nm. Although there is a 15-fold increase in cutting speed, there is only a 15% decrease in the cutting force and a 50% decrease in thrust force at undeformed chip thicknesses larger than 700 nm.

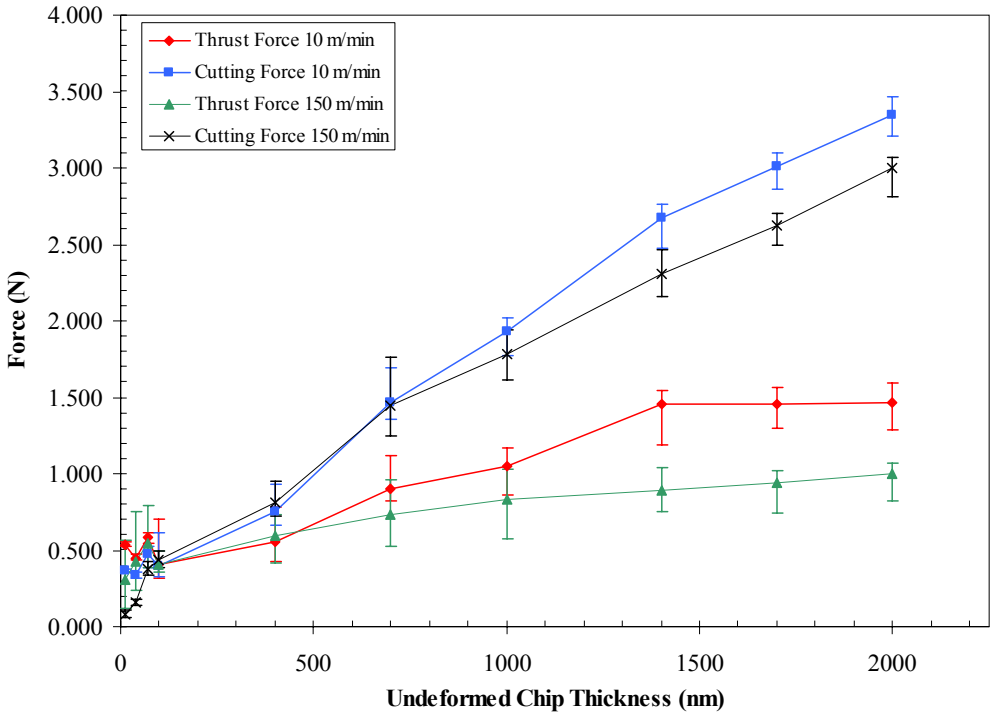

Figure 4.6: Effect of Undeformed Chip Thickness and Cutting Speed on Cutting and Thrust Forces (AL7075)

The graph of the force data for the undeformed chip thickness range of 10 - 700 nm is re-produced in Figure 4.7 to observe the effect of cutting speed on force values. There appears to be no significant difference between the cutting and thrust forces acquired at the two cutting speeds. The cutting and thrust forces also seem to converge at approximately 0.4 N at an undeformed chip thickness value of 100 nm at both cutting speeds. However, further studies have to be conducted to provide a possible explanation for this observed phenomenon.

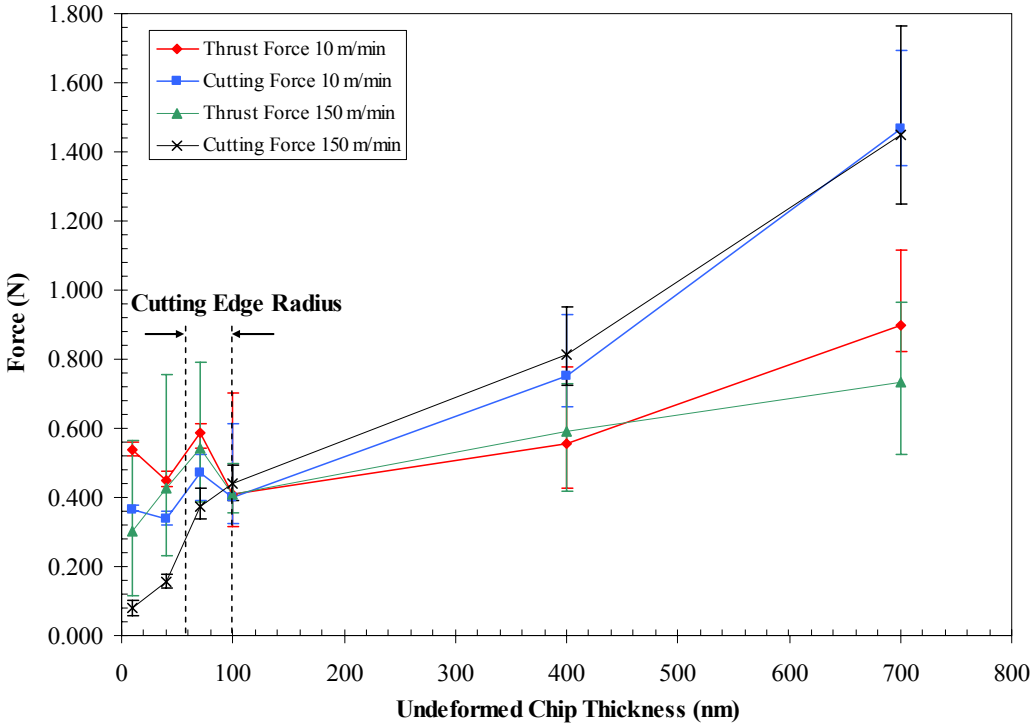

Figure 4.7: Effect of Undeformed Chip Thickness and Cutting Speed on Cutting and Thrust Forces (Magnified View from 10 nm to 700 nm; AL7075)

4.2.1.3 Variability of Cutting Force Data

Variability of the force data was evaluated by calculating the spread of the data from the mean. The percentage of the maximum deviation of the force data from the mean force value for each factor level was evaluated and presented in Tables B.13 and B.14 in Appendix B for cutting speeds of 10 m/min and 150 m/min, respectively. At the cutting speed of 10 m/min, the average percentage deviation of the cutting and thrust forces from the mean force value are 15% and 21%, respectively. At the cutting speed of 150 m/min, the average percentage deviation of the cutting and thrust forces from the mean force value is 14% and 37%, respectively.

The variability of the cutting and thrust forces can be attributed to the following factor. The edge radius of a commercial cutting insert varies along the edge (Schimmel,

2000). Edge preparation processes such as polishing are generally stochastic processes, and such processes cannot guarantee that the edge radius along the entire cutting edge is exact. Therefore, variations of 20 – 45% in edge radius along the cutting edge are not uncommon (Schimmel, 2000). These variations in the cutting edge radius could cause similar variations in the force data. In addition, variations in the edge radius along the cutting edge may have a greater influence on the force data at smaller undeformed chip thickness values. Possible sources of edge radius variations include the edge preparation process as well as smearing of the work material on the cutting tool during experiments.

The evaluated variability of the cutting and thrust forces for AL7075 experiments is between 14 – 37 % of the mean cutting and thrust forces at both cutting speeds. This is within the variability range suggested by Schimmel et al. (2000). Hence the variability observed in the cutting and thrust forces is within reasonable range.

4.2.1.4 Size-Effect

The specific cutting and thrust energies were evaluated for all factor levels and the results are shown in Tables B.15 and B.16 in Appendix B. The data in Tables B.15 and B.16 were subsequently used to generate graphs of specific energy as a function of undeformed chip thickness and cutting speed, which are presented in Figures 4.8 and 4.9.

Figures 4.8 and 4.9 indicate that the specific cutting energy remains at a constant value of around 2 GPa until an undeformed chip thickness value of 100 nm. At undeformed chip thicknesses of less than 100 nm, the specific cutting energy increases significantly as the undeformed chip thickness decreases. A similar trend is also observed in the specific thrust energy.

The value of 100 nm lies approximately within the estimated range of the SCD tool's edge radius. Hence, it can be inferred that the edge radius does influence the specific cutting energy when micro and nano scale cutting are performed. Although this observation is similar to trends observed by Lucca et al. (1991, 1993) in their experimental studies, numerous possible explanations for size-effect have since been proposed and described in Chapter 2 (Nakayama and Tamura, 1968; Dinesh et al., 2001; Shaw, 2003; Atkins, 2003; Joshi and Melkote, 2004). However, it is inconclusive at this point in time that the edge radius is the sole cause of the size-effect phenomenon observed in this investigation. Separate scientific investigations that consider the grain size, grain orientation and the strain gradient of the work material have to be conducted to provide a more conclusive cause of the size-effect phenomenon (Liu and Melkote, 2004). It is also observed from Figures 4.8 and 4.9 that the cutting speeds do not affect the specific cutting and thrust energies significantly.

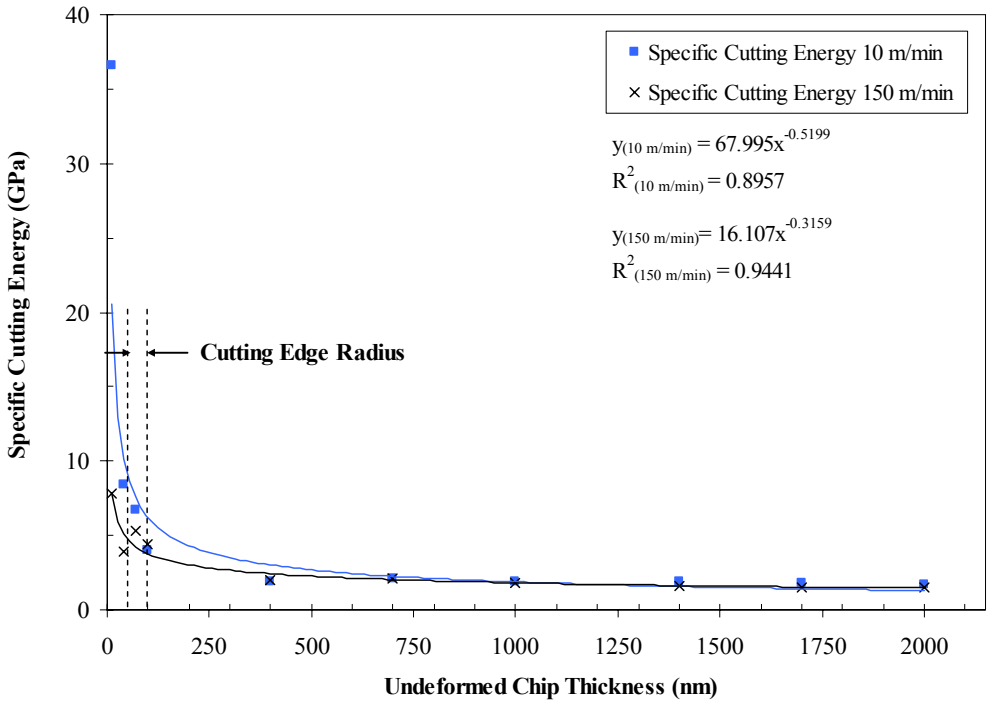

Figure 4.8: Effect of Undeformed Chip Thickness and Cutting Speed on Specific Cutting Energy (AL7075)

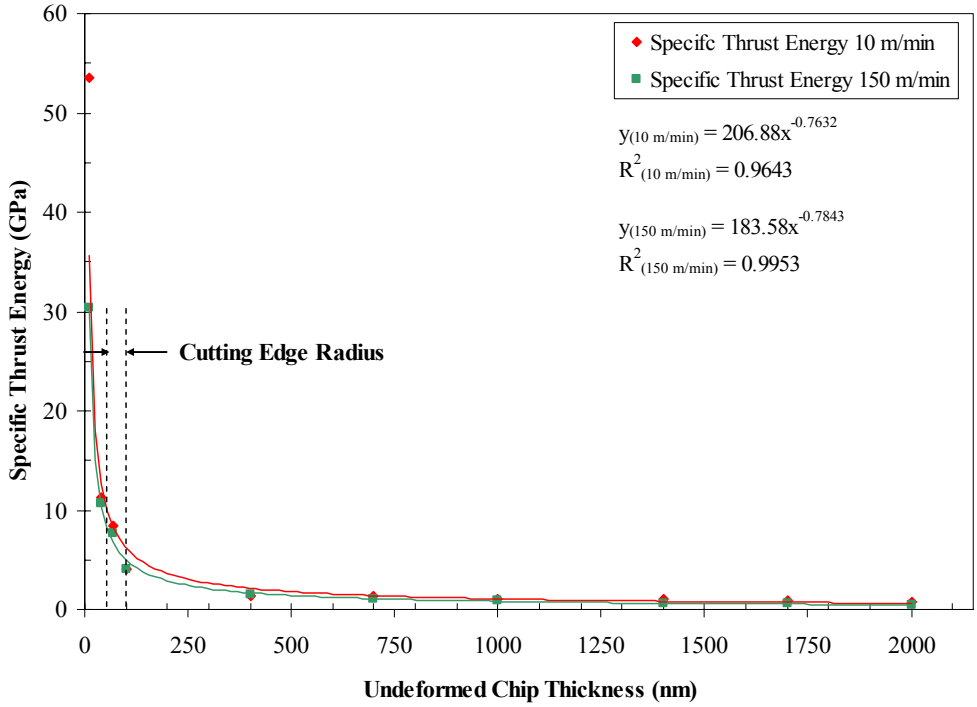

Figure 4.9: Effect of Undeformed Chip Thickness and Cutting Speed on Specific Thrust Energy (AL7075)

4.2.2 Chip Geometry

4.2.2.1 Chip Chart

AL7075 chips were collected and imaged on an SEM at each factor level during the cutting experiments. Figures 4.10 and 4.11 show the chip chart of chips collected at selected factor levels. The complete chip chart for all factor level is presented in Figures B.1 and B.2 in Appendix B.

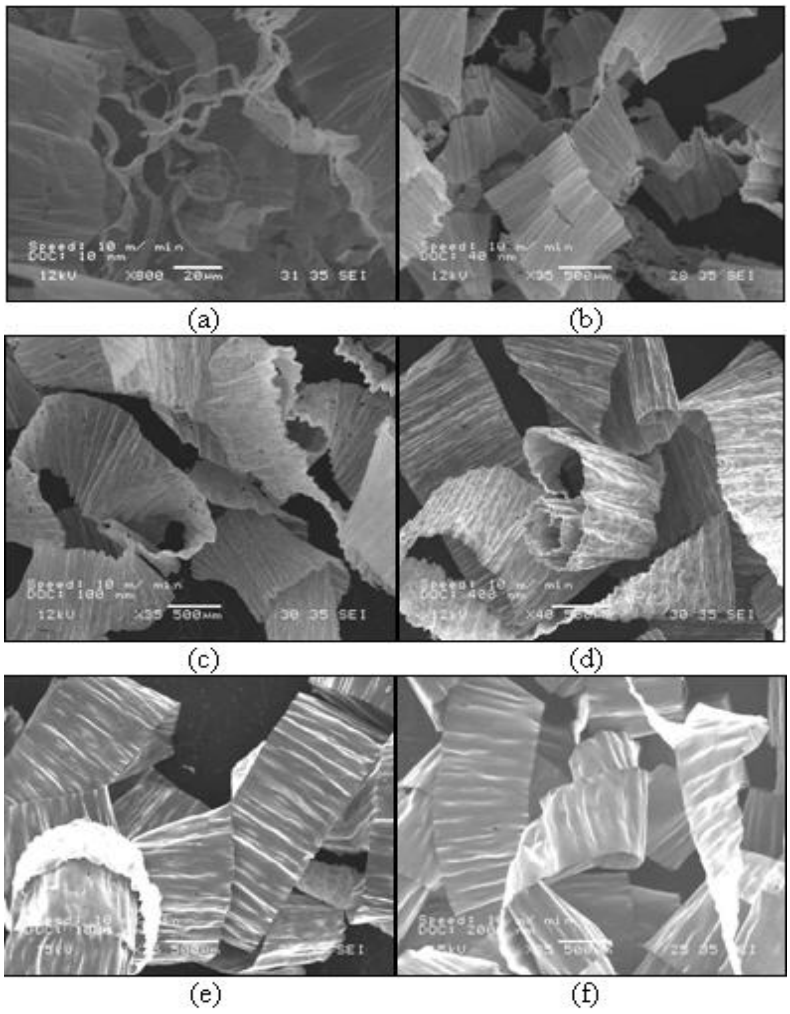

Figure 4.10: AL7075 Chip Chart at Selected Undeformed Chip Thickness for Cutting Speed of 10 m/min. (a) 10 nm (b) 40 nm (c) 100 nm (d) 400 nm (e) 1000 nm (f) 2000 nm

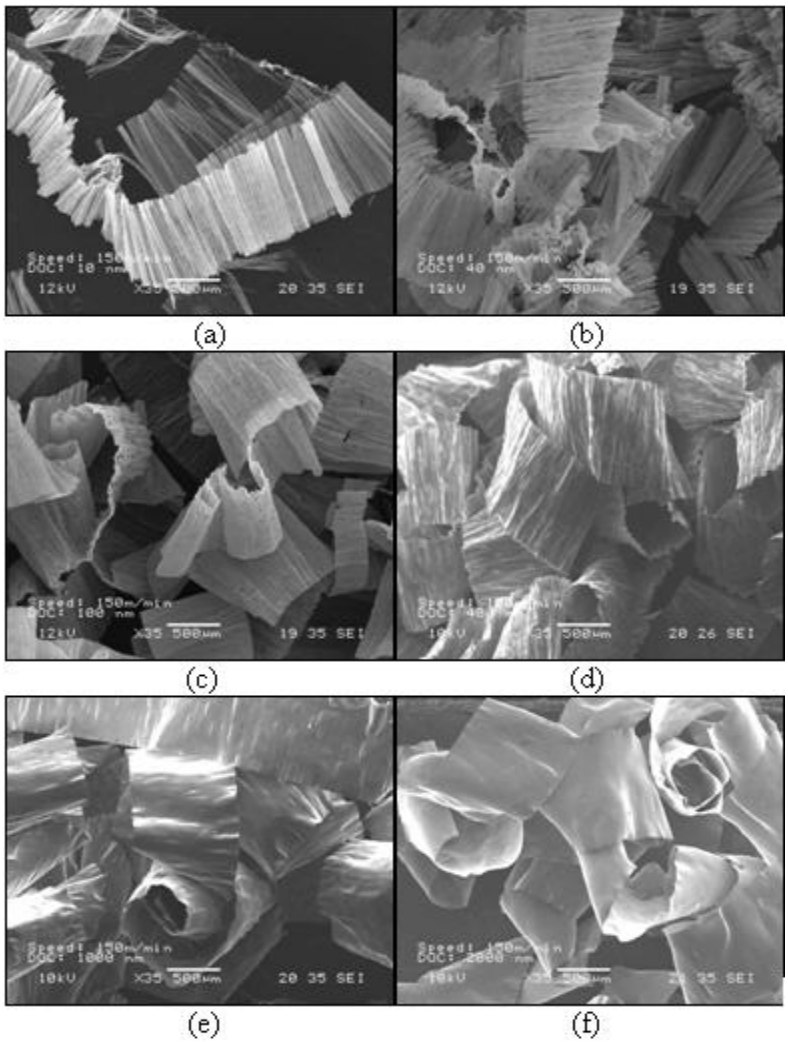

Figure 4.11: AL7075 Chip Chart at Selected Undeformed Chip Thickness for Cutting Speed of 150 m/min. (a) 10 nm (b) 40 nm (c) 100 nm (d) 400 nm (e) 1000 nm (f) 2000 nm

Figures 4.10 and 4.11 show continuous chips were collected for the entire range of the cutting experiment (10 nm – 2000 nm) at both cutting speeds. The chips produced at undeformed chip thicknesses of 10 nm – 100 nm at both cutting speeds are very thin and fragile. The chips collected within this range are powdery in nature, breaking and smearing easily upon contact. However, chips produced at undeformed chip thicknesses of greater than 400 nm are thicker and exhibit more strength than chips at smaller undeformed chip thicknesses. Hence, they are relatively easier to handle.

It is noticed that the curl of the chip increases with increased undeformed chip thickness at both cutting speeds. The chip charts also illustrate that the cutting speed does exert an influence on the thickness of the chips produced during micro and nano scale cutting. The deformed chip thickness appears to be visibly thicker at a lower cutting speed. This is consistent with what occurs in macro-scale cutting.

4.2.2.2 Chip Thickness

The deformed chip thickness was measured using an SEM after the cutting experiments. The chip was placed on the stage of the SEM with its side profile perpendicular to the optical imaging device in the SEM. Due to the fragility of the chip, it was impossible to ensure the orthogonality of the side of the chip with the optical imaging device. However, necessary actions were taken to ensure that the error mentioned was minimized.

The side profile of the chip was subsequently imaged at high magnifications (5500x – 8000x) and an estimate of the deformed chip thickness then obtained from the image. An example of the image used for the measurement of the deformed chip thickness is presented in Figure 4.12.

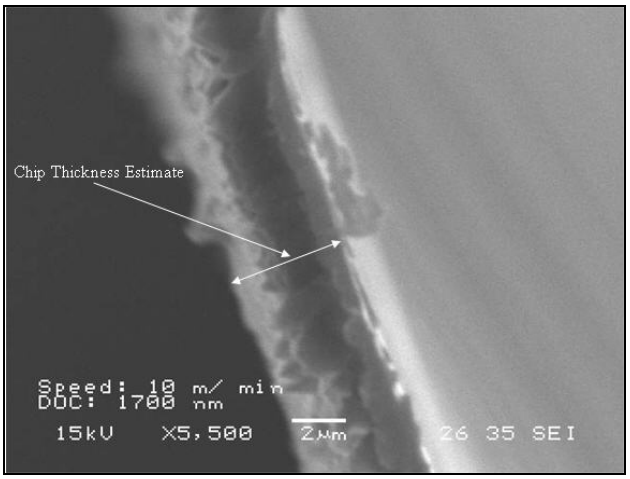

Figure 4.12: Illustration of Chip Thickness Measurement for AL7075

Figure 4.12 illustrates the chip thickness measurement when the cutting experiment was conducted at an undeformed chip thickness of 1700 nm and at a cutting speed of 10 m/min. The chip thickness can be estimated by measuring the width of the chip, as indicated by the white arrow in the image, and comparing it to the scale bar in the image. Five measurements at each factor level were made along each cross section and the values were averaged to characterize the average deformed chip thickness.

The estimates of the deformed chip thickness, the maximum and minimum deformed chip thicknesses and the standard deviations of the measurements at each factor level are presented in Tables B.17 and B.18 in Appendix B. However, some entries are omitted from the tables because it was impossible to align the chip orthogonally to the imaging device in the SEM due to the fragility of the chips. Therefore, no measurements could be obtained at these factor levels and they are left as blank entries in the corresponding tables. The graph of the effect of the undeformed chip thickness and cutting speed on the deformed chip thickness is presented in Figure 4.13.

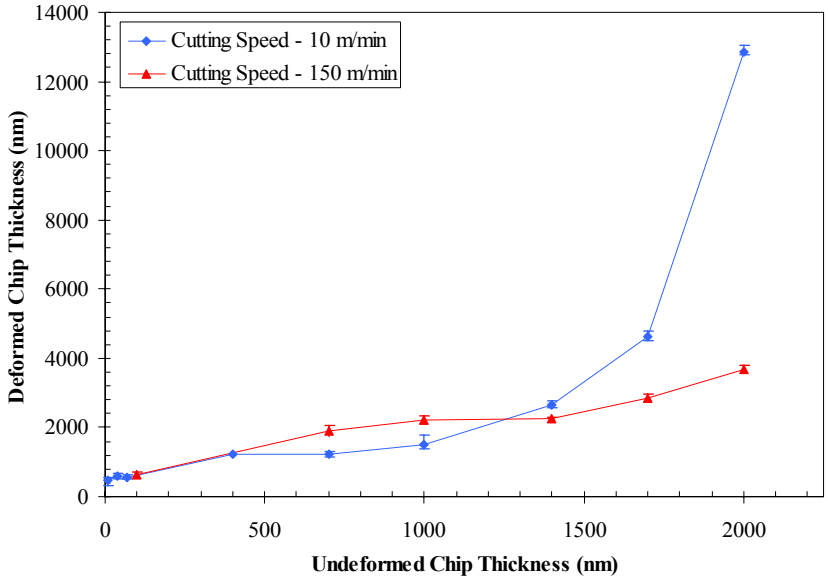

Figure 4.13: Effect of Undeformed Chip Thickness and Cutting Speed on Deformed Chip Thickness (AL7075)

Figure 4.13 illustrates that the deformed chip thickness increases with an increase in the undeformed chip thickness for both cutting speeds. This observed trend is similar to that observed by Trent (1984) in macro-scale cutting operations. It is also noticed that the deformed chip thickness is only significantly influenced by the cutting speed at undeformed chip thicknesses greater than 1700 nm. This observation is consistent with the force data in Figure 4.6, which shows that cutting speed has a negligible influence on the cutting and thrust forces until an undeformed chip thickness exceeding 700 nm.

After an undeformed chip thickness of 1000 nm, the deformed chip thickness at the cutting speed of 10 m/min increases more rapidly than at a cutting speed of 150 m/min. Trent (1984) describes similar findings commenting that increases in cutting speed decrease both the cutting force as well as the deformed chip thickness. One possible explanation for this phenomenon is that an increase in cutting speed increases the cutting temperature, which in turn reduces the friction between the chip and tool rake

face. The reduction in friction reduces the restriction to motion as the chip translates along the tool rake face. As the restriction to motion decreases, it is apparent from the law of continuity that thinner deformed chips would be produced. An analysis of the friction coefficient of the cutting process demonstrates that the friction coefficient does indeed decrease with increasing undeformed chip thickness and cutting speed. The analysis of the friction coefficient which supports this explanation is presented in section 4.2.4.2.

4.2.2.3 Shear Angle

The deformed chip thickness facilitates the evaluation of the shear angle in cutting. The shear angle is an essential parameter used for the derivation of other cutting process parameters. The shear angle is related to the cutting ratio as described by Equation 4.1:

$$\varphi = \tan^{-1} \frac{r \cos \alpha}{1 - r \sin \alpha} \tag{4.1}$$

where φ is the shear angle, r is the cutting ratio and α is the rake angle. The relationship between the cutting ratio, undeformed chip thickness and deformed chip thickness is described by Equation 4.2:

$$r = \frac{t}{t_c} \tag{4.2}$$

where t is the undeformed chip thickness and t_c is the deformed chip thickness. The rake angle of the SCD cutting tool is 0˚ for undeformed chip thicknesses greater than or equal to the edge radius of the tool. However, the effective rake angle is negative for cutting experiments where the undeformed chip thickness is smaller than the cutting edge radius. The effective rake angle for undeformed chip thicknesses smaller than the cutting edge

radius is estimated using a technique similar to that used by Nakayama and Tamura (1968). The effective rake angle of the cutting process is defined by the angle between the vertical axis and the tangent to the contact point between the cutting tool and the undeformed chip thickness as illustrated in Figure 4.14.

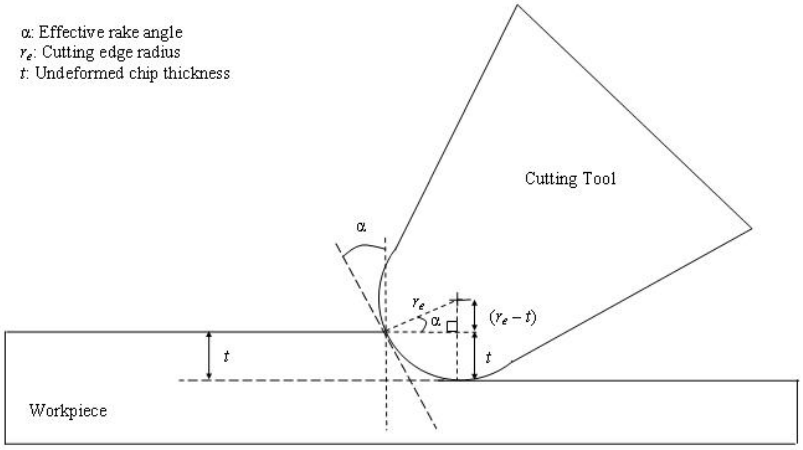

Figure 4.14: Determination of Effective Rake Angle (After Nakayama and Tamura, 1968)

Thus, the relationship between the effective rake angle, undeformed chip thickness and the cutting edge radius for undeformed chip thicknesses smaller than the cutting edge radius can be represented by Equation 4.3:

$$\alpha = \sin^{-1} \frac{(r_e - t)}{r_e} \tag{4.3}$$

where r_e is the value of the cutting edge radius, t is the deformed chip thickness and α is the effective rake angle. The edge radius of the SCD tool is assumed to be 60 nm when evaluating the shear angle. The effective rake angle determined using this technique was found to be in good agreement with the average rake angle model proposed by Manjunathaiah and Endres (2000).

The average rake angle model proposed by Manjunathaiah and Endres (2000) uses the undeformed chip thickness, edge radius, nominal orthogonal rake of the tool and angle θ, which defines the separation point on the tool-chip contact, to predict the average rake angle. The tool-chip contact in a cutting process can either end on the rake face or the edge radius of the tool. Hence, two separate equations are used by Manjunathaiah and Endres to predict the average rake angle depending on the end point of the tool-chip contact. When the tool-chip contact point ends on the edge radius, the average predicted rake angle is always negative and can be expressed as (Manjunathaiah and Endres, 2000):

$$\gamma_{ave} = -\tan^{-1}\left[\frac{\sqrt{(2ch/r_n - 1)ch/r_n} - \sin\theta}{ch/r_n - 1 + \cos\theta}\right] \tag{4.4}$$

where γ_{ave} is the predicted average rake angle, c is a constant greater than 1, h is the undeformed chip thickness, r_n is the edge radius, θ is the angle which defines the separation point and γ_0 is the nominal orthogonal rake angle of the tool.

The cutting ratio, effective rake angle and the shear angle for AL7075 were evaluated and presented in Tables 4.1 and 4.2. The effect of undeformed chip thickness and cutting speed on both the cutting ratio and shear angle are illustrated graphically in Figures 4.15 and 4.16.

Table 4.1: Cutting Ratio and Shear Angle – Cutting Speed of 10 m/min (AL7075)

Undeformed Chip Thickness (nm)	Average Deformed Chip Thickness (nm)	Effective rake angle, α (˚)	Cutting ratio, r	Shear Angle, φ (˚)
10	455	-56.44	0.022	0.68
40	605	-19.47	0.066	3.49
70	568	0	0.123	7.02
100		0		
400	1212	0	0.330	18.26
700	1222	0	0.573	29.80
1000	1485	0	0.673	33.94
1400	2666	0	0.525	27.70
1700	4632	0	0.367	20.15
2000	12851	0	0.156	8.85

Table 4.2: Cutting Ratio and Shear Angle – Cutting Speed of 150 m/min (AL7075)

Undeformed Chip Thickness (nm)	Average Deformed Chip Thickness (nm)	Effective rake angle, α (˚)	Cutting ratio, r	Shear Angle, φ (˚)
10		-56.44		
40		-19.47		
70		0		
100	639	0	0.156	8.89
400		0		
700	1887	0	0.371	20.35
1000	2232	0	0.448	24.13
1400	2253	0	0.621	31.85
1700	2855	0	0.595	30.77
2000	3670	0	0.545	28.58

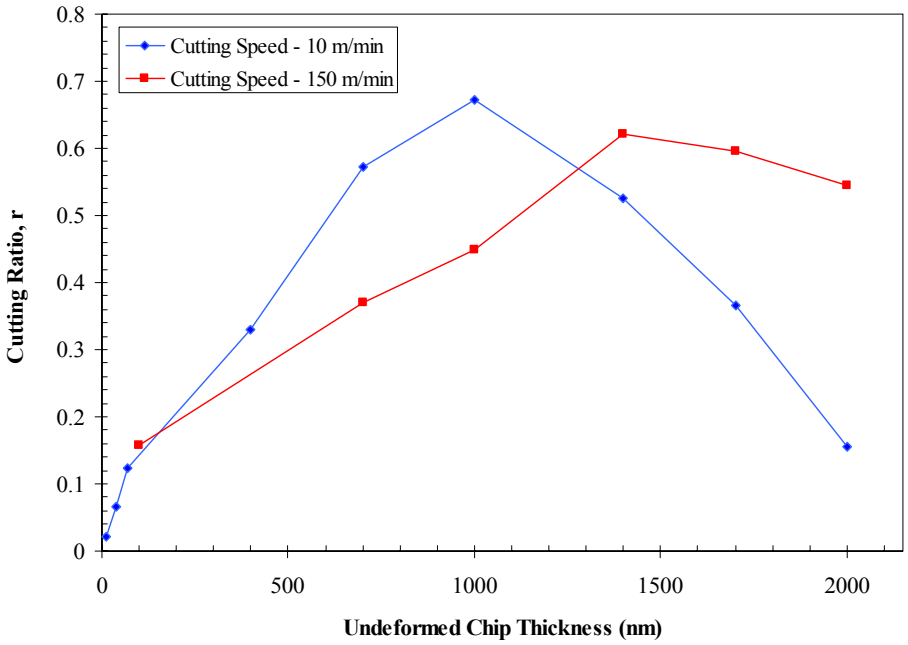

Figure 4.15: Effect of Undeformed Chip Thickness and Cutting Speed on Cutting Ratio (AL7075)

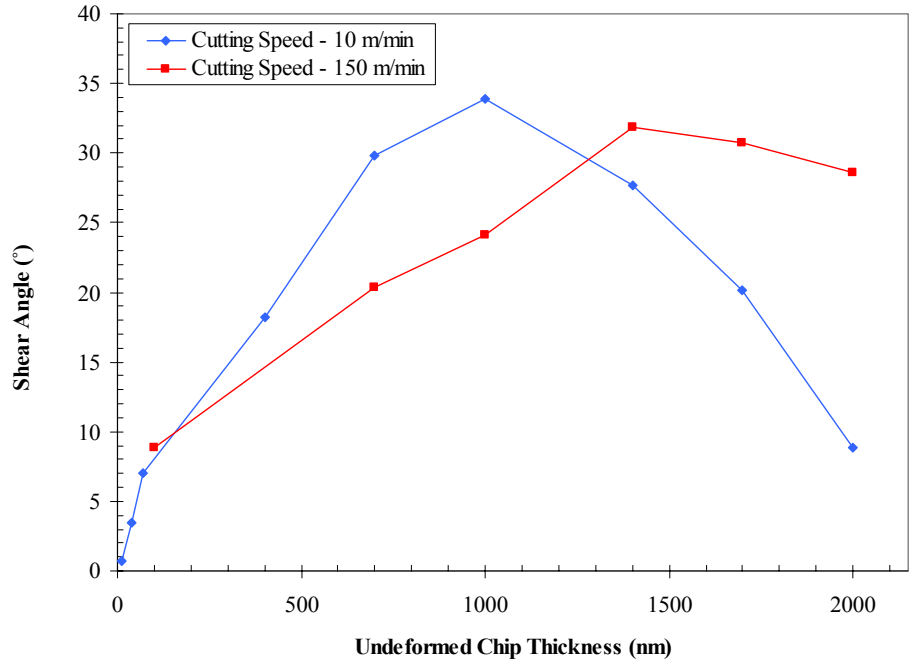

Figure 4.16: Effect of Undeformed Chip Thickness and Cutting Speed on Shear Angle (AL7075)

Both the cutting ratio and shear angle increase with an increase in undeformed chip thickness of up to 1000 nm and 1500 nm for cutting speeds of 10 m/min and 150 m/min, respectively. At undeformed chip thicknesses greater than the stated values, both the cutting ratio and shear angle decrease with subsequent increase in undeformed chip thickness. The cutting ratio is smaller at the cutting speed of 150 m/min when compared to that at 10 m/min in the undeformed chip thickness range of 100 - 1300 nm. Beyond 1300 nm, the trend of the cutting ratio for the cutting speeds of 150 m/min and 10 m/min are reversed. Since the cutting ratio is derived from the ratio of the undeformed chip thickness to the deformed chip thickness, the trend observed in Figure 4.15 is consistent with that observed in Figure 4.13.

It has been proposed by Zorev (1966) that the observed trend in the cutting ratio can be attributed to changes in the friction coefficient between the work material and the tool rake face due to the formation of a built-up edge at a critical undeformed chip thickness. The formation of the built-up edge changes the rake angle and angle of action of the cutting process. Consequently, the chip deformation process also changes, resulting in the observed trend in the cutting ratio. Although there was no evidence of built-up edge formation, trends in the friction coefficient similar to those described by Zorev were observed in this study. In addition, Shaw (1984) also presented similar findings on the relationship between the friction coefficient, shear angle and cutting ratio. Hence, trends observed in the cutting ratio in the current study can be explained via Zorev's and Shaw's comments. Similar trends in the shear angle were also observed by Manjunathaiah and Endres (2000).

A possible explanation for the influence of cutting speed on the cutting ratio and shear angle is that an increase in cutting speed increases the cutting temperature, which in turn causes thermal softening of the workpiece material. The thermal softening of the workpiece material decrease the cutting and thrust forces. This decrease in cutting and thrust forces is a result of the increase in the shear angle. It is shown in Figure 4.6 that the cutting and thrust forces are not significantly reduced as a result of an increase in cutting speed until an undeformed chip thickness of around 700 nm. After 700 nm, the cutting force at 150 m/min is smaller than that at 10 m/min. Therefore it is anticipated that the shear angle of the cutting process at 150 m/min would only be higher than that at 10 m/min after an undeformed chip thickness of 700 nm as shown in Figure 4.16.

4.2.3 Surface Morphology

Surfaces generated at selected cutting conditions were imaged in an SEM. Figures 4.17 and 4.18 show the surfaces generated at the selected cutting conditions.

A visual inspection of the surfaces indicate that cutting at low undeformed chip thickness produces smoother surfaces at both cutting speeds. It is also noticed that cutting at a higher speed also produces smoother surfaces, ceteris paribus.

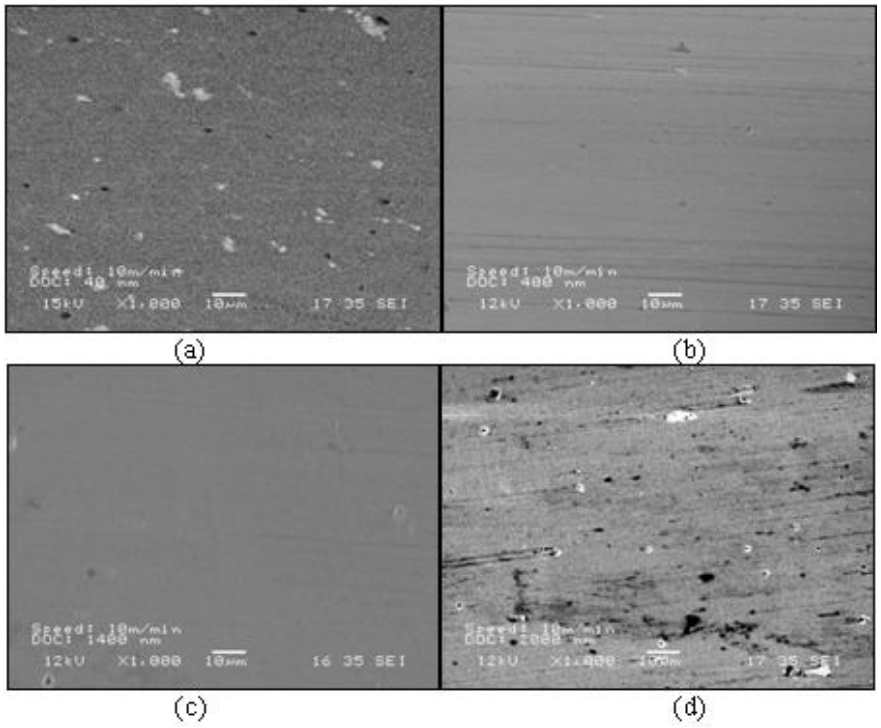

Figure 4.17: Effect of Undeformed Chip Thickness on Surface Roughness – Cutting Speed of 10 m/min (a) 40 nm (b) 400 nm (c) 1400 nm (d) 2000 nm (AL7075)

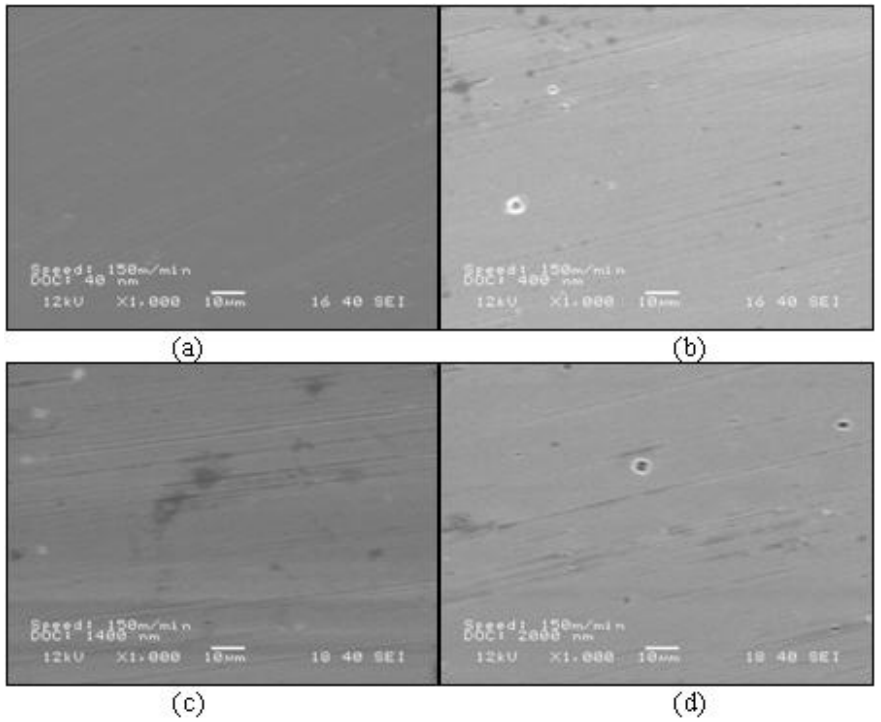

Figure 4.18: Effects of Undeformed Chip Thickness on Surface Roughness – Cutting Speed of 150 m/min (a) 40 nm (b) 400 nm (c) 1400 nm (d) 2000 nm (AL7075)

The surfaces generated were subsequently characterized using the Zygo white light interferometer. Areal surface roughness measurements were used to characterize the surface generated during the cutting experiments. Three-dimensional S_a and S_q roughness parameters were obtained from the measurements. A representative three-dimensional topographical map of the surface is presented in Figure 4.19. The results of the surface characterization are shown in Tables B.19 and B.20 in Appendix B. Graphical representations of the characterized surfaces are presented in Figures 4.20 and 4.21.

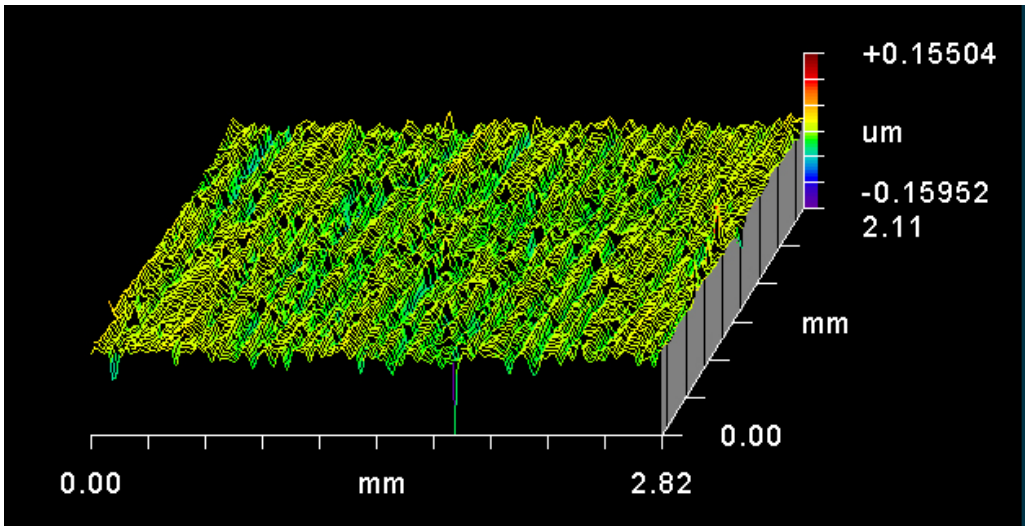

Figure 4.19: 3-D Topography Map of Surface Generated at 150 m/min at an Undeformed Chip Thickness of 40 nm (AL7075)

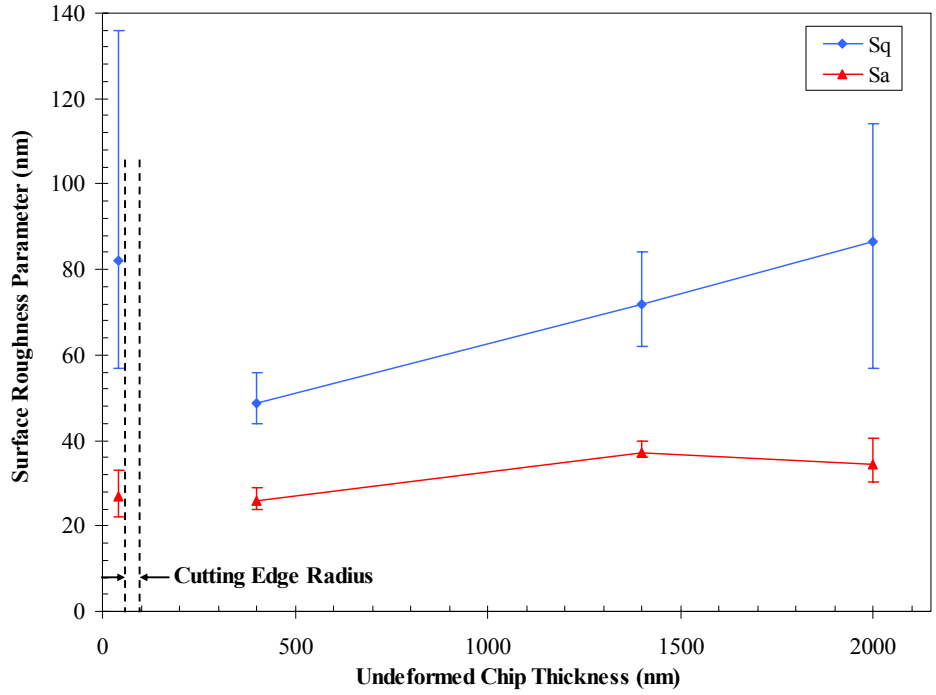

Figure 4.20: Effect of Undeformed Chip Thickness on Surface Roughness at Cutting Speed of 10 m/min (AL7075)

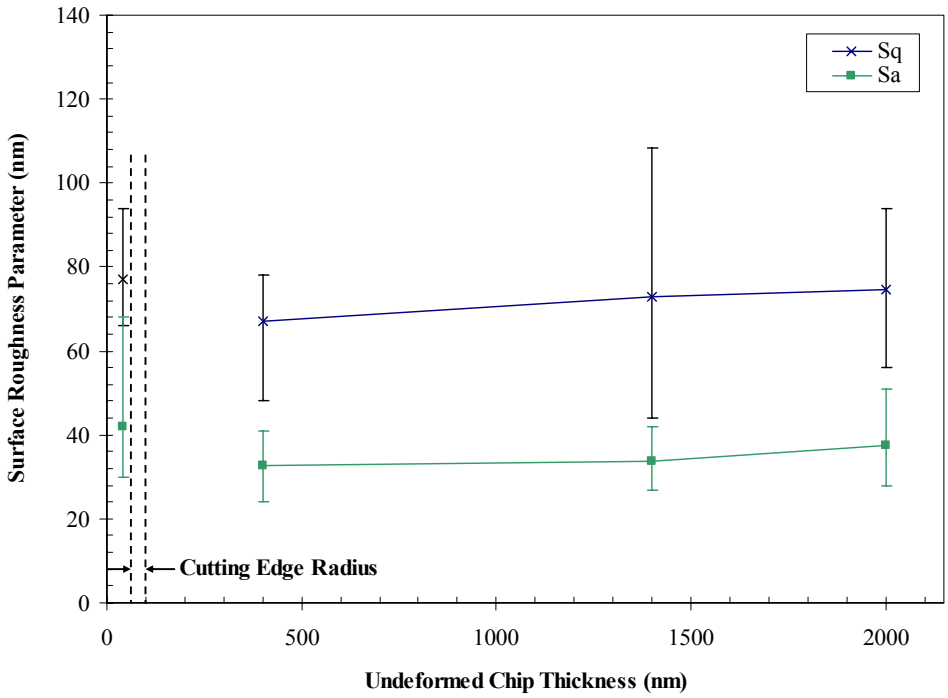

Figure 4.21: Effect of Undeformed Chip Thickness on Surface Roughness at Cutting Speed of 150 m/min (AL7075)

At undeformed chip thicknesses greater than the edge radius of the tool, surface roughness increases linearly as illustrated in Figures 4.20 and 4.21. However, when cutting is performed at undeformed chip thicknesses smaller than the edge radius of the tool, the surface generated is rougher than that when undeformed chip thicknesses are greater than the edge radius of the tool. This can be attributed to the dominant effect of the ploughing process when cutting at undeformed chip thicknesses smaller than the edge radius of the tool. A ploughing process typically displaces the material sideways and ahead of the cutting tool. This process hence generates a surface which is typically rougher as compared to a surface generated by shearing of the work material. This observation is in agreement with observations from macro-scale cutting operations, where surface roughness generated generally increases with undeformed chip thickness.

The variance in the measured surface roughness is fairly large. This variance can be attributed to the inclusions in the material as observed in Figure 4.17 and 4.18. The presence of the inclusions inevitably skews the areal surface characterization process.

4.2.4 Experimental Observations

4.2.4.1 Edge Radius of Cutting Tool

The edge radius of the tool was monitored and imaged on the SEM before and after each cutting experiment. The image of the cutting edge of a new tool is presented in Figure 3.10 in the previous chapter. However, due to smearing of the work material on the cutting tool during experiments, the subsequent images taken to characterize the edge radius of the tool are fuzzy under high magnification. These fuzzy images cannot be used to accurately determine the edge radius of the tool.

However, the tool was subsequently used to conduct replications of the experiment. The force data gathered in subsequent cutting experiments show good agreement with previous replications. This indicates that the cutting tool is not worn nor adversely affected by the smearing of the work material on it. Hence, the edge radius of the tool is assumed to remain sharp with a measurement of 60 nm for the entire experimental investigation.

4.2.4.2 Rake Face of Cutting Tool

The rake face of the SCD tool was monitored during cutting experiments. An image of the rake face taken after the experiment with an undeformed chip thickness of 2000 nm at a cutting speed of 10 m/min is shown in Figure 4.22.

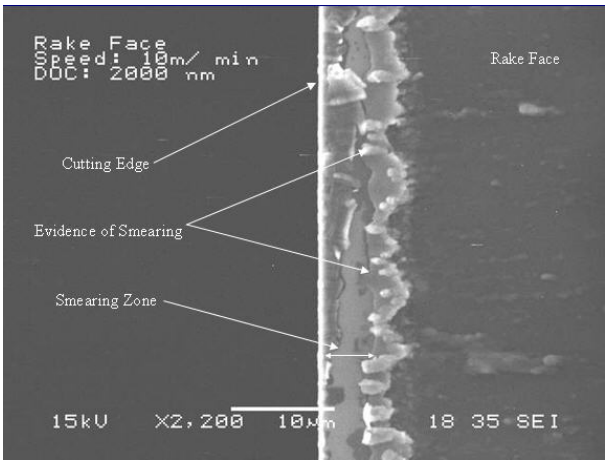

Figure 4.22: SEM Image of the Rake Face of SCD Tool

Figure 4.22 shows evidence of smearing of the workpiece material on the rake face of the cutting tool. The smear marks can be used to estimate the tool chip contact length and thereby offer possible explanations for the increase in friction coefficient with decreasing undeformed chip thickness. By the same token, the smearing on the tool's

rake face can also be used to explain the leveling-off effect of the thrust force observed in this study.

The friction coefficients were evaluated by taking the ratio of the of the cutting force to the thrust force for each factor level and are presented in Tables B.21 and B.22 in Appendix B. A graphical representation of the effects of cutting speed and undeformed chip thickness on the friction coefficient is shown in Figure 4.23.

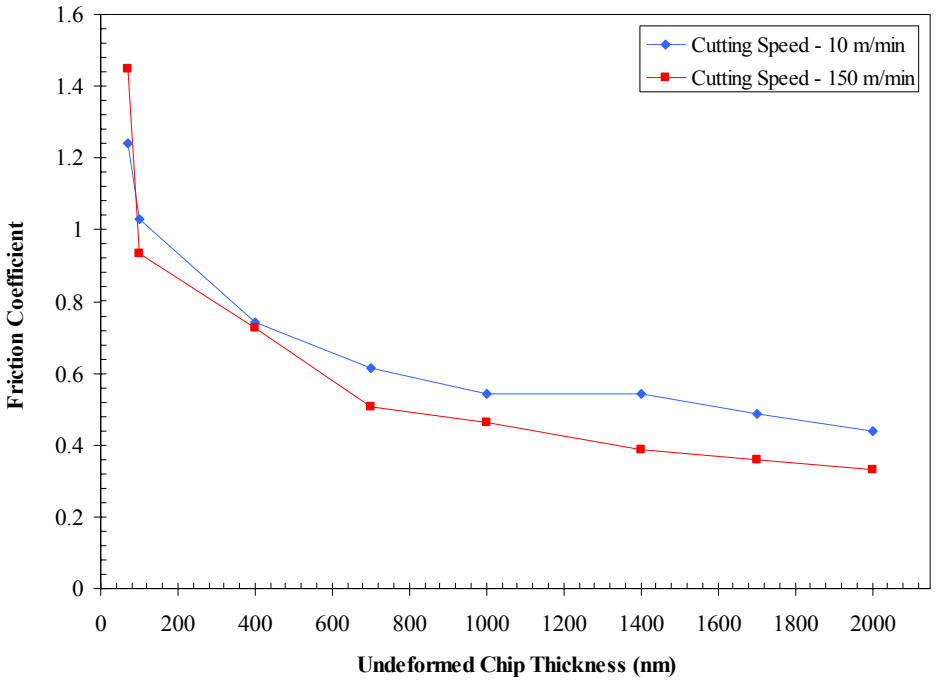

The friction coefficient decreases at both cutting speeds as the undeformed chip thickness increases. It has been reported that an increase in friction with decreasing specimen size is observed in forging and extrusion processes. This phenomenon was studied by Tiesler (2002) and aptly termed "frictional size-effect." This effect is similarly

observed in this experimental study, hence demonstrating that the frictional size-effect is also an occurrence in mechanical cutting processes. This frictional size-effect could be explained by the morphology of the surface generated and the smearing of the workpiece material on the rake face of the tool.

The roughness of the surface generated increases when cutting at around or less than the value of the cutting edge radius, as shown in Figures 4.20 and 4.21. The rougher surface is likely to have increased the real area of contact between the chip and the tool rake face. This increase in real area of contact between the tool rake face and the chip contributes to an increase in friction force. This might be a possible reason for the frictional size-effect observed in Figure 4.23.

Figures 4.24 and 4.25 show a selected series of SEM images of the SCD tool rake face at a cutting speed of 10 m/min. The complete series of SEM images of the cutting tool's rake face at a cutting speed of 10 m/min is presented in Figure B.3 in Appendix B. The tool-chip contact length can be estimated from the length of the smear zone as shown in Figures 4.24 and 4.25. Figure 4.24 shows that the area of the region smeared by the work material increases non-linearly with increasing undeformed chip thickness. The smearing on the rake face increases significantly from the cutting edge as the undeformed chip thickness increases. It can be inferred from the series of SEM images that the tool-chip contact length increases non-linearly with increasing undeformed chip thickness at small undeformed chip thicknesses. However, at large undeformed chip thicknesses, it is observed that the smear zone increases more or less linearly with increasing undeformed chip thickness, as seen in Figure 4.24. This observation is consistent with the experimental findings reported by Zorev (1966) in dry cutting of 20K free cutting steel.

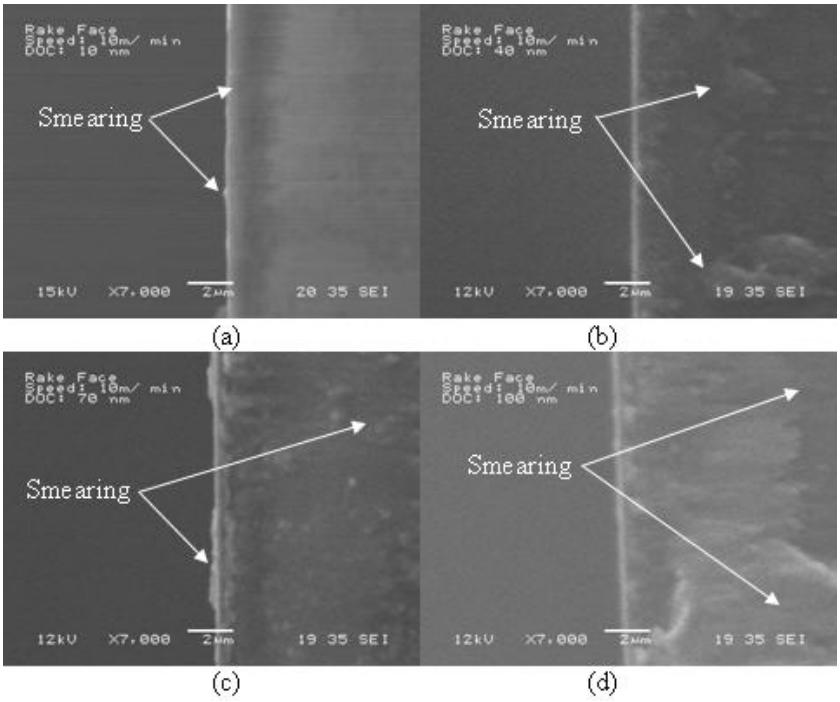

Figure 4.24: SEM Image of the Rake Face of SCD Tool at Selected Undeformed Chip Thickness - Cutting Speed of 10 m/min (a) 10 nm (b) 40 nm (c) 70 nm (d) 100 nm

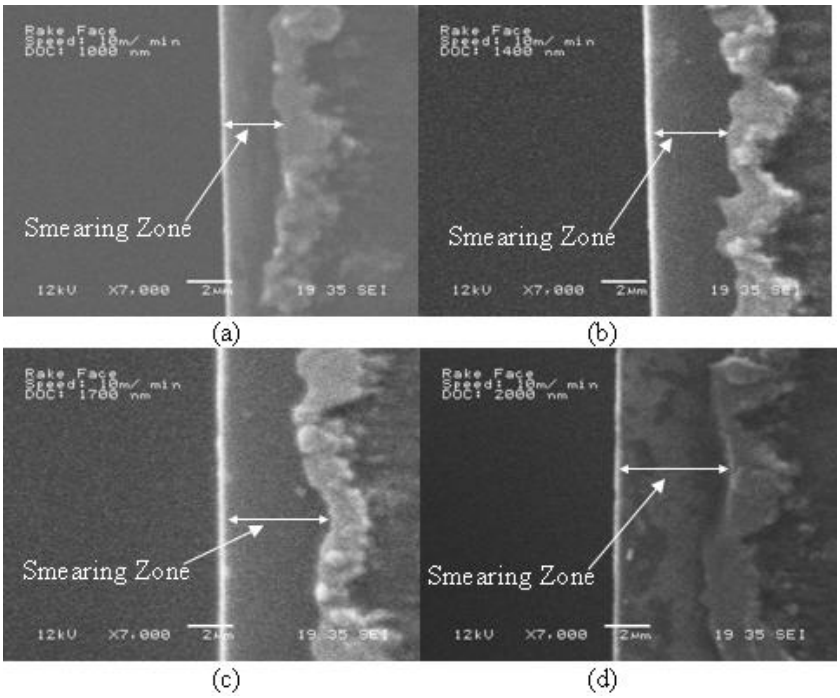

Figure 4.25: SEM Image of the Rake Face of SCD Tool at Selected Undeformed Chip Thickness - Cutting Speed of 10 m/min (a) 1000 nm (b) 1400 nm (c) 1700 nm (d) 2000 nm

It is evident from Figure 4.4 that the cutting force does not decrease linearly with decreasing undeformed chip thickness when transiting from a shearing to a ploughing process at small undeformed chip thicknesses. Hence, it seems likely that a non-linear decrease in cutting force and tool-chip contact area increases the normal pressure exerted on the tool-chip interface with decreasing undeformed chip thickness. The higher normal pressure exerted on the tool-chip interface might have increased the real contact surface area between the chip and the tool rake face. The increase in real contact surface area between the tool rake face and chip inevitably increases the frictional force between the two surfaces as the chip translates across the tool rake face. This results in higher frictional forces at small undeformed chip thicknesses. This might be a possible reason for the frictional-size effect observed at small undeformed chip thicknesses in Figure 4.23.

However, at large undeformed chip thicknesses, the tool-chip contact length increases linearly with increasing undeformed chip thickness, as shown in Figure 4.25. Consequently, the normal pressure exerted on the tool-chip interface probably remains relatively constant at large undeformed chip thicknesses. Therefore, the real contact surface area between the chip and the tool rake face remains relatively uniform despite the increase in the tool-chip contact length. As a result, the frictional force between the tool and the chip stabilizes at large undeformed chip thicknesses. Hence, the friction coefficient also stabilizes at large undeformed chip thicknesses as observed in Figure 4.23. This might have resulted in the leveling-off effect in the thrust force observed in Figure 4.2.

Figures 4.26 and 4.27 show another selected series of SEM images of the SCD tool rake face at a cutting speed of 150 m/min. The complete series of SEM images of the cutting tool rake face at a cutting speed of 150 m/min is presented in Figure B.4 in Appendix B. It is observed that smearing of the workpiece material on the tool rake face still occurs at this cutting speed. Comparisons between Figures 4.26 and 4.27 indicate that smearing on the rake face is more prominent at small undeformed chip thicknesses than at large undeformed chip thicknesses. This is contrary to the observation made at the cutting speed of 10 m/min.

However, the trend observed in the tool-chip contact length in Figure 4.26 is comparable to that at a cutting speed of 10 m/min. Hence, the frictional size-effect observed at small undeformed chip thicknesses at the cutting speed of 150 m/min can be explained in a similar fashion with that at a cutting speed of 10 m/min. Smearing on the tool rake face also continues to occur at large undeformed chip thicknesses at the cutting speed of 150 m/min. The tool-chip contact length is not well-defined in the SEM images of the tool rake face as there are no distinct smearing zones, as shown in Figure 4.27. Although the tool-chip contact length is not well-defined, similar explanations will be used to describe the stabilizing of the friction coefficient since similar trends in the friction coefficient are observed at both cutting speeds as seen in Figure 4.23.

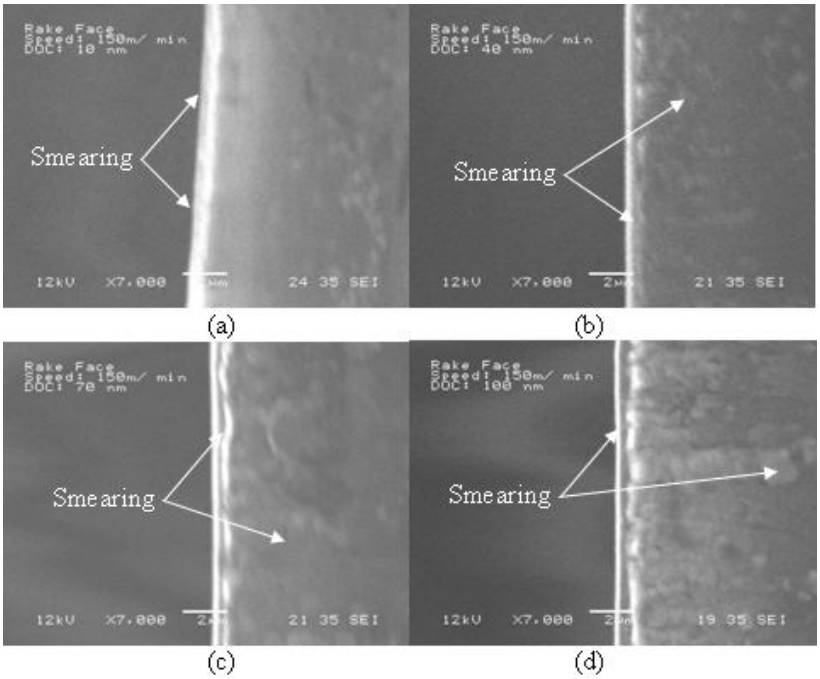

Figure 4.26: SEM Image of the Rake Face of SCD Tool at Selected Undeformed Chip Thickness - Cutting Speed of 150 m/min (a) 10 nm (b) 40 nm (c) 70 nm (d) 100 nm

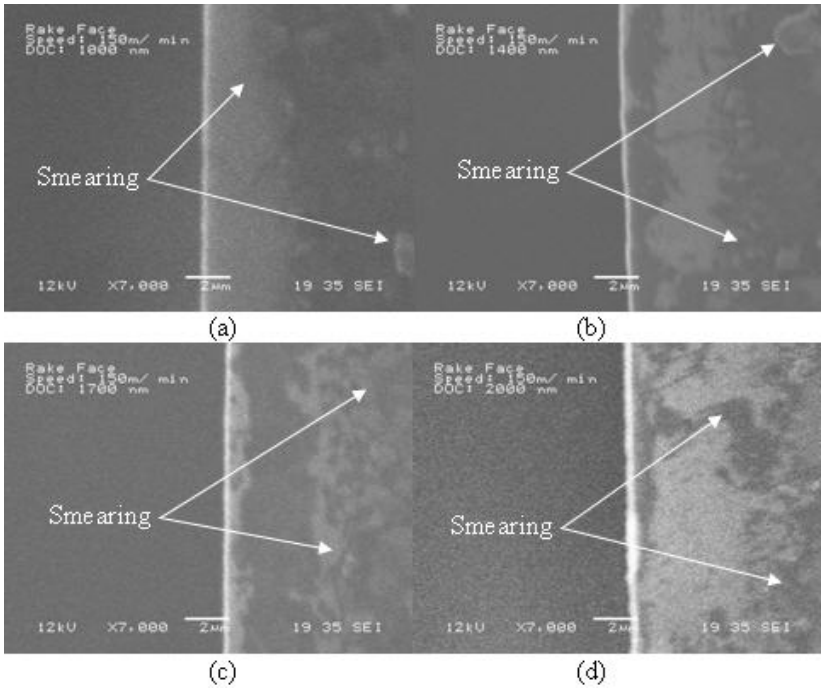

Figure 4.27: SEM Image of the Rake Face of SCD Tool at Selected Undeformed Chip Thickness - Cutting Speed of 150 m/min (a) 1000 nm (b) 1400 nm (c) 1700 nm (d) 2000 nm

There is also a slight decrease in the friction coefficient with an increase in the cutting speed as illustrated in Figure 4.23. This decrease in friction as a result of an increase in the cutting speed is in agreement with Trent's (1984) observations. The increase in cutting speed is likely to have decreased the shear strength of the work material due to increase in cutting temperatures. The decrease in shear strength of the materials might have reduced the force required for the shearing of the chip at the tool-chip interface. This reduction in the shearing force at the tool-chip interface might have led to the decrease in friction force at the higher cutting speed. Furthermore, the reduction in the friction coefficient is consistent with the observation of thinner deformed chips at the higher cutting speed of 150 m/min.

4.2.5 Derived Parameters using Merchant's Theory

4.2.5.1 Shear Stress

The average shear stress values estimated from the cutting experiments at both cutting speeds are presented in Table 4.3. The nominal shear stress value obtained from the ASM Specialty Handbook for Aluminum and Aluminum Alloys is also presented in Table 4.3.

Table 4.3: Estimated and Nominal Shear Stress Values (ASM Specialty Handbook for Aluminum and Aluminum Alloys)

	10 m/min	150 m/min
Average Shear Stress (MPa)	524.4	542.9
Nominal Shear Stress (MPa)	330	

The shear stress is estimated using the following equation:

$$\tau = \frac{(F_c \cos\varphi - F_T \sin\varphi)\sin\varphi}{wt} \tag{4.5}$$

Table 4.3 shows that the estimated average shear stress of the material from the cutting experiments is significantly higher than the nominal shear stress values obtained from the handbook. This is expected since the shear yield strength of the material would have to be exceeded in order for the work material to undergo plastic deformation. Furthermore, it is suggested by Atkins (2003) that the reason for high values of shear yield stress being derived at small undeformed chip thicknesses is due to the neglect of specific surface work during cutting analysis. It is noticed that the estimated average shear stress values are similar at both cutting speeds. This observation is consistent with the force data presented as the cutting force is not significantly influenced by the cutting speed until undeformed chip thickness of 1000 nm. Hence, the similarity in the evaluated shear stress values is consistent with the force data acquired

4.2.5.2 Energy Per Unit Volume

Energy consumption during mechanical cutting processes is often evaluated in macro-scale machining operations. The total energy consumed offers useful information on the minimum energy required to effectively complete a particular machining task. The total energy per unit volume consumed in a cutting operation can be approximated by the sum of shear energy per unit volume consumed on the shear plane and the friction energy per unit volume consumed on the tool face. The relationship between these three parameters can be expressed by the following equation, Equation 4.6:

$$u \approx u_s + u_f \tag{4.6}$$

where u is total energy per unit volume, u_s is the shear energy per unit volume consumed on the shear plane and u_f is the friction energy per unit volume consumed on the tool face.

These parameters are evaluated and presented in Figures 4.28 and 4.29. It is observed that a large portion of the total energy per unit volume is consumed as shear energy on the shear plane at both cutting speeds. This observation is comparable to conventional macro-scale machining operations when shearing is the dominant operating mechanism.

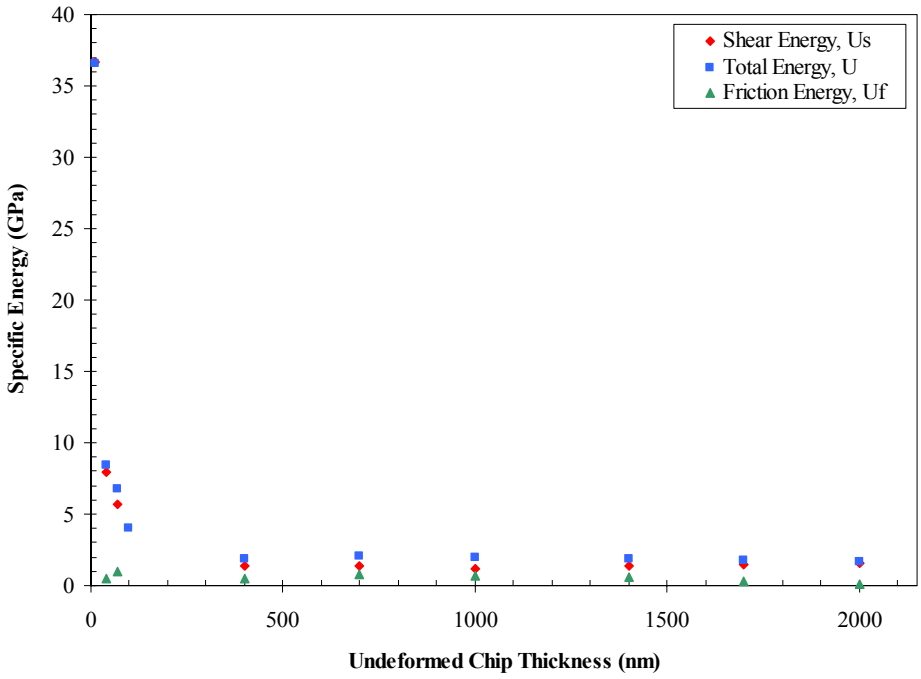

Figure 4.28: Effects of Undeformed Chip Thickness on Total, Shear and Friction Energies Per Unit Volume – Cutting Speed of 10 m/min (AL7075)

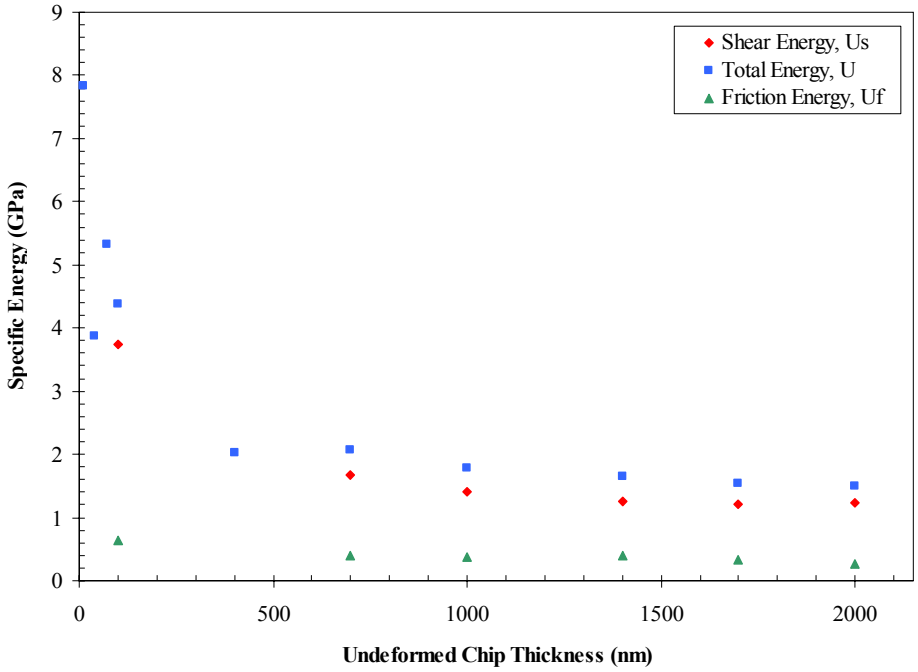

Figure 4.29: Effects of Undeformed Chip Thickness on Total, Shear and Friction Energies Per Unit Volume – Cutting Speed of 150 m/min (AL7075)

4.3 Micro-/ Nano-Scale Machining of P20 Mold Steel

Micro and nano scale orthogonal dry cutting experiments were conducted on P20 mold steel over an undeformed chip thickness range of 0.3 - 2 µm on the Toshiba machine. The range of the undeformed chip thickness was subsequently extended from 5 - 60 µm on the Hardinge lathe. The cutting experiments were conducted at cutting speeds of 10 m/min and 115 m/min, respectively.

4.3.1 Cutting Forces and Size- Effect

4.3.1.1 Time Series Profile

The cutting force time series profiles for undeformed chip thicknesses of 0.7 µm and 10 µm at a cutting speed of 10 m/min are shown in Figures 4.30 and 4.31. The two illustrations are representative time series profiles for P20 micro and nano scale cutting

experiments conducted on the Toshiba machine and Hardinge lathe. The time series profiles were similarly used to identify setup rigidity issues as well as to determine the steady state force as described in the corresponding section for AL7075.

Figure 4.30 shows that the transient engagement force experienced by the tool is not significantly greater than the steady state cutting force. However, the time series profile shown in Figure 4.31 illustrates that the transient engagement force experienced by the tool is significantly greater than the steady state cutting force. Although the transient engagement force in both time series profiles differed, the time taken for both forces to settle into the steady state is comparable.

It is also noticed that the time series profile obtained from an undeformed chip thickness of 0.7 μm exhibits more oscillations when compared to the 10 μm time series profile. These oscillations are the result of the ploughing mechanism since the cutting experiment was performed at undeformed chip thicknesses considerably smaller than the edge radius of the tool. This ploughing mechanism produces fragmented chips and generates rougher surfaces, which in turn plays a pivotal role in introducing undesired oscillations in the acquired force signal. A detailed elucidation of this observation will be presented in a later section.

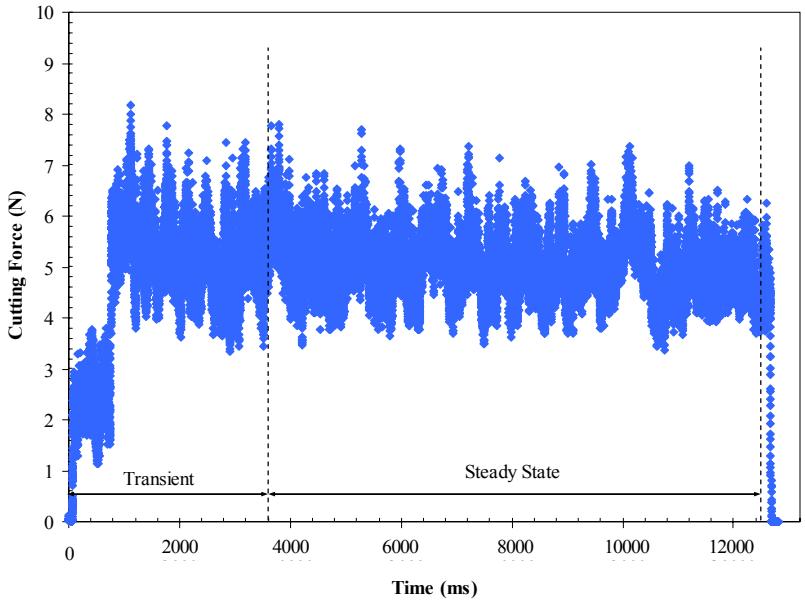

Figure 4.30: Force-Time Series Profile for Micro-/ Nano-Scale Cutting of P20 Steel (Cutting Speed: 10 m/min; Undeformed Chip Thickness: 0.7 µm)

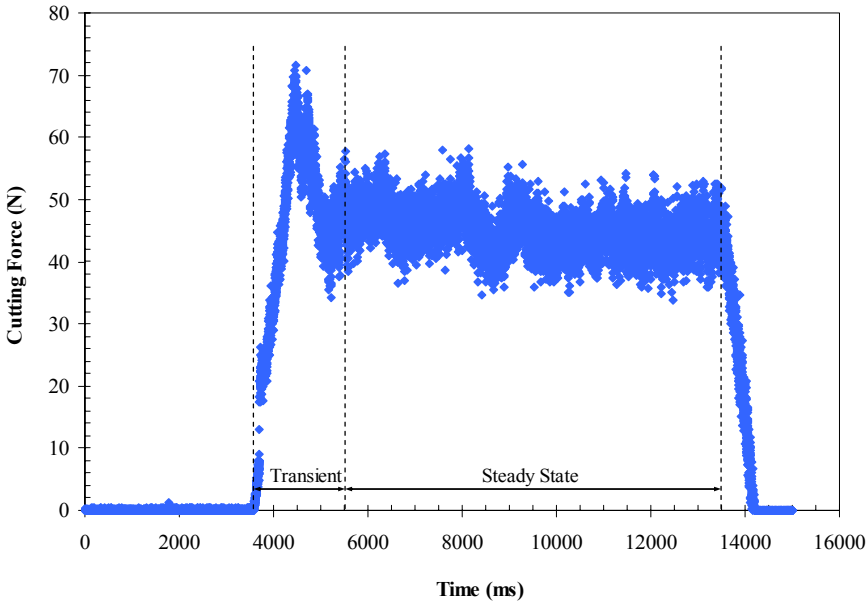

Figure 4.31: Force-Time Series Profile for Micro-/ Nano-Scale Cutting of P20 Steel (Cutting Speed: 10 m/min; Undeformed Chip Thickness: 10 µm)

4.3.1.2 Average Force Values and Trends

The steady state cutting and thrust forces for each factor level were averaged over the five cutting experimental replications. The average force values listed in Tables B.23 and B.24 in Appendix B are for cutting speeds of 10 m/min and 115 m/min, respectively. The measured force values for each cutting experiment are also provided in Tables B.25 - B.34 of Appendix B. The data presented in Tables B.23 and B.24 show the range and the mean force values obtained during cutting experiments. The cutting force data in Tables B.23 and B.24 are graphed as a function of the undeformed chip thickness on a log-log scale as shown in Figures 4.32 and 4.33.

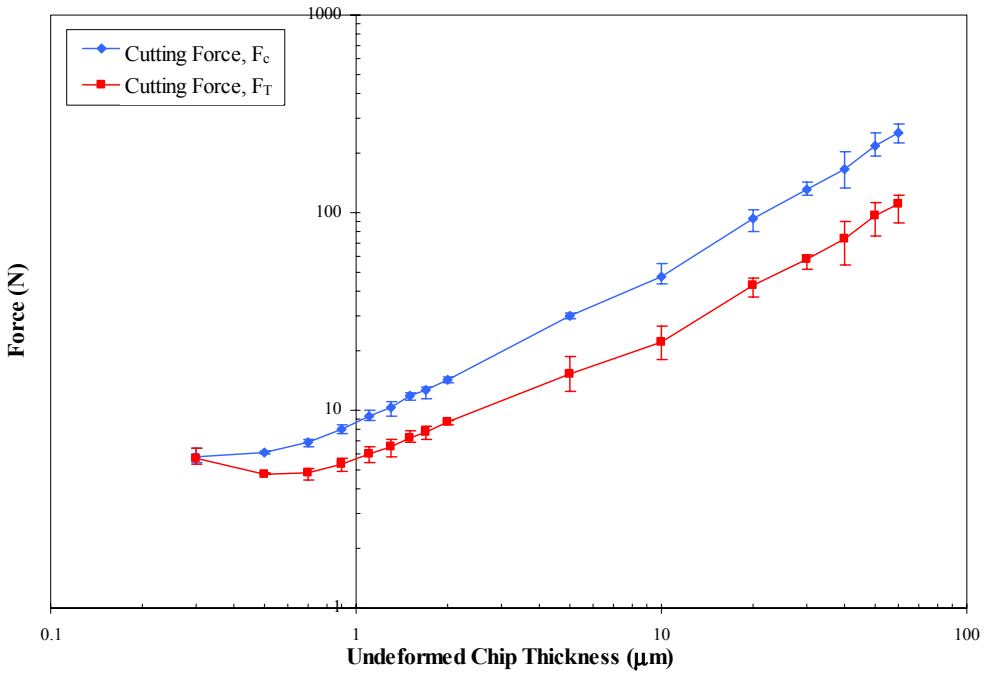

Figure 4.32: Effect of Undeformed Chip Thickness on Cutting and Thrust Forces at a Cutting Speed of 10 m/min (P20)

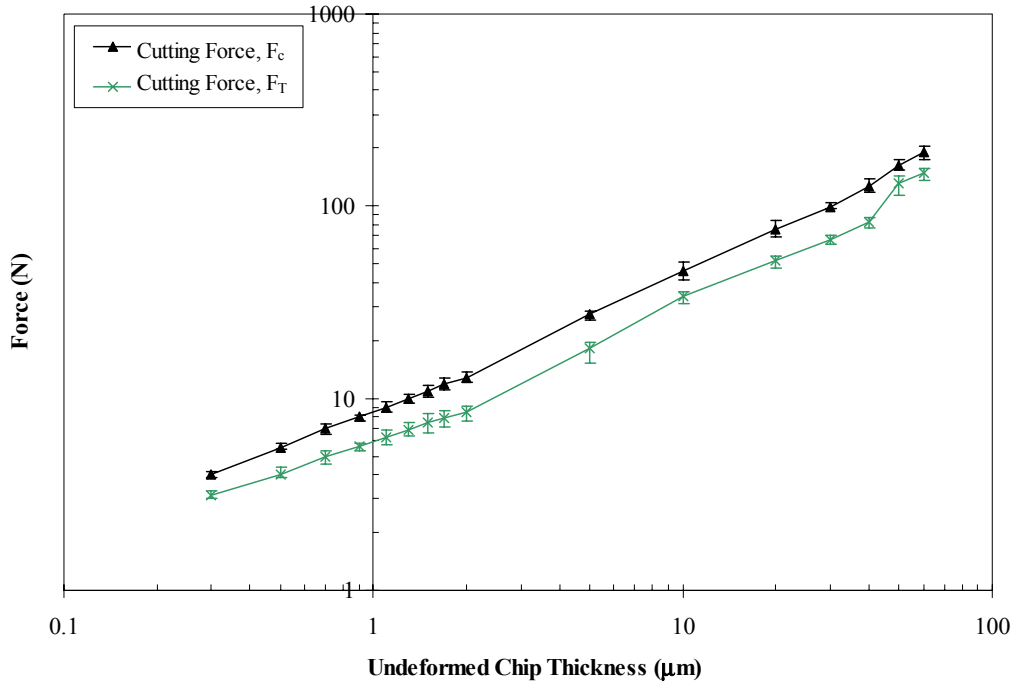

Figure 4.33: Effect of Undeformed Chip Thickness on Cutting and Thrust Forces at a Cutting Speed of 115 m/min (P20)

It is observed from Figure 4.32 that at a cutting speed of 10 m/min, the cutting and thrust forces do not exhibit a linear trend at undeformed chip thicknesses of less than 1 µm. Figure 4.33 shows that at the cutting speed of 115 m/min, both the cutting and thrust forces increase linearly with an increase in the undeformed chip thickness. The magnitude of the cutting force is also greater than the magnitude of the thrust force over the entire undeformed chip thickness range of the cutting experiment. The edge radius of the insert was estimated to be in the range of 5 – 15 µm. It was observed in the AL7075 experiments that when cutting was conducted at undeformed chip thicknesses at or below the edge radius of the tool, the thrust force was generally larger than the cutting force. The possible explanations for this trend have been previously discussed. Hence, it should be anticipated that the thrust force will be greater than the cutting force at undeformed

chip thicknesses smaller than the edge radius of the tool. However, the reversal in the cutting and thrust forces does not occur at both cutting speeds. Therefore, this observation does not compare well with existing trends in macro-scale force data.

In addition, Figure 4.32 shows that the cutting and thrust forces do not decrease linearly with a corresponding decrease in undeformed chip thickness at undeformed chip thicknesses smaller than 1 μm and at a cutting speed of 10 m/min. This observation is similar to that observed in the AL7075 experiments. The cutting and thrust forces also converge at approximately 5.8 N at an undeformed chip thickness of 0.3 μm. At undeformed chip thicknesses smaller than 0.3 μm at a cutting speed of 10 m/min, the process ceased to produce chips. The cutting insert merely rubbed against the workpiece, creating a high-pitched noise. This could be a probable explanation for the convergence of the cutting and thrust forces at 0.3 μm at the cutting speed of 10 m/min.

However, at a cutting speed of 115 m/min, the cutting and thrust forces do not converge at 0.3 μm. Furthermore, the cutting and thrust forces decrease linearly with a corresponding decrease in undeformed chip thickness at undeformed chip thicknesses smaller than 1 μm. Although the trend illustrated in Figure 4.33 seems to suggest that the cutting experiments can be further conducted at undeformed chip thicknesses smaller than 0.3 μm, this was proven to be untrue. When further experiments were conducted at undeformed chip thicknesses smaller than 0.3 μm, the cutting process ceased to produce chips.

The effect of cutting speed and undeformed chip thickness on the cutting and thrust forces is illustrated in Figure 4.34. It is observed that cutting speed does not have a significant effect on the cutting and thrust forces until an undeformed chip thickness of

around 5 μm. Although there is a 10-fold increase in cutting speed, there is only an average of 24% decrease in the cutting force. However, it is observed that there is a corresponding 20% increase in the thrust force.

The decrease in the cutting and thrust forces as a result of the increase in cutting speed is a typical occurrence. This observation can be attributed to material softening due to an increase in cutting temperature as a direct result of the increase in cutting speed. However, increase in the thrust force with an increase in cutting speed is atypical since all other experimental conditions were held constant. A possible reason for such an occurrence is that an increase in the cutting speed changes the tool-chip interaction, which consequently increases the thrust force. The images of the tool rake face provided limited evidence since there were no visible smear marks left on the rake face. A subsequent analysis of the friction coefficient supported this explanation. The analysis indicates that the friction coefficient increased with an increase in cutting speed. Thus, the increase in thrust force is explained by the increase in the friction coefficient. The increase in friction coefficient can be attributed to a change in the tool-chip interaction due to the increase in cutting speed and temperature. Since frictional forces affect the thrust force significantly, it is not surprising that an increase in the frictional force causes an increase in the thrust force. Analyses of the images of the tool rake face and the friction coefficient will be presented in section 4.3.4.2.

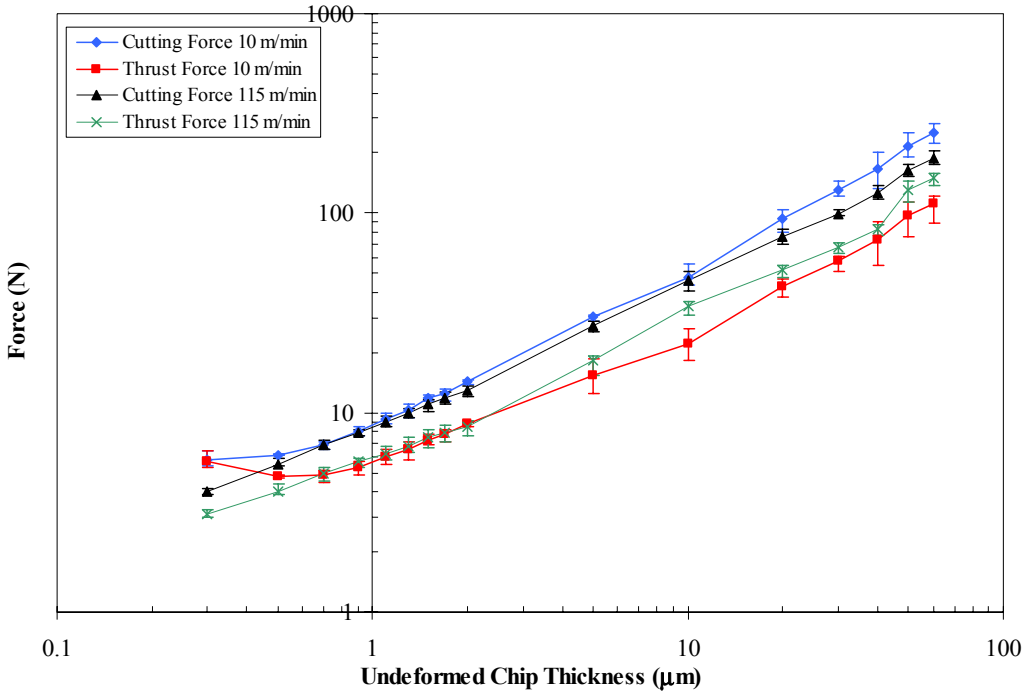

Figure 4.34: Effect of Undeformed Chip Thickness and Cutting Speed on Cutting and Thrust Forces (P20)

4.3.1.3 Variability of Cutting Force Data

Variability of the force data was evaluated by calculating the spread of the data from the mean. The maximum percentage deviation of the force data from the mean force value for each factor level was evaluated and presented in Tables B.35 and B.36 in Appendix B for cutting speeds of 10 m/min and 115 m/min, respectively. At a cutting speed of 10 m/min, the average percentage deviation of the cutting and thrust forces from the mean force value are 9% and 13%, respectively. At a cutting speed of 115 m/min, the average percentage deviation of the cutting and thrust forces from the mean force value is 7% and 9%, respectively.

The trend in the variability of the cutting and thrust forces is similar to that observed in AL7075 cutting experiments. Hence, possible sources of this variability can be explained in a similar fashion as noted for AL7075.

4.3.1.4 Size-Effect

The specific cutting and thrust energies were evaluated for all factor levels and the results are shown in Tables B.37 and B.38 in Appendix B. The data in Tables B.37 and B.38 were subsequently graphed as a function of undeformed chip thickness and cutting speed. The generated graphs are presented in Figures 4.35 and 4.36.

Figures 4.35 and 4.36 illustrate that the specific cutting energy remains at a constant value of around 5 GPa until an undeformed chip thickness value of 10 μm. At undeformed chip thicknesses of less than 10 μm, the specific cutting energy increases significantly. A similar trend is also observed in the specific thrust energy. The specific thrust energy surges when the undeformed chip thickness becomes smaller than 10 μm.

The value of 10 μm is within the estimated range of the edge radius of the carbide insert used in the cutting experiment. In addition, the trend observed in the specific cutting and thrust energies for P20 steel is identical to the observation made in AL7075 experiments. Since both the specific cutting and thrust energies increase drastically when cutting experiments were conducted below the cutting edge radius for both materials, it can be inferred from this study that the edge radius of the tool does have a significant influence on the size-effect phenomenon. However, it is imperative to again highlight that more scientific investigations are required to examine the specific contributions of the edge radius of the tool to the observed size-effect phenomenon.

It is also observed from Figures 4.35 and 4.36 that the cutting speed does not affect the specific cutting and thrust energies significantly.

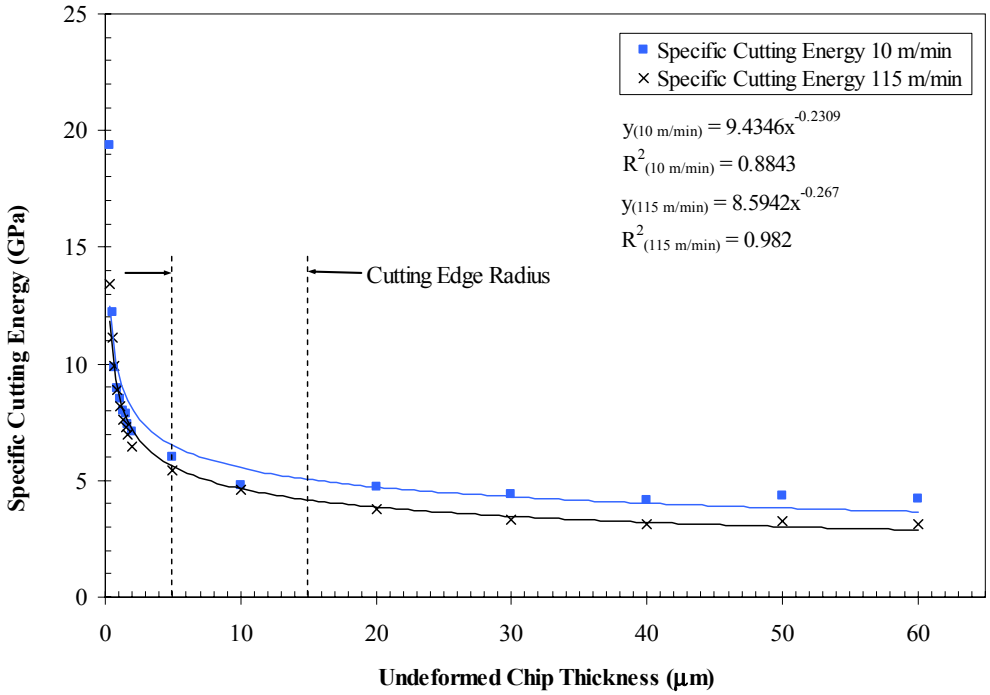

Figure 4.35: Effect of Undeformed Chip Thickness and Cutting Speed on Specific Cutting Energy (P20)

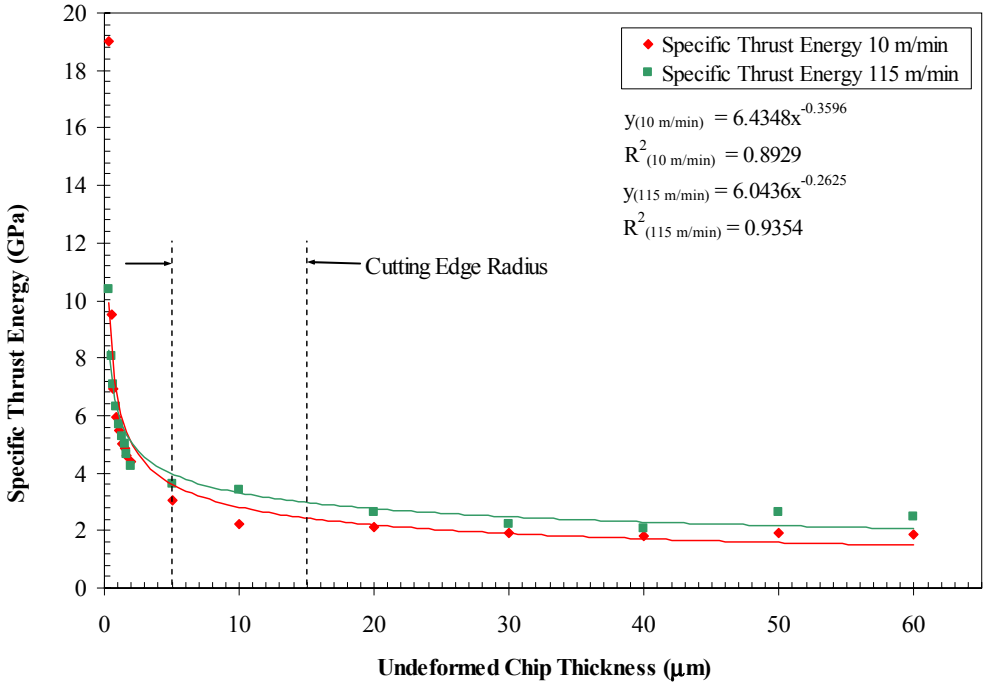

Figure 4.36: Effect of Undeformed Chip Thickness and Cutting Speed on Specific Thrust Energy (P20)

4.3.2 Chip Geometry

4.3.2.1 Chip Chart

P20 steel chips were collected and imaged in an SEM and a digital camera for each factor level in the cutting experiments. Figures 4.37 and 4.38 show the chip chart of chips collected at selected factor levels. The complete P20 chip charts for all factor levels are presented in Figures B.5 and B.6 in Appendix B.

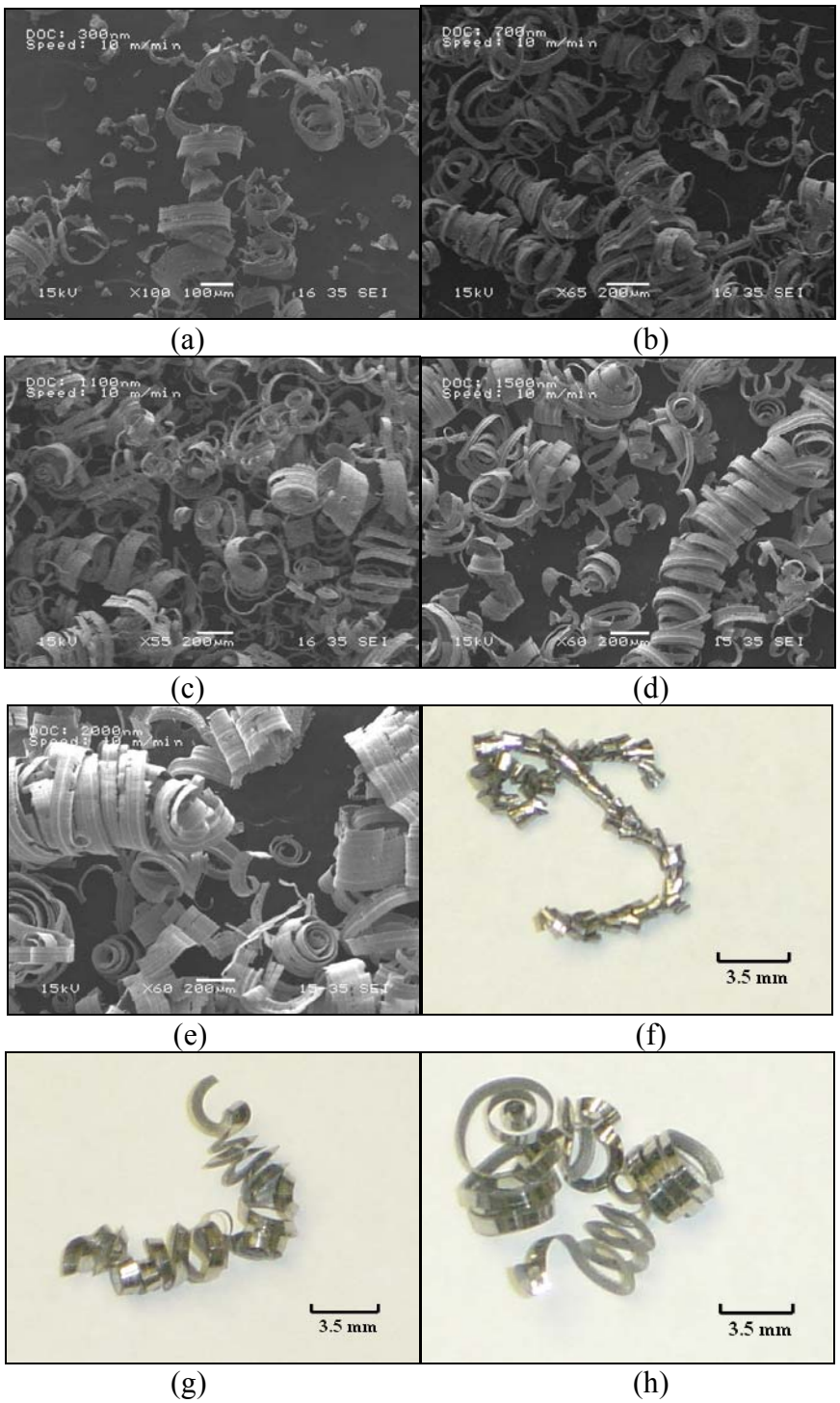

Figure 4.37: P20 Chip Chart at Selected Undeformed Chip Thickness for Cutting Speed of 10 m/min. (a) 0.3 µm (b) 0.7 µm (c) 1.1 µm (d) 1.5 µm (e) 2 µm (f) 10 µm (g) 30 µm (h) 50 µm

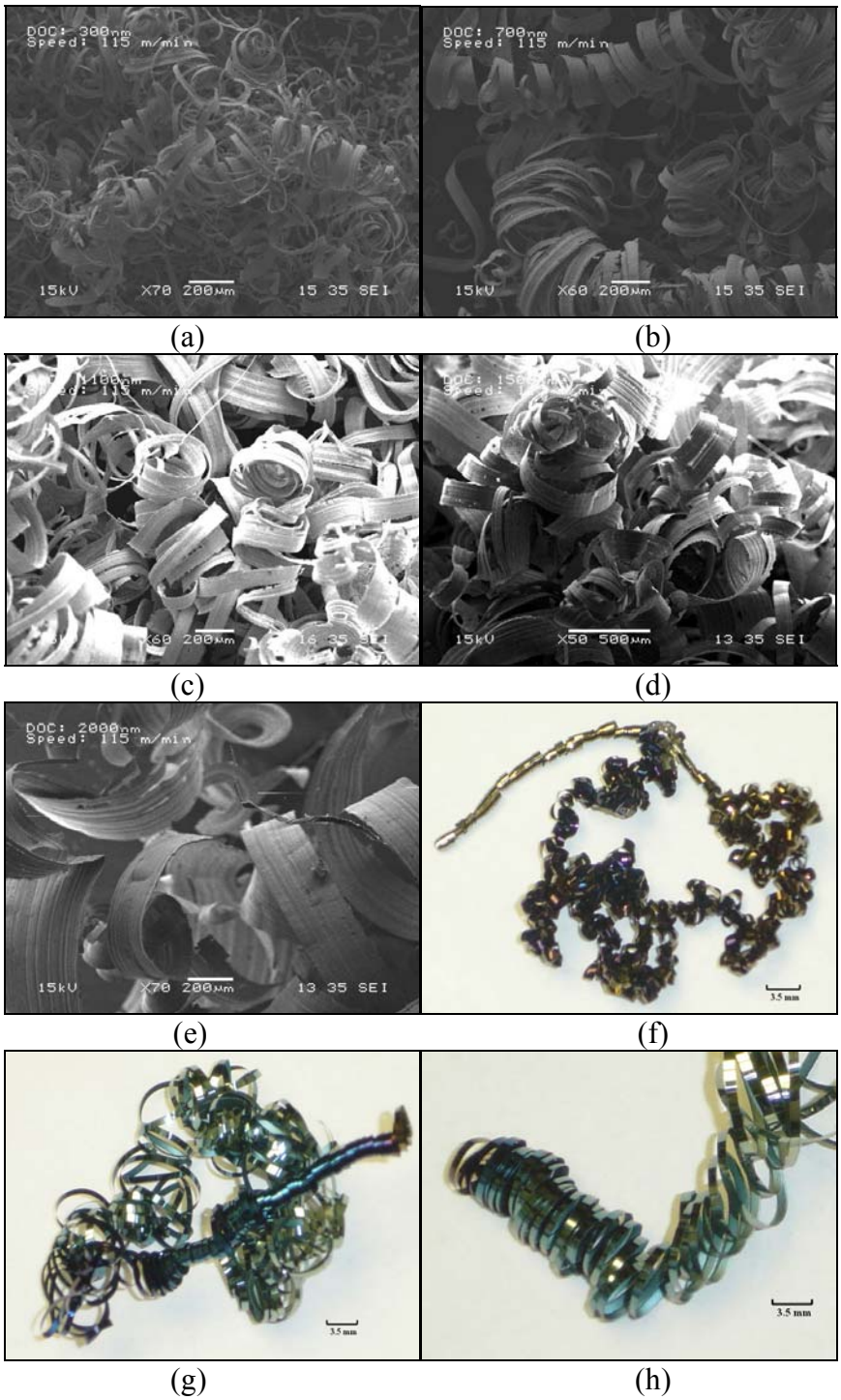

Figure 4.38: P20 Chip Chart at Selected Undeformed Chip Thickness for Cutting Speed of 115 m/min. (a) 0.3 µm (b) 0.7 µm (c) 1.1 µm (d) 1.5 µm (e) 2 µm (f) 10 µm (g) 30 µm (h) 50 µm

The chips collected at undeformed chip thicknesses ranging from 0.3 - 2 μm were fragmented and discontinuous at both cutting speeds. The chip charts also demonstrate that the width of the chips collected in this range varied despite the width of cut being held constant for the entire experiment.

The effective rake angle for cutting experiments in the undeformed chip thickness range of 0.3 - 2 μm can be used to offer possible insight into this observation. The effective rake angle of the cutting processes fluctuated between -79.7º and -59.1º when cutting experiments in the undeformed chip thickness range of 0.3 - 2 μm were conducted. The range of the effective rake angle is considered to be highly negative. As highlighted and discussed in previous sections, the ploughing process becomes the dominant mechanism in the cutting process at very large negative rake angles. Since the ploughing process is somewhat stochastic in nature, the chips produced are generally discontinuous. The fragmentation of the chips during the micro and nano scale cutting experiments was also reflected as oscillations in the time series profile presented in section 4.3.1.1.

The chips collected at the undeformed chip thickness range of 5 – 60 μm are continuous chips at both cutting speeds as shown in Figures 4.37 and 4.38. The chips collected at the higher cutting speed have a bluish tinge, indicative of high cutting temperatures. The curl of the chips collected at the cutting speed of 115 m/min is also larger than that at 10 m/min.

4.3.2.2 Chip Thickness

Since the micro and nano scale cutting experiments produced discontinuous and fragmented chips, no consistent and useful information could be obtained for the chip

thickness. Furthermore, one of the underlying assumptions of Merchant's theory is that continuous chips are produced during the cutting experiments. Hence only deformed chips produced in the undeformed chip thickness range of 5 – 10 μm are examined in this section. The deformed chip thickness was measured using an optical microscope after the cutting experiments. The chips were imaged using the optical microscope as previously described in the corresponding section for AL7075. An example of the image used for the measurement of the deformed chip thickness is presented in Figure 4.39.

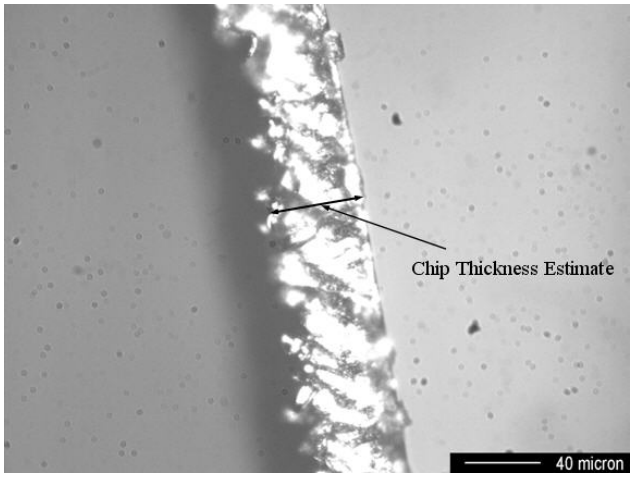

Figure 4.39: Illustration of Chip Thickness Measurement for P20 Steel Chip

Figure 4.39 illustrates the chip thickness measurement when the cutting experiment was conducted at an undeformed chip thickness of 50 μm and a cutting speed of 115 m/min. The estimates of the deformed chip thickness, the maximum and minimum deformed chip thickness and the standard deviations of the measurements at each factor level are presented in Tables B.39 and B.40 in Appendix B. The graph of the effect of the undeformed chip thickness and cutting speed on the deformed chip thickness is presented in Figure 4.40.

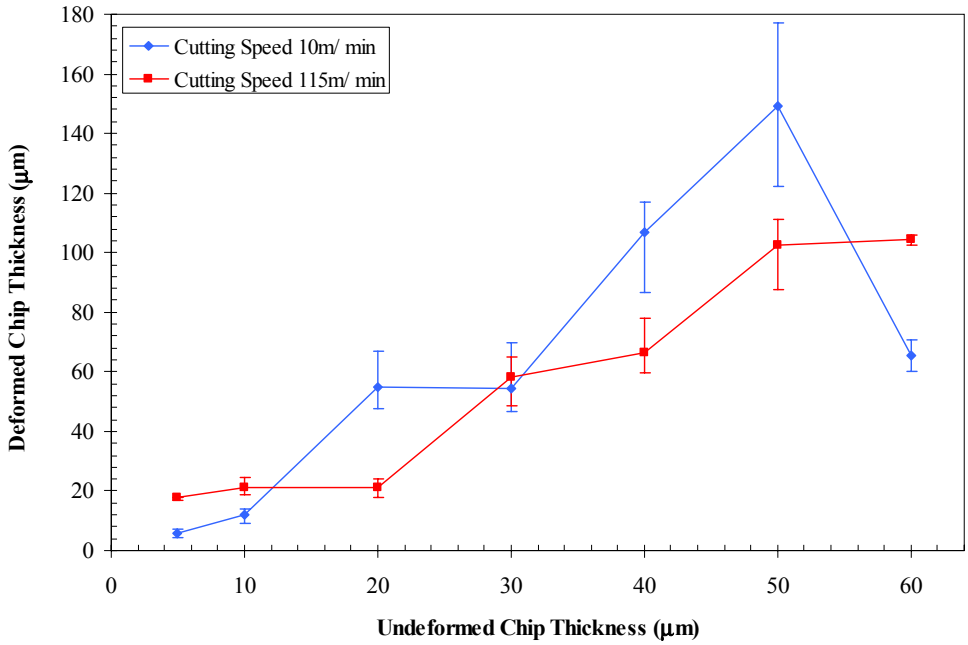

Figure 4.40: Effect of Undeformed Chip Thickness and Cutting Speed on Deformed Chip Thickness (P20)

Figure 4.40 shows that the deformed chip thickness increases as an increasing function of the undeformed chip thickness at the cutting speeds of 115 m/min. This is consistent with the trend observed in the AL7075 experiments and existing macro-scale machining data. However, at the cutting speed of 10 m/min, the deformed chip thickness increases with increasing undeformed chip thickness and then decreases after an undeformed chip thickness of 50 µm. The decrease in the undeformed chip thickness after 50 µm is surprising since both existing machining data and trends observed in this study indicate otherwise. It is also observed that at undeformed chip thicknesses of 40 µm and 50 µm, there are unusually high variations in measurement of the deformed chip thickness. This might indicate impending variations in the influence of some cutting conditions to the chip deformation process. This change to the chip deformation process might have been initiated at the undeformed chip thickness of 60 µm, which explains the

drastic drop in the deformed chip thickness. This could be a possible explanation for this anomaly.

The increase in cutting speed also decreases the deformed chip thickness. This trend is in complete contrast to that observed in the AL7075 experiments. This is because the increase in cutting speed corresponds to an increase in the friction coefficient, contrary to the observations in the AL7075 experiments. If a similar explanation proposed in the corresponding section in AL7075 was to be used, the deformed chip thickness should decrease with the cutting speed. However, the relationship between friction coefficient and deformed chip thickness in this study, to be presented in section 4.3.4.2, is not simple and direct. Various other cutting process parameters also exert significant influence on the chip deformation process. Furthermore, trends observed in cutting experiments are also workpiece material dependent. This increases the complexity in providing possible explanation for the trends observed. Therefore, to fully explain the relationships in the observed trend, further studies have to be conducted.

4.3.2.3 Shear Angle

The cutting ratio, rake angle and shear angle were evaluated using the same technique as described in the corresponding section for AL7075. These evaluated parameters are presented in Tables 4.4 and 4.5. The effect of undeformed chip thickness and cutting speed on the cutting ratio and shear angle are illustrated graphically in Figure 4.41 and 4.42.

Table 4.4: Cutting Ratio and Shear Angle – Cutting Speed of 10 m/min (P20)

Undeformed Chip Thickness (μm)	Average Deformed Chip Thickness (μm)	Effective rake angle, α (˚)	Cutting ratio, r	Shear Angle, φ (˚)
5	5.7	-37.3	0.873	24.4
10	11.9	-15.7	0.843	33.4
20	54.9	5.0	0.613	32.8
30	54.4	5.0	0.551	30.0
40	106.8	5.0	0.374	21.1
50	149.2	5.0	0.335	19.0
60	65.5	5.0	0.916	44.8

Table 4.5: Cutting Ratio and Shear Angle – Cutting Speed of 115 m/min (P20)

Undeformed Chip Thickness (μm)	Average Deformed Chip Thickness (μm)	Effective rake angle, α (˚)	Cutting ratio, r	Shear Angle, φ (˚)
5	17.6	-39.9	0.467	10.4
10	21.4	-18.7	0.945	21.0
20	21.2	5.0	0.515	45.7
30	58.2	5.0	0.601	28.3
40	66.6	5.0	0.487	32.3
50	102.7	5.0	0.575	26.9
60	104.4	5.0	0.467	31.1

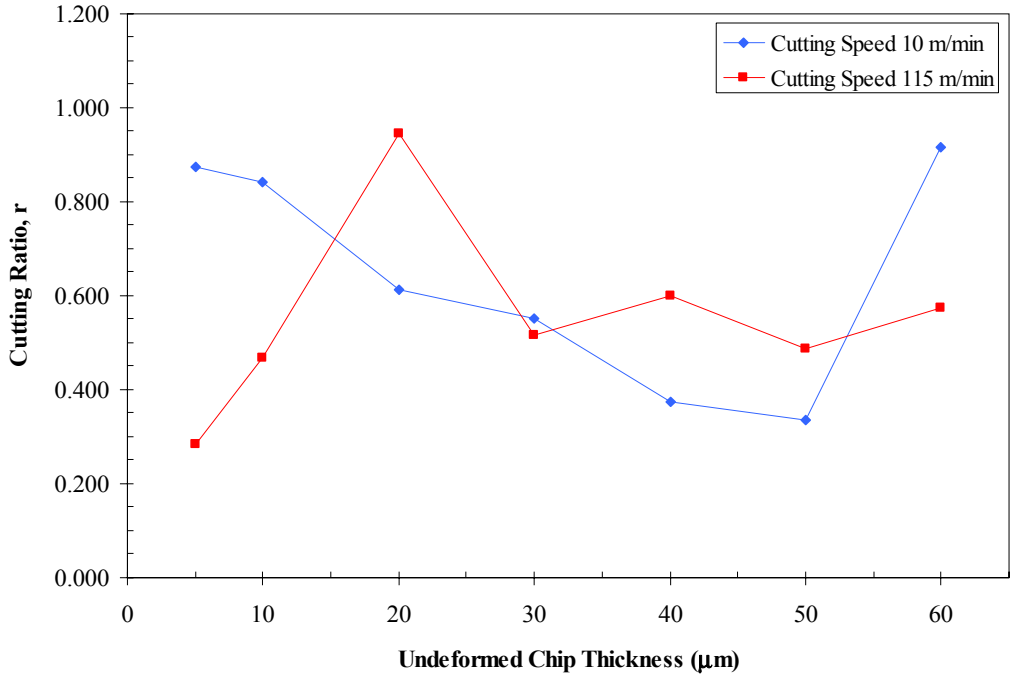

Figure 4.41: Effect of Undeformed Chip Thickness and Cutting Speed on Cutting Ratio (P20)

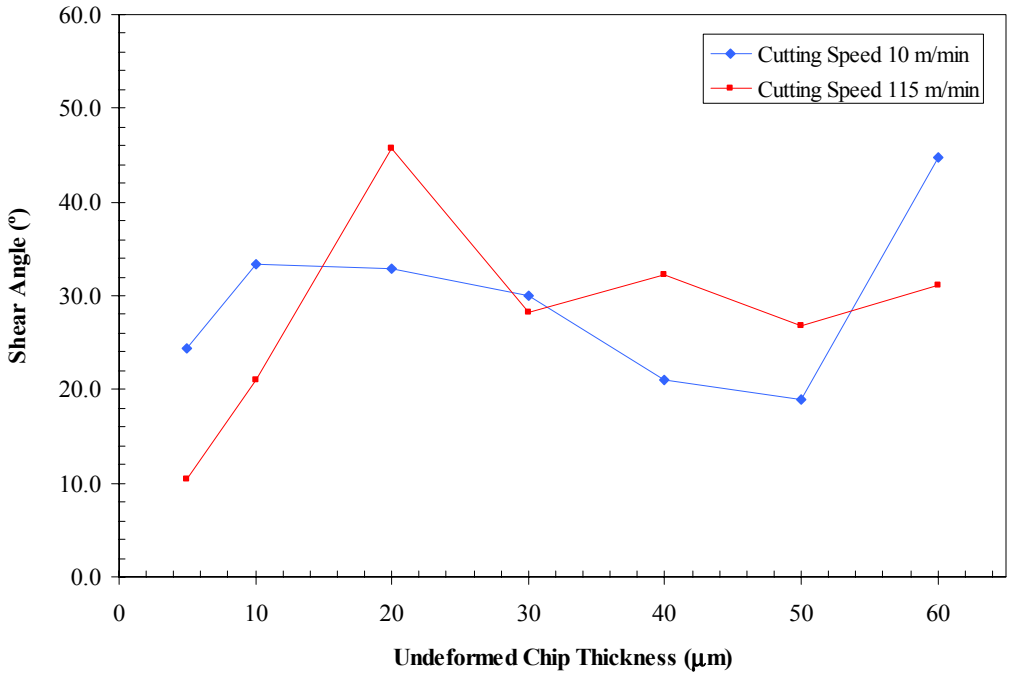

Figure 4.42: Effect of Undeformed Chip Thickness and Cutting Speed on Shear Angle (P20)

At a cutting speed of 10 m/min the cutting ratio generally decreases with increasing undeformed chip thickness except at the undeformed chip thickness of 60 μm. At the undeformed chip thickness of 60 μm, the cutting ratio increases. At the cutting speed of 115 m/min, the cutting ratio increases initially, subsequently decreases and then fluctuates about a value of 0.5. The trends in the observed cutting ratio are similar to that observed in the AL7075 experiments with the exception of the anomaly at the undeformed chip thickness of 60 μm. The shear angle displayed a similar trend as the cutting ratio. It is comparable to the trends observed in the AL7075 experiments and existing machining data (Zorev, 1966; Shaw 1984; Manjunathaiah and Endres, 2000).

Although comparable trends in both cutting ratio and shear angle were observed in both cutting experiments, similar elucidations cannot be used to explain the observations. This is because further analysis revealed that the cutting speed has an opposite effect on the tool-chip interface friction coefficient for AL7075 and P20 steel. Hence, no logical explanations for the observed trends in the cutting ratio and shear angle in P20 experiment can be suggested. This is due to the lack of visual evidence on the tool rake face, estimates of tool-chip interface temperature and data on the behavior of P20 with temperature fluctuations. Further experimental studies to determine these parameters might provide more insight and offer possible explanations for the observed trends.

4.3.3 Surface Morphology

Surfaces generated at selected cutting conditions were imaged in an SEM and the Zygo white light interferometer for each factor level during the cutting experiments. A

representative three dimensional topographical map of the surface is presented in Figure 4.43.

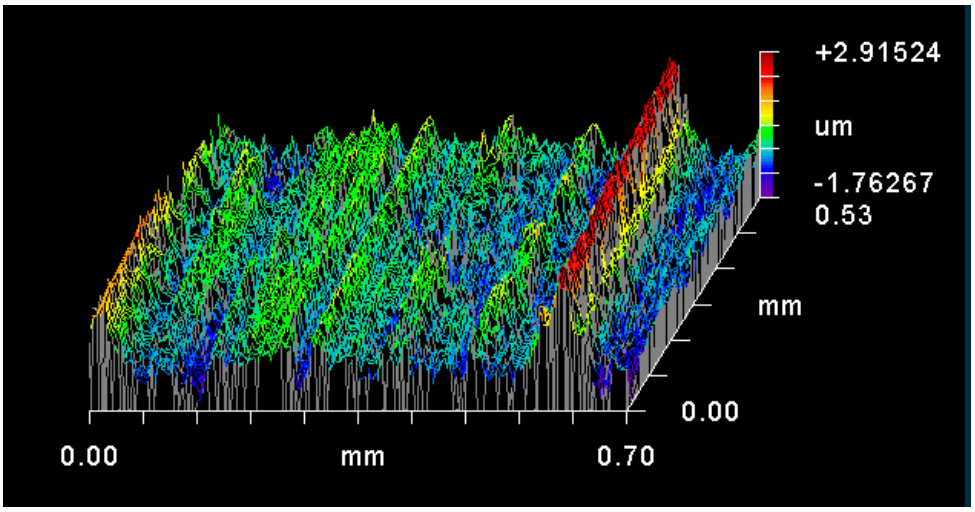

Figure 4.43: 3-D Topography Map of Surface Generated at 115 m/min at an Undeformed Chip Thickness of 10 μm (P20)

A visual inspection of the surfaces generated at the pre-determined cutting conditions revealed a similar trend to that in the AL7075 cutting experiments. Smoother surfaces were produced when the workpiece was machined at lower undeformed chip thicknesses and at higher cutting speeds. The surfaces generated displayed evidence of built-up edge formation during the cutting process. Figures 4.44 and 4.45 show the surfaces generated at the selected cutting conditions.

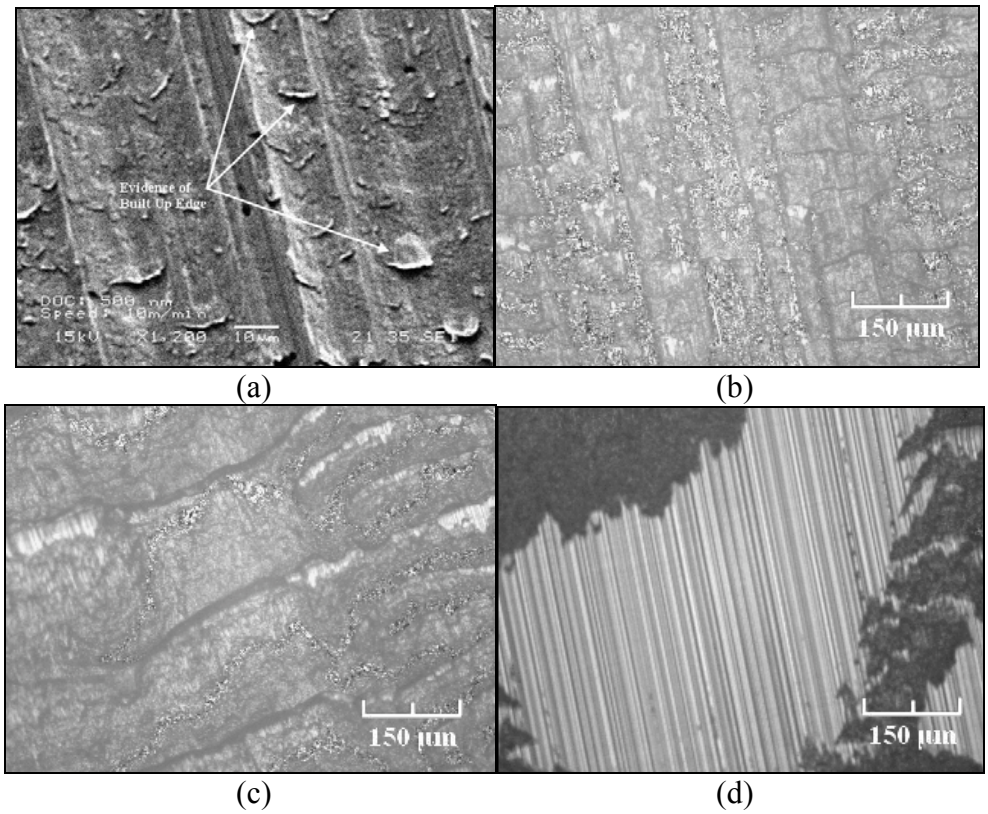

(a) (b)

(c) (d)

Figure 4.44: Effect of Undeformed Chip Thickness on Surface Morphology at a Cutting Speed of 10 m/min. Undeformed Chip Thickness: (a) 0.5 µm (b) 10 µm (c) 40 µm (d) 60 µm (P20)

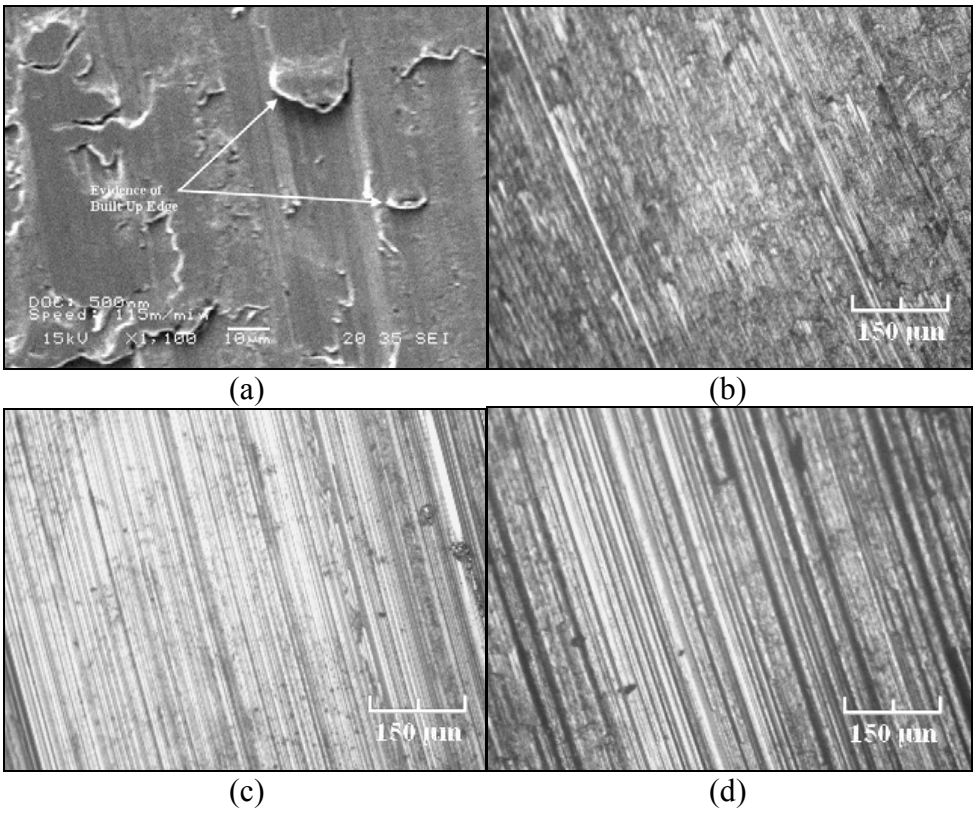

(a) (b)

(c) (d)

Figure 4.45: Effect of Undeformed Chip Thickness on Surface Morphology at a Cutting Speed of 115 m/min. Undeformed Chip Thickness: (a) 0.5 µm (b) 10 µm (c) 40 µm (d) 60 µm (P20)

The surfaces generated, as shown in Figures 4.44 and 4.45, were similarly characterized using the Zygo white light interferometer. The surface generated at an undeformed chip thickness of 60 µm at a cutting speed of 10 m/min is very rough. Consequently, the reflectivity of the surface generated is low and it cannot be characterized. The results of the surface characterization are shown in Tables B.41 and B.42 in Appendix B. Graphical representations of the characterized surfaces are presented in Figures 4.46 and 4.47.

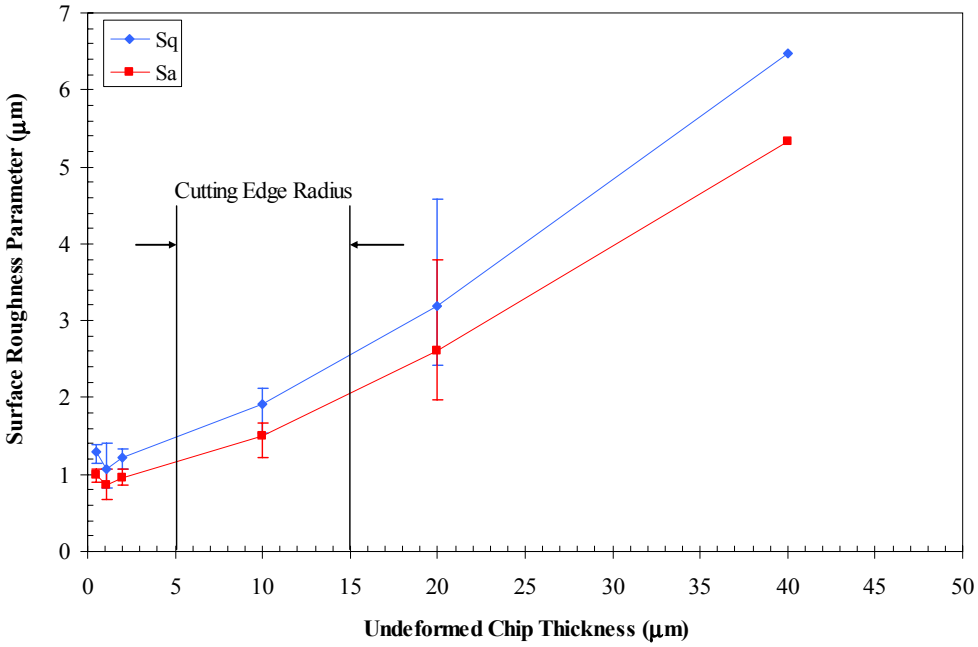

Figure 4.46: Effect of Undeformed Chip Thickness on Surface Roughness at a Cutting Speed of 10 m/min (P20)

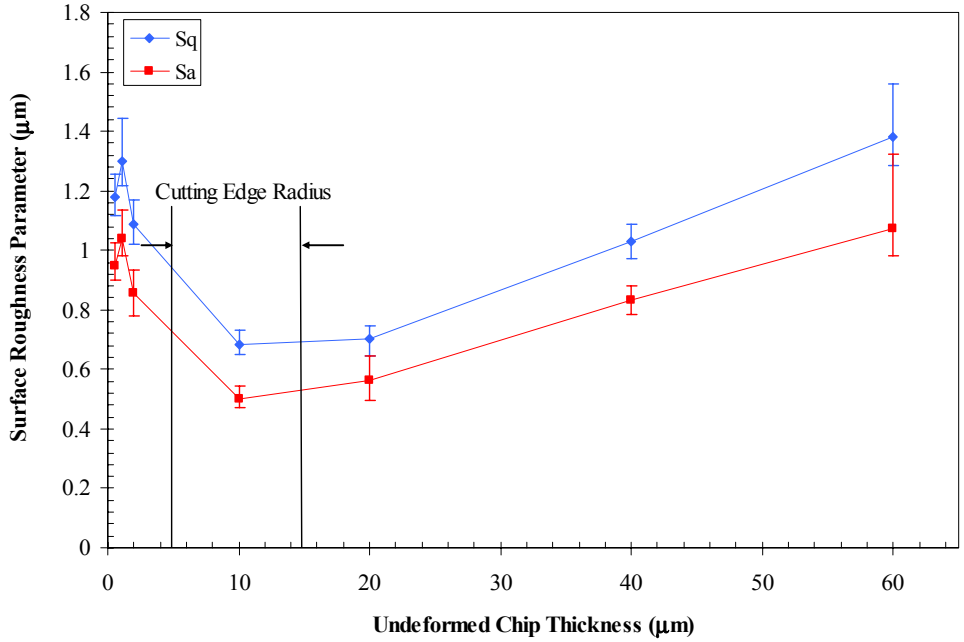

Figure 4.47: Effect of Undeformed Chip Thickness on Surface Roughness at a Cutting Speed of 115 m/min (P20)

The trends observed in Figures 4.46 and 4.47 are similar to the trends observed in the AL7075 cutting experiments. Hence, similar explanations can be used to justify the trends observed.

4.3.4 Experimental Observations

4.3.4.1 Cutting Edge Radius of Cutting Tool

The cutting edge radius of the carbide inserts were monitored and imaged on the SEM before and after each cutting experiment. Figure 4.48 shows the images of the cutting edge radius of the carbide insert after cutting experiments were conducted at undeformed chip thicknesses of 0.3 µm and 1.5 µm, respectively.

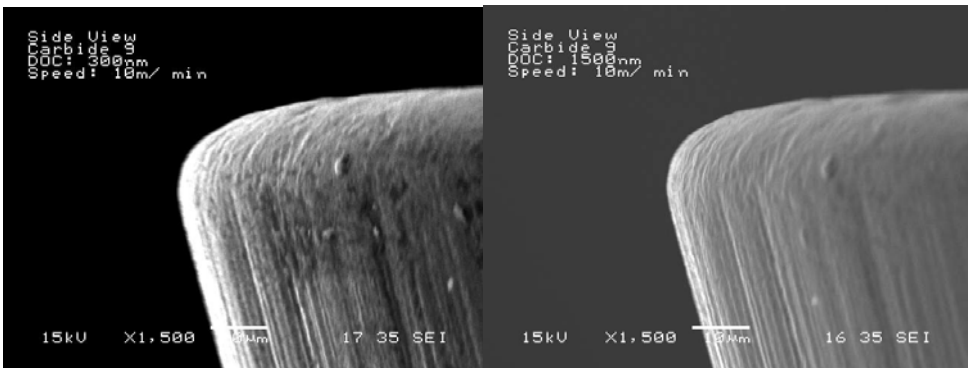

(a) (b)

Figure 4.48: Effect of Undeformed Chip Thickness on Edge Radius – Cutting Speed of 10 m/min. Undeformed Chip Thickness: (a) 0.3 µm (b) 1.5 µm

It can be observed from Figure 4.48 that there is no significant change in the cutting edge radius. Subsequent measurements of the cutting edge radius, presented in Tables A.5 and A.6, also indicate minimal variations of about 10 – 20% in the edge radius of the carbide insert when an insert is used for a single replication of cutting experiment. Hence, the influence of tool wear on the data acquired is not a major concern

in this study. Furthermore, new "up-sharp" inserts were used for each replication of the cutting experiment to eliminate this potential source of error.

4.3.4.2 Rake Face of Cutting Tool

The rake faces of the carbide inserts were also monitored during the cutting experiments. An image of the insert's rake face taken after the experiment at an undeformed chip thickness of 0.9 μm and a cutting speed of 10 m/min is illustrated in Figure 4.49.

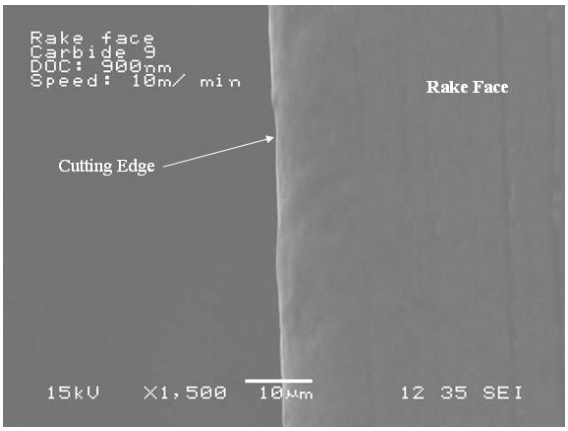

Figure 4.49: SEM Image of the Rake Face of Carbide Insert

Figure 4.49 shows a typical image of the insert's rake face for the entire range of P20 experiments. It reveals no evidence of smearing of the workpiece material on the rake face of the insert. Consequently, it is impossible to estimate the tool-chip contact length. The friction coefficients were subsequently evaluated for each factor level and are presented in Tables B.43 and B.44 in Appendix B. A graphical representation of the effect of cutting speed and undeformed chip thickness on the friction coefficient is shown in Figure 4.50.

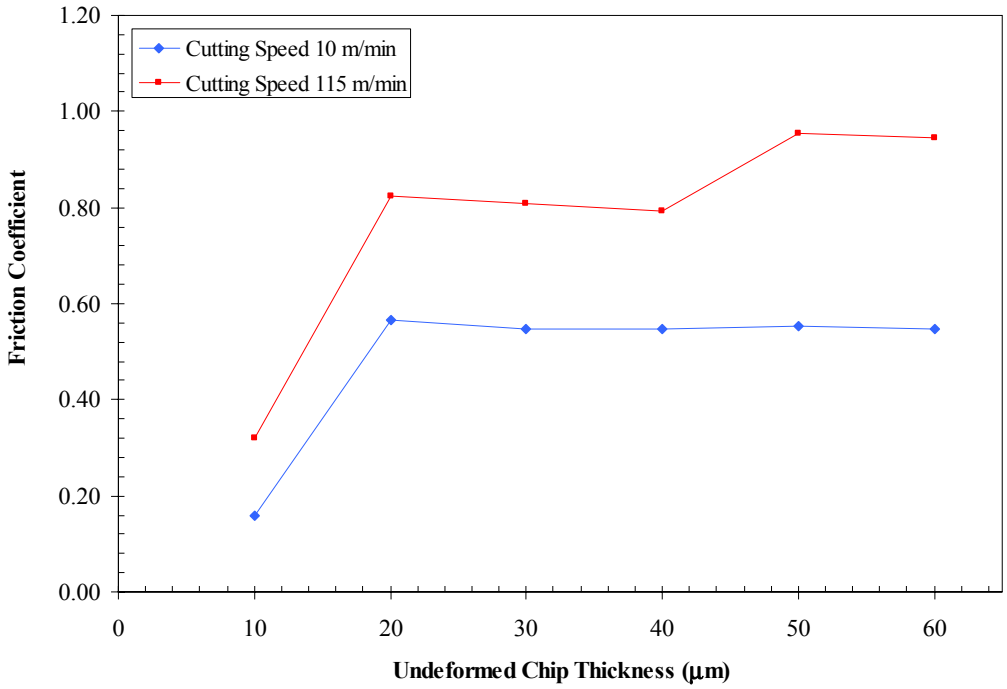

Figure 4.50: Effect of Undeformed Chip Thickness and Cutting Speed on Friction Coefficient (P20)

It is seen that the friction coefficient increases initially and then remains fairly constant for both cutting speeds. The friction coefficient also increases with an increase in the cutting speed. This observation does not compare well with the AL7075 micro and nano scale cutting experiments. However, it should be noted that friction is influenced by many factors such as the chemistry of the materials in contact, the cutting speed and the tool-chip interaction at pre-determined cutting conditions. Hence, direct comparisons cannot be made between the friction coefficient for the P20 experiments and the AL7075 experiments since different workpiece material and tools are used. Furthermore, the lack of information regarding the tool-chip contact length also contributes to the complexity in offering possible explanations for this phenomenon.

A possible explanation for the observation of the fairly constant friction coefficient at both cutting speeds is as follows. It is likely that the real area of contact between the chip and tool rake face remained constant as the undeformed chip thickness was increased. Since there is no change in the real area of contact between the chip and the tool rake face, the friction coefficient remained fairly constant.

The increase in friction coefficient with an increase in the cutting speed can also be explained in a similar fashion. It is observed from Figure 4.34 that the thrust force increased with an increase in the cutting speed. This might suggest that the increase in the cutting speed is likely to have led to an increase in the real area of contact between the tool and the chip. The increase in tool-chip interface contact area is likely to have increased the frictional force at the tool-chip interface. Hence, the effect of an increase in the cutting speed is an increase in the friction coefficient.

4.3.5 Derived Parameters using Merchant's Theory

4.2.5.1 Shear Stress

The average shear stress values estimated from the cutting experiments at both cutting speeds for P20 steel using Equation 4.5 are presented in Table 4.6. The nominal shear stress values obtained from the Engineering Properties of Steel Handbook are presented in Figure 4.51.

Table 4.6: Estimated Shear Stress Values From Cutting Experiments

	10 m/min	115 m/min
Average Shear Stress (MPa)	1384.4	820.7

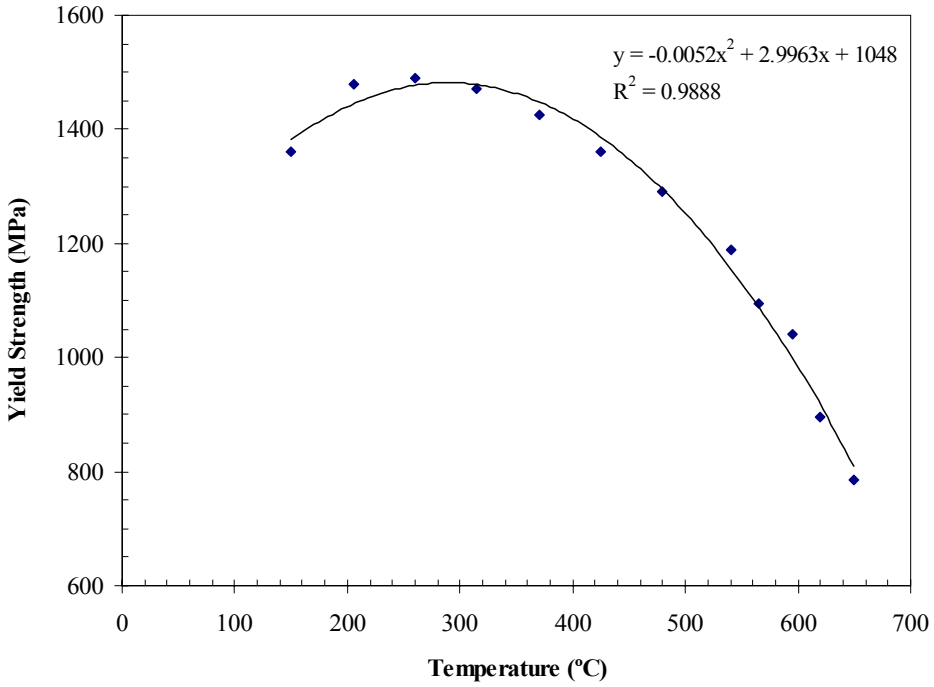

Figure 4.51: Effects of Temperature on Yield Strength of P20 (After the Engineering Properties of Steel Handbook)

The shear yield strength of P20 varies significantly with temperature as shown in Figure 4.51. There is a large disparity observed between the average shear stress values evaluated from the cutting experiment at the cutting speed of 10 m/min and 150 m/min. The disparity in the evaluated shear stress values between the two cutting speeds can be explained as follows. It is evident from the color of the chips in the P20 chip charts shown in Figures 4.37 and 4.38 that at a cutting speed of 115 m/min, the cutting temperatures are significantly higher than that at the cutting speed of 10 m/min. Hence, the differences in the evaluated shear stress values are consistent with the chips shown in the P20 chip chart since the yield strength of P20 is lower at a higher temperature as shown in Figure 4.51.

4.2.5.2 Energy Per Unit Volume

Energy consumption parameters for P20 steel were also evaluated and are presented in Figures 4.52 and 4.53. It is observed that a large portion of the total energy per unit volume is consumed as shear energy on the shear plane at a cutting speed of 10 m/min over all undeformed chip thicknesses except at an undeformed chip thickness of 60 µm. This observation is similar to the trends observed in the AL7075 experiments. However, at a cutting speed of 115 m/min, shown in Figure 4.53, equal amounts of energy is consumed by the shearing process on the shear plane and by friction on the tool face as undeformed chip thickness is increased. Frictional forces are known to significantly affect the thrust forces. Hence, this observation is consistent with the trend in the thrust force data, which was shown to increase when the cutting speed was increased from 10 m/min to 115 m/min.

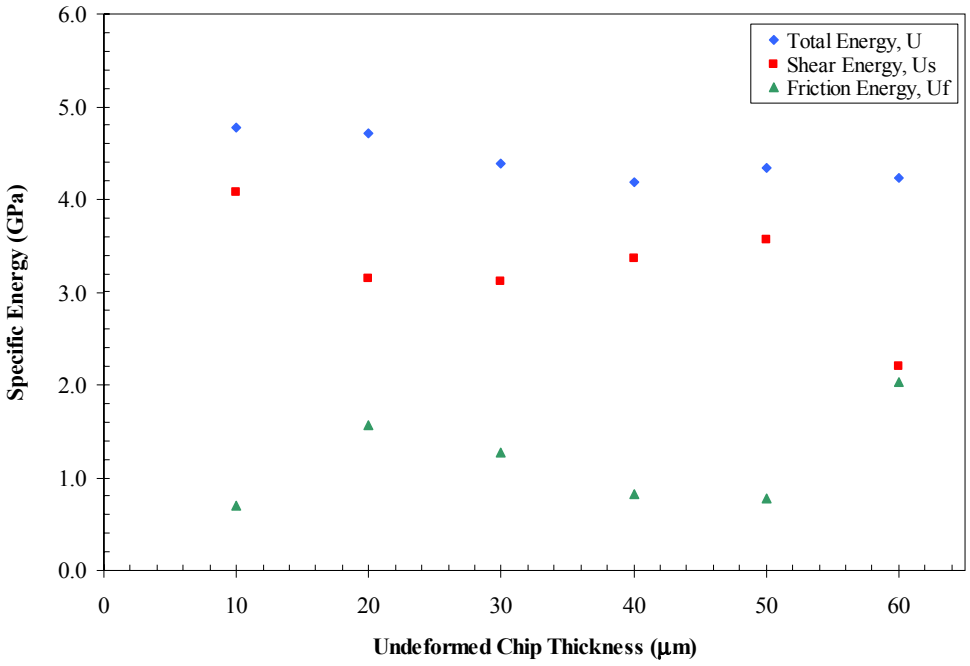

Figure 4.52: Effect of Undeformed Chip Thickness on the Total, Shear and Friction Energies Per Unit Volume – Cutting Speed of 10 m/min (P20)

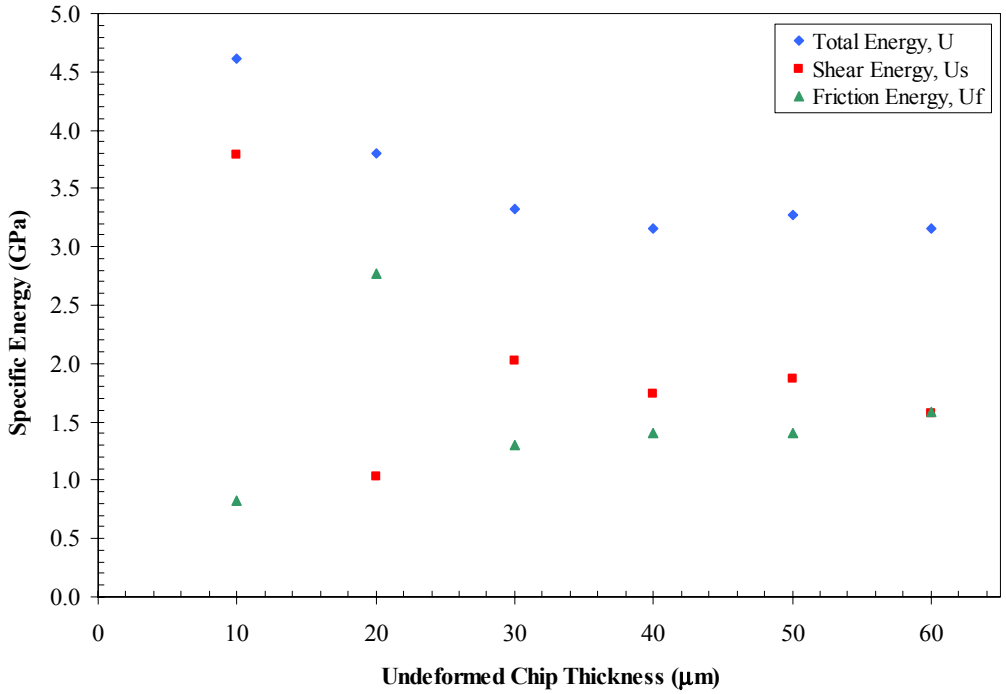

Figure 4.53: Effect of Undeformed Chip Thickness on the Total, Shear and Friction Energies Per Unit Volume – Cutting Speed of 115 m/min (P20)

4.4 Summary

This chapter presented the experimental results acquired in this study. The experimental results presented include the cutting force, chip geometry, surface morphology, experimental observations and parameters derived using Merchant's Theory. In addition, possible explanations for some of the phenomena observed were also proposed and discussed.

The significant findings in this chapter can be summarized as follows:

Cutting Force

- The cutting force exhibits a linear relationship with the undeformed chip thickness when micro and nano scale machining is conducted above the edge radius of the tool.
- When the undeformed chip thickness is smaller than the edge radius of the tool, a non-linear variation in the cutting forces is observed.
- The specific cutting and thrust energies increase significantly in a non-linear fashion when micro and nano scale machining is performed at undeformed chip thicknesses smaller than the edge radius of the tool.
- The cutting speed has negligible effect on the cutting force at undeformed chip thicknesses less than 1 μm for both materials studied.

Chip Geometry

- Continuous chips are observed over the entire range of undeformed chip thicknesses (10 – 2000 nm) investigated for AL7075.
- Continuous chips were only observed in the P20 cutting experiments at undeformed chip thicknesses greater than 2 μm.
- The cutting ratio and shear angle increase initially and then decrease as the undeformed chip thickness is increased for both AL7075 (10 – 2000 nm) and P20 (5 – 60 μm).

Surface Morphology

- The surfaces generated in micro and nano scale machining exhibit similar surface roughness characteristics as those observed in macro-scale machining.
- Machining at higher cutting speeds (150 m/min for A7075 and 115 m/min for P20 steel) and lower undeformed chip thicknesses (40 nm for AL7075 and 10 μm for P20 steel) produces a smoother surface.
- Machining when performed at undeformed chip thicknesses smaller than the edge radius of the tool generally creates rougher surfaces.

Experimental Observations

- Tool wear resulting in changes in the edge radius of the tool is not a vital issue in this study of micro and nano scale cutting.
- Significant amount of smearing of AL7075 on the diamond cutting tool is observed.
- Frictional size effect is also observed in the AL7075 cutting experiment.

CHAPTER 5

APPLICABILITY OF EXISTING PROCESS MODELS

Numerous cutting process models have been developed to analyze the complex behavior of cutting processes, as well as to predict cutting parameters. In this chapter, two machining process models will be used to predict the cutting process parameters micro and nano scale cutting. One of the process models is a conventional macro-scale process model developed by Oxley (Oxley's Model) (1989). The second process model was proposed by Manjunathaiah and Endres (Endres' Model) (2000), which predicts the cutting forces while taking into account the tool's edge radius. The outline and justification of the choice of both Oxley's model (1989) and Endres' model (2000) will be presented. The experimental data presented in the preceding chapters will be used to verify the accuracy of the prediction. The applicability of both process models in predicting micro and nano scale cutting process parameters will then be discussed.

5.1 Conventional Macro-Scale Process Model (Oxley's Model)

5.1.1 Oxley's Model

Oxley's model (1989) is an analytical technique used for predicting machining process parameters such as cutting forces, shear angle and cutting temperatures using a material constitutive law. The model only requires the input of cutting conditions and the work material's mechanical properties to predict the cutting process response. In addition, Oxley's model is commonly applied to predict process responses in conventional macro-scale cutting and to obtain flow stress data for a material at high

strain rates and temperatures (Arsecularatne and Oxley, 1997; Lei et al, 1998; Shatla et al, 2001a, 2001b; Ramesh, 2002; Adibi-Saleh et al, 2003; Arsecularatne et al., 2004). Hence, Oxley's model is selected because of its predictive nature and its relative simplicity in application. A brief outline of Oxley's model is presented.

The flow stress equation used in Oxley's model is the Johnson and Cook (1983) equation, illustrated in Equation 5.1.

$$\sigma = \left(A + B\varepsilon^{n}\right)\left[1 + C\ln\left(\frac{\dot{\varepsilon}}{\dot{\varepsilon}_{o}}\right)\right]\left[D - E\left(\frac{T - T_{\infty}}{T_{m} - T_{\infty}}\right)^{m}\right] \tag{5.1}$$

where σ is the flow stress, ε is the strain, $\dot{\varepsilon}$ is the strain rate, $\dot{\varepsilon}_{o}$ is a reference strain rate, T is the instantaneous temperature, T_m is the melting temperature of the material, T_∞ is the ambient temperature and A, B, C, n and m are the material constants.

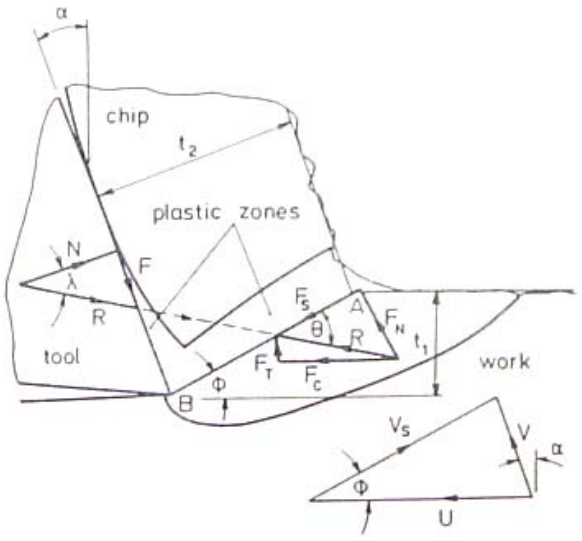

Figure 5.1: Model of Chip Formation (Oxley, 1989)

Figure 5.1 illustrates the chip formation model used in Oxley's development. Oxley's model analyzes the stress distribution along the shear plane AB and the tool-chip

interface BF in terms of parameters such as the shear angle φ and work material properties. A force balance between the resultant forces transmitted by the shear plane and the tool-chip interface yields a numerical solution for the shear angle φ. After the value of the shear angle φ is determined, other process parameters such as the deformed chip thickness and cutting forces can subsequently be derived from geometrical relationships and the material constitutive law (Johnson and Cook, 1983).

Machining process variables required as inputs to the model include α, the effective rake angle, *V,* the cutting velocity, *t*, the undeformed chip thickness, *w*, the width of cut, T_w, the initial temperature of the work material and the material constants A, B, C, D, E, n and m.

Simplifying assumptions were made in the formulation of the theory. Plane strain, steady state conditions are assumed to apply in the analysis. The cutting tool is also assumed to be perfectly sharp.

A flowchart detailing the algorithm of Oxley's model is presented in Figure 5.2.

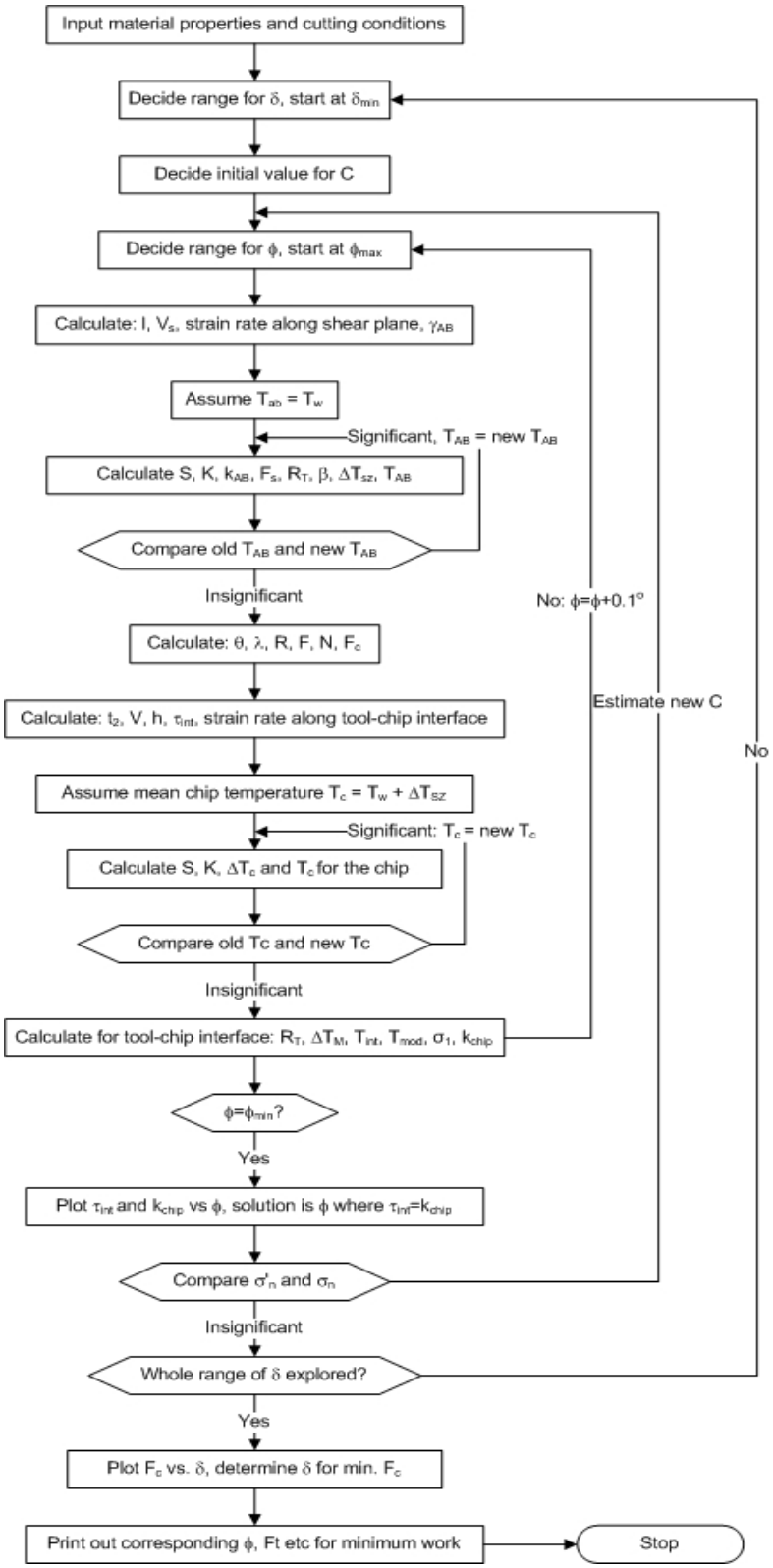

Figure 5.2: Flowchart Detailing Algorithm used for Predicting Machining Forces Based on Oxley's Model (Oxley, 1989)

5.1.2 AL7075

The material constants utilized as inputs to the Johnson and Cook equation for AL7075 were acquired from the experimental investigation by Lee et al. (2000). The material constants are summarized in Table 5.1.

Table 5.1: Material Constants for AL7075 (Lee et al., 2000; $\dot{\varepsilon}$ = 2400 s^{-1}; $0 \leq \varepsilon \leq 0.4$; 25 ºC ≤ T ≤ 300ºC)

Material Constant	Coefficient
A	330
B	245
C	0.09
D	1
E	1.18
m	0.85
n	0.2

Additional material properties required as inputs to the model are listed in Table A.2 in Appendix A. The initial workpiece temperature is taken to be ambient room temperature of 25ºC. The effective rake angle, listed in Tables 4.1 and 4.2, is used instead of the nominal rake angle to account for the edge radius of the cutting tool. Oxley's model was used to predict the cutting force, thrust force and shear angle for AL7075 at cutting conditions identical to that used in the cutting experiments described in section 3.5.

5.1.2.1 Cutting Forces

The predicted cutting and thrust force values are presented in Tables C.3 and C.4 of Appendix C for cutting speeds of 10 m/min and 150 m/min, respectively. The

measured forces from the cutting experiments are provided in Tables C.1 and C.2 of Appendix C. The data presented in Tables C.1 – C.4 are also graphed as a function of undeformed chip thickness and presented in Figures 5.3 – 5.6.

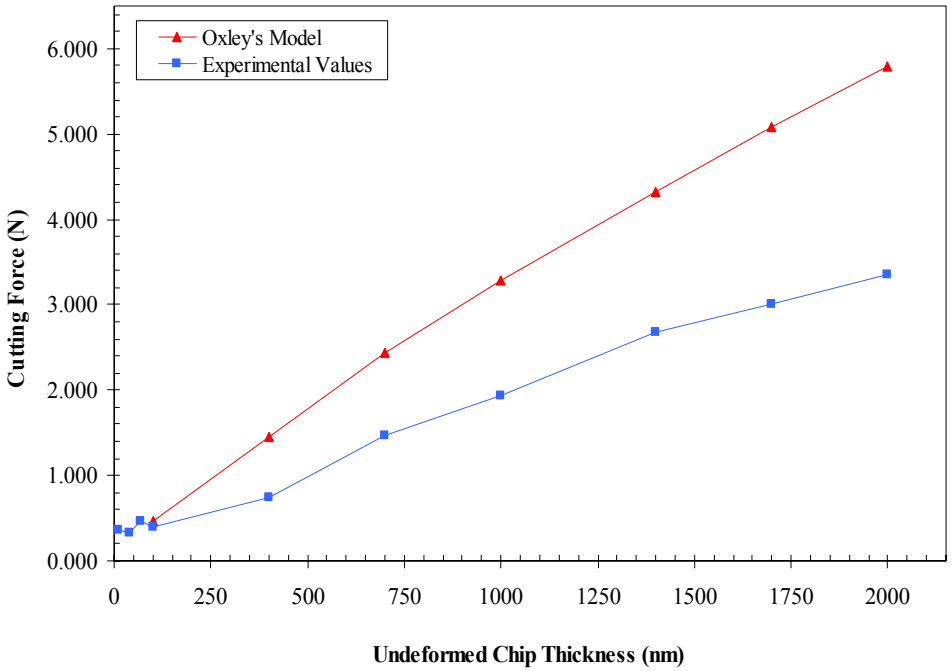

Figure 5.3: Effect of Undeformed Chip Thickness on Cutting Force – Cutting Speed 10 m/min (AL7075)

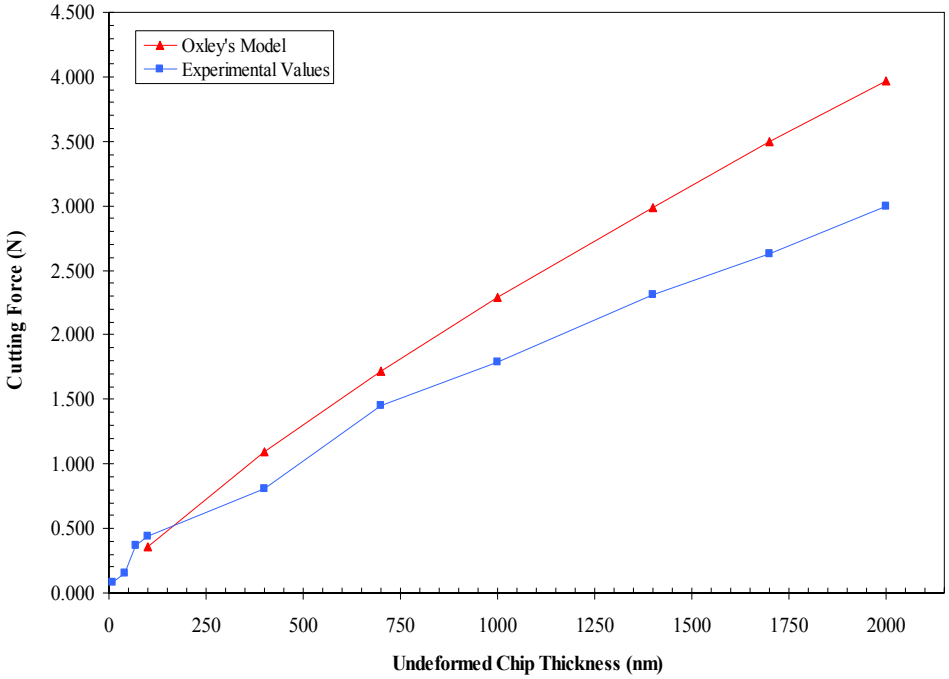

Figure 5.4: Effect of Undeformed Chip Thickness on Cutting Force – Cutting Speed 150 m/min (AL7075)

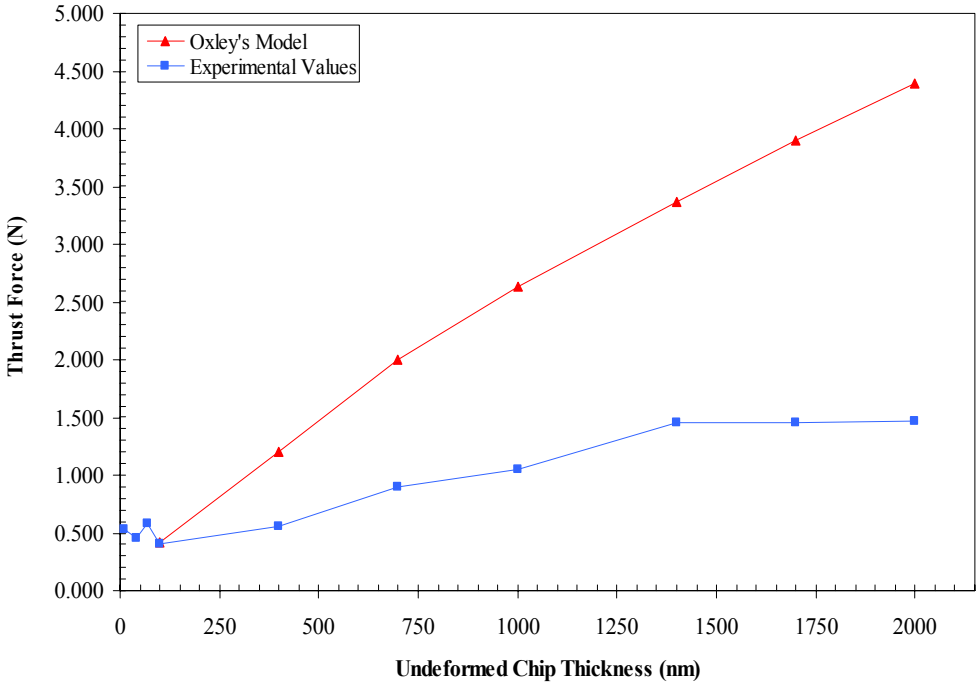

Figure 5.5: Effect of Undeformed Chip Thickness on Thrust Force – Cutting Speed 10 m/min (AL7075)

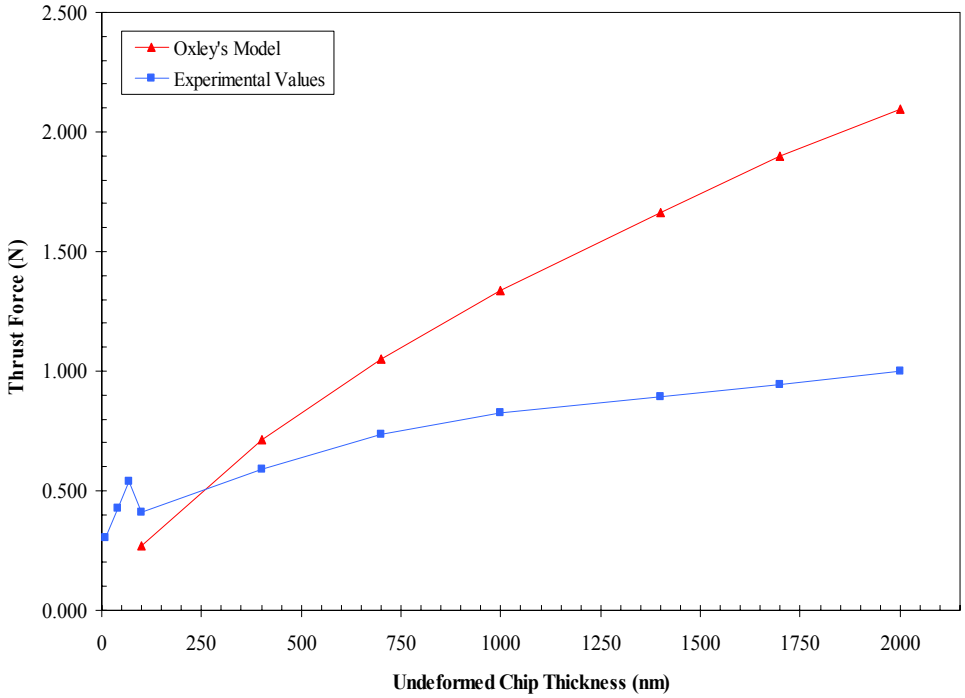

Figure 5.6: Effect of Undeformed Chip Thickness on Thrust Force – Cutting Speed 150 m/min (AL7075)

Figures 5.3 – 5.6 show that predicted values of cutting and thrust forces do not match well with the experimental data. There are in fact significant differences between the predicted and acquired experimental values. The difference between the predicted and experimental values is less at the higher cutting speed of 150 m/min for both cutting and thrust forces. It is also observed that Oxley's model consistently over-predicts both the cutting and thrust forces.

Although significant difference exists between the predicted and experimental values, Figure 5.3 and 5.4 seem to suggest that Oxley's model can be used to project the trend of the cutting force. However, there seems to be an increasing difference between the predicted and experimental values as the undeformed chip thickness is increased.

Oxley's model is unable to predict the trend of the thrust force as shown in Figures 5.5 and 5.6.

Oxley's model is also observed to break down at an undeformed chip thickness of 100 nm. The strain rate coefficients presented in Tables C.3 and C.4 of Appendix C indicate that the strain rate coefficient changes from 8 to 8.5 when the undeformed chip thickness is reduced from 400 nm to 100 nm at a cutting speed of 10 m/min. Similarly, the strain rate coefficient also increases from 7.5 to 8 when the undeformed chip thickness is reduced from 400 nm to 100 nm at the cutting speed of 150 m/min. Since a model should use consistent material constitutive relation when predicting values (Schimmel et al., 2002), the model is considered to have failed when any of the constant coefficient changes value. Although it is expected that the strain rate might change with the undeformed chip thickness, the change in the strain rate may be reflected by a corresponding change in the shear velocity and the length of the shear plane and not in the material constant (strain rate coefficient). Hence, it can be inferred from the change in the strain rate coefficient that Oxley's model has failed when used in predicting forces at an undeformed chip thickness of 100 nm.

Furthermore, 100 nm is also within the estimated range of the edge radius of the SCD tool. This suggests that Oxley's model can be used to predict cutting forces only for undeformed chip thicknesses larger than the edge radius of the tool. However, it is not surprising for Oxley's model to fail under this condition since one of the underlying assumptions of the model is that the tool is sharp.

The use of incompatible material constants for the Johnson and Cook equation could be a possible reason for the mismatch between the predicted and experimental

values. The material constants, as presented in Table 5.1, are acquired from Lee et al.'s (2000) experimental investigation. Although similar materials are used, experimental conditions might differ in both studies. Therefore, it is likely for the material to exhibit dissimilar stress strain behavior, strain rate effect and even respond differently to similar temperature effects. This might be a possible source of the disparity between the predicted and experimental values. Furthermore, the predicted values are closer to the experimental values at the higher cutting speed. This might indicate that the material constants used are perhaps a better match for the material behavior at the higher cutting speed of 150 m/min.

5.1.2.2 Shear Angle

The values of the predicted shear angle are presented Tables C.3 and C.4 of Appendix C for cutting speeds of 10 m/min and 150 m/min, respectively. The values of the shear angle estimated from the cutting experiment are provided in Tables C.1 and C.2 in Appendix C. The shear angle data presented in Tables C.1 – C.4 are also graphed as a function of the undeformed chip thickness and are shown in Figures 5.7 – 5.8.

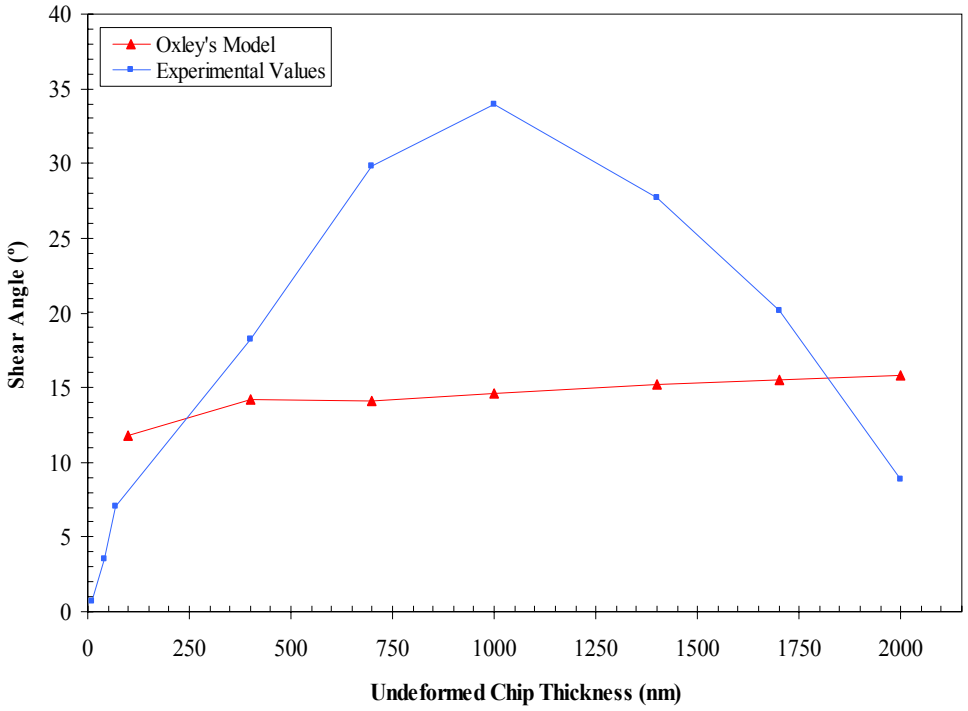

Figure 5.7: Effect of Undeformed Chip Thickness on Shear Angle – Cutting Speed 10 m/min (AL7075)

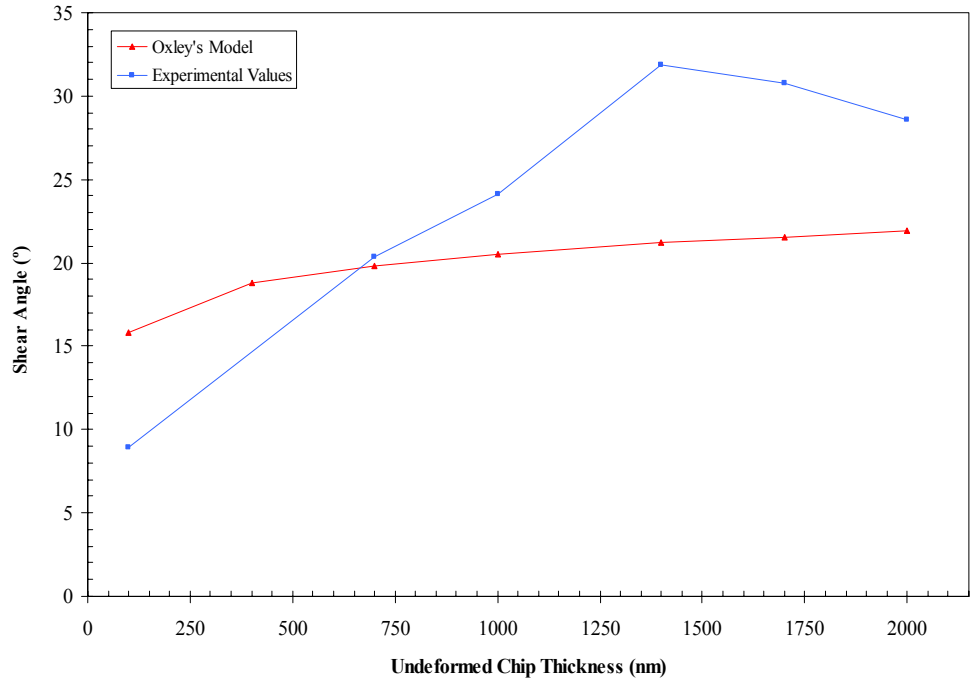

Figure 5.8: Effect of Undeformed Chip Thickness on Shear Angle – Cutting Speed 150 m/min (AL7075)

Figures 5.7 and 5.8 show that the predicted values of the shear angle do not match well with the experimental data. There are again significant differences between the predicted and acquired experimental values. The predicted trend in the shear angle at both cutting speeds of 10 m/min and 150 m/min do not match the trend observed in the cutting experiments. A similar elucidation used to explain the disparities in the predicted and experimental values of the cutting and thrust forces can be used to explain the mismatch between the predicted and experimental values of the shear angle.

5.1.3 P20 Steel

The material constants utilized as inputs to the Johnson and Cook equation for P20 steel are acquired from the work by Shatla et al. (2001). The material constants are summarized in Table 5.2.

Table 5.2: Material Constants for P20 Steel (Shatla et al., 2001; $2 \times 10^4 \leq \dot{\varepsilon} \leq 8 \times 10^5$ s^{-1}; $0.9 \leq \varepsilon \leq 1.5$; 600 ºC $\leq T \leq$ 1200ºC)

Material Constant	Coefficient
A	145
B	565.5
C	0.03
D	1.26
E	1.07
m	1.8
n	0.154

Similarly, additional material properties required as inputs to the model are listed in Table A.4 of Appendix A. The initial workpiece temperature is also taken to be 25ºC. The effective rake angle, presented in Tables 4.4 and 4.5, is used instead of the nominal

rake angle to account for the edge radius of the cutting tool. Oxley's model was similarly used to generate the cutting force, thrust force and shear angle predictions for P20 steel cutting conditions identical to that used in the cutting experiments described in section 3.5.

5.1.3.1 Cutting Forces

The values of the predicted cutting and thrust forces are presented Tables C.7 and C.8 of Appendix C for cutting speeds of 10 m/min and 115 m/min, respectively. The measured forces are given in Tables C.5 and C.6 in Appendix C. The data presented in Tables C.5 – C.8 are also graphed as a function of the undeformed chip thickness and shown in Figures 5.9 – 5.12.

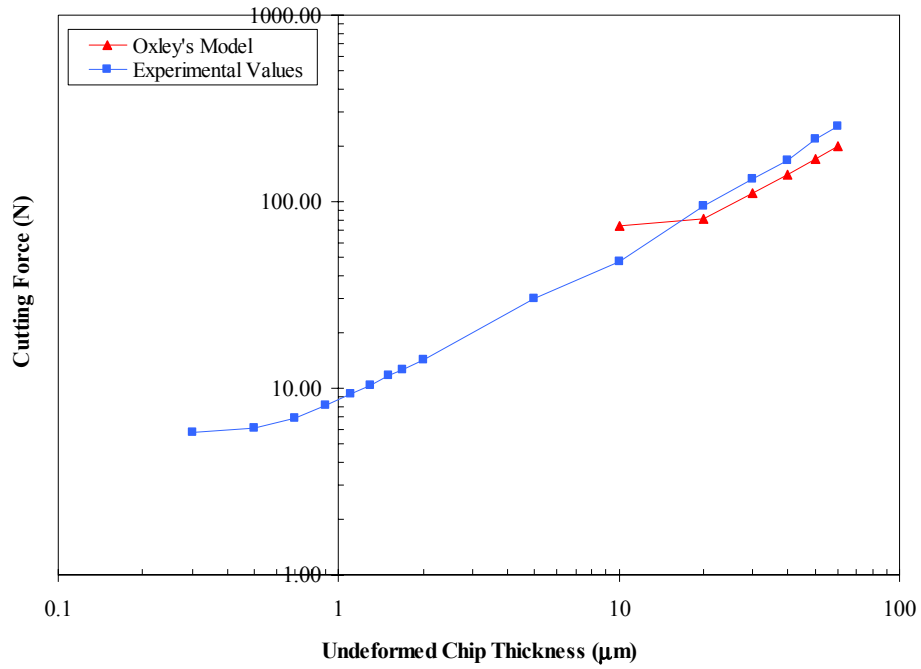

Figure 5.9: Effect of Undeformed Chip Thickness on Cutting Force – Cutting Speed 10 m/min (P20)

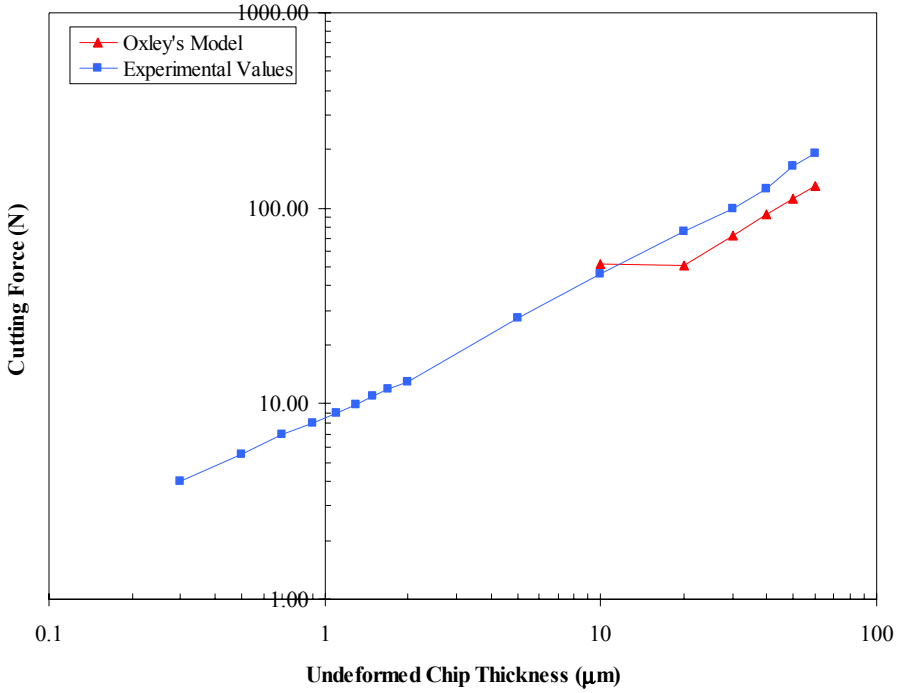

Figure 5.10: Effect of Undeformed Chip Thickness on Cutting Force – Cutting Speed 115 m/min (P20)

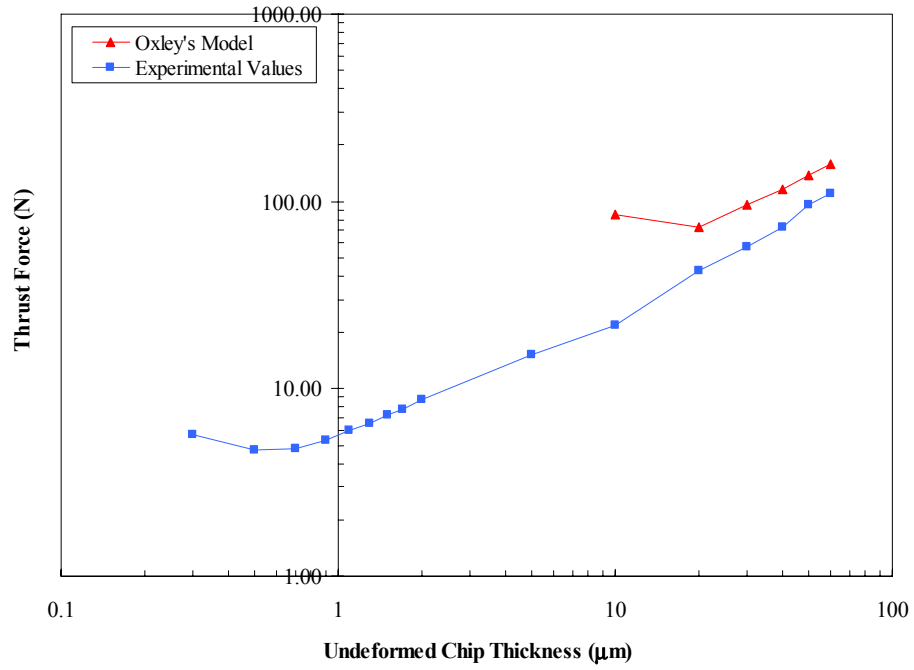

Figure 5.11: Effect of Undeformed Chip Thickness on Thrust Force – Cutting Speed 10 m/min (P20)

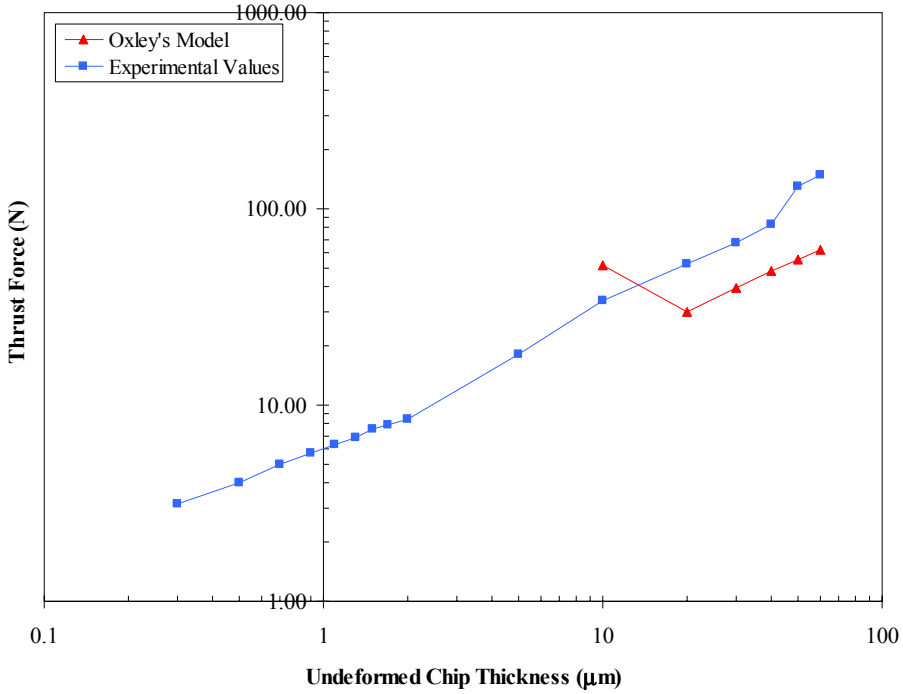

Figure 5.12: Effect of Undeformed Chip Thickness on Thrust Force – Cutting Speed 115 m/min (P20)

Figures 5.9 – 5.12 show that the trends of the predicted values of cutting and thrust forces compare well with the experimental data. Although there are differences in the magnitude of the predicted forces, it is observed that Oxley's model is able to predict the trend of the forces accurately for undeformed chip thicknesses greater than 10 µm. This is reflected by the approximately constant difference between the predicted and experimental values. It is also observed that Oxley's model consistently under-predicts both the cutting and thrust forces with the exception of the thrust force at a cutting speed of 10 m/min.

However, Oxley's model fails when used to predict cutting forces at the undeformed chip thickness of 10 µm. This is reflected by the sudden deviation of the predicted value at the undeformed chip thickness of 10 µm, as shown in Figures 5.9 –

5.12. Additionally, the breakdown of the model is also reflected in the change in the strain rate coefficient (presented in Tables C.7 and C.8) at both cutting speeds. The value of 10 μm is also within the estimated range of the edge radius of the carbide insert used in the cutting experiments. Oxley's model seems to fail at around the edge radius of the tool again. The breakdown of the model occurs identically at the cutting tool's edge radius despite significant differences in the edge radius of the cutting tool used in the AL7075 and P20 experiments. The use of incompatible coefficients for the Johnson and Cook equation can again be used to explain the differences between the predicted and experimental values.

5.1.3.2 Shear Angle

The predicted shear angle values are presented in Tables C.7 and C.8 of Appendix C for cutting speeds of 10 m/min and 115 m/min, respectively. The values of the shear angle estimated from the cutting experiment are provided in Tables C.5 and C.6 of Appendix C. The shear angle data presented in Tables C.5 – C.8 are also graphed as a function of the undeformed chip thickness and shown in Figures 5.13 – 5.14.

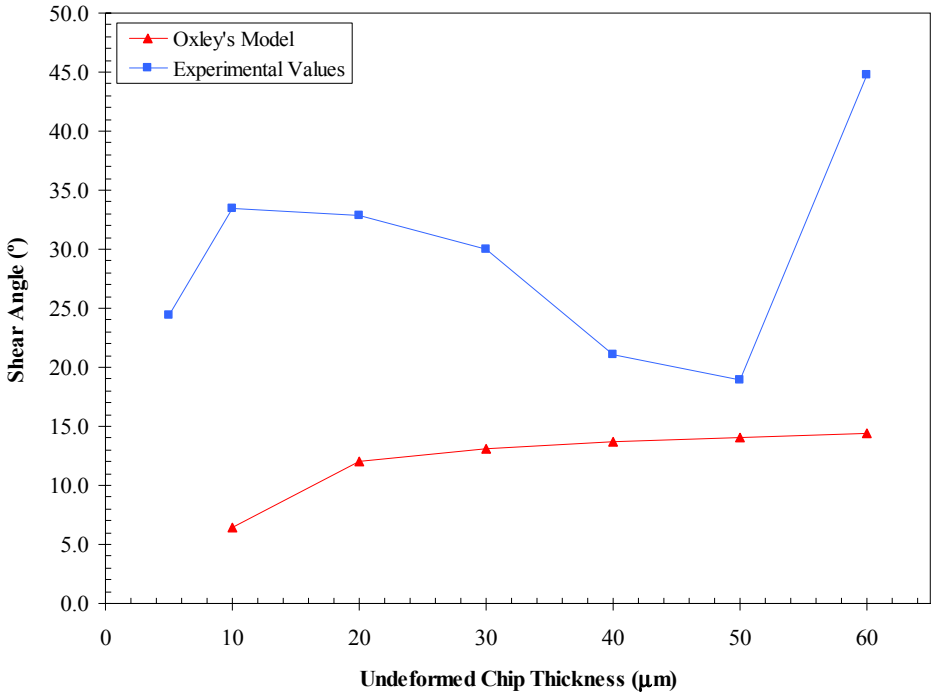

Figure 5.13: Effect of Undeformed Chip Thickness on Shear Angle – Cutting Speed 10 m/min (P20)

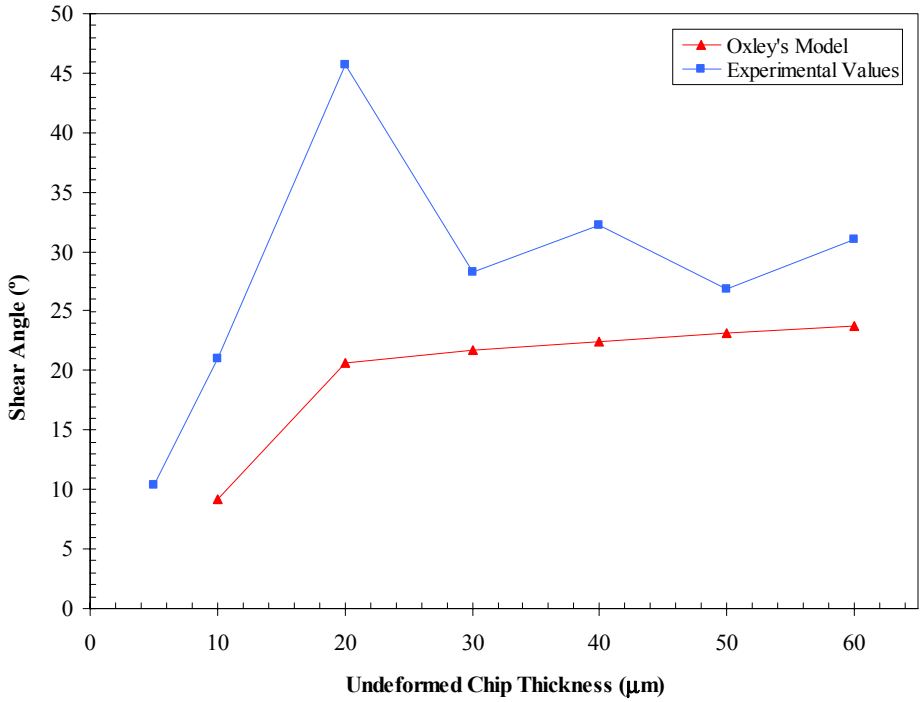

Figure 5.14: Effect of Undeformed Chip Thickness on Shear Angle – Cutting Speed 115 m/min (P20)

Figure 5.13 shows that the prediction of the shear angle again does not match well with the experimentally acquired data at the cutting speed of 10 m/min. Although there are significant differences between the predicted and measured values, the error appears to reduce at undeformed chip thicknesses higher than 40 μm. Specifically, the predicted shear angle is observed to converge with the experimental values at undeformed chip thicknesses of 40 μm and 50 μm. However, there is an anomaly in the experimental trend of the shear angle at 60 μm. Hence, an increase in the difference between the predicted and experimental values is observed.

The shear angle prediction at the cutting speed of 115 m/min seems to be a better match with the experimental data, as illustrated in Figure 5.14. There is also a constant difference between the predicted and experimental values after an undeformed chip thickness of 30 μm. The general trend of the shear angle predicted using Oxley's model also seem to compare well with the trend observed in the cutting experiments.

Additionally, it is noticed that an increase in the undeformed chip thickness improves the accuracy of prediction of the shear angle for the cutting process. This seems to imply that Oxley's model is more applicable for predicting shear angles for as undeformed chip thickness is increased. The mismatch shown in Figure 5.13 and 5.14 can be attributed to similar elucidation provided previously to explain the mismatch between the predicted and experimental values for AL7075.

5.2 Edge-Radiused Tool Process Model (Endres' Model)

5.2.1 Endres' Model

The edge-radiused tool process model developed by Manjunathaiah and Endres (2000) is modified and used in this study to predict micro and nano scale machining forces. The model is selected because of its relative simplicity and capability to predict cutting forces without the need to conduct complex experimental work to determine input parameters. A brief outline of the Manjunathaiah and Endres' model is presented. A geometric model of the cutting process with an edge-radius tool is presented in Figure 5.15.

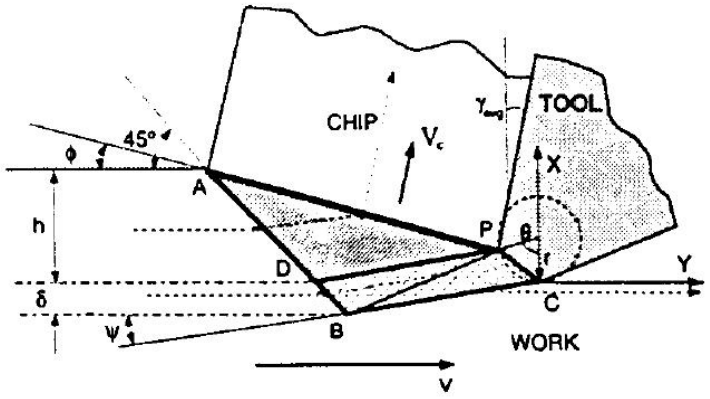

Figure 5.15: Geometric Model of the Cutting Process with an Edge-Radiused Tool (Manjunathaiah and Endres, 2000)

Figure 5.15 shows a tool of edge radius r_n removing material of undeformed chip thickness h as measured from the bottom of the tool C (same as level D). Material flowing at the bottom level of the tool passes through point D and rises up to the chip separation point P on the edge radius of the cutting tool. The chip separation point P, where the flow separates, is defined by the separation angle θ. The vertical height of point

P is taken to be p, which is also referred to as the penetration depth and is a function of both θ and r_n. The upper boundary of the deformation zone is bounded by the shear plane inclined at an angle φ. The lower boundary of the deformation zone below the tool is characterized by the angle ψ. The depth of deformation, δ, is hence related to the angle ψ. The machining force model is developed by conducting a force balance on the lower boundary of the deformation as illustrated by Figure 5.16.

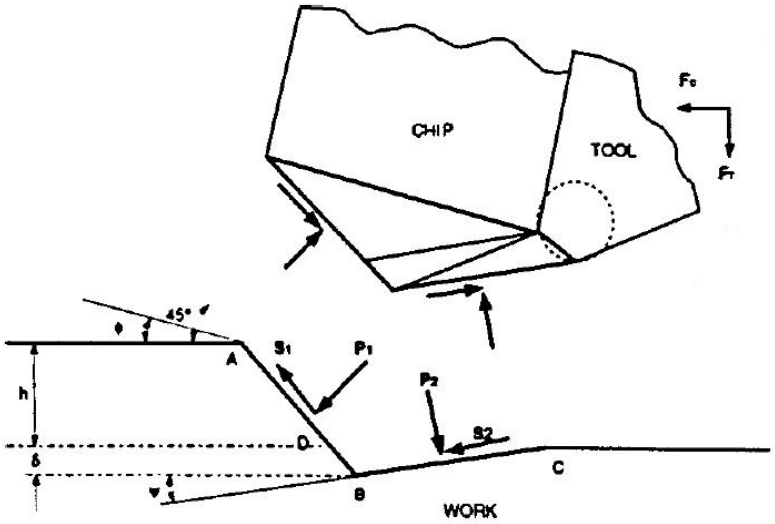

Figure 5.16: Force Balance on the Lower Boundary of the Shear Zone (Manjunathaiah and Endres, 2000)

The force balance on the lower boundary of the shear zone yields the following equations of the force model.

$$F_c = \{(h-p)\cot\phi + h + r_n \sin\theta - (k-1)\delta\}S \tag{5.2}$$

$$F_T = \{(h-p)\cot\phi - h + r_n \sin\theta + (k-1)\delta\cot\psi\}S \tag{5.3}$$

A constant value 30 º for θ has been adopted in the force model based on prior analysis and experiments by Komanduri (1971). A constant value of 20º has also been assumed for ψ based on experimental analysis. The adopted values for the constant

parameters used in Endres' model are summarized in Table 5.3 and will be used for the prediction of the cutting forces for both AL7075 and P20 steel.

Through a simple orthogonal cutting experiment to determine the shear angle φ, the cutting and thrust forces, the values of *S*, shear stress, and *k*, normal stress factor, can be obtained. These values of *S* and *k* are subsequently adopted to be constants. Equations 5.2 and 5.3 can then be employed to predict the cutting and thrust forces when the shear angle values are provided.

Table 5.3: Constants used in Endres' Model (Manjunathaiah and Endres, 2000)

Parameter	Value
Inclination angle of deformation zone, ψ	20º
Separation angle, θ	30º

5.2.2 AL7075

Using the assumed values of ψ and θ as provided in Table 5.3, the shear stress coefficient, S, and the coefficient of the normal stress factor, k, were computed. The values of the coefficients of S and k were estimated from the cutting force, thrust force and shear angle measured at an undeformed chip thickness of 2000 nm during the cutting experiments. The estimated values of S and k at the two cutting speeds are presented in Tables 5.4 and 5.5, respectively. These coefficients are subsequently assumed as constants in Endres' model to predict the cutting and thrust forces for all other factor levels.

Table 5.4: Coefficient of S and k used in Endres' Model – Cutting Speed 10 m/min for AL7075 (Estimated from Cutting Experiment)

Parameter	Coefficient
Shear Stress, S (N/mm^2)	206876
Normal Stress Factor, k	0.5291

Table 5.5: Coefficient of S and k used in Endres' Model – Cutting Speed 150 m/min for AL7075 (Estimated from Cutting Experiment)

Parameter	Coefficient
Shear Stress, S (N/mm^2)	533756
Normal Stress Factor, k	1.1467

5.2.2.1 Cutting Forces

The predicted cutting and thrust forces are presented in Tables C.9 and C.10 of Appendix C for cutting speeds of 10 m/min and 150 m/min respectively. The force data presented in Tables C.1, C.2, C.9 and C.10 are also graphed as a function of the undeformed chip thickness and are presented in Figures 5.17 – 5.20.

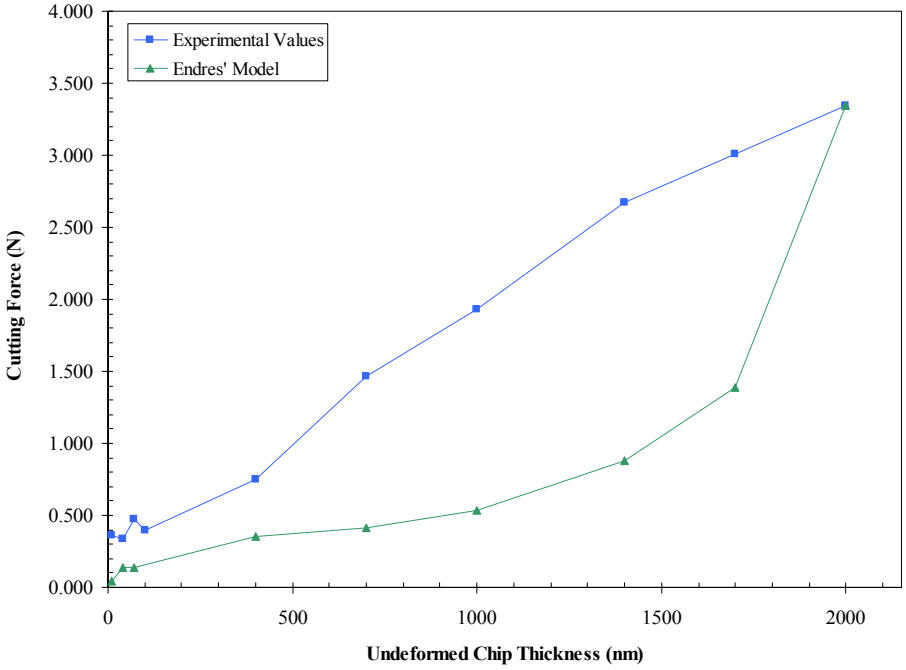

Figure 5.17: Effect of Undeformed Chip Thickness on Cutting Force – Cutting Speed 10 m/min (AL7075)

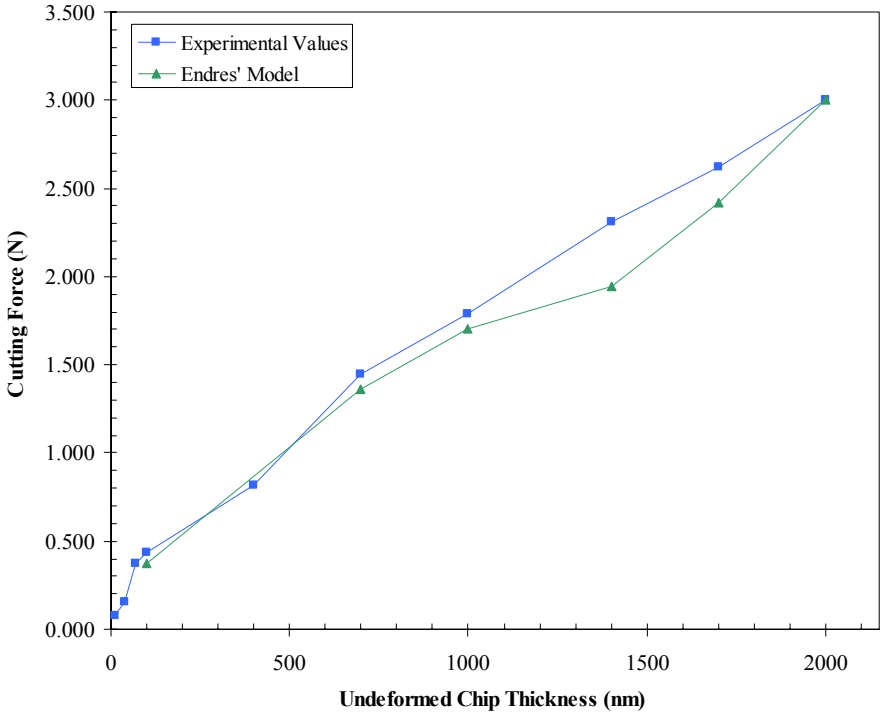

Figure 5.18: Effect of Undeformed Chip Thickness on Cutting Force – Cutting Speed 150 m/min (AL7075)

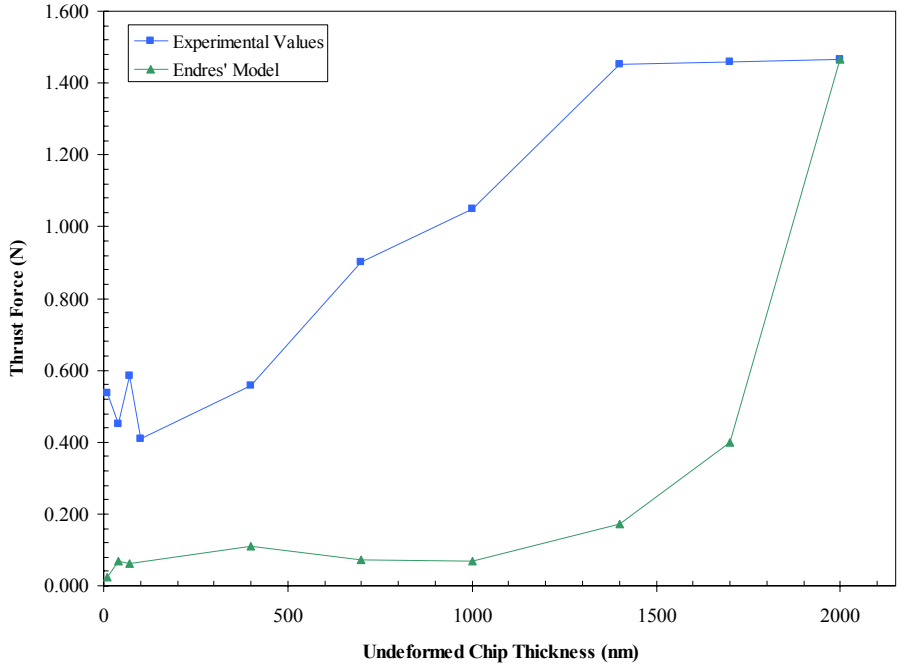

Figure 5.19: Effect of Undeformed Chip Thickness on Thrust Force – Cutting Speed 10 m/min (AL7075)

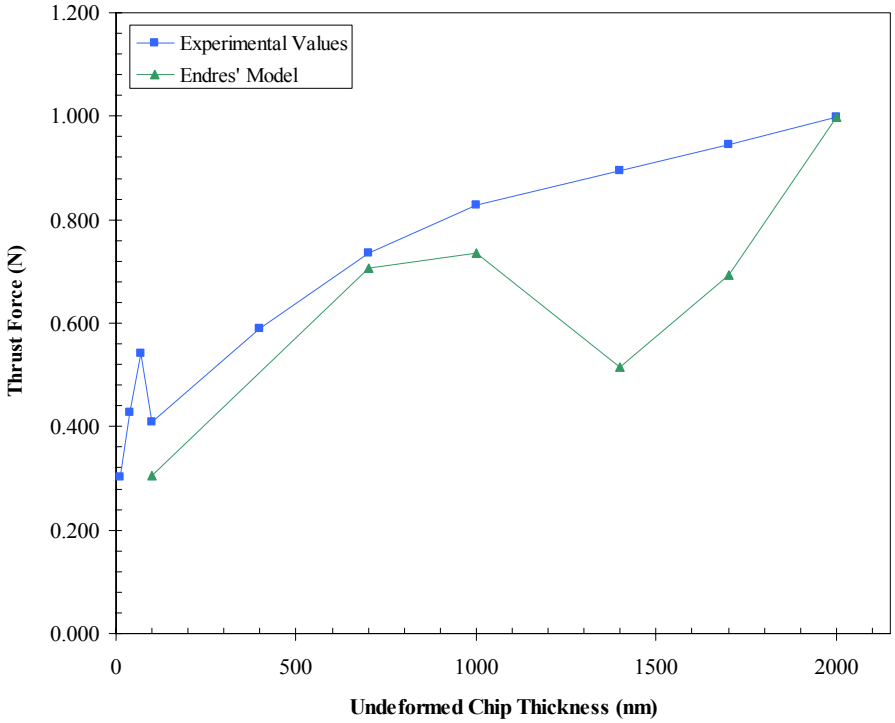

Figure 5.20: Effect of Undeformed Chip Thickness on Thrust Force – Cutting Speed 150 m/min (AL7075)

Figures 5.17 and 5.19 illustrate that the predicted cutting and thrust forces at the cutting speed of 10 m/min do not compare well with the experimental data. There are large differences between the predicted and experimental values. Similarly, the trend of the forces projected by Endres' model at this cutting speed also does not match well with the experimental data. However, the predicted values of the cutting force at the cutting speed of 115 m/min matches better with the experimental values, as illustrated in Figure 5.18. Both the predicted cutting force and the trend agree with the experimental data. Endres' model is again unable to provide good predictions of the thrust force. It is also observed that Endres' model under-predicts both the cutting and thrust forces.

A possible explanation for this observation is as follows. The shear stress factor, S, is assumed to be constant when used in this study to predict forces. This assumption is made so that Endres' model can be used in a predictive manner to obtain an estimate of the cutting and thrust forces. However, the shear stress, S, is shown by Manjunathaiah and Endres (2000) to decrease with increasing undeformed chip thickness. This variation in shear stress, S, is related to strain and strain rate hardening as a result of variations in the undeformed chip thickness. Hence, the assumption that shear stress, S, is constant might have produced the difference between the predicted and experimental data at the lower cutting speed. The shear stress, S, might probably assume a more constant value at the higher cutting speed of 150 m/min. Hence, the cutting force prediction matches better with the experimental data, as seen in Figure 5.18.

5.2.3 P20 Steel

The estimated values for the constant parameters used in Endres' model summarized in Table 5.3 are similarly used for the prediction of cutting forces for P20 steel. The values of the coefficients of S and k are estimated in a similar fashion as that described in the preceding section. The cutting force, thrust force and shear angle measured at an undeformed chip thickness of 60 μm at both cutting speeds are used to compute the coefficient of S and k. The coefficient of S and k for the two cutting speeds are presented in Tables 5.6 and 5.7. These coefficients are similarly assumed as constants in Endres' model to predict the cutting and thrust forces for all other factor levels.

Table 5.6: Coefficient of S and k used in Endres' Model – Cutting Speed 10 m/min for P20 Steel (Estimated from Cutting Experiment)

Parameter	Coefficient
Shear Stress, S (N/mm^2)	1005000
Normal Stress Factor, k	0.827

Table 5.7: Coefficient of S and k used in Endres' Model – Cutting Speed 115 m/min for P20 Steel (Estimated from Cutting Experiment)

Parameter	Coefficient
Shear Stress, S (N/mm^2)	1250830
Normal Stress Factor, k	2.463

5.2.3.1 Cutting Forces

The predicted cutting and thrust forces are presented in Tables C.11 and C.12 of Appendix C for cutting speeds of 10 m/min and 115 m/min, respectively. The force data presented in Tables C.5, C.6, C.11 and C.12 are also graphed a function of the undeformed chip thickness and are shown in Figures 5.21 – 5.24.

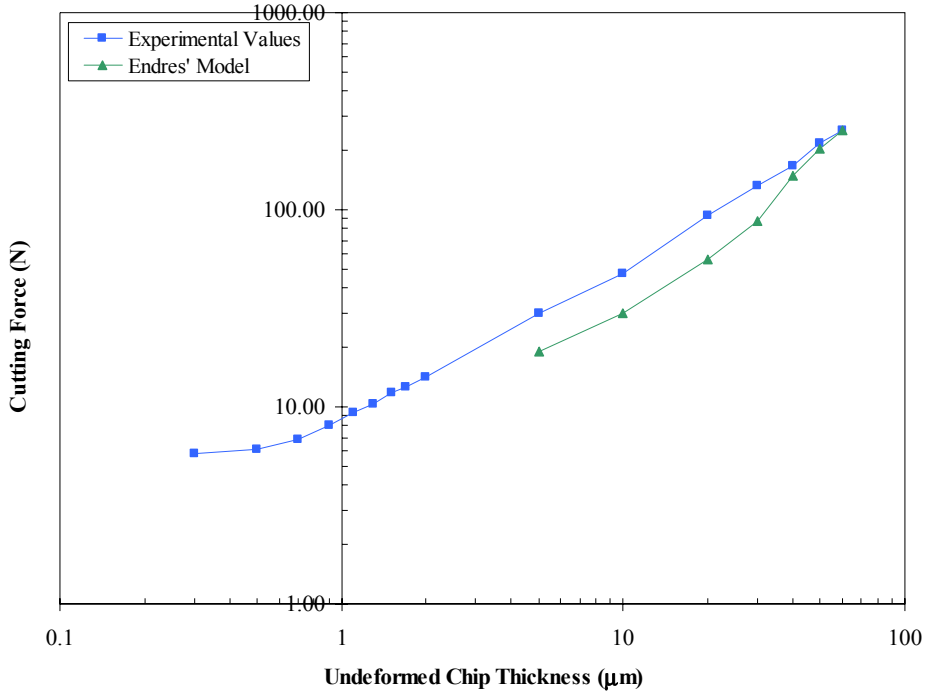

Figure 5.21: Effect of Undeformed Chip Thickness on Cutting Force – Cutting Speed 10 m/min (P20)

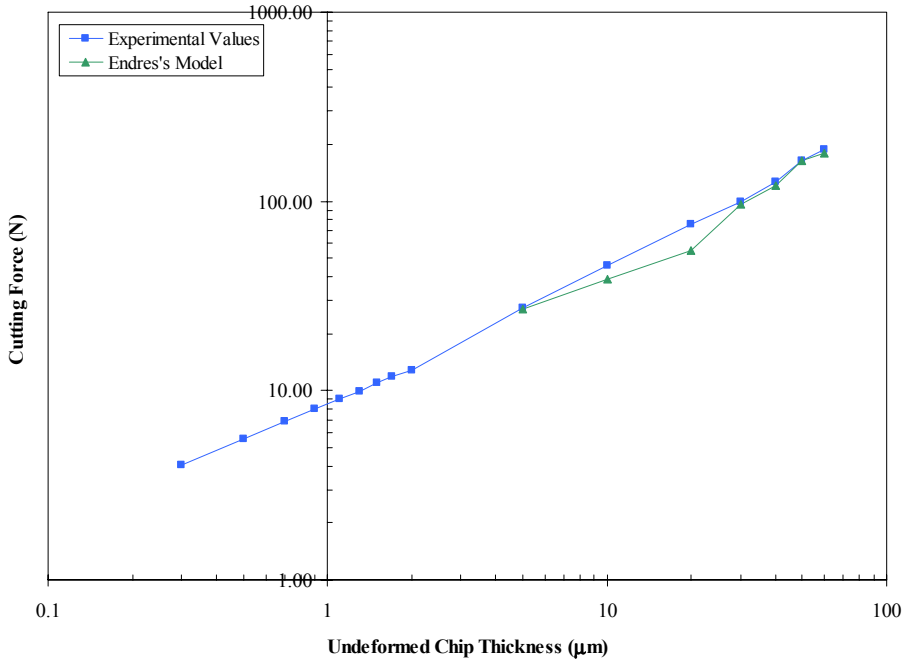

Figure 5.22: Effect of Undeformed Chip Thickness on Cutting Force – Cutting Speed 115 m/min (P20)

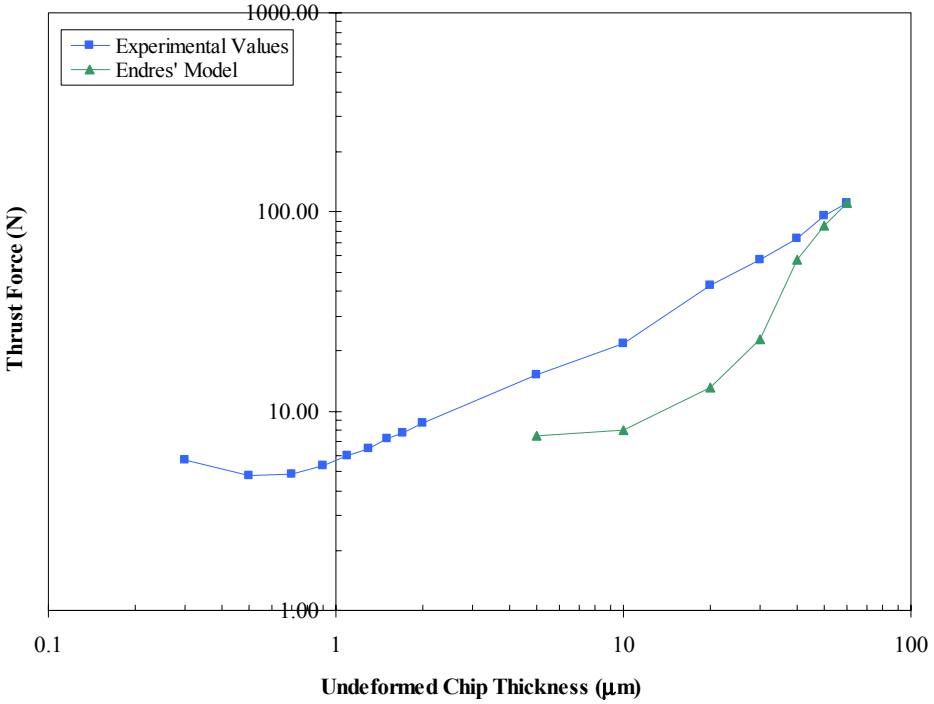

Figure 5.23: Effect of Undeformed Chip Thickness on Thrust Force – Cutting Speed 10 m/min (P20)

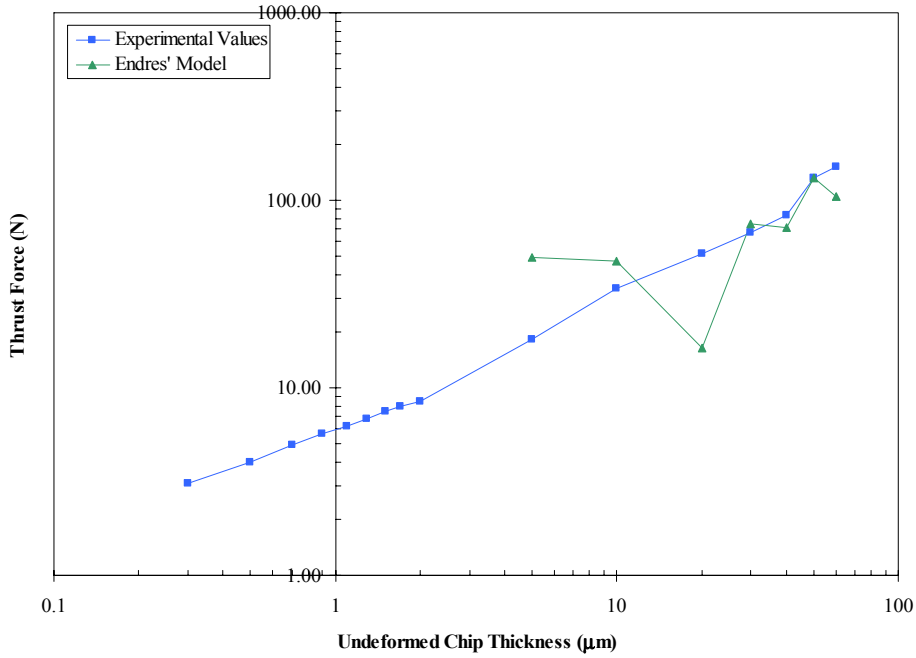

Figure 5.24: Effect of Undeformed Chip Thickness on Thrust Force – Cutting Speed 115 m/min (P20)

Figure 5.21 illustrates that the predicted values of cutting force at the cutting speed of 10 m/min compare quite well with the experimental data. The predicted cutting force converges with the experimental data after an undeformed chip thickness of 40 μm. In the undeformed chip thickness range of 5 - 30 μm, there is a constant difference (40%) between the predicted and experimental values. The projected trend of the cutting force within this range also matches quite well with the trend exhibited by the experimental data. At the cutting speed of 115 m/min, the predicted cutting force matches the experimental data. Endres' model is able to provide reasonably good estimates of the cutting force at the cutting speed of 115 m/min, as illustrated in Figure 5.22.

Figures 5.23 and 5.24 reiterate the point that Endres' model is unable to provide good estimates for the thrust forces. The predictions of the thrust forces at both cutting speeds do not compare well with the experimental values. Although Endres' model can be used to generate good estimates of the cutting force for P20 steel, the model is unable to provide accurate predictions of the thrust forces, similar to that observed in the study of AL7075. A possible explanation for this discrepancy is the assumption of a constant value for the shear stress, S, over the entire range of undeformed chip thicknesses used in the experiments.

5.3 Comparison of Models

Oxley's and Endres' models are compared and contrasted in this section to determine the applicability of both models in predicting process responses in micro and nano scale cutting.

5.3.1 AL7075

Oxley's model consistently over-predicted the cutting and thrust forces at both cutting speeds as shown in Figures 5.3 – 5.6. Endres' model, on the other hand, consistently under-predicted the cutting and thrust forces at both cutting speeds, shown in Figure 5.17 – 5.20. At the cutting speed of 10 m/min, both Oxley's and Endres' models were unable to predict the trend of the cutting and thrust forces. However, both Oxley's and Endres' models were able to predict the trend of the cutting force at the cutting speed of 150 m/min. Nevertheless, Endres' model is more applicable at the cutting speed of 150m/min because it was able to predict the cutting force more accurately.

Both Oxley's and Endres' model were unable to provide good predictions of the thrust force at both cutting speeds. The predicted thrust forces do not match well with the experimental data results. There are significant differences between the predicted and experimental values at both cutting speeds.

In general, the applicability of both process models is limited when used in predicting micro and nano scale cutting of AL7075. The predicted and experimental values of both the cutting and thrust forces do not match well over a wide range of cutting conditions.

5.3.2 P20

Oxley's and Endres' models were able to accurately predict the trend of the cutting force at the cutting speed of 10 m/min, shown in Figure 5.9 and 5.21. Although both models can be used to predict the trend of the cutting force at the cutting speed of 10 m/min, there are still differences between the predicted and experimental values.

Endres' model was able to better predict the cutting force at the cutting speed of 115 m/min, shown in Figure 5.22. However, there was a small deviation of the predicted values from the experimental data between 10 – 20 μm. Oxley's model was again unable to accurately predict the cutting force at the cutting speed of 115 m/min, shown in Figure 5.10. However, it was able to predict the trend of the cutting force, showing a constant difference of 30% between the predicted and experimental values.

Both Oxley's and Endres' model were unable to accurately predict the thrust force at both cutting speeds. However, Oxley's model was able to predict the trend of the thrust force at both cutting speeds.

In general, Oxley's model seems to be more applicable over the undeformed chip thickness range of 5 – 60 μm for P20 steel since it was shown to be able to provide good predictions of the trend of both the cutting and thrust forces.

5.4 Summary

Two process models, namely Oxley's model and Endres' model were used to predict cutting forces and shear angle in this chapter. The predicted cutting process responses were then compared with the experimental data obtained in this study. The applicability of both process models in predicting micro and nano scale cutting process responses was also discussed.

The main findings in this chapter can be summarized as follows:

- Oxley's model was unable to accurately predict cutting force, thrust force and shear angle in micro and nano scale cutting of AL7075 over the undeformed chip thickness range of 10 nm – 2000 nm.

- Oxley's model was able to predict the trend in the cutting force, thrust force and shear angle in micro scale cutting of P20 steel over the undeformed chip thickness range of 5 μm – 60 μm.
- Oxley's model was observed to break down at around the estimated cutting edge radius of the tool for both AL7075 and P20 steel.
- Endres' model was only able to give good predictions of the cutting force at the cutting speed of 150 m/min for AL7075 over the undeformed chip thickness range of 10 nm – 2000 nm.
- Endres' model was only able to give good predictions of the cutting force but not the thrust force for P20 steel over the undeformed chip thickness range of 5 μm – 60 μm.

CHAPTER 6

CONCLUSIONS AND RECOMMENDATIONS

6.1 Conclusions

This experimental investigation demonstrated the effects of undeformed chip thickness and cutting speed on cutting forces, chip geometry and surface morphology during mechanical cutting of AL7075 and P20 at the micro and nano scale. Some of the significant findings from this study can be summarized as follows:

- Micro and nano scale cutting exhibit comparable trends in chip geometry and surface morphology to those observed in macro-scale cutting.
- The edge radius of the cutting tool is observed to influence the cutting process significantly when micro and nano scale machining was conducted.
- Deviations of micro and nano scale machining trends from conventional macro-scale machining trends initiate at or around the edge radius of the cutting tool for both materials studied.
- The applicability of the selected process models in predicting cutting forces and shear angle in micro and nano scale machining is limited.

A more detailed summary of the essential findings on the effects of cutting conditions on the cutting forces, chip geometry, machined surface morphology, experimental observations and applicability of process model for both AL7075 and P20 steel are provided in the following sections.

6.1.1 Cutting Forces

- The cutting force exhibits a linear relationship with the undeformed chip thickness when micro and nano scale machining is conducted above the edge radius of the tool.
- When the undeformed chip thickness is smaller than the edge radius of the tool, a non-linear variation in the cutting forces is observed.
- The specific cutting and thrust energies increase significantly in a non-linear fashion when micro and nano scale machining is performed at undeformed chip thicknesses smaller than the edge radius of the tool.
- The cutting speed has negligible effect on the cutting force at undeformed chip thicknesses less than 1 μm for both materials studied.

6.1.2 Chip Geometry

- Continuous chips are observed over the entire range of undeformed chip thicknesses (10 – 2000 nm) investigated for AL7075.
- Continuous chips were only observed in the P20 cutting experiments at undeformed chip thicknesses greater than 2 μm.
- The cutting ratio and shear angle increase initially and then decrease as the undeformed chip thickness is increased for both AL7075 (10 – 2000 nm) and P20 (5 – 60 μm).

6.1.3 Surface Morphology

- The surfaces generated in micro and nano scale machining exhibit similar surface roughness characteristics as those observed in macro-scale machining.
- Machining at higher cutting speeds (150 m/min for A7075 and 115 m/min for P20 steel) and lower undeformed chip thicknesses (40 nm for AL7075 and 10 μm for P20 steel) produces a smoother surface.
- Machining when performed at undeformed chip thicknesses smaller than the edge radius of the tool generally creates rougher surfaces.

6.1.4 Experimental Observations

- Tool wear resulting in changes in the edge radius of the tool is not a vital issue in this study of micro and nano scale cutting.
- Significant amount of smearing of AL7075 on the diamond cutting tool is observed.
- Frictional size effect is also observed in the AL7075 cutting experiment.

6.1.5 Applicability of Process Models

- Oxley's model is unable to accurately predict cutting force, thrust force and shear angle in micro and nano scale cutting of AL7075 over the undeformed chip thickness range of 10 nm – 2000 nm.
- Oxley's model is able to predict the trend in the cutting force, thrust force and shear angle in micro scale cutting of P20 steel over the undeformed chip thickness range of 5 μm – 60 μm.

- Oxley's model is observed to break down at around the estimated cutting edge radius of the tool for both AL7075 and P20 steel.
- Endres' model is only able to give good predictions of the cutting force at the cutting speed of 150 m/min for AL7075 over the undeformed chip thickness range of 10 nm – 2000 nm.
- Endres' model is only able to give good predictions of the cutting force but not the thrust force for P20 steel over the undeformed chip thickness range of 5 μm – 60 μm.

6.2 Current Limitations in Micro-/ Nano-Machining

The lack of developed metrology techniques and process models to accurately predict process parameters in micro and nano scale processes are the two main limitations in the advancement of the understanding of micro and nano scale machining operations. Metrology techniques are vital in scientific investigation in the area of micro and nano scale machining. Numerous measurements have to be made during micro and nano scale cutting experiments to accurately quantify and explain observed trends. Current limitations in micro and nano scale machining are summarized as follows:

6.2.1 Metrology Techniques

- There are currently no developed and reliable metrology techniques that can be used to accurately measure shear angle, deformed chip thickness, edge radius of the cutting tool and the cutting temperatures at micro and nano scale.

- Non-contact imaging measurement techniques such as that used in this study present accuracy issues.

6.2.2 Process Models

- There is currently a lack of process models for micro and nano cutting that can accurately predict cutting process responses such as forces over a wide range of cutting conditions.
- Current commercial finite element software packages such as Third Wave Systems AdvantEdge® and DEFORM® 2D cannot be used to simulate the micro and nano scale cutting process. These softwares are unable to generate sufficient elements within the area of interest to analyze cutting process at very small length scale (less than 1μm).

6.3 Recommendations for Future Work

Analysis of the experimental data suggests that the edge radius has considerable influence on machining forces and size-effect in the specific cutting energies. However, the edge radius of the cutting tool is kept constant in both experimental investigations in this study. Hence, studying the effect of varying the edge radius of the cutting tool on machining forces and specific cutting energies is proposed. This would provide a more conclusive response to the specific contribution of the edge radius in micro and nano scale cutting experiments. In addition, studying the effect of varying the grain size of the work material on machining forces and specific cutting energies is also proposed. This is

because the microstructure of the work material has also been put forth as a possible cause for the size-effect phenomenon observed in the specific cutting energies.

Micro and nano scale metrology is an area where there is a pressing need for further development. As highlighted in the preceding section, accurate measurement of parameters such as shear angle, deformed chip thickness, edge radius of the cutting tool and cutting temperatures are vital for the advancement of our knowledge of micro and nano scale machining operations. Current measurement techniques are inadequate for providing precise and accurate quantification of the afore-mentioned parameters with little uncertainty. Hence, development of metrology techniques would no doubt improve the accuracy and reliability of the trends observed in micro and nano scale machining.

The measurement and analysis of cutting temperatures in micro and nano scale machining is also another area for future research. This would significantly aid the development of predictive models for cutting temperatures in micro and nano scale machining. On the same note, the development of thermo-mechanical machining process models that are not computationally intensive and yet capable of accurately describing the material behavior and predicting cutting process parameters in micro and nano scale machining should also be further pursued.

APPENDIX A: MACHINE, TOOL AND WORK MATERIAL SPECIFICATION

Machine external view

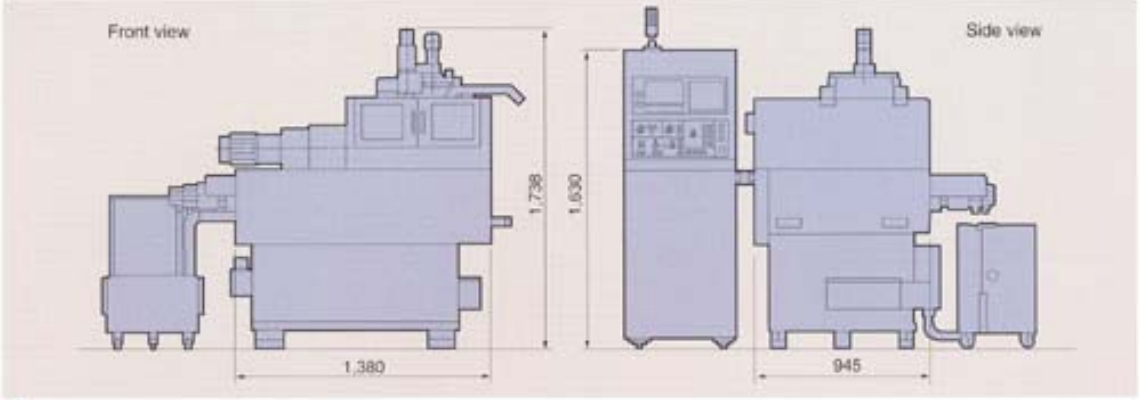

Main machine specifications

			ULG-100C(H³)	ULG-100A(HY)
Travel	X-axis travel (cross movement of wheel spindle)		300 mm	220 mm
	Y-axis travel (vertical movement of wheel spindle)		75 mm	20 mm
	Z-axis travel (work spindle longitudinal movement)		150 mm	150 mm
	C-axis (work spindle rotation)		Infinite	—
Work spindle (C-axis)	Diameter of high-precision cylindrical aerostatic bearing		80 mm	80 mm
	Spindle speed		10~1 500 min⁻¹	20~1 500 min⁻¹
	Diameter of workpiece facing plate (vacuum chuck)		100 mm	100 mm
	Maximum workpiece diameter to be machined		120 mm	120 mm
Wheel spindle	Diameter of high-precision cylindrical aerostatic bearing		32 mm	32 mm
	Spindle speed		5 000~40 000 min⁻¹	5 000~40 000 min⁻¹
	Type of spindle nose		Collet chuck attached	Collet chuck attached
Feedrate	Rapid traverse rate(unit: 0.01 μm)	X-, Y- and Z-axes	450 mm/min	450 mm/min (Y-axis: 300 mm/min)
		C-axis	22 000°/min	—
	Feedrate (unit: 0.01 μm)	X-, Y- and Z-axes	0.1~450 mm/min	0.1~450 mm/min (Y-axis: 1~300 mm/min)
		C-axis	1~22 000°/min	—
	Rapid traverse rate(unit: 0.001 μm)	X-, Y- and Z-axes	160 mm/min	—
	Feedrate (unit: 0.001 μm)	X-, Y- and Z-axes	0.1~160 mm/min	—
Least input increment		X-, Y- and Z-axes	0.000001 mm	0.00001 mm (Y-axis: 0.0001 mm)
		C-axis	0.0001°	—
NC system and No. of controlled axes	FANUC Series 15-MB No. of controlled axes (Simultaneous controllable axes)		4 axes (X, Y, Z, C)	3 axes (X, Z)
Mass of machine	(Including NC system)		2 600 kg	1 400 kg

Options

1. Coolant supply unit
2. Mist supply unit
3. Collet chuck
4. Truing fixture
5. Tool holder
6. Air supply system
7. Tilting spindle unit
8. Aspheric surface compensation software
9. f-θ lens machining software
10. Flying-cut fixture
11. Consumable parts, etc.

* We reserve the right to change any of the specifications in this catalog without notice in order to effect improvement.
** Model ULG-100A(HY) is developed under the guidance of Professor T. Higuchi (Tokyo University) and Researcher Y. Yamagata(RIKEN) in 1993, and has been improved.

SHIBAURA TOSHIBA MACHINE CO.,LTD.

TOKYO MAIN BRANCH
No.2-11, 4chome Ginza, Chuo-ku, Tokyo 104-8141, JAPAN
Tel: 03-3567-0520 Fax: 03-3562-5220

NUMAZU PLANT
2068-3, Ooka, Numazu-shi, Shizuoka-ken 410-8510, JAPAN
Tel:0559-25-5057 Fax:0559-25-6540

SM02153-1,000-TB
Printed in Japan

Figure A.1: Technical Specifications of the Toshiba ULG-100C (H^3) Machine

Figure A.2: Technical Specifications of the Hardinge Conquest T42SP Lathe

General purpose SEM **JSM-5500**

An easy-to-use multipurpose SEM equipped with electron optics and a specimen chamber and specimen stage that are comparable to a research grade model. The control panel, composed of a minimum necessary number of switches and knobs suited for routine work, is designed to allow anybody to operate it with ease. Also, the auto functions such as focusing, astigmatism correction and exposure, and the memory function are highly reliable ones incorporating the latest techniques.

Principal specifications

● Resolution	3.5nm
● Accelerating voltage	0.5 to 30kV (53 steps)
● Magnification	×18 to 300,000
● Specimen size	150 mm diam. (max.)
● Specimen movements	X=20mm, Y=10mm Z=43mm (WD=5 to 48mm) T=−10 to 90°, R=360°

Figure A.3: Technical Specifications of the JEOL JSM-5500 SEM

NewView 200

Objectives

Physical Characteristics

Typical Dimensions:	See figures in illustration.
Type:	2.5X and 5X are Michelson objectives; 10X, 20X, and 50X are Mirau objectives. Coherence bandwidth centered within depth of focus. Useful for measuring the top surfaces of transparent and partially transparent materials, as well as curved and angled opaque surfaces with 4 to 100% reflectivity. 10X, 20X, and 50X are parfocal.
Magnification Range:	2.5X, 5X, 10X, 20X, 50X
Viewing Magnification on Video Monitor:	20 times the objective magnification.

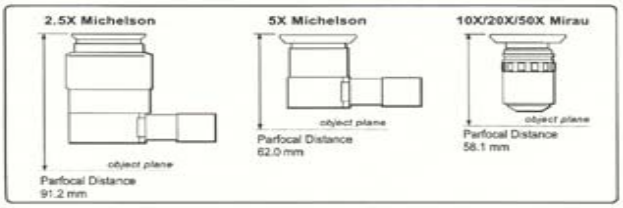

Power	Sys Mag	NA	Working Distance (mm)	Focus Depth (µm)	Inter Depth (µm)	Lateral Res (µm)	Field of View H x V (mm)	Spatial Samp (typ) (µm) StdRes	HiRes
NewView 200									
2.5X	50X	0.075	10.3	±51.6	4.0	4.72	2.82 x 2.11	8.80	4.40
5X	100X	0.130	9.3	±17.2	4.0	2.72	1.41 x 1.06	4.40	2.20
10X	200X	0.300	7.4	±3.2	4.0	1.18	0.70 x 0.53	2.20	1.10
20X	400X	0.400	4.7	±1.8	3.6	0.88	0.35 x 0.26	1.10	0.55
50X	1000X	0.550	3.4	±1.0	2.0	0.64	0.14 x 0.11	0.44	0.22
NewView 200 CHR									
2.5X	50X	0.075	10.3	±51.6	4.0	4.72	2.53 x 1.90	7.92	3.96
5X	100X	0.130	9.3	±17.2	4.0	2.72	1.27 x 0.95	3.96	1.98
10X	200X	0.300	7.4	±3.2	4.0	1.18	0.63 x 0.48	1.98	0.99
20X	400X	0.400	4.7	±1.8	3.6	0.88	0.32 x 0.24	0.99	0.50
50X	1000X	0.550	3.4	±1.0	2.0	0.64	0.13 x 0.10	0.40	0.22

Objective Table Notes

Power	Magnifying power of the objective.
Sys Mag	System magnification, enlargement of the surface, as viewed on the video monitor.
NA	Numerical aperture, a number representing the resolving power of the objective.
Working Distance	Distance from the end of the objective to the test surface when focused.
Focus Depth	Vertical distance within which any specimen detail will simultaneously be in focus.
Inter Depth	Interference depth, vertical distance over which interference can occur.
Lateral Res	Lateral resolution, optical resolution of the imaging system.
Field of View	Size of area imaged and measured.
Spatial Samp	Spatial sampling, the apparent pixel size at each magnification
StdRes, HiRes	Maximum camera size in pixels: StdRes = 320 x 240 pixels; HiRes = 640 x 480.

Performance

Max. Vertical Step Height	100 µm, all magnifications
Extended Scan	> 100 µm (up to 5 mm)
Step Height Accuracy (over 100 µm)	
NewView 200 CHR	≤ 0.75%[1]
NewView 200	≤ 3.0%[2]
Step Height Repeatability	≤ 0.5%
Minimum Vertical Resolution	≈ 0.10 nm (all magnifications)
Instrument Repeatability	< 0.6 nm R_q @ 0 avgs, < 0.3 nm R_q @ 8 avgs (Mean + 2σ, all magnifications)
Digitization	8 bits
Data Scan Rate (Cam. Mode)	
25 Hz	2.0 µm/sec., 320 x 240 pixels
25 Hz	0.5 µm/sec., 640 x 480 pixels
50 Hz	4.0 µm/sec., 320 x 240 pixels (fast)

Objectives

Magnification Range	2.5X, 5X, 10X, 20X, 50X
Mounting	Single Objective Dovetail
Reference Quality	λ/20 PV flatness (typical)

Sample

Sample Material	Coated and uncoated metals, glass, ceramics, plastics, and other materials, with specular and nonspecular surfaces
Maximum Thickness	89 mm (3.5 in.)
Reflectivity	≈ 4% to 100%
Maximum Roughness	100 µm R_p

Electronics/Software Platform

CPU	HP 715
Software	MetroPro™

System Imaging

CCD Array Density	320 x 240, 640 x 480
Pixel Size	
NewView 200	11 x 11 µm
NewView 200 CHR	9.9 x 9.9 µm
Demagnification Option	0.375X
Image Zoom Option	0.5X to 2.0X continuous

Alignment

Focus	Iris focusing

Illuminator

Light Source	Filtered White Light Selectable Coherence

Dimensions (H x W x D)

Workstation Table	889 x 1143 x 864 mm (35 x 45 x 34 in.)
Microscope	1013 x 292 x 429 mm (39.9 x 11.5 x 16.9 in.)
Video Monitor	233 x 253 x 249 mm (9.2 x 9.9 x 9.8 in.)
Electronics Enclosure	375 x 333 x 127 mm (14.8 x 13.1 x 5 in.)

[1] For any single scan, or 1.0% @ 2σ for all scans, if calibrated within 24 hours @ ±2.0° C (±3.6° F).

[2] For any single scan, or 4.0% @ 2σ for all scans, if calibrated within 24 hours @ ±0.2° C (±0.4° F).

Figure A.4: Technical Specifications of the ZYGO NewView 200

Technical Data

Type			9256A1	9256A2
Range	F_x, F_y, F_z	N	–250 ... 250	
Calibrated partial range	F_x, F_y, F_z	N	0 ... 25	
Overload	F_x, F_y, F_z	N	–300/300	
Threshold		N	<0,002	
Sensitivity	F_x, F_z	pC/N	≈–11	
	F_y	pC/N	≈–13	
Linearity, all ranges		% FSO	≤±0,4	
Hysteresis, all ranges		% FSO	≤0,5	
Cross talk		%	≤±2	
Rigidity	c_x, c_z	N/µm	>250	
	c_y	N/µm	>300	
Natural frequency	f_o (x)	kHz	≈5,1	≈4,0
(mounted on	f_o (y)	kHz	≈5,5	≈4,8
rigid base)	f_o (z)	kHz	≈5,5	≈4,6
Operating temperature range		°C	0 ... 70	
Insulation resistance		TΩ	>10	
Ground isolation		MΩ	>100	
Degree of protection			IP 67 **)	
Weight		kg	0,75	0,87
Clamping area		mm	39x80	55x80

**)With connecting cable Type 1697A5

Dimensions

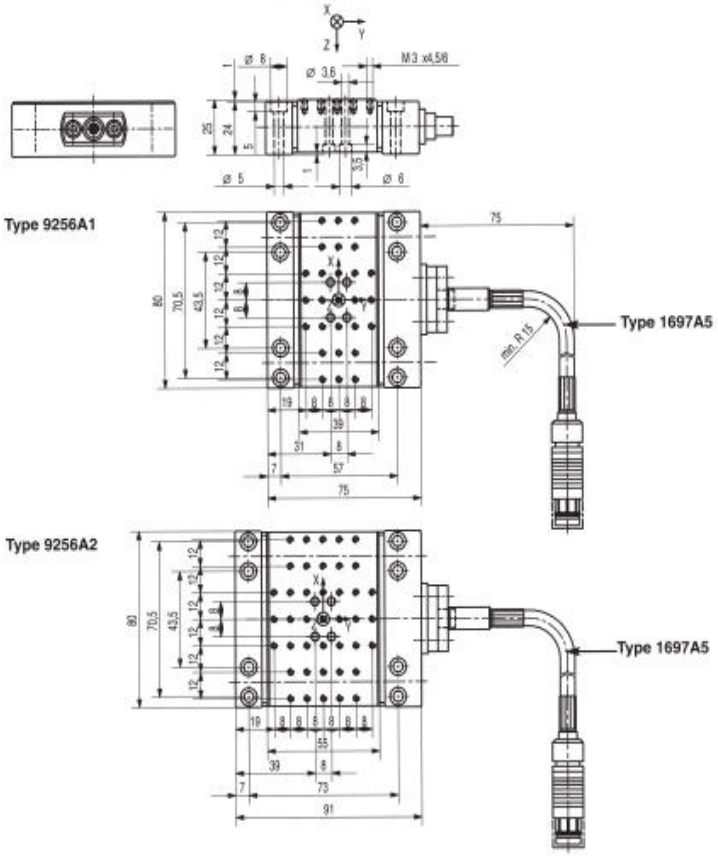

Figure A.5: Technical Specifications of Kistler Type 9256, Three-Component Force Mini-Dynamometer

Technical Data

Range	F_x, F_y, F_z	kN	–5 ... 5 *)
F_z for F_x and F_y ≤0,5 F_z	F_z	kN	–5 ... 10 **)
Calibrated partial range 1	F_x, F_y	N	0 ... 500
	F_z	N	0 ... 1000
Calibrated partial range 2	F_x, F_y	N	0 ... 50
	F_z	N	0 ... 100
Overload	F_x, F_y, F_z	kN	–7,5/7,5
F_z for F_x and F_y ≤0,5 F_z	F_z	kN	–7,5/15
Threshold		N	<0,01
Sensitivity	F_x, F_y	pC/N	≈–7,5
	F_z	pC/N	≈–3,7
Linearity, all ranges		% FSO	≤±1
Hysteresis, all ranges		% FSO	≤0,5
Cross talk		%	≤±2
Rigidity	c_x, c_y	kN/µm	>1
	c_z	kN/µm	>2
Natural frequency	f_o (x, y, z)	kHz	≈3,5
Natural frequency	f_o (x, y)	kHz	≈2,3
(mounted on flanges)	f_o (z)	kHz	≈3,5
Operating temperature range		°C	0 ... 70
Temperature coefficient of sensitivity		%/°C	–0,02
Capacitance (of channel)		pF	≈220
Insulation resistance (20 °C)		Ω	>10^{13}
Ground insulation		Ω	>10^{8}
Protection class		–	IP 67 ***)
Weight		kg	7,3

Dimensions

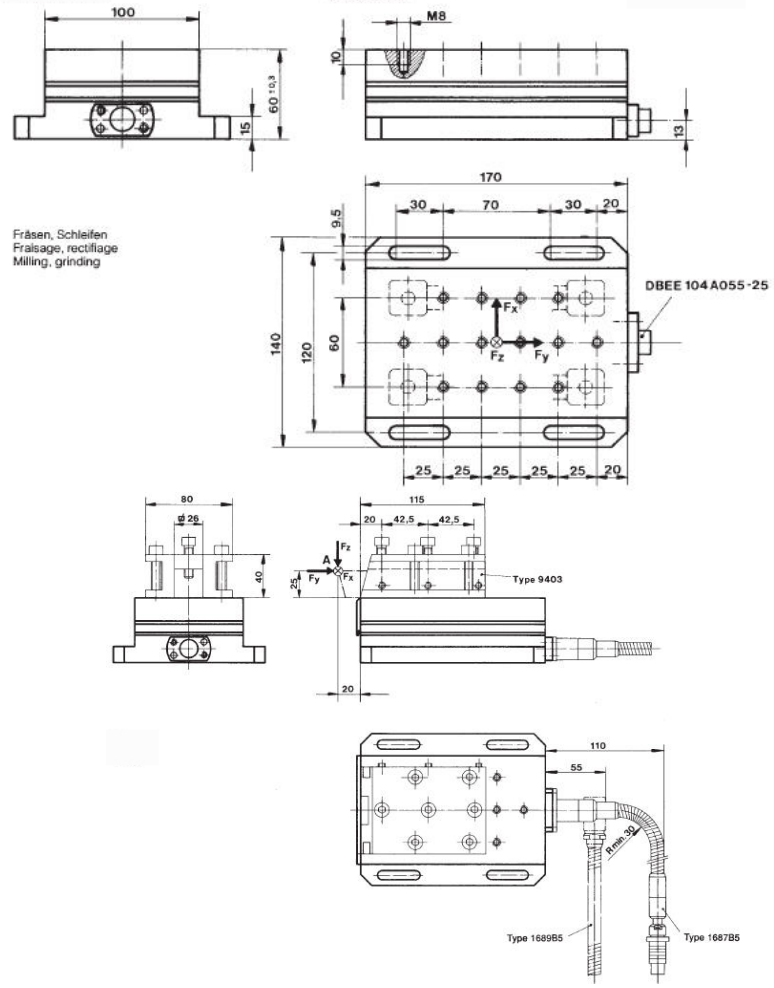

Figure A.6: Technical Specifications of Kistler Type 9257, Three-Component Force Dynamometer

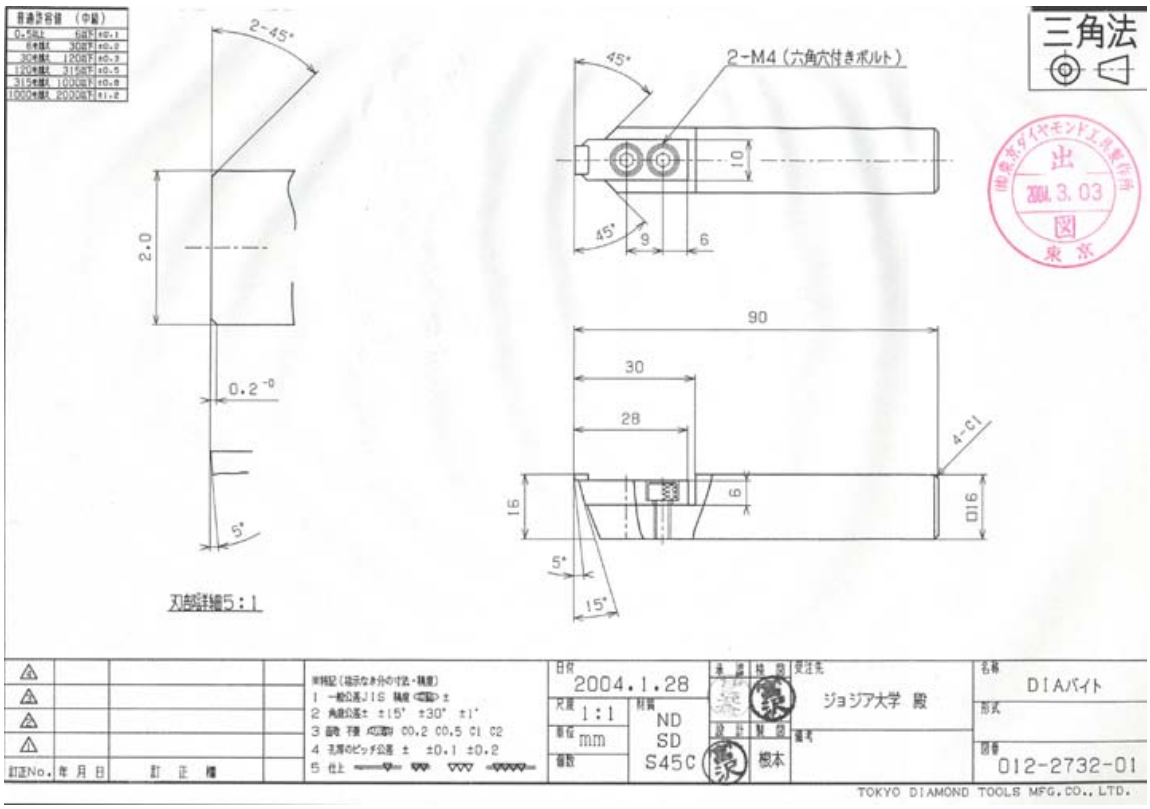

Figure A.7: Dimension of Single Crystal Diamond Tool

NGP3125R Dimensions

ANSI Catalog	NGP3125R
ISO Catalog #	NGP3125R
Unit of Tool	Inch/Metric
T	3.810
CM	11.000
W	3.175
W min	0.025
W max	0.025
RL max	0.254
RL min	0.254
R max	0.254
R min	0.127
M	10.287
ZCE	2 Cutting Edges
S	8.738
W1	4.978

Grade	Grade Material	Coating System	Coating	Kennametal Number
KC730	Carbide	PVD	TiN	1114352
Additional Product Information				
K68	Carbide	Uncoated	Uncoated	1114666
KC850	Carbide	CVD	TiC/TiCN/TiN	1114934
Additional Product Information				
KD100	Diamond	Uncoated	Uncoated	1283333
KC5410	Carbide	PVD	TiB2	1818386

Figure A.8: Dimension of Carbide Inserts

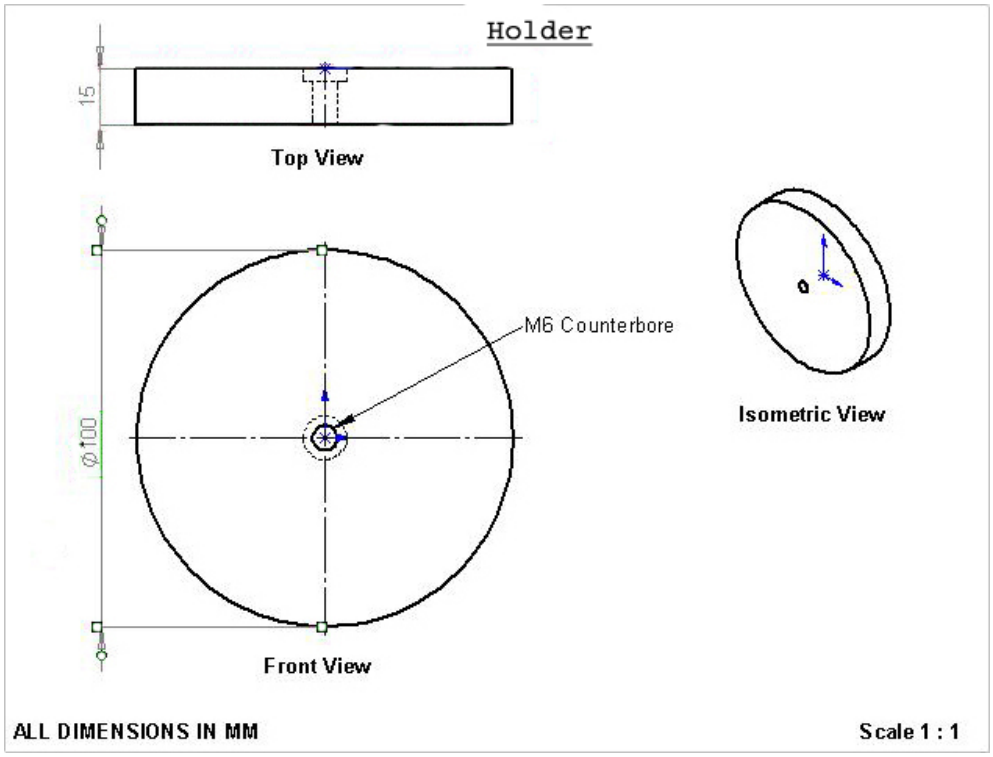

Figure A.9: Dimensions of Holder

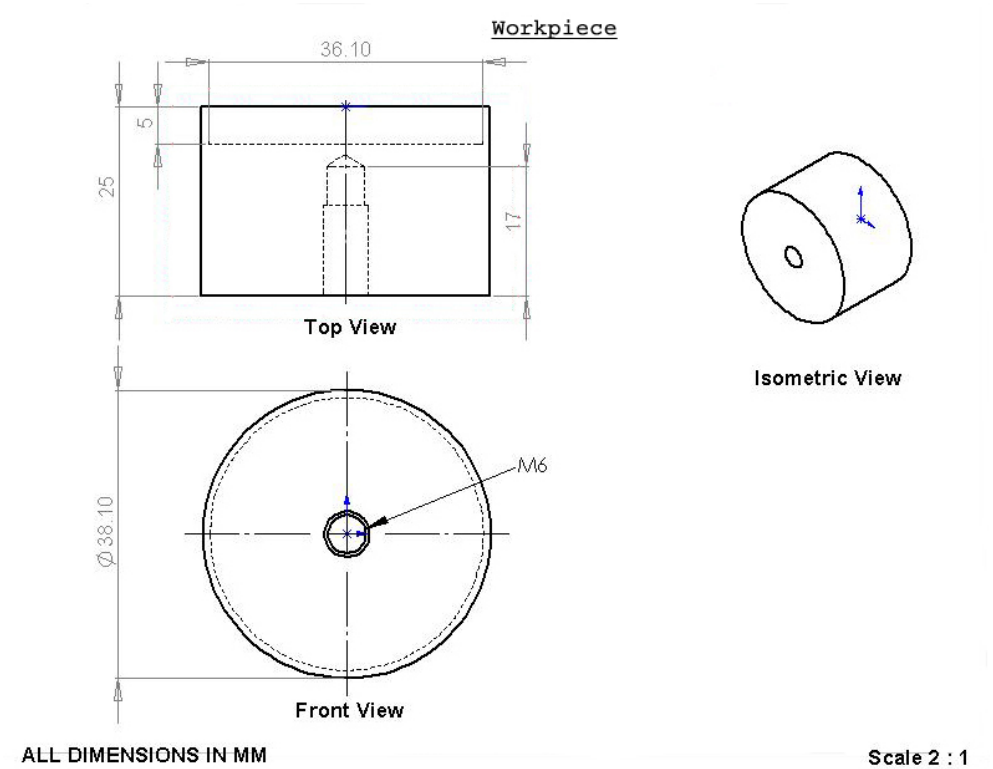

Figure A.10: Dimensions of Workpiece

Table A.1: Material properties of AL7075

Physical Properties	**Metric**
Density	2.81 g/cc

Mechanical Properties	**Metric**
Hardness, Brinell	150
Hardness, Knoop	191
Hardness, Rockwell A	53.5
Hardness, Rockwell B	87
Hardness, Vickers	175
Ultimate Tensile Strength	572 MPa
Tensile Yield Strength	503 MPa
Elongation at Break	11% (AA; Typical; 1.6 mm Thickness)
Elongation at Break	11% (AA; Typical; 12.7 mm Diameter)
Modulus of Elasticity	71.7 GPa
Poisson's Ratio	0.33
Fatigue Strength	159 MPa
Fracture Toughness	20 MPa-m ½; K(IC) in S-L direction
Fracture Toughness	25 MPa-m ½; K(IC) in T-L direction
Fracture Toughness	29 MPa-m ½; K(IC) in L-T direction
Machinability	70%
Shear Modulus	26.9 GPa
Shear Strength	330 MPa

Electrical Properties	**Metric**
Electrical Resistivity	$5.15e^{-006}$ ohm-cm

Thermal Properties	**Metric**
CTE, linear 68°F	23.6 µm/m-°C
CTE, linear 250°C	25.2 µm/m-°C
Heat Capacity	0.96 J/g-°C
Thermal Conductivity	130 W/m-K
Melting Point	477 – 635 °C
Solidus	477 °C
Liquidus	635 °C

Table A.2: Material Properties of P20

Physical Properties	**Metric**
Density	7.85 g/cc

Mechanical Properties	**Metric**
Hardness, Brinell	300
Machinability	80%
Hardness, Rockwell C	30
Tensile Strength, Ultimate	965 – 1030 MPa
Tensile Strength, Yield	827 – 862 MPa
Shear Strength, Yield	785 – 1490 MPa
Elongation at Break	20%
Modulus of Elasticity	205 GPa
Compressive Strength	862 MPa
Charpy Impact	27.1 – 33.9 J

Thermal Properties	**Metric**
CTE, linear 68°F	12.8 µm/m-°C
Melting Point	1427 °C
Specific Heat	460 J/kg°C
Coefficient of Thermal Expansion	29 J/m.s.°C
Thermal Conductivity	29 – 34 W/m-K

Table A.3: Cutting Edge Radius of Carbide Inserts at Each Undeformed Chip Thickness – Cutting Speed of 10 m/min

Undeformed Chip Thickness (μm)	Cutting Edge Radius (μm)
0.3	12.73
0.5	10.00
0.7	10.00
0.9	12.06
1.1	11.18
1.3	13.53
1.5	13.24
1.7	13.24
2	11.18
5	12.70
10	13.72
20	13.72
30	15.49
40	13.72
50	12.47
60	12.70

Table A.4: Cutting Edge Radius of Carbide Inserts at Each Undeformed Chip Thickness – Cutting Speed of 115 m/min

Undeformed Chip Thickness (μm)	Cutting Edge Radius (μm)
0.3	18.64
0.5	16.77
0.7	16.77
0.9	16.47
1.1	17.06
1.3	16.47
1.5	15.88
1.7	13.82
2	14.12
5	13.97
10	14.72
20	18.29
30	11.94
40	15.24
50	12.87
60	16.56

APPENDIX B: EXPERIMENTAL DATA

Table B.1: Average Force Data for all Replications – Cutting Speed of 10 m/min (AL7075)

Undeformed Chip Thickness (nm)	Average F_c (N)	Max F_c (N)	Min F_c (N)	Average F_t (N)	Max F_t (N)	Min F_t (N)
10	0.366	0.378	0.358	0.536	0.559	0.520
40	0.337	0.361	0.321	0.450	0.476	0.433
70	0.471	0.526	0.389	0.585	0.613	0.544
100	0.398	0.613	0.326	0.410	0.702	0.316
400	0.750	0.930	0.664	0.556	0.779	0.426
700	1.467	1.694	1.361	0.900	1.116	0.821
1000	1.932	2.018	1.774	1.051	1.165	0.857
1400	2.672	2.766	2.472	1.453	1.547	1.193
1700	3.006	3.095	2.866	1.460	1.563	1.295
2000	3.348	3.465	3.209	1.466	1.598	1.289

Table B.2: Average Force Data for all Replications – Cutting Speed of 150 m/min (AL7075)

Undeformed Chip Thickness (nm)	Average F_c (N)	Max F_c (N)	Min F_c (N)	Average F_t (N)	Max F_t (N)	Min F_t (N)
10	0.078	0.104	0.057	0.303	0.563	0.116
40	0.155	0.180	0.137	0.429	0.754	0.233
70	0.373	0.426	0.339	0.540	0.789	0.386
100	0.438	0.492	0.391	0.409	0.496	0.357
400	0.813	0.950	0.724	0.589	0.729	0.417
700	1.447	1.765	1.250	0.735	0.964	0.525
1000	1.786	1.936	1.614	0.827	1.029	0.579
1400	2.309	2.470	2.160	0.893	1.038	0.750
1700	2.625	2.704	2.492	0.944	1.018	0.746
2000	3.000	3.074	2.812	0.997	1.070	0.820

Table B.3: Force Data 1st Set– Cutting Speed of 10 m/min (AL7075)

Undeformed Chip Thickness (nm)	Average F_c (N)	Average F_t (N)
10	0.358	0.52
40	0.321	0.433
70	0.526	0.613
100	0.613	0.702
400	0.93	0.779
700	1.694	1.116
1000	2.003	1.102
1400	2.729	1.457
1700	3.027	1.48
2000	3.301	1.395

Table B.4: Force Data 2nd Set– Cutting Speed of 10 m/min (AL7075)

Undeformed Chip Thickness (nm)	Average F_c (N)	Average F_t (N)
10	0.378	0.559
40	0.361	0.476
70	0.389	0.544
100	0.337	0.316
400	0.664	0.485
700	1.361	0.822
1000	1.774	0.857
1400	2.472	1.193
1700	2.866	1.295
2000	3.209	1.289

Table B.5: Force Data 3rd Set– Cutting Speed of 10 m/min (AL7075)

Undeformed Chip Thickness (nm)	Average F_c (N)	Average F_t (N)
10	0.358	0.52
40	0.321	0.433
70	0.526	0.613
100	0.326	0.329
400	0.682	0.426
700	1.422	0.868
1000	1.909	1.05
1400	2.698	1.531
1700	3.095	1.563
2000	3.465	1.598

Table B.6: Force Data 4th Set– Cutting Speed of 10 m/min (AL7075)

Undeformed Chip Thickness (nm)	Average F_c (N)	Average F_t (N)
10	0.378	0.559
40	0.361	0.476
70	0.389	0.544
100	0.342	0.34
400	0.741	0.546
700	1.427	0.873
1000	2.018	1.165
1400	2.766	1.539
1700	3.071	1.501
2000	3.440	1.568

Table B.7: Force Data 5th Set– Cutting Speed of 10 m/min (AL7075)

Undeformed Chip Thickness (nm)	Average F_c (N)	Average F_t (N)
10	0.358	0.520
40	0.321	0.433
70	0.526	0.613
100	0.372	0.361
400	0.734	0.543
700	1.429	0.821
1000	1.958	1.080
1400	2.695	1.547
1700	2.970	1.459
2000	3.327	1.480

Table B.8: Force Data 1st Set– Cutting Speed of 150 m/min (AL7075)

Undeformed Chip Thickness (nm)	Average F_c (N)	Average F_t (N)
10	0.068	0.256
40	0.137	0.380
70	0.360	0.508
100	0.391	0.357
400	0.724	0.417
700	1.250	0.525
1000	1.614	0.579
1400	2.160	0.750
1700	2.492	0.746
2000	2.812	0.820

Table B.9: Force Data 2nd Set– Cutting Speed of 150 m/min (AL7075)

Undeformed Chip Thickness (nm)	Average F_c (N)	Average F_t (N)
10	0.087	0.449
40	0.18	0.754
70	0.393	0.789
100	0.429	0.496
400	0.747	0.539
700	1.343	0.618
1000	1.692	0.689
1400	2.259	0.814
1700	2.635	0.936
2000	3.021	0.979

Table B.10: Force Data 3rd Set– Cutting Speed of 150 m/min (AL7075)

Undeformed Chip Thickness (nm)	Average F_c (N)	Average F_t (N)
10	0.104	0.563
40	0.138	0.535
70	0.346	0.509
100	0.43	0.426
400	0.843	0.664
700	1.478	0.838
1000	1.861	0.946
1400	2.398	0.981
1700	2.704	1.014
2000	3.033	1.054

Table B.11: Force Data 4th Set– Cutting Speed of 150 m/min (AL7075)

Undeformed Chip Thickness (nm)	Average F_c (N)	Average F_t (N)
10	0.076	0.133
40	0.161	0.241
70	0.426	0.510
100	0.492	0.373
400	0.800	0.597
700	1.400	0.732
1000	1.825	0.894
1400	2.260	0.884
1700	2.650	1.007
2000	3.061	1.07

Table B.12: Force Data 5th Set– Cutting Speed of 150 m/min (AL7075)

Undeformed Chip Thickness (nm)	Average F_c (N)	Average F_t (N)
10	0.057	0.116
40	0.160	0.233
70	0.339	0.386
100	0.448	0.392
400	0.950	0.729
700	1.765	0.964
1000	1.936	1.029
1400	2.470	1.038
1700	2.643	1.018
2000	3.074	1.064

Table B.13: Average Force Data for all Replications – Cutting Speed of 10 m/min (AL7075)

Undeformed Chip Thickness (nm)	Average F_c (N)	Max Deviation (%)	Average F_t (N)	Max Deviation (%)
10	0.366	3	0.536	4
40	0.337	7	0.450	6
70	0.471	17	0.585	7
100	0.398	54	0.410	71
400	0.750	24	0.556	40
700	1.467	16	0.900	24
1000	1.932	8	1.051	18
1400	2.672	7	1.453	18
1700	3.006	5	1.460	11
2000	3.348	4	1.466	12

Table B.14: Average Force Data for all Replications – Cutting Speed of 150 m/min (AL7075)

Undeformed Chip Thickness (nm)	Average F_c (N)	Max Deviation (%)	Average F_t (N)	Max Deviation (%)
10	0.078	33	0.303	86
40	0.155	16	0.429	76
70	0.373	14	0.540	46
100	0.438	12	0.409	21
400	0.813	17	0.589	29
700	1.447	22	0.735	31
1000	1.786	10	0.827	30
1400	2.309	7	0.893	16
1700	2.625	5	0.944	21
2000	3.000	6	0.997	18

Table B.15: Specific Cutting and Thrust Energy – Cutting Speed of 10 m/min (AL7075)

Undeformed Chip Thickness (nm)	Specific Cutting Energy (GPa)	Specific Thrust Energy (GPa)
10	36.6	53.6
40	8.4	11.3
70	6.7	8.4
100	4.0	4.1
400	1.9	1.4
700	2.1	1.3
1000	1.9	1.1
1400	1.9	1.0
1700	1.8	0.9
2000	1.7	0.7

Table B.16: Specific Cutting and Thrust Energy – Cutting Speed of 150 m/min (AL7075)

Undeformed Chip Thickness (nm)	Specific Cutting Energy (GPa)	Specific Thrust Energy (GPa)
10	7.8	30.3
40	3.9	10.7
70	5.3	7.7
100	4.4	4.1
400	2.0	1.5
700	2.1	1.1
1000	1.8	0.8
1400	1.6	0.6
1700	1.5	0.6
2000	1.5	0.5

Table B.17: Deformed Chip Thickness Measurement – Cutting Speed of 10 m/min (AL7075)

Undeformed Chip Thickness (nm)	Average Deformed Chip Thickness (nm)	Max Deformed Chip Thickness (nm)	Min Deformed Chip Thickness (nm)	σ (nm)
10	455	555	333	82
40	605	666	512	56
70	568	625	531	34
100				
400	1212	1312	1125	71
700	1222	1500	1111	162
1000	1485	1587	1396	72
1400	2666	2833	2555	111
1700	4632	4840	4560	121
2000	12851	12970	12673	129

Table B.18: Deformed Chip Thickness Measurement – Cutting Speed of 150 m/min (AL7075)

Undeformed Chip Thickness (nm)	Average Deformed Chip Thickness (nm)	Max Deformed Chip Thickness (nm)	Min Deformed Chip Thickness (nm)	σ (nm)
10				
40				
70				
100	639	721	618	46
400				
700	1887	2040	1734	153
1000	2232	2320	2160	71
1400	2253	2278	2215	34
1700	2855	2965	2724	122
2000	3670	3797	3544	89

Table B.19: Surface Roughness Measurement – Cutting Speed of 10 m/min (AL7075)

Undeformed Chip Thickness (nm)	S_q (nm)	σ (nm)	S_a (nm)	σ (nm)
40	82.2	31.6	26.8	4.5
400	48.8	5.0	26.0	1.9
1400	71.8	8.1	37.0	1.7
2000	86.6	23.5	34.4	3.7

Table B.20: Surface Roughness Measurement – Cutting Speed of 150 m/min (AL7075)

Undeformed Chip Thickness (nm)	S_q (nm)	σ (nm)	S_a (nm)	σ (nm)
40	77.2	12.9	42.0	16.8
400	67.2	13.2	32.6	7.5
1400	73.0	27.6	33.6	5.7
2000	74.6	15.2	37.4	8.4

Table B.21: Friction Coefficient – Cutting Speed of 10 m/min (AL7075)

Undeformed Chip Thickness (nm)	Friction Coefficient
70	1.242
100	1.029
400	0.741
700	0.614
1000	0.544
1400	0.544
1700	0.486
2000	0.438

Table B.22: Friction Coefficient – Cutting Speed of 150 m/min (AL7075)

Undeformed Chip Thickness (nm)	Friction Coefficient
70	1.450
100	0.933
400	0.725
700	0.508
1000	0.463
1400	0.387
1700	0.360
2000	0.332

Table B.23: Average Force Data for all Replications – Cutting Speed of 10 m/min (P20)

Undeformed Chip Thickness (µm)	Average F_c (N)	Max F_c (N)	Min F_c (N)	Average F_t (N)	Max F_t (N)	Min F_t (N)
0.3	5.81	6.43	5.40	5.71	6.39	5.33
0.5	6.12	6.19	6.06	4.75	4.86	4.71
0.7	6.89	7.12	6.56	4.83	5.11	4.45
0.9	8.08	8.43	7.63	5.36	5.71	4.91
1.1	9.35	9.95	8.83	6.01	6.50	5.47
1.3	10.38	11.01	9.37	6.53	7.13	5.77
1.5	11.78	12.30	11.35	7.31	7.84	6.85
1.7	12.57	13.03	11.44	7.80	8.25	7.15
2	14.25	14.65	13.90	8.74	8.90	8.50
5	30.06	30.98	28.85	15.34	18.71	12.37
10	47.69	55.30	43.51	21.98	26.51	18.24
20	94.14	103.53	80.38	42.83	47.07	37.66
30	131.61	143.78	122.67	57.72	61.15	51.43
40	167.29	203.19	133.09	73.17	90.58	54.63
50	216.90	252.77	192.63	96.47	113.46	76.72
60	253.75	281.87	225.33	111.08	122.40	88.36

Table B.24: Average Force Data for all Replications – Cutting Speed of 115 m/min (P20)

Undeformed Chip Thickness (μm)	Average F_c (N)	Max F_c (N)	Min F_c (N)	Average F_t (N)	Max F_t (N)	Min F_t (N)
0.3	4.03	4.17	3.89	3.11	3.29	3.00
0.5	5.55	5.85	5.45	4.03	4.42	3.88
0.7	6.92	7.29	6.50	4.95	5.35	4.58
0.9	7.99	8.22	7.65	5.67	5.87	5.35
1.1	8.98	9.52	8.46	6.25	6.81	5.76
1.3	9.93	10.53	9.37	6.83	7.49	6.34
1.5	10.96	11.68	10.07	7.49	8.26	6.64
1.7	11.80	12.65	10.97	7.94	8.65	7.12
2	12.86	13.68	12.03	8.47	9.07	7.60
5	27.24	28.63	25.62	18.17	19.42	15.33
10	46.12	51.03	40.94	34.13	36.05	30.98
20	75.97	83.46	69.81	52.20	54.87	47.98
30	99.64	104.00	96.57	67.09	70.56	63.18
40	126.06	138.01	117.69	83.19	87.76	77.29
50	163.65	175.81	153.64	131.13	143.79	113.24
60	189.53	203.80	175.32	149.99	157.55	136.54

Table B.25: Force Data 1st Set– Cutting Speed of 10 m/min (P20)

Undeformed Chip Thickness (μm)	Average F_c (N)	Average F_t (N)
0.3	6.433	6.387
0.5	6.104	4.709
0.7	6.773	4.655
0.9	7.878	5.015
1.1	8.834	5.467
1.3	9.365	5.771
1.5	11.611	6.911
1.7	12.462	7.506
2	14.213	8.5
5	29.67	16.93
10	49.71	22.95
20	90.03	40.12
30	134.74	61.15
40	164.40	74.58
50	252.77	113.46
60	281.87	122.40

Table B.26: Force Data 2nd Set– Cutting Speed of 10 m/min (P20)

Undeformed Chip Thickness (μm)	Average F_c (N)	Average F_t (N)
0.3	5.397	5.430
0.5	6.107	4.737
0.7	6.863	4.839
0.9	8.032	5.454
1.1	9.949	6.503
1.3	10.255	6.359
1.5	11.402	7.130
1.7	11.443	7.149
2	14.650	8.900
5	30.620	18.710
10	55.300	26.510
20	103.530	47.070
30	125.760	57.310
40	184.850	81.920
50	210.670	92.640
60	241.430	108.320

Table B.27: Force Data 3rd Set– Cutting Speed of 10 m/min (P20)

Undeformed Chip Thickness (μm)	Average F_c (N)	Average F_t (N)
0.3	5.884	5.787
0.5	6.188	4.856
0.7	7.114	5.103
0.9	8.430	5.706
1.1	9.553	6.264
1.3	11.002	7.125
1.5	12.224	7.807
1.7	13.008	8.239
2	13.915	8.726
5	30.180	13.770
10	44.080	18.240
20	94.290	43.740
30	143.780	60.410
40	203.190	90.580
50	229.220	103.330
60	259.980	121.070

Table B.28: Force Data 4th Set– Cutting Speed of 10 m/min (P20)

Undeformed Chip Thickness (μm)	Average F_c (N)	Average F_t (N)
0.3	5.406	5.328
0.5	6.058	4.722
0.7	7.123	5.110
0.9	8.434	5.709
1.1	9.578	6.282
1.3	11.005	7.127
1.5	12.297	7.840
1.7	13.025	8.251
2	13.896	8.712
5	28.850	12.370
10	43.510	20.500
20	80.380	37.660
30	122.670	51.430
40	133.090	54.630
50	199.220	96.220
60	260.150	115.260

Table B.29: Force Data 5th Set– Cutting Speed of 10 m/min (P20)

Undeformed Chip Thickness (μm)	Average F_c (N)	Average F_t (N)
0.3	5.929	5.624
0.5	6.161	4.733
0.7	6.564	4.453
0.9	7.628	4.909
1.1	8.843	5.544
1.3	10.271	6.258
1.5	11.346	6.850
1.7	12.914	7.841
2	14.565	8.873
5	30.980	14.900
10	45.860	21.680
20	102.470	45.540
30	131.080	58.320
40	150.920	64.160
50	192.630	76.720
60	225.330	88.360

Table B.30: Force Data 1st Set– Cutting Speed of 115 m/min (P20)

Undeformed Chip Thickness (μm)	Average F_c (N)	Average F_t (N)
0.3	4.168	3.288
0.5	5.493	4.007
0.7	6.921	5.011
0.9	7.922	5.758
1.1	8.770	6.129
1.3	9.374	6.343
1.5	10.069	6.638
1.7	10.969	7.118
2	12.032	7.604
5	26.130	19.420
10	47.120	35.620
20	76.700	53.760
30	100.320	70.560
40	121.890	87.760
50	170.070	137.380
60	188.000	156.300

Table B.31: Force Data 2nd Set– Cutting Speed of 115 m/min (P20)

Undeformed Chip Thickness (μm)	Average F_c (N)	Average F_t (N)
0.3	3.977	3.000
0.5	5.494	3.952
0.7	6.497	4.581
0.9	7.645	5.347
1.1	8.455	5.760
1.3	9.618	6.550
1.5	10.869	7.445
1.7	11.084	7.400
2	12.230	7.877
5	28.630	18.900
10	45.330	30.980
20	75.460	51.850
30	99.250	64.420
40	132.230	80.600
50	153.640	125.990
60	192.420	149.090

Table B.32: Force Data 3rd Set– Cutting Speed of 115 m/min (P20)

Undeformed Chip Thickness (μm)	Average F_c (N)	Average F_t (N)
0.3	4.049	3.118
0.5	5.453	3.890
0.7	7.215	5.138
0.9	8.190	5.776
1.1	9.111	6.338
1.3	10.063	6.890
1.5	11.102	7.589
1.7	12.649	8.647
2	12.932	8.730
5	28.440	18.260
10	51.030	35.290
20	83.460	54.870
30	104.000	69.960
40	138.010	87.360
50	175.810	143.790
60	203.800	157.550

Table B.33: Force Data 4th Set– Cutting Speed of 115 m/min (P20)

Undeformed Chip Thickness (μm)	Average F_c (N)	Average F_t (N)
0.3	4.049	3.118
0.5	5.445	3.884
0.7	6.692	4.678
0.9	7.994	5.598
1.1	9.021	6.238
1.3	10.051	6.881
1.5	11.053	7.529
1.7	12.223	8.234
2	13.675	9.060
5	25.620	15.330
10	46.170	36.050
20	74.420	52.530
30	96.570	63.180
40	117.690	77.290
50	156.550	135.260
60	175.320	150.490

Table B.34: Force Data 5th Set– Cutting Speed of 115 m/min (P20)

Undeformed Chip Thickness (μm)	Average F_c (N)	Average F_t (N)
0.3	3.893	3.040
0.5	5.849	4.419
0.7	7.293	5.345
0.9	8.220	5.868
1.1	9.523	6.808
1.3	10.527	7.494
1.5	11.682	8.259
1.7	12.072	8.295
2	13.406	9.072
5	27.400	18.930
10	40.940	32.690
20	69.810	47.980
30	98.070	67.350
40	120.490	82.950
50	162.180	113.240
60	188.110	136.540

Table B.35: Average Force Data for all Replications – Cutting Speed of 10 m/min (P20)

Undeformed Chip Thickness (μm)	Average F_c (N)	Max Deviation (%)	Average F_t (N)	Max Deviation (%)
0.3	5.81	11	5.71	12
0.5	6.12	1	4.75	2
0.7	6.89	5	4.83	8
0.9	8.08	6	5.36	8
1.1	9.35	6	6.01	9
1.3	10.38	10	6.53	12
1.5	11.78	4	7.31	7
1.7	12.57	9	7.80	8
2	14.25	3	8.74	3
5	30.06	4	15.34	22
10	47.69	16	21.98	21
20	94.14	15	42.83	12
30	131.61	9	57.72	11
40	167.29	21	73.17	25
50	216.90	17	96.47	20
60	253.75	11	111.08	20

Table B.36: Average Force Data for all Replications - Cutting Speed of 115 m/min (P20)

Undeformed Chip Thickness (μm)	Average F_c (N)	Max Deviation (%)	Average F_t (N)	Max Deviation (%)
0.3	4.03	3	3.11	6
0.5	5.55	5	4.03	10
0.7	6.92	6	4.95	8
0.9	7.99	4	5.67	6
1.1	8.98	6	6.25	9
1.3	9.93	6	6.83	10
1.5	10.96	8	7.49	11
1.7	11.80	7	7.94	10
2	12.86	6	8.47	10
5	27.24	6	18.17	16
10	46.12	11	34.13	9
20	75.97	10	52.20	8
30	99.64	4	67.09	6
40	126.06	9	83.19	7
50	163.65	7	131.13	14
60	189.53	8	149.99	9

Table B.37: Specific Cutting and Thrust Energy – Cutting Speed of 10 m/min (P20)

Undeformed Chip Thickness (μm)	Specific Cutting Energy (GPa)	Specific Thrust Energy (GPa)
0.3	19.4	19.0
0.5	12.2	9.5
0.7	9.8	6.9
0.9	9.0	6.0
1.1	8.5	5.5
1.3	8.0	5.0
1.5	7.9	4.9
1.7	7.4	4.6
2	7.1	4.4
5	6.0	3.1
10	4.8	2.2
20	4.7	2.1
30	4.4	1.9
40	4.2	1.8
50	4.3	1.9
60	4.2	1.9

Table B.38: Specific Cutting and Thrust Energy – Cutting Speed of 115m/min (P20)

Undeformed Chip Thickness (μm)	Specific Cutting Energy (GPa)	Specific Thrust Energy (GPa)
0.3	13.4	10.4
0.5	11.1	8.1
0.7	9.9	7.1
0.9	8.9	6.3
1.1	8.2	5.7
1.3	7.6	5.3
1.5	7.3	5.0
1.7	6.9	4.7
2	6.4	4.2
5	5.4	3.6
10	4.6	3.4
20	3.8	2.6
30	3.3	2.2
40	3.2	2.1
50	3.3	2.6
60	3.2	2.5

Table B.39: Deformed Chip Thickness Measurement – Cutting Speed of 10 m/min (P20)

Undeformed Chip Thickness (μm)	Average Deformed Chip Thickness (μm)	Max Deformed Chip Thickness (μm)	Min Deformed Chip Thickness (μm)	σ (μm)
5	5.7	7.0	4.5	1.0
10	11.9	13.8	9.3	1.8
20	54.9	66.7	47.8	7.7
30	54.4	70.0	46.7	9.3
40	106.8	116.8	86.5	13.1
50	149.2	177.3	122.2	21.7
60	65.5	70.7	60.0	4.9

Table B.40: Deformed Chip Thickness Measurement – Cutting Speed of 115 m/min (P20)

Undeformed Chip Thickness (μm)	Average Deformed Chip Thickness (μm)	Max Deformed Chip Thickness (μm)	Min Deformed Chip Thickness (μm)	σ (μm)
5	17.6	18.0	17.0	0.5
10	21.4	24.6	18.6	2.2
20	21.2	24.1	17.8	2.5
30	58.2	65.0	48.6	6.5
40	66.6	77.8	59.5	7.5
50	102.7	111.4	87.6	9.8
60	104.4	105.9	102.7	1.6

Table B.41: Surface Roughness Measurement – Cutting Speed of 10 m/min (P20)

Undeformed Chip Thickness (μm)	S_q (μm)	σ (μm)	S_a (μm)	σ (μm)
0.5	1.29	0.09	0.99	0.08
1.1	1.07	0.22	0.86	0.15
2	1.21	0.12	0.96	0.08
10	1.91	0.24	1.51	0.18
20	3.20	0.86	2.61	0.73
40	6.48		5.33	

Table B.42: Surface Roughness Measurement – Cutting Speed of 115 m/min (P20)

Undeformed Chip Thickness (μm)	S_q (μm)	σ (μm)	S_a (μm)	σ (μm)
0.5	1.18	0.07	0.95	0.06
1.1	1.30	0.09	1.04	0.06
2	1.09	0.06	0.86	0.06
10	0.68	0.04	0.50	0.03
20	0.71	0.04	0.56	0.05
40	1.03	0.05	0.83	0.05
60	1.38	0.13	1.07	0.14

Table B.43: Friction Coefficient – Cutting Speed of 10 m/min (P20)

Undeformed Chip Thickness (μm)	Friction Coefficient
1.1	0.16
2	0.56
10	0.55
20	0.55
40	0.55
60	0.55

Table B.44: Friction Coefficient – Cutting Speed of 115 m/min (P20)

Undeformed Chip Thickness (μm)	Friction Coefficient
1.1	0.321
2	0.824
10	0.808
20	0.793
40	0.956
60	0.944

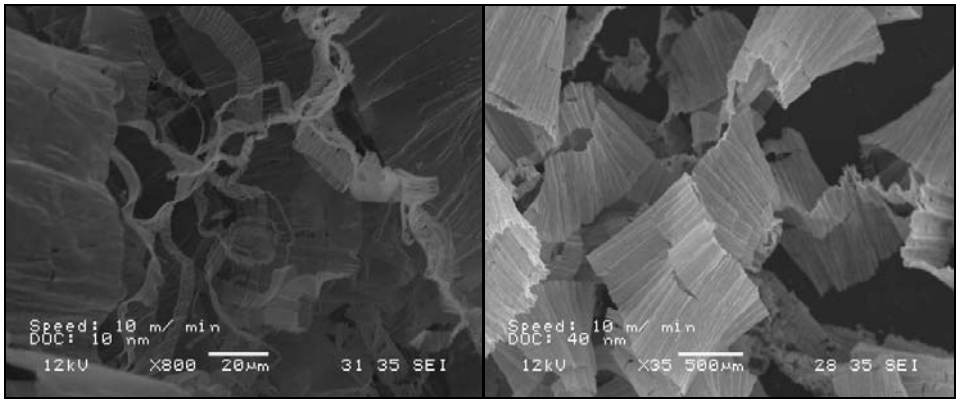

(a) (b)

Figure B.1: AL7075 Chip Chart at Cutting Speed of 10 m/min. Undeformed Chip Thickness: (a) 10 nm (b) 40 nm (c) 70 nm (d) 100 nm (e) 400 nm (f) 700 nm (g) 1000 nm (h) 1400 nm (i) 1700 nm (j) 2000 nm

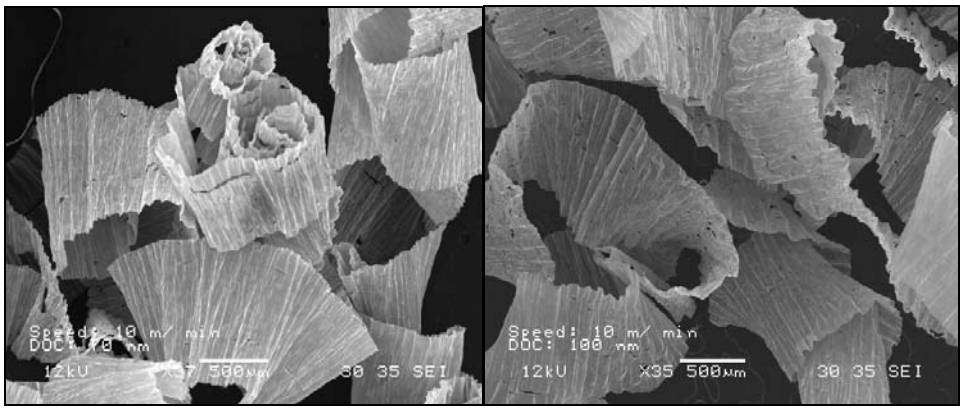

(c) (d)

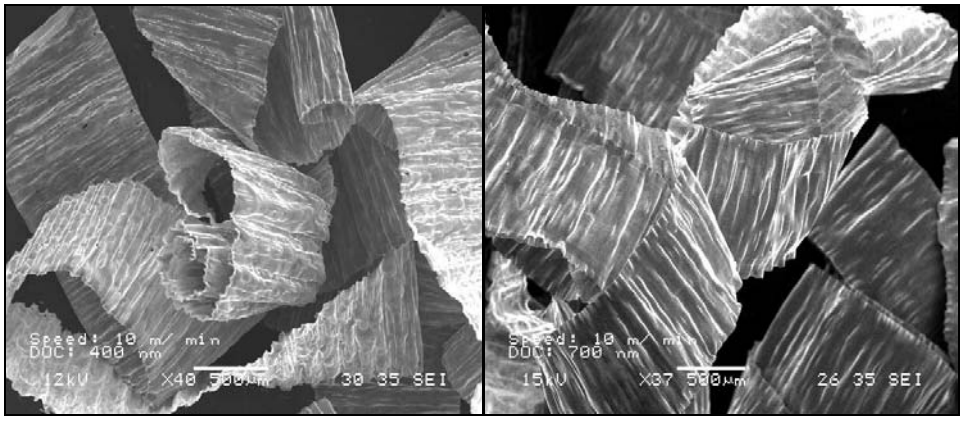

(e) (f)

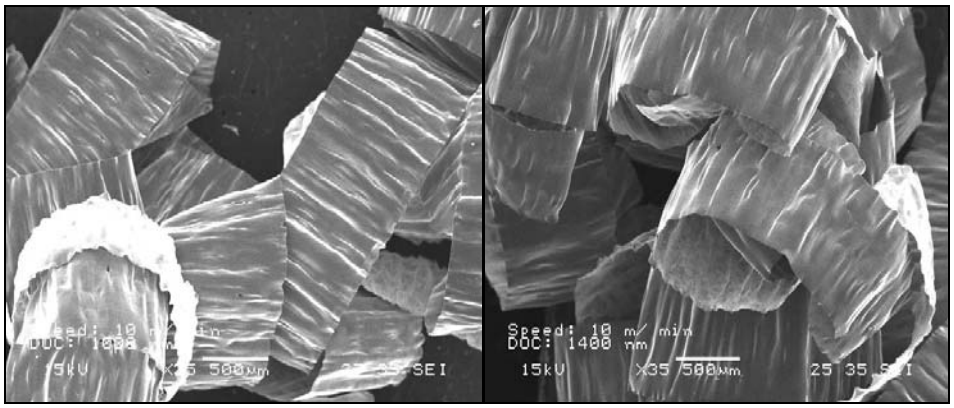

(g) (h)

Figure B.1 (continued)

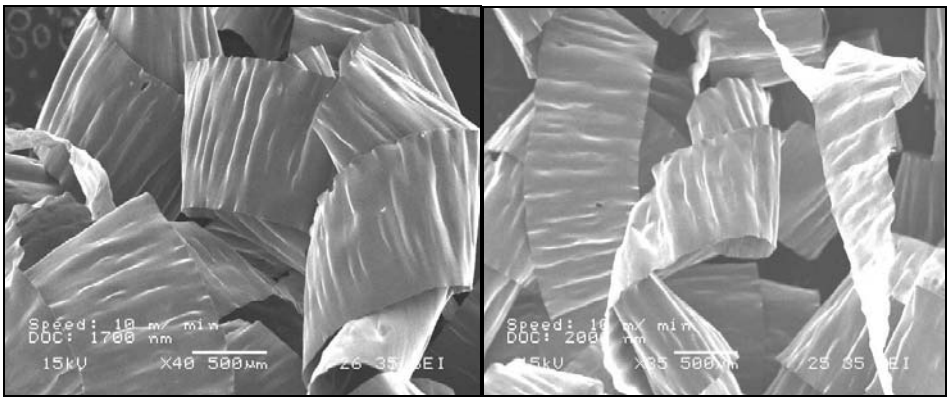

(i) (j)

Figure B.1 (continued)

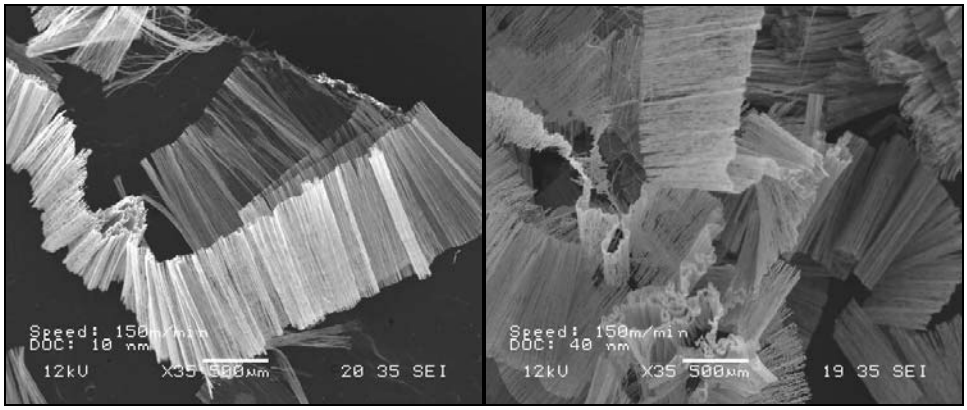

(a) (b)

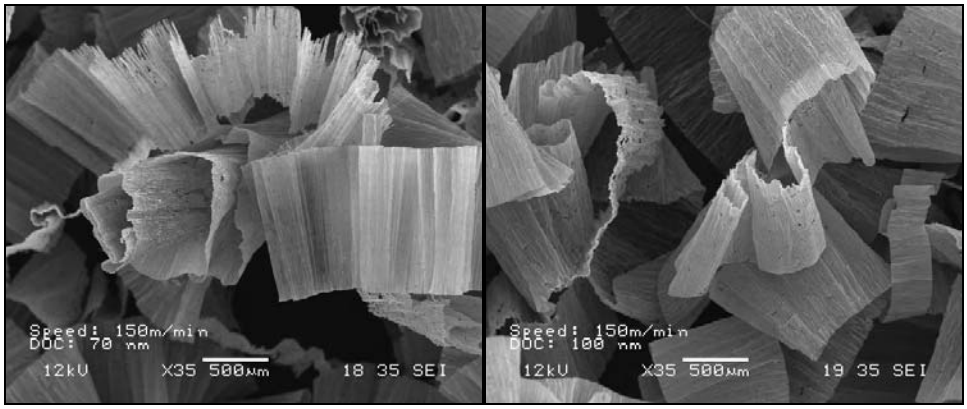

(c) (d)

Figure B.2: AL7075 Chip Chart at Cutting Speed of 150 m/min. Undeformed Chip Thickness: (a) 10 nm (b) 40 nm (c) 70 nm (d) 100 nm (e) 400 nm (f) 700 nm (g) 1000 nm (h) 1400 nm (i) 1700 nm (j) 2000 nm

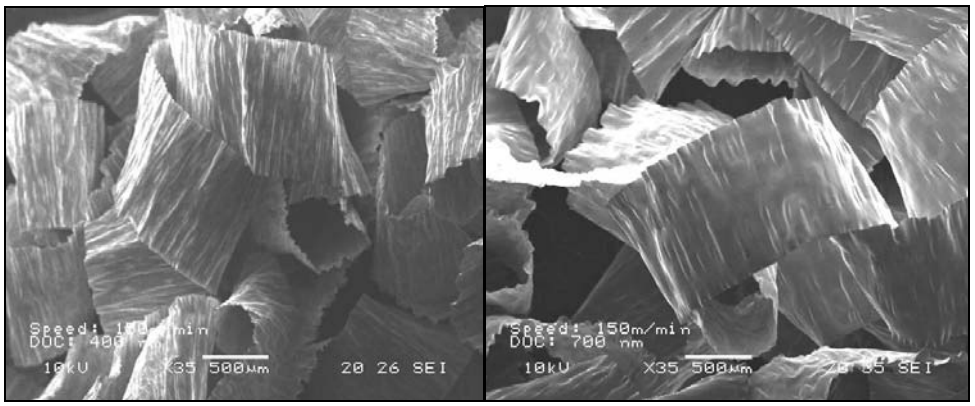

(e) (f)

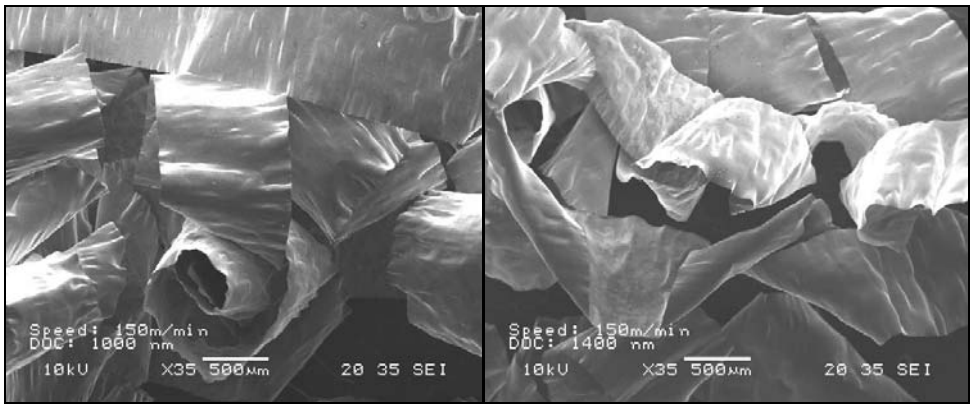

(g) (h)

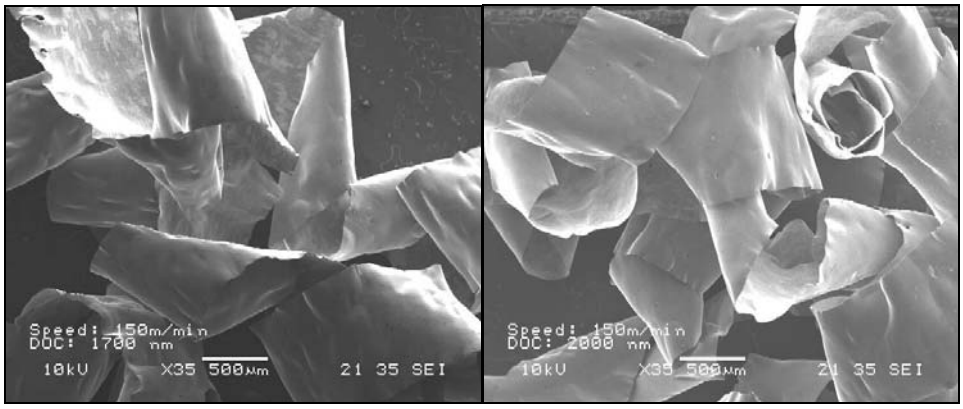

(i) (j)

Figure B.2 (continued)

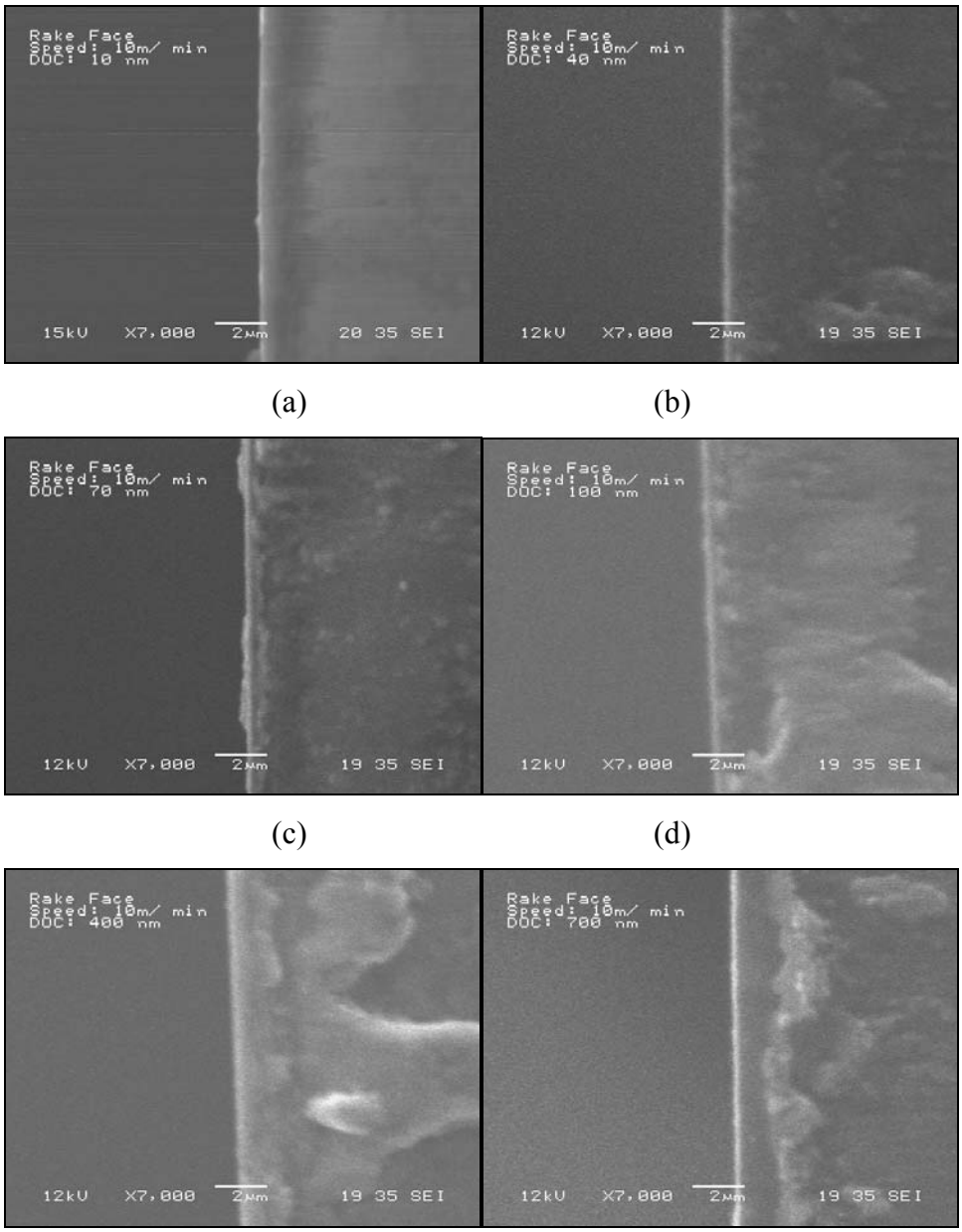

Figure B.3: SEM Image of the Rake Face of Diamond Cutting Tool at Cutting Speed of 10 m/min. Undeformed Chip Thickness: (a) 10 nm (b) 40 nm (c) 70 nm (d) 100 nm (e) 400 nm (f) 700 nm (g) 1000 nm (h) 1400 nm (i) 1700 nm (j) 2000 nm

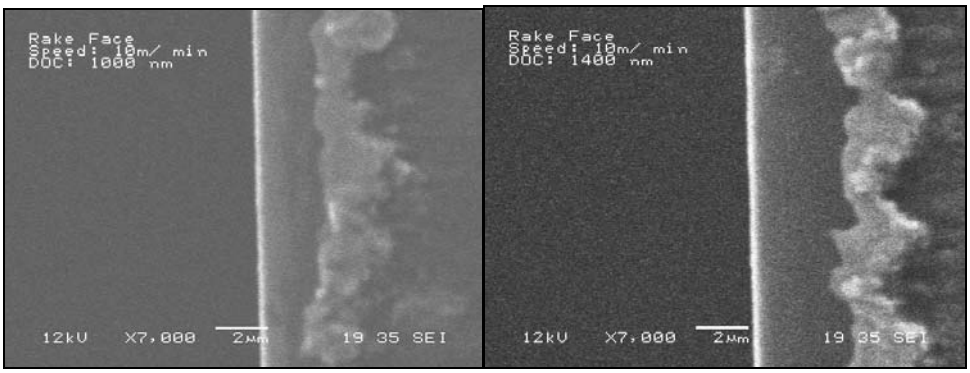

(g) (h)

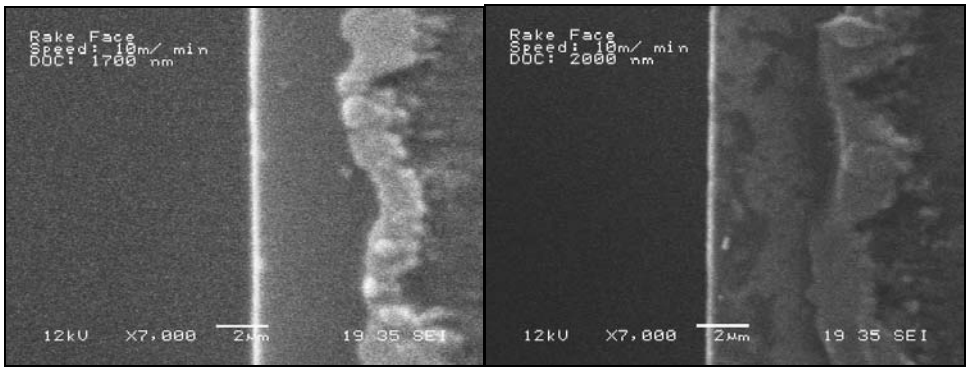

(i) (j)

Figure B.3 (continued)

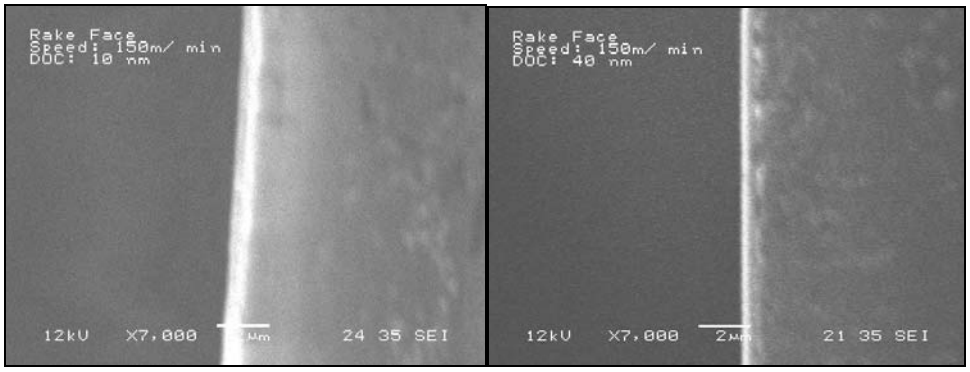

(a) (b)

Figure B.4: SEM Image of the Rake Face of Diamond Cutting Tool at Cutting Speed of 150 m/min. Undeformed Chip Thickness: (a) 10 nm (b) 40 nm (c) 70 nm (d) 100 nm (e) 400 nm (f) 700 nm (g) 1000 nm (h) 1400 nm (i) 1700 nm (j) 2000 nm

(c) (d)

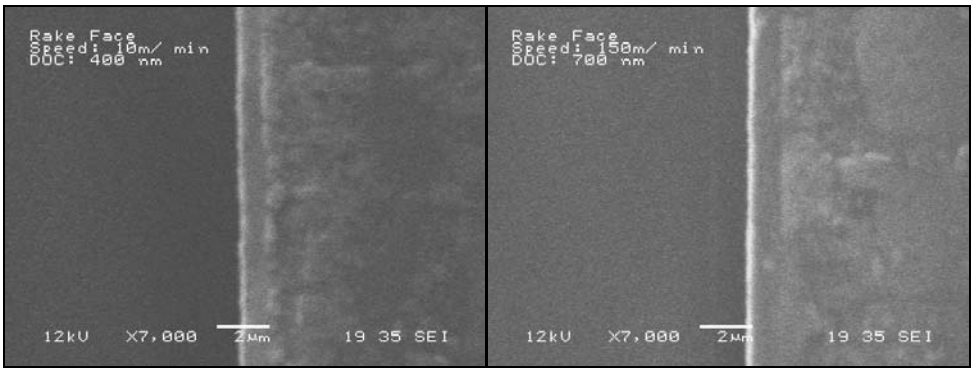

(e) (f)

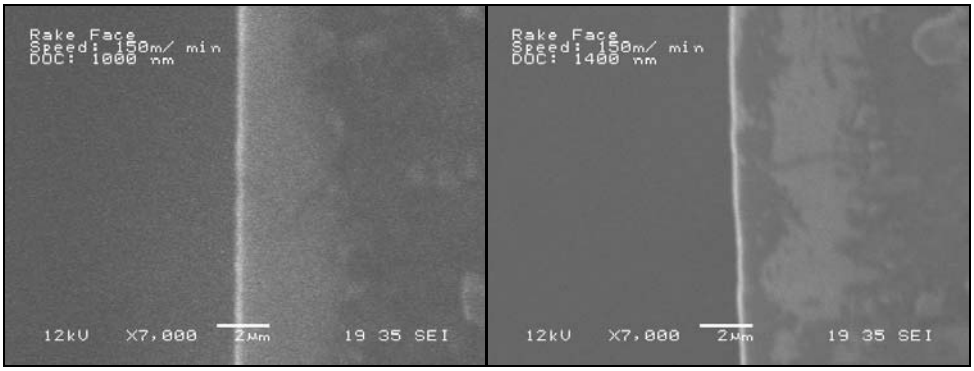

(g) (h)

Figure B.4 (continued)

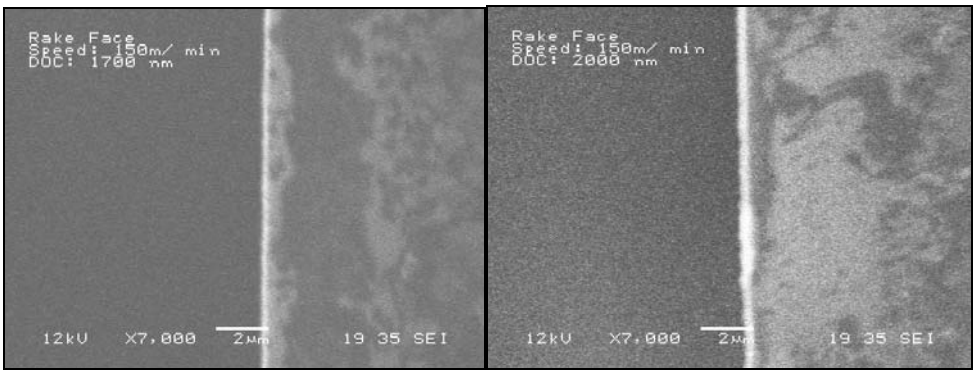

(i) (j)

Figure B.4 (continued)

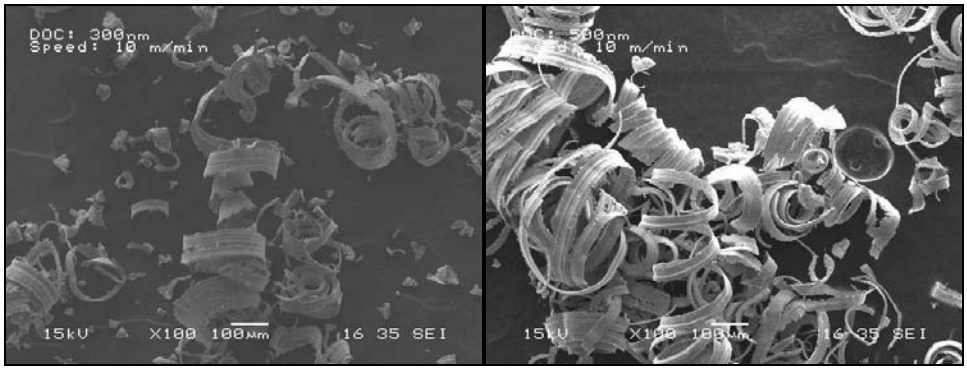

(a) (b)

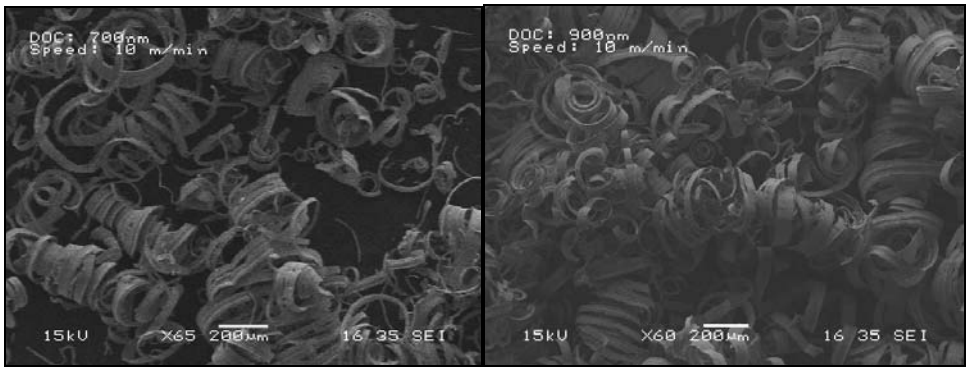

(c) (d)

Figure B.5: P20 Chip Chart at Cutting Speed of 10 m/min. Undeformed Chip Thickness: (a) 0.3 µm (b) 0.5 µm (c) 0.7 µm (d) 0.9 µm (e) 1.1 µm (f) 1.3 µm (g) 1.5 µm (h) 1.7 µm (i) 2 µm (j) 5 µm (k) 10 µm (l) 20 µm (m) 30 µm (n) 40 µm (o) 50 µm (p) 60 µm

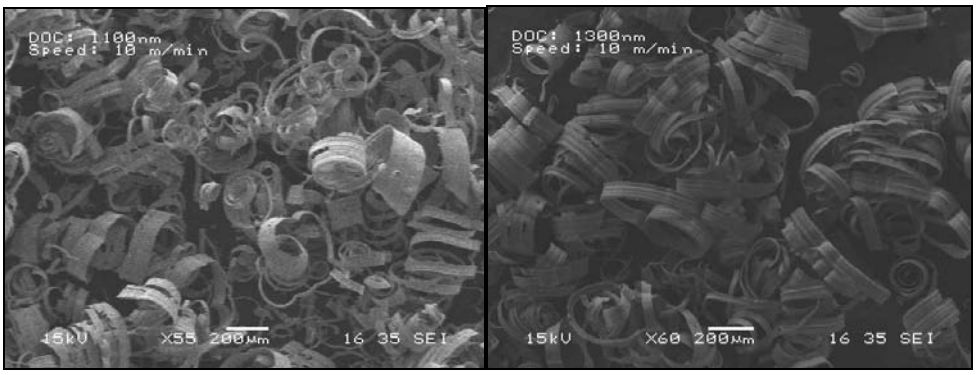

(e) (f)

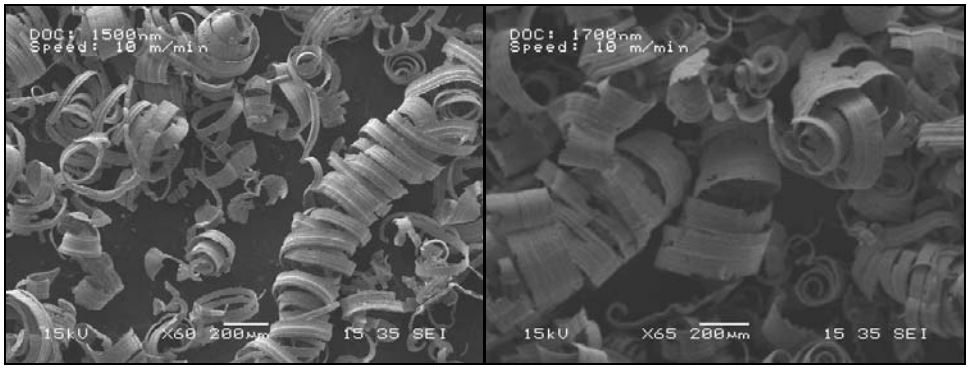

(g) (h)

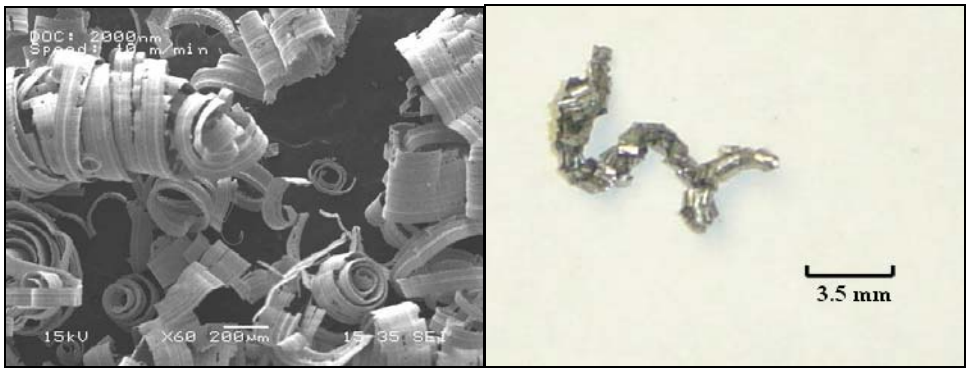

(i) (j)

Figure B.5 (continued)

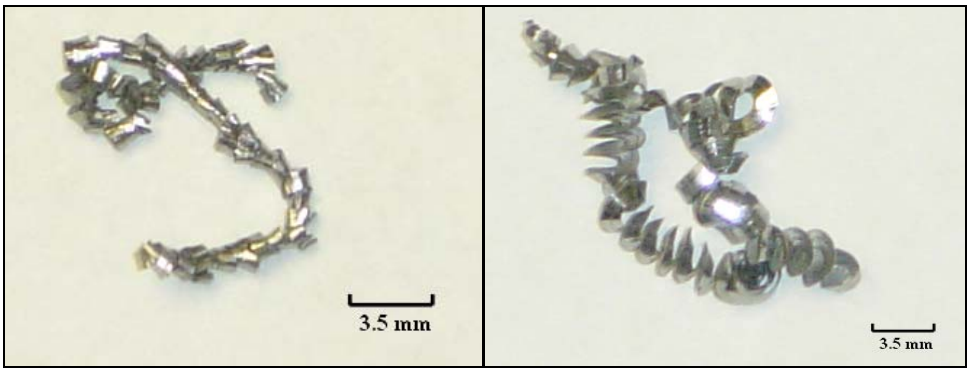

(k) (l)

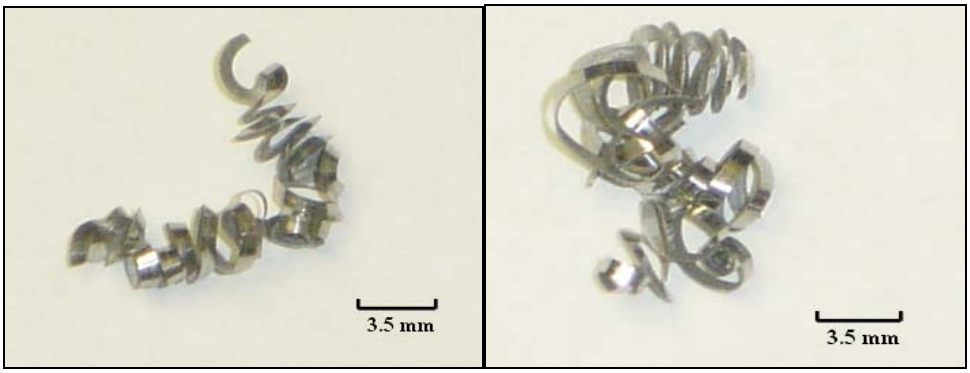

(m) (n)

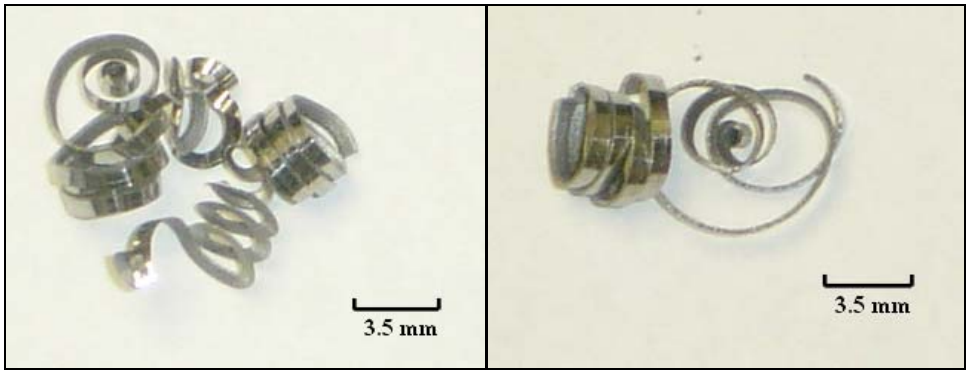

(o) (p)

Figure B.5 (continued)

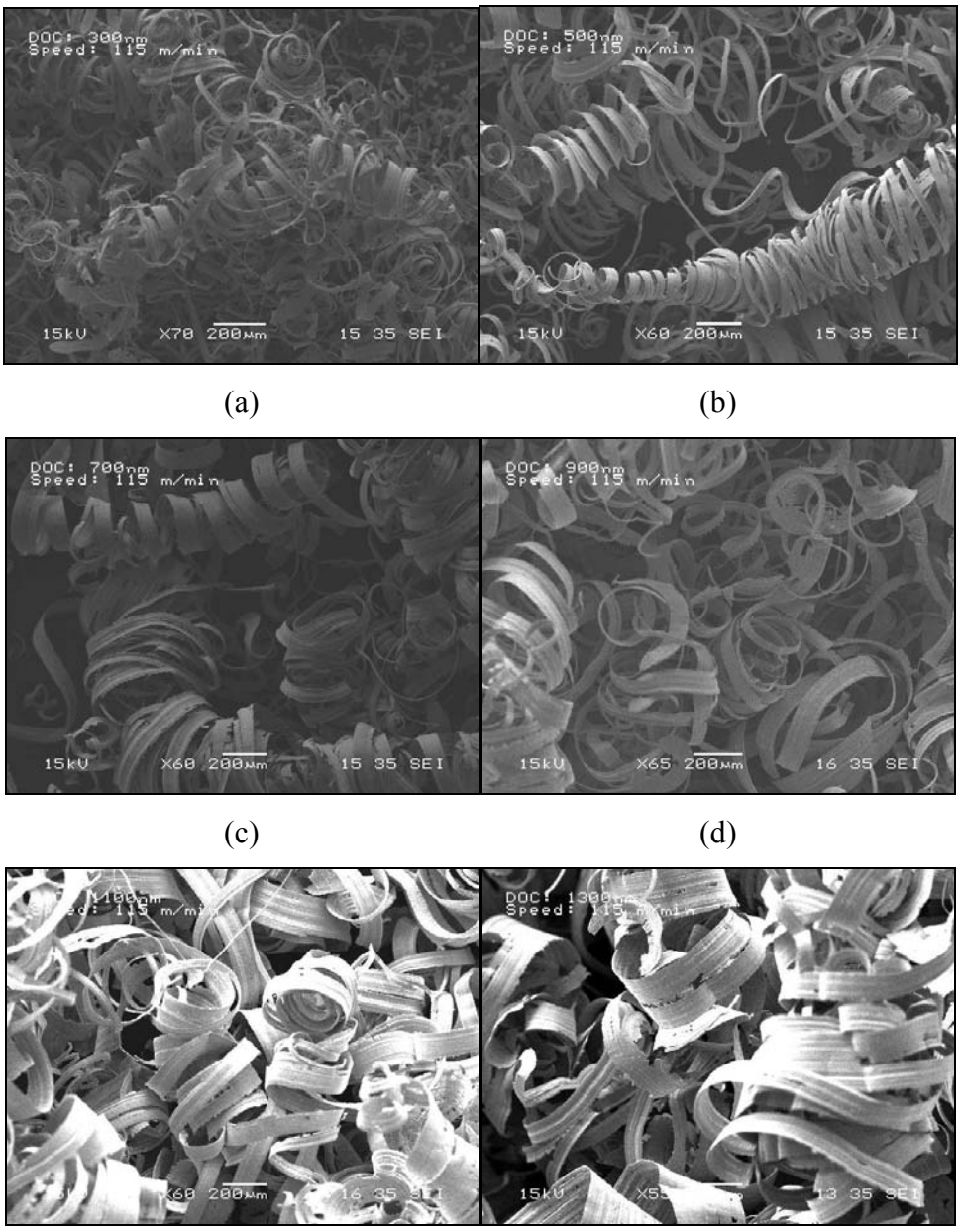

Figure B.6: P20 Chip Chart at Cutting Speed of 115 m/min. Undeformed Chip Thickness: (a) 0.3 µm (b) 0.5 µm (c) 0.7 µm (d) 0.9 µm (e) 1.1 µm (f) 1.3 µm (g) 1.5 µm (h) 1.7 µm (i) 2 µm (j) 5 µm (k) 10 µm (l) 20 µm (m) 30 µm (n) 40 µm (o) 50 µm (p) 60 µm

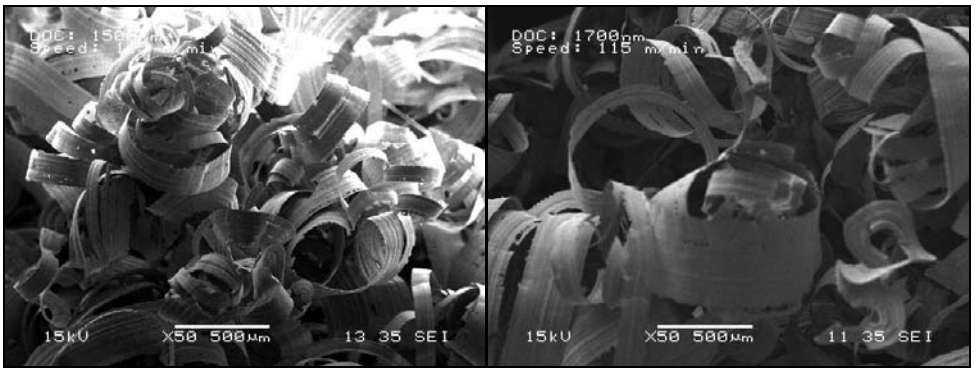

(g) (h)

(i) (j)

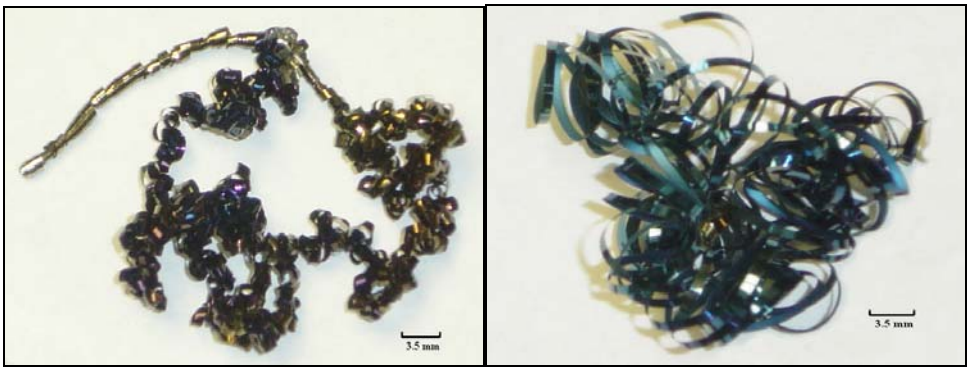

(k) (l)

Figure B.6 (continued)

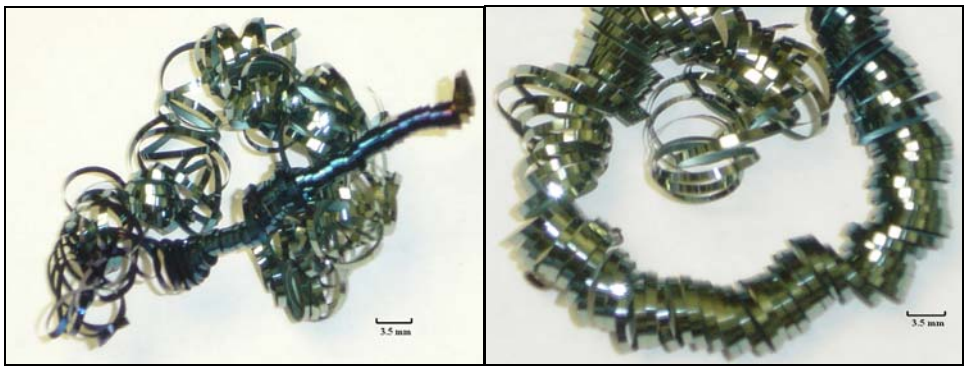

(m) (n)

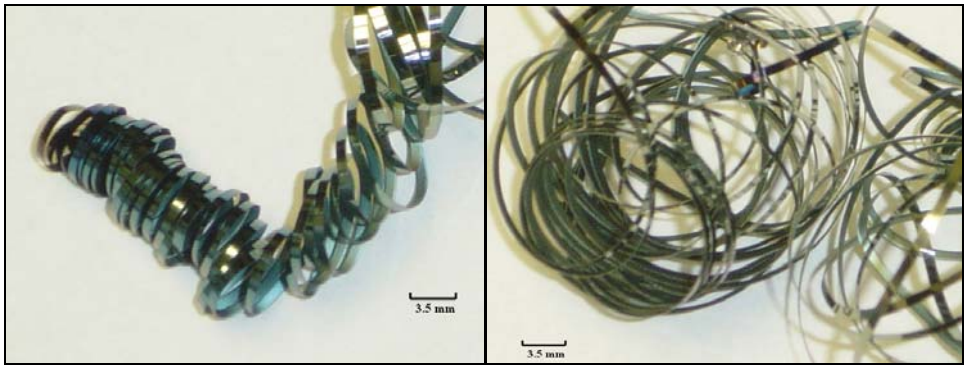

(o) (p)

Figure B.6 (continued)

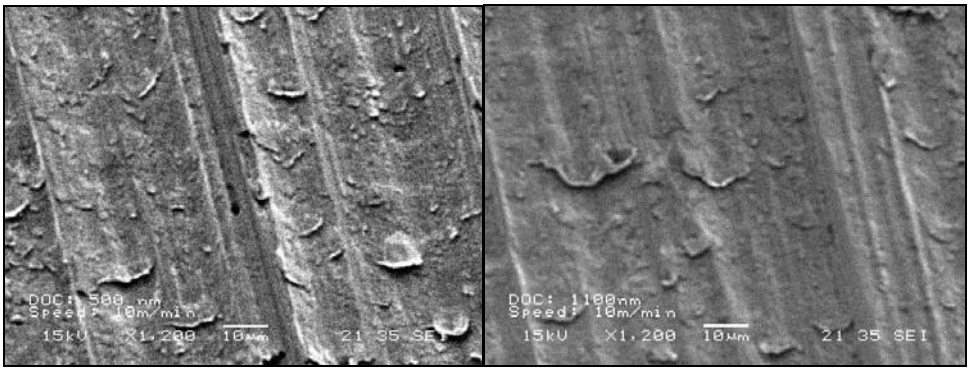

(a) (b)

Figure B.7: Effects of Undeformed Chip Thickness on Surface Roughness at Cutting Speed of 10 m/min. Undeformed Chip Thickness: (a) 0.5 µm (b) 1.1 µm (c) 2.0 µm (d) 10 µm (e) 20 µm (f) 40 µm (g) 60 µm

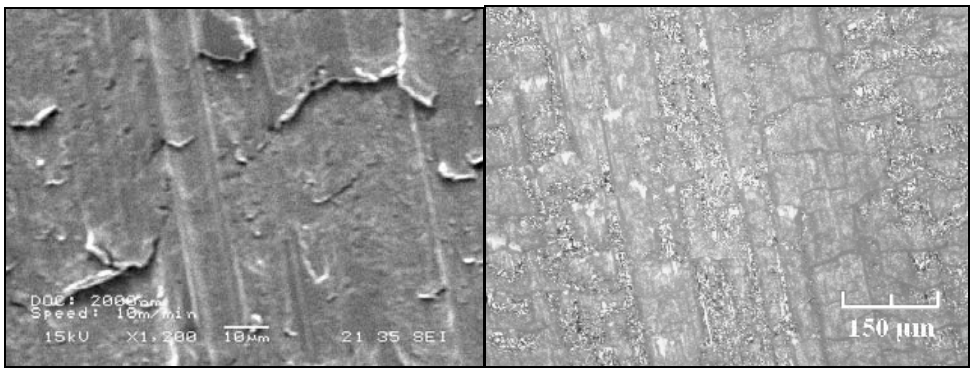

(c) (d)

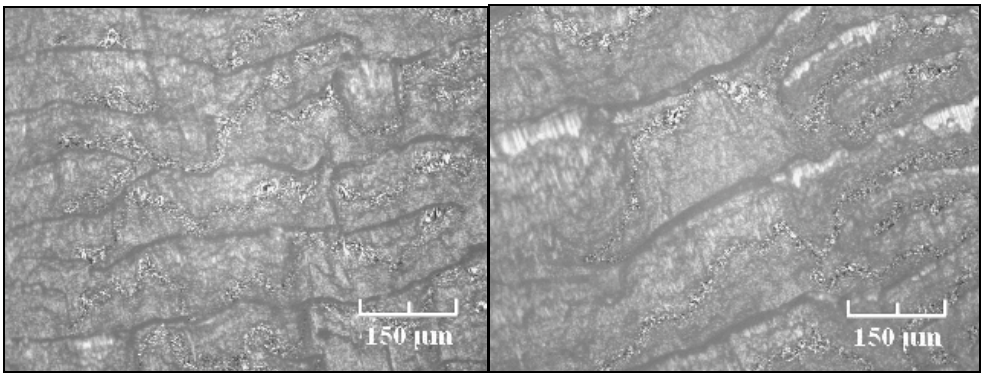

(e) (f)

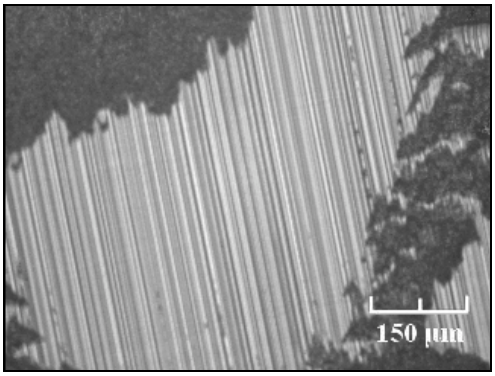

(g)

Figure B.7 (continued)

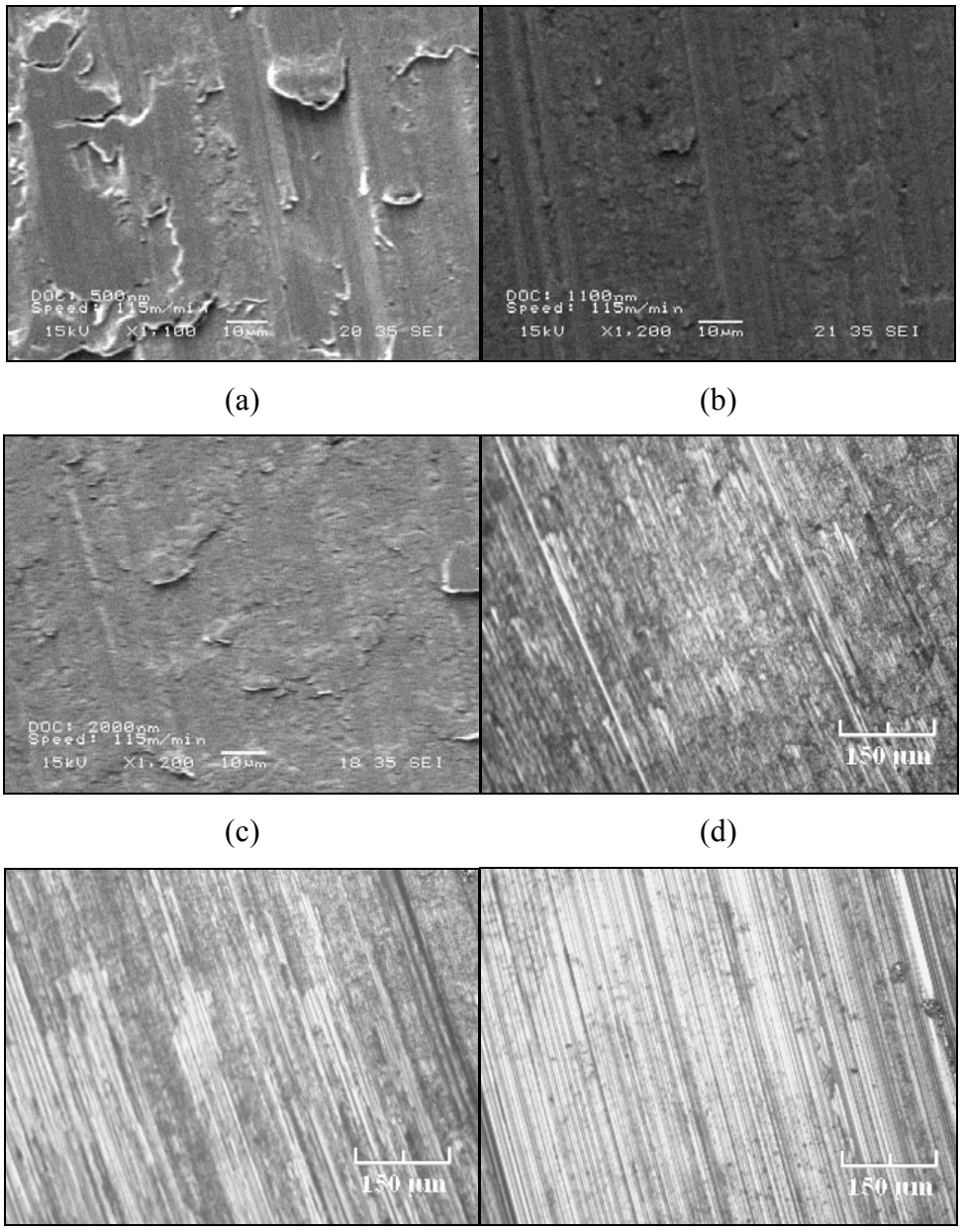

Figure B.8: Effects of Undeformed Chip Thickness on Surface Roughness at Cutting Speed of 115 m/min. Undeformed Chip Thickness: (a) 0.5 µm (b) 1.1 µm (c) 2.0 µm (d) 10 µm (e) 20 µm (f) 40 µm (g) 60 µm

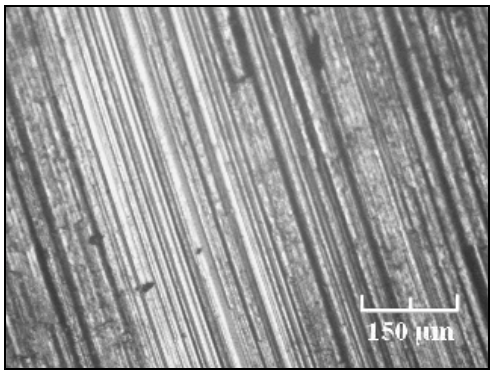

(g)

Figure B.8 (continued)

APPENDIX C: MODEL PREDICTION VALUES

Table C.1: Average Force Value and Shear Angle – Cutting Speed of 10 m/min (AL7075)

Undeformed Chip Thickness (nm)	Cutting Force, F_c (N)	Thrust Force, F_t (N)	Shear Angle, ϕ (º)
10	0.366	0.536	0.7
40	0.337	0.450	3.5
70	0.471	0.585	7.0
100	0.398	0.410	
400	0.750	0.556	18.3
700	1.467	0.900	29.8
1000	1.932	1.051	33.9
1400	2.672	1.453	27.7
1700	3.006	1.460	20.2
2000	3.348	1.466	8.8

Table C.2: Average Force Value and Shear Angle – Cutting Speed of 150 m/min (AL7075)

Undeformed Chip Thickness (nm)	Cutting Force, F_c (N)	Thrust Force, F_t (N)	Shear Angle, ϕ (º)
10	0.078	0.303	
40	0.155	0.429	
70	0.373	0.540	
100	0.438	0.409	8.9
400	0.813	0.589	
700	1.447	0.735	20.3
1000	1.786	0.827	24.1
1400	2.309	0.893	31.9
1700	2.625	0.944	30.8
2000	3.000	0.997	28.6

Table C.3: Predicted Force Value and Shear Angle Using Oxley's Model – Cutting Speed of 10 m/min (AL7075)

Undeformed Chip Thickness (nm)	Strain Rate Coefficient, C	Predicted Cutting Force, F_c (N)	Predicted Thrust Force, F_t (N)	Predicted Shear Angle, ϕ (º)
100	8.5	0.461	0.419	11.8
400	8	1.447	1.207	14.2
700	8	2.432	1.994	14.1
1000	8	3.281	2.629	14.6
1400	8	4.320	3.364	15.2
1700	8	5.076	3.899	15.5
2000	8	5.794	4.387	15.8

Table C.4: Predicted Force Value and Shear Angle Using Oxley's Model – Cutting Speed of 150 m/min (AL7075)

Undeformed Chip Thickness (nm)	Strain Rate Coefficient, C	Predicted Cutting Force, F_c (N)	Predicted Thrust Force, F_t (N)	Predicted Shear Angle, ϕ (º)
100	8	0.359	0.272	15.8
400	7.5	1.092	0.714	18.8
700	7.5	1.719	1.053	19.8
1000	7.5	2.287	1.336	20.5
1400	7.5	2.986	1.660	21.2
1700	7.5	3.495	1.901	21.5
2000	7.5	3.965	2.093	21.9

Table C.5: Average Force Value and Shear Angle – Cutting Speed of 10 m/min (P20)

Undeformed Chip Thickness (μm)	Cutting Force, F_c (N)	Thrust Force, F_t (N)	Shear Angle, ϕ (º)
0.3	5.81	5.71	
0.5	6.12	4.75	
0.7	6.89	4.83	
0.9	8.08	5.36	
1.1	9.35	6.01	
1.3	10.38	6.53	
1.5	11.78	7.31	
1.7	12.57	7.80	
2.0	14.25	8.74	
5.0	30.06	15.34	24.4
10	47.69	21.98	33.4
20	94.14	42.83	32.8
30	131.61	57.72	30.0
40	167.29	73.17	21.1
50	216.90	96.47	19.0
60	253.75	111.08	44.8

Table C.6: Average Force Value and Shear Angle – Cutting Speed of 115 m/min (P20)

Undeformed Chip Thickness (μm)	Cutting Force, F_c (N)	Thrust Force, F_t (N)	Shear Angle, ϕ (º)
0.3	4.03	3.11	
0.5	5.55	4.03	
0.7	6.92	4.95	
0.9	7.99	5.67	
1.1	8.98	6.25	
1.3	9.93	6.83	
1.5	10.96	7.49	
1.7	11.80	7.94	
2.0	12.86	8.47	
5.0	27.24	18.17	10.4
10	46.12	34.13	21.0
20	75.97	52.20	45.7
30	99.64	67.09	28.3
40	126.06	83.19	32.3
50	163.65	131.13	26.9
60	189.53	149.99	31.1

Table C.7: Predicted Force Value and Shear Angle Using Oxley's Model – Cutting Speed of 10 m/min (P20)

Undeformed Chip Thickness (μm)	Strain Rate Coefficient, C	Predicted Cutting Force, F_c (N)	Predicted Thrust Force, F_t (N)	Predicted Shear Angle, ϕ (º)
10	7	74.42	84.85	6.4
20	6	80.98	73.31	12.0
30	6	110.67	95.35	13.1
40	6	140.15	116.85	13.7
50	6	169.18	137.72	14.1
60	6	197.75	158.10	14.4

Table C.8: Predicted Force Value and Shear Angle Using Oxley's Model – Cutting Speed of 115 m/min (P20)

Undeformed Chip Thickness (μm)	Strain Rate Coefficient, C	Predicted Cutting Force, F_c (N)	Predicted Thrust Force, F_t (N)	Predicted Shear Angle, ϕ (º)
10	7	51.66	51.14	9.2
20	5	51.20	30.02	20.7
30	5	72.47	39.51	21.7
40	5	92.88	48.01	22.4
50	5	112.17	55.42	23.1
60	5	130.38	61.64	23.8

Table C.9: Predicted Force Value and Shear Angle Using Endres' Model – Cutting Speed of 10 m/min (AL7075)

Undeformed Chip Thickness (nm)	Predicted Cutting Force, F_c (N)	Predicted Thrust Force, F_t (N)
10	0.047	0.025
40	0.136	0.070
70	0.137	0.063
100		
400	0.356	0.111
700	0.415	0.073
1000	0.531	0.068
1400	0.878	0.174
1700	1.388	0.398
2000	3.348	1.466

Table C.10: Predicted Force Value and Shear Angle Using Endres' Model – Cutting Speed of 150 m/min (AL7075)

Undeformed Chip Thickness (nm)	Predicted Cutting Force, F_c (N)	Predicted Thrust Force, F_t (N)
10		
40		
70		
100	0.372	0.306
400		
700	1.360	0.707
1000	1.706	0.736
1400	1.941	0.515
1700	2.416	0.693
2000	3.000	0.997

Table C.11: Predicted Force Value and Shear Angle Using Endres' Model – Cutting Speed of 10 m/min (P20)

Undeformed Chip Thickness (μm)	Predicted Cutting Force, F_c (N)	Predicted Thrust Force, F_t (N)
5.0	19.11	7.56
10	29.79	8.09
20	55.99	13.18
30	87.82	22.97
40	149.59	57.75
50	202.23	84.90
60	253.63	111.03

Table C.12: Predicted Force Value and Shear Angle Using Endres' Model – Cutting Speed of 115 m/min (P20)

Undeformed Chip Thickness (μm)	Predicted Cutting Force, F_c (N)	Predicted Thrust Force, F_t (N)
5.0	26.98	49.21
10	38.93	47.30
20	54.81	16.23
30	97.03	74.68
40	121.23	71.91
50	163.67	131.14
60	181.06	105.19

REFERENCES

1. Adams, D.P., Vasile, M.J., Benavides, G., Campbell, A.N., 2001, Micromilling of metal alloys with focused ion beam-fabricated tools, Precision Engineering, Vol. 25, 107-113

2. Adibi-Saleh, A., H., Madhavan, V., Bahr, B., 2003, Extension of Oxley's Analysis of Machining to Use Different Material Model, Journal of Manufacturing Science and Engineering, v 125, 656 – 666

3. Albrecht, P., 1960, New Developments in the Theory of the Metal-Cutting Process Part 1. The Ploughing Process in Metal Cutting, Journal of Engineering for Industry, Vol 82, 348 – 358

4. Albrecht, P., 1961, New Developments in the Theory of The Metal-Cutting Process Part 2. The Theory of Chip Formation, Journal of Engineering for Industry, Vol 83, 557 – 571

5. Amatucci, E., Dagalakis, N., Damazo, B., Davies, M., Evans, J., Song, J., Teague, C., Vorburger, T., 2000, An Overview of Nano-Micro-Meso Scale Manufacturing at the National Institute of Standards and Technology (NIST), Nanotribology: Critical Assessment and Future Research Needs

6. Anon, 2000, The properties and characteristics of aluminium alloys and their suitability for moulding thermoplastics, Metallurgia Italiana, v 92, n 3, 38 – 39

7. Armarego, E.J.A., 1969, The Machining of Metals, Prentice-Hall, Inc.

8. Arsecularatne, J.A., Oxley P. L. B., 1997, Prediction of cutting forces in machining with restricted contact tools, J. Mach. Sc. & Tech., 1(1), 95-112.

9. Arsecularatne, J.A., Kristyanto, B., Mathew, P., 2004, An Investigation of the High Speed Machining Process Using A Variable Flow Stress Machining Theory, Machining Science and Technology, v 8 n 2, 211 – 233

10. Ashida, K., Morita, N., Yoshida, Y., 2001, Study on Nano-machining Process Using Mechanism of a Friction Force Microscope, JSME International Journal Series C, Vol. 44, 244-253

11. Atkins, A.G., 2005, Toughness and Cutting: A New Way of Simultaneously Determining Ductile Fracture Toughness and Strength, Engineering Fracture Mechanics, 72, 849 – 860

12. Atkins, A.G., 2003, Modelling Metal Cutting Using Modern Ductile Fracture Mechanics: Quantitative Explanations for Some Longstanding Problems, International Journal of Mechanical Sciences, 45, 373 – 396

13. Backer, W.R., Marshall, E.R., Shaw, M.C., 1952, The Size Effect in Metal Cutting, Transactions of the ASME, 61-72

14. Banks, D., 1997, General Introduction to Micromachining, IEE Colloquium (Digest), n 76, 1 – 6

15. Bhattacharyya, B., Doloi, B., Sridhar, P.S., 2001, Electrochemical micro-machining: new possibilities for micro-manufacturing, Journal of Materials Processing Technology, Vol. 113, 301-305

16. Blau, P. J., 1996, Friction Science and Technology, Marcel-Dekker Inc.

17. Breguet, JM., Schmitt, C., Clavel, R., 2000, Micro/Nanofactory: Concept and State Of The Art, SPIE Vol. 4 4194, 1-12

18. Chang, W.J., Fang, T.H., Weng, C.I., 2004, Inverse Determination of the Cutting Force on Nanoscale Processing Using Atomic Force Microscopy, Nanotechnology, Vol. 15, 427-430

19. Corbett, J., McKeown, P.A., Peggs, G.N., Whatmore, R., 2000, Nanotechnology: International Developments and Emerging Products, Annals of the CIRP Vol. 49, 1-23

20. Cox, D., Newby, G., Park, H.Y., Liang, S.Y., 2004, Performance Evaluation of A Miniaturized Machining Center for Precision Manufacturing, ASME International Mechanical Engineering Congress and Exposition

21. Drescher, J.D., Dow, T.A., 1990,Tool force model development for diamond turning, Precision Engineering, Vol. 12, 29-35

22. Eda, H., Kishi, K., Nomura, K., Hashimoto, H., Ito, H., 1985, Formation Mechanism of Ultraprecision Machined Surface with a Single Point Diamond Tool, Bull. Japan Soc, of Prec. Emgg., Vol. 19, No. 2, 126-128

23. Endres, W.J., Devor, R.E., Kapoor, S.G., 1995, A Dual-Mechanism Approach to the Prediction of Machining Forces, Part 1: Model Development, Journal of Engineering for Industry, Vol. 117, 526 – 533

24. Endres, W.J., Devor, R.E., Kapoor, S.G., 1995, A Dual-Mechanism Approach to the Prediction of Machining Forces, Part 2: Calibration and Validation, Journal of Engineering for Industry, Vol. 117, 534 – 541

25. Evans, C., 1991, Cryogenic Diamond Turning of Stainless Steel, Annals of the CIRP, Vol. 40, 571-575

26. Fang F.Z., Venkatesh, V.C., 1998, Diamond Cutting of Silicon with Nanometric Finish, Annals of the CIRP - Manufacturing Technology, v 47, n 1, 45 – 49

27. Fang, N., 2003, Slip-line Modeling of Machining with a Rounded-Edged Tool – Part 1: New Model and Theory, Journal of the Mechanics and Physics of Solids, 51, 715 – 742

28. Fang, N., 2003, Slip-line Modeling of Machining with a Rounded-Edged Tool – Part 2: Analysis of the Size Effect and the Shear Strain-Rate, Journal of the Mechanics and Physics of Solids, 51, 743 – 762

29. Friedrich, C.R., 2002, Micromechanical machining of high aspect ratio prototypes, Microsystem Technologies, Vol. 8, 343-347

30. Friedrich, C., Kikkeri, B., 1995, Rapid Fabrication of molds by mechanical micromilling: Process Development, Proceedings of the SPIE - The International Society for Optical Engineering, Vol. 2640, 161-171

31. Furukawa, Y., Moronuki, N., 1988, Effect of Material Properties on Ultra Precise Cutting Processes, CIRP Annals, Vol. 137, 113-116

32. Gao, W., Hocken, R. J., Patten, J. A., Lovingood, J., 2000, Experiments Using a Nano-Machining Instrument for Nano-Cutting Brittle Material, Annals of the CIRP Vol 49 n 1, 439 – 442

33. Gao, W., Hocken, R. J., Patten, J. A., Lovingood, J., Lucca, Don A., 2000, Construction and Testing of A Nanomachining Instrument, Journal of the International Societies for Precision Engineering and Nanotechnology 24, 320-328

34. Geiger, M., Kleiner, M., Eckstein, R., Tiesler, N., Engel, U., 2001, Microforming, Annals of the CIRP Vol. 50, 1-18

35. Hasegawa, Y., Hanasaki, S., Yasutomi, M., 1975, The Cutting Mechanism of Large Crystals of Fe-3.5% Si, Journal of the Japan Institute of Metals, v 39 n 8, 809-817

36. Hsu, T.R., 2002, MEMS & Microsystems Design and Manufacture, McGraw-Hill

37. Ikawa, N., Shimada, S., Tanaka, H., 1992, Minimum Thickness of Cut in Micromachining, Nanotechnology, Vol. 3, 6-9

38. Ikawa, N., Shimada, S., Tanaka, H., Ohmori, G., 1991, An Atomistic Analysis of Nanometric Chip Removal as Affected by Tool-Work Interaction in Diamond Turning, Annals of the CIRP, Vol. 40, 551-554

39. Inamura, T., Takezawa, N., Kumaki, Y., 1993, Mechanics and Energy Dissipation in Nanoscale Cutting, Annals of the CIRP Vol. 42, 79-82

40. Johnson, G. J., Cook, W. H., 1983, A Constitutive Model and Data for Metals Subjected to Large Strains, High Strain Rates and High Temperatures, Proceedings of the 7th International Symposium on Ballistics, 541–547

41. Joshi, S.S., Melkote, S.N., 2004, An Explanation for the Size-Effect in Machining Using Strain Gradient Plasticity, Journal of Manufacturing Science and Engineering, Vol. 126, 679-684

42. Kemmann, O., Schaumburg, C., Weber, L., 1999, Micro moulding behaviour of engineering plastics, Symposium on Design, Test and Microfabrication of MEMS and MOEMS, Paris, France, SPIE Vol. 3680, 464-471

43. Kim, C.J., Bono, M., Ni, J., 2002, Experimental Analysis of Chip Formation in Micro-Milling, Transaction of NAMRI/ SME, Vol. XXX, 247 – 254

44. Kim, J.D., Kim, D.S., 1996, On the Size Effect of Micro-Cutting Force in Ultra Precision Machining, JSME International Journal, Series C Vol. 39 No. 1, 164 – 169

45. Kim, K.W., Lee, W.Y., Sin, H.C., 1999, A Finite Element Analysis for the Characteristics of Temperature and Stress in Micro-Machining Considering the Size Effect, International Journal of Machine Tool and Manufacture, V 39, 1507 – 1524

46. Kiwamu, A., Noboru, M., Yoshitaro, Y., 2001, Study on Nano-machining Process Using Mechanism of a Friction Force Microscope, JSME International Journal, Vol. 44, No.1, 244-253

47. Komanduri, R., Chandrasekaran, N., Raff, L.M., 1998, Effect of Tool Geometry in Nanometric Cutting: A Molecular Dynamics Simulation Approach, Wear, 219, 84 – 97

48. Komanduri, R., 1971, Some Aspects of Machining with Negative Rake Tools Simulating Grinding, Int. J. Mach. Tool Des. Res., Vol. 11, 223 – 233

49. Kopalinsky, E. M., Oxley, P. L. B., 1984, Size effects in metal removal process 3rd Conf. Mech. Prop. High Rates of Strain, Oxford, 389–396.

50. Kountanya, R.K., Endres, W.J., 2001, A High-Magnification Experimental Study of Orthogonal Cutting with Edge-Honed Tools, Proceedings of 2001 ASME International Mechanical Engineering Congress and Exposition

51. Kountanya, R.K., Endres, W.J., 2004, Flank Wear of Edge-Radiused Cutting Tools Under Ideal Straight Edged Orthogonal Conditions, Journal of Manufacturing Science and Technology, Vol. 126, 496 – 505

52. Lee, K., Dornfield, D.A., 2002, An Experimental Study on Burr Formation in Micro Milling Aluminum and Copper, Transaction of NAMRI/ SME, Vol XXX, 255 – 262

53. Lee W.B., Cheung C.F., 2001, Dynamic Surface Topography Model for the Prediction of Nano-Surface Generation in Ultra-Precision Machining, International Journal of Mechanical Sciences, v 43, n 4, 961 – 991

54. Lee, W.B., Cheung, C.F., To, S., 2001, Characteristics of Microcutting Force Variation In Ultraprecision Diamond Turning, Materials and Manufacturing Processes, 16(2), 177-193

55. Lee, W.B., To, S., Sze, Y.K., Cheung, C.F., 2003, Effect of material anisotropy on shear angle prediction in metal cutting – a mesoplasticity approach, International Journal of Mechanical Sciences, Vol. 45, 1739-1749

56. Lee, W.S., Sue, W.C., Lin, C.F., Wu, C.J., 2000, The Strain Rate and Temperature Dependence of the Dynamic Impact Properties of 7075 Aluminum Alloy, Journal of Materials Processing Technology, 100, 116 – 122

57. Li, X.P., Rahman, M., Neo, K.S., Chan, C.C., 2003, Nano-Precision Measurement of Diamond Tool Edge Radius for Wafer Fabrication, Journal of Materials Processing Technology, v 140, 358 – 362

58. Liang, Y., Moronuki, N., Furukawa, Y., 1994, Calculations of the effect of material anisotropy on microcutting processes, Precision Engineering, vol. 16, 2, 132 - 138

59. Lin, Z.C., Huang, J.C., 2004, A Nano-Orthogonal Cutting Model Based on A Modified Molecular Dynamics Technique, Nanotechnology, 15, 510 – 519

60. Liu, K., Melkote, S.N., 2004, A Strain Gradient Based Finite Element Model for Micro/ Meso-scale Orthogonal Cutting Process, Proceedings of 2004 Japan-USA Symposium on Flexible Automation

61. Liu, K., Li, X.P., Liang, S.Y., 2003, Nanometer Scale Ductile Cutting of Tungsten Carbide, Transactions of NAMRI/SME, Vol. XXXI, 153-160

62. Liu, X., Devor R.E., Kapoor, S.G., 2004, The Mechanics of Machining at the Microscale: Assessment of the Current State of the Science, Journal of Manufacturing Science and Engineering, Vol. 126, 666-678

63. Liu, X.Y., Jun, M.B.G., Devor, R.E., Kapoor, S.G., 2004, Cutting Mechanisms and Their Influence on Dynamic Forces, Vibrations and Stability in Micro-Endmilling, ASME International Mechanical Engineering Congress

64. Lu, Z.N., Yoneyama, T., 1999, Micro Cutting In The Micro Lathe Turning System, International Journal of Machine Tools & Manufacture 39, 1171-1183

65. Lucca, D.A., Rhorer, R.L., Komanduri, R, 1991, Energy dissipation in the ultraprecision machining of copper, CIRP Annals, v 40 n 1, Manufacturing Technology, 69-72

66. Lucca, D.A., Seo, Y.W., 1994, Aspects of Surface Generation in Orthogonal Ultraprecision Machining, Annals of the CIRP, Vol. 43, 43-46

67. Lucca, D.A., Seo, Y.W., 1993, Effect of Tool Edge Geometry on Energy Dissipation in Ultraprecision Machining, Annals of the CIRP, Vol. 42, 83-86

68. Lucca, D.A., Seo, Y.W., Rhorer, R.L., 1994, Energy dissipation and tool-workpiece contact in ultra-precision machining, S T L E Tribology Transactions, v 37 n 3, 651-655

69. MacGeough, J.A., Leu, M.C., Rajurkar, K.P., De Silva, A.K.M., Liu, Q., 2001, Electroforming Process and Application to Micro/Macro Manufacturing, Annals of the CIRP, Vol. 50 No. 2, 1-16

70. Maekawa, K., Itoh, A., Hojo, Y., 1995, Molecular Dynamics Investigation of Tribological Phenomena in Nanoscale Machining, Transactions of the Japan Society of Mechanical Engineers, Part A, v 61, n 586, 1391-1397

71. Manjunathaiah, J., Endres, W. J., 2000, A New Model and Analysis of Orthogonal Machining With an Edge-Radiused Tool, Journal of Manufacturing Science and Engineering, Vol. 122, 384 – 390

72. Manjunathaiah, J., Endres, W. J., 2000, A Study of Apparent Negative Rake Angle and its Effect on Shear Angle During Orthogonal Cutting with Edge-Radiused Tools, Transaction of NAMRI/ SME, Vol. XXVIII, 197 – 202

73. Masuzawa, T., 2000, State of the Art of Micromachining, Annals of the CIRP Vol. 49, 1-13

74. Masuzawa, T., Tonshoff H.K., 1997, Keynote Papers: Three-Dimensional Micromachining by Machine Tools, Annals of the CIRP Vol.46, 621-628

75. Merchant, M.E., 1945, Mechanics of the Metal Cutting Process 1. Orthogonal Cutting and a Type 2 Chip, Journal of Applied Physics, Vol. 16, 267 – 275

76. Moneim, A., 1980, Tool Edge Roundness in Finish Machining at High Cutting Speeds, Wear, Vol. 58, 173-192

77. Moriwaki, T., Okuda, K., Shen, J. G., 1993, Study of Ultraprecision Orthogonal Microdiamond Cutting of Single-Crystal Copper, JSME International Journal, Series C, Vol 36, No. 3, 400 – 406

78. Moronuki, N., Liang, Y., Furukawa, Y., 1994, Experiments on the effect of material properties on microcutting processes, Precision Engineering, Vol., 16, No. 2, 124-131

79. Mu, Y.H., Hung, N.P., Ngoi, K.A., 2000, Monitoring a Sub-Newton Cutting Force for Ultra-Precision Machining, The International Journal of Advanced Manufacturing Technology, Vol. 16, 229-232

80. Nakao, M., Tsuchiya, K., Matsumoto, K., Hatamura, Y., 2001, Micro Handling with Rotational Needle-type Tools Under Real Time Observation, Annals of the CIRP Vol. 50, 9-12

81. Nakayama, K., Tamura, K., 1968, Size Effect in Metal-Cutting Force, Journal of Engineering for Industry, 119-126

82. Nakayama, K., 1997, Topics on Fundamentals of Precision Machining, Machining Science and Technology 1(2), 251 – 262

83. Nomura, T., Suzuki, R., 1992, Six-axis controlled nanometer-order positioning stage for microfabrication, Nanotechnology, Vol. 3, 21-28

84. Ohmori, G., Takada, S., 1982, Primary Factors Affecting Accuracy in Ultra-Precision Machining by Diamond Tool, Bull. Japan Soc. Of Prec. Engg., Vol. 16, No. 1, 3-7

85. Oxley, P.L.B., 1989, Mechanics of Machining, An Anlaytical Approach to Assessing Machinability", Halsted Press, New York

86. Piotter, V., Benzler, T., Hanemann, T., Wollmer, H., Ruprecht, R., Hauβelt, J., 1999, Innovative Moulding Technologies for the Fabrication of Components for Microsystems, Symposium on Design, Test and Microfabrication of MEMS and MOEMS, Paris, France, SPIE Vol. 3680, 456-463

87. Ramesh, A., 2002, Prediction of Process Induced Microstructural Changes and Residual Stresses in Orthogonal Hard Machining, Ph.D. Dissertation, Georgia Institute of Technology, Department of Mechanical Engineering

88. Raczy, A., Elmadagli, M., Altenhof, W.J., Alpas, A.T., 2004, An Eulerian Finite-Element Model For Determination of Deformation State of a Copper Subjected to Orthogonal Cutting, Metallurgical and Materials Transactions A, Vol. 35, 2393 – 2400

89. Rentsch, R., 2000, Atomistic Simulation and Experimental Investigation of Ultra-Precision Cutting Processes, Materials Research Society Symposium Proceedings, Vol. 578, 261-266

90. Rother, B.K., 2004, Micromachining in Exotic Materials, ASME International Mechanical Engineering Congress and RD&D Exhibition

91. Sato, M., Yamazaki, T., Shimizu, Y., Takabayashi, T., 1991, A Study on the Microcutting of Aluminum Single Crystals, JSME International Journal Series III, Vol. 34, No. 4, 540-545

92. Schimmel, R.J., Endres, W.J., 2002, Application of an Internally Consistent Material Model to Determine the Effect of Tool Edge Geometry in Orthogonal Machining, Journal of Manufacturing Science and Technology, Vol. 124, 536 – 543

93. Schimmel, R.J., Manjunathaiah, J., and Endres, W.J., 2000, "Edge Radius Variability and Force Measurement Considerations," Journal of Manufacturing Science and Engineering., 122, 590-593;

94. Shatla, M., Kerk, C., Altan, T., 2001, Process Modeling in Machining. Part I: Determination of Flow Stress Data, International Journal of Machine Tool & Manufacture, v 41, 1511 – 1534

95. Shatla, M., Kerk, C., Altan, T., 2001, Process Modeling in Machining, Part II: Validation and Applications of the Determined Flow Stress Data, International Journal of Machine Tools and Manufacture, v 41, 1659-1680

96. Shaw, M.C., 1984, Metal Cutting Principles, Oxford Press Inc. NY

97. Shaw, M.C., 2003, The Size Effect in Metal Cutting, Sadhana, Vol. 28, 875-896

98. Shimada, S., Ikawa, N., Ohmori, G., Tanaka, H., Uchikoshi, J., 1992, Molecular Dynamics Analysis as Compared with Experimental Results of Micromachining, Annals of the CIRP, Vol. 41, 117-120

99. Shimada, S., Ikawa, N., Tanaka, H., Ohmori, G., Uchikoshi, J., 1993, Molecular Dynamics Analysis of Cutting Force and Chip Formation Process in Microcutting, Journal of the Japan Society for Precision Engineering, Vol. 59, 2015-2021

100. Shinno H., Hashizume H., Ito Y. and Sato C., 1992, Structural Configuration and Performances of Machining Environment-Controlled Ultraprecision Diamond Turning Machine `CAPSULE', Annals of the CIRP, 41-1, 425-428

101. Sumomogi, T., Nakamura, M., Endo, T., Goto, T., Kaji, S., 2002, Evaluation of surface and subsurface cracks in nanoscale-machined single-crystal silicon by scanning force microscope and scanning laser microscope, Materials Characterization, Vol. 48, 141-145

102. Takeuchi, Y., Murota, M., Kawai, T., Sawada, K., 2003, Creation of Flat-End V-Shaped Microgrooves by Non-Rotational Cutting Tools, Annals of the CIRP, vol. 52, No. 1, 41-44

103. Tanaka, M., 2001, Development of desktop machining microfactory, RIKEN Review, Vol. No. 34, 46-49

104. Tiesler, N.A., 2002, Microforming – Size Effect in Friction and Their Influence on Extrusion Process, Wire, v 52, 34 – 38

105. To, S., Lee, W.B., Chan, C.Y., 1997, Ultraprecision Diamond Turning of Aluminium Single Crystals, Journal of Materials Processing Technology, Vol. 63, 157-162

106. Toyoshiro, I., Nobuhiro, T., Yasuhiro, K., 1993, Mechanics and Energy Dissipation in Nanoscale Cutting, Annals of the CIRP, Vol. 42, 79-82

107. Toyoshiro, I., Nobuhiro, T., Yasuhiro, K., Toshio, S., 1994, On A Possible Mechanism of Shear Deformation in Nanoscale Cutting, Annals of the CIRP, Vol., 43, 47-50

108. Trent, E.M., 1984, Metal Cutting, London; Boston : Butterworths

109. Ueda, K., Fu, H.N., Manabe, K., 1999, Atomic Scale Level Chip Formation of Amorphous Metal Investigated by Using AFM and MD-RPFEM Simulation, Machining Science and Technology, Vol. 3, 61-75

110. Ueda, K., Manabe, K., 1992, Chip Formation Mechanism in Microcutting of an Amorphous Metal, Annals of the CIRP, Vol. 41, 129-132

111. Ueda, T., Sato, M., Kanada, Y., Sugita, T., 1994, Chip Forming Temperature on Micro Cutting (1st Report) – Measurement of Tool Tip Temperature by Infrared Radiation Pyrometer with Optical Fiber, Journal of the Japan Society for Precision Engineering, Vol. 60 No. 3, 383-387

112. Van Brussel, H., Peirs, J., Reynaerts, D., Delchambre, A., Reinhart, G., Roth, N., Weck, M., Zussman, E., 2000, Assembly of Microsystems, Annals of the CIRP Vol. 49, 1-21

113. Volger, M.P., Liu, X., Kapoor, S.G., Devor, R.E., Ehmann, K.F., 2002, Development of Meso-Scale Machine Tool (mMT) Systems, Transactions of NAMRI/ SME, Vol. XXX, 653 – 661

114. Volger, M.P., Kapoor, S.G., Devor, R.E., 2004, On the Modeling and Analysis of Machining Performance Part I: Surface Generation, Journal of Manufacturing Science and Engineering, Vol. 126, 685 – 694

115. Volger, M.P., Kapoor, S.G., Devor, R.E., 2004, On the Modeling and Analysis of Machining Performance Part II: Cutting Force Prediction, Journal of Manufacturing Science and Engineering, Vol. 126, 695 – 705

116. Von Turkovich, B.F., Black, J.T., 1970, Micro-Machining of Copper and Aluminum Crystals, Journal of Engineering for Industry, Vol. 92, Series B n 1, 130-134

117. Waldorf, D.J., Devor, R.E., Kapoor, S.G., 1998, A Slip-Line Field for Ploughing During Orthogonal Cutting, Journal of Manufacturing Science and Engineering, Vol. 120, 693 – 699

118. Waldorf, D.J., Devor, R.E., Kapoor, S.G., 1999, An Evaluation of Ploughing Models for Orthogonal Machining, Journal of Manufacturing Science and Engineering, Vol. 121, 550 – 558

119. Weck, M., Fischer, S., 1999, Manufacturing of Microstructures using Ultraprecision Machine Tools, SPIE, Vol. 3680, 450-455

120. Weule, H., Huntrup, V., Tritschler, H., 2001, Micro-Cutting of Steel to Meet New Requirements in Miniaturization, CIRP Annals – Manufacturing Technology, 50, 61-64

121. Yuan Z.J., He J.C., Yao Y.X., 1992, The Optimum Crystal Plane of Natural Diamond Tool for Precision Machining, Annals of the CIRP, v 41, n 1, 605-608

122. Zorev, N.N., 1966, Metal Cutting Mechanics, Pergamon Press Ltd.